Cosmic Rays and the Radio Neutrino Observatory Greenland (RNO-G)

der Naturwissenschaftlichen Fakultät
der Friedrich-Alexander-Universität Erlangen-Nürnberg
zur Erlangung des Doktorgrades Dr. rer. nat.

vorgelegt von

Lilly Marie Pyras

Als Dissertation genehmigt
von der Naturwissenschaftlichen Fakultät
der Friedrich-Alexander-Universität Erlangen-Nürnberg

Tag der mündlichen Prüfung: 22.07.2024

Gutachter/in:
Prof. Dr. Anna Nelles
Prof. Dr. Mauricio Bustamante

Abstract

Neutrinos are unique messengers, as they travel unimpeded over cosmological distances, pointing back to their sources. As their production is tightly coupled to that of ultra-high energy cosmic rays, they could help us to understand the ultra-high energy universe. However, the expected neutrino flux at the highest energies is very low, and the detection of neutrinos is difficult due to their small cross section. Therefore, measuring the neutrino flux requires large detection volumes of dense media. One such effort is the Radio Neutrino Observatory Greenland (RNO-G), which targets the detection of neutrinos above PeV energies in the Greenlandic ice shield. When a neutrino interacts with a nucleus in the ice, it induces particle cascades that produce radio emission via the Askaryan effect. The attenuation length of glacial ice is $\mathcal{O}(1\,\mathrm{km})$ at radio frequencies which allows for large, and sparsely instrumented detection volumes. The hybrid design, consisting of antennas deep in the ice and shallow antennas just below the surface, also provides sensitivity to cosmic ray air showers, which improves background rejection for in-ice neutrino events.

The focus of this work is the precise estimation of air showers in RNO-G and the identification of atmospheric muons originating from air showers. For this purpose, the surface signal chain of the shallow detector component and its diode trigger are characterized. The digitizer board and trigger are tested for functionality and performance prior to deployment. These studies are essential for understanding the measured signals and making robust event rate predictions. To obtain the number of detected cosmic rays, a detailed Monte Carlo study is performed, which suggests that 5^{+5}_{-2} air showers per day and seven RNO-G stations are expected to be measured. The energy threshold is around 10^{17} eV and depends strongly on the trigger threshold. The performance in air shower detection has a direct impact on the identification of neutrinos, since ultra-high energy muons from air showers are a relevant background for in-ice neutrino detection. Their event rate is subject to large uncertainties due to the extrapolation of hadronic interactions from accelerator energies to the highest energies and the uncertainty of the measured composition of cosmic rays. For every muon, the detection of the corresponding air shower can be used as a veto mechanism. A measurement of the atmospheric muon flux above PeV energies would provide a handle on the forward charm production in quantum chromodynamics.

Zusammenfassung

Neutrinos sind einzigartige Botenteilchen, da sie ungehindert kosmologische Distanzen überwinden und ihre Richtung direkt auf den Ort ihre Entstehung verweist. Ihre Produktion ist eng an die von ultrahochenergetischer kosmischer Strahlung gekoppelt. So können sie uns helfen das Universum bei ultrahohen Energien zu verstehen. Allerdings ist der erwartete Neutrinofluss bei den höchsten Energien sehr gering, und ihr Nachweis ist aufgrund des geringen Wirkungsquerschnitts schwierig. Die Messung des Neutrinoflusses erfordert daher ein großes Detektorvolumen eines dichten Mediums. Das Radio-Neutrino-Observatorium Grönland (RNO-G) ist ein Versuch, Neutrinos oberhalb von PeV Energien im Grönländischen Eisschild zu messen. Wenn ein Neutrino mit einem Atmokern im Eis wechselwirkt, löst es Teilchenkaskaden aus, die durch den Askaryan-Effekt Radioemissionen erzeugen. Die Dämpfungslänge von Gletschereis ist $\mathcal{O}(1\,\mathrm{km})$ bei Radiofrequenzen und ermöglicht große und sparsam instrumentierte Detektionsvolumen. Das hybride Design, bestehend aus Antennen tief im Eis und Antennen knapp unter der Oberfläche, bietet auch die Möglichkeit Luftschauer, ausgelöst von kosmischer Strahlung, zu messen, und so die Hintergrundsignale für die Messung von Neutrinos im Eis zu reduziert.

Der Schwerpunkt dieser Arbeit liegt auf der präzisen Vorhersage von Luftschauern und ihrer Messung mit RNO-G sowie der Identifizierung von atmosphärischen Myonen, die aus Luftschauern stammen. Dafür wird die Signalverarbeitung des Oberflächendetektors von RNO-G sowie der Diodentrigger charakterisiert. Die Leiterplatte mit dem Digitalisierer sowie der Trigger werden vor ihrer Inbetriebnahme auf Funktion und Performance getestet. Diese Untersuchungen sind unerlässlich, um die gemessenen Signale zu verstehen und Vorhersagen der Ereignisrate zu erstellen. Um die Anzahl der Luftschauer zu ermitteln, wird eine detaillierte Monte-Carlo-Studie durchgeführt, die zeigt, dass die Messung von 5^{+5}_{-2} Luftschauer pro Tag und sieben RNO-G Stationen erwartet werden kann. Die Energieschwelle liegt bei 10^{17} eV und hängt stark von der Auslöseschwelle des Triggers ab. Die Effizienz der Luftschauerdetektion wirkt sich direkt auf die Identifizierung von Neutrinoereignissen aus, da die ultrahochenergetische Myonen, einen relevanten Hintergrund für eine Neutrino detektion im Eis darstellen. Ihre Ereignisrate ist aufgrund der Extrapolation der hadronischen Wechselwirkungen von Beschleunigerenergien bis zu den höchsten Energien und der unbekannten Zusammensetzung der kosmischen Strahlung mit großen Unsicherheiten behaftet. Bei jedem Myon kann die Detektion des entsprechenden Luftschauers als Veto-Mechanismus verwendet werden. Eine Messung des atmosphärischen Myonenflusses oberhalb von PeV-Energien würde Aufschluss über die Produktion von Hadronen mit Charm Quarks bei kleinen Winkeln in der Quantenchromodynamik geben.

Table of Contents

1 Introduction

The study of cosmic rays and neutrinos is the study of nature at its most extreme. These particles span the gap between seemingly disparate disciplines that make up astroparticle physics: relativity and quantum mechanics. The first governs the large, describing phenomena like the collapse of stars, the formation of galaxies, and the bending of spacetime. The latter describes the extremely small such as how two particles can annihilate into purß0e energy and be gone forever.

Cosmic rays and neutrinos are produced in some of the most violent events in the universe, such as accretion to a black hole and large stellar explosions. After traveling in the near-vacuum of space over millions of light years these particles might arrive at Earth. In this way, cosmic rays and neutrinos live in both extremes, exhibiting properties of both large-scale relativity and particle-sized quantum mechanics.

This thesis is about the detection of ultra-high energy (UHE) cosmic rays and neutrinos. The challenge is that the flux of these particle rapidly falls with higher energies, resulting in only a few cosmic rays per square kilometer per year and even fewer neutrinos. Cosmic rays are measured up to energies of 10^{20} eV, which is far beyond the energies which are accessible by human made colliders, the Large Hadron Collider at CERN accelerates protons only up 6.5×10^{12} eV [1]. These high energies make the question of the origin for example of cosmic rays all the more intriguing. The interaction of UHE cosmic rays with matter or with photons produces pions, whose decay results in a flux of UHE neutrinos. Neutrinos, being electrically neural and having a low cross section rarely interact and can therefore travel unimpeded through the Universe. Once detected at Earth, they point back to their source. However, these same properties also make them extremely difficult to measure. Larger detection volumes than those currently instrumented are needed.

One promising technique to detect UHE neutrinos is the measurement of the radio emission generated by neutrino induced particle cascades in ice. The Askaryan effect results in a nanosecond radio pulse from cascades. Due to the kilometer scale attenuation length of radio waves in ice, the antenna array can have a spacing of ~1 km. This makes it feasible to cover large detection volumes at moderate cost. The Radio Neutrino Observatory Greenland (RNO-G) is one effort to measure UHE neutrinos and shed light on the origin of UHE cosmic rays. Using a hybrid design, consisting of antennas deep in the ice and antennas just below the surface, RNO-G is also sensitive to cosmic ray air showers and provides a possibility to study air showers and their remnants above and inside the ice, which are a likely background to neutrino detection.

This work contributes to the detection of UHE neutrinos by characterizing and modeling the surface component of RNO-G with special emphasis on the cosmic ray trigger. The expected cosmic ray rate is calculated and the background introduced by ultra-high energy muons from the air shower particle cascades is studied and possible mitigation strategies analyzed.

The following chapter (Chapter 2) is an introduction to ultra-high energy cosmic rays and neutrinos and their common origin. The implications of neutrino flux measurements

above PeV energies are briefly discussed. The detection mechanism using the radio emission of the particle cascade in air and ice is explained in Chapter 3, followed by an instrument description of RNO-G (Chapter 4). In order to measure and robustly identify a neutrino or cosmic ray, the detector itself must be characterized and able to perform as designed, so extensive laboratory studies, characterizing the signal chain and the cosmic ray trigger and testing the hardware prior to deployment were performed, all of which is described in Chapter 5. Based on the hardware measurements, a detailed Monte Carlo study predicting the number of cosmic rays in RNO-G is presented in Chapter 6. In Chapter 7, the expected event rate of atmospheric muons at PeV energies originating from air showers is estimated, as they can act as a background to a neutrino. Detecting the corresponding air shower provides a veto on the muon and allows for a measurement of the atmospheric muon flux above PeV energies.

Finding the sources of ultra-high energy cosmic rays

2

The existence of cosmic rays has been known for more than a hundred years, beginning with the balloon flights of Victor Hess in 1913. He observed an increase in the ionization rate of the air with altitude, which he attributed to radiation entering the atmosphere from outer Space [2]. Later studies in the 1930s, investigating the effect of the Earth's magnetic field on this radiation, found that the radiation is highly dominated by charged (massive) particles [3]. This observation led to the term cosmic rays, and a new field of research called astroparticle physics. Cosmic rays are measured up to energies of 10^{20} eV, which is far beyond of energies which are accessible by human made colliders. These high energies make the question of their origin all the more intriguing. Despite several large-scale experiments and a variety of theories about their origin, the sources of cosmic rays remain hard identify.

When cosmic rays are accelerated, they occasionally interact with matter or photon fields at or near the source, resulting in a flux of high-energy neutrinos. Unlike cosmic rays, which are deflected by magnetic fields and interact with intervening matter and radiation, neutrinos point back to their sources and can reach Earth from large distances. Their low interaction cross section allows them to even escape the acceleration regions of high energy cosmic rays, making them an ideal messenger particle. However, these same properties also make them extremely difficult to detect. To observe neutrinos in the PeV-EeV energy range, larger detection volumes than those covered by current experiments are required. The radio detection of particle cascades in ice is a promising technique to instrument large volumes, due to the kilometer scale attenuation length of radio waves in ice.

The first part of this chapter is an introduction to ultra-high energy cosmic rays, focusing on their sources. The second part discusses their relation to gamma rays and neutrinos, followed by an introduction to high-energy neutrinos. The last part discusses the prospects and implications of detecting a neutrino above PeV energies.

2.1 Ultra-high energy cosmic rays

Over the past 90 years our understanding of cosmic rays with energies > 10^{18} eV, called ultra-high energy cosmic rays (UHECR), has improved significantly. Today we know that high energy cosmic rays are strongly dominated by ionized nuclei with an energy dependent composition [4]. At energies higher than 10^{14} eV cosmic rays are detected by the cascades of secondary particles they initiate when entering the Earth's atmospheres, known as extensive air showers. In the following, the assumed acceleration mechanism and the measured spectrum of cosmic rays are briefly explained. The features of the spectrum are discussed in their relation to the composition and propagation effects.

2.1.1 Acceleration mechanism and implications for possible sources

The existence of cosmic rays with energies up to 1×10^{20} eV suggests that there are hidden sources in the Universe that are very efficient accelerators. The generally accepted acceleration mechanism for galactic cosmic rays is *first-order Fermi acceleration* within astrophysical shocks [4]. In this scenario, material is ejected from a source and collides with another medium at rest, creating a shock front. The diffusively propagating particles are accelerated through repeated crossing of the shock front, while being trapped by magnetic fields. In each crossing, the particle gains an amount of energy ΔE, which is proportional to its prior energy, and has the probability P_{esc} to escape the acceleration region. This cycle repeats until the particle diffuses out of the shock region and acceleration stops. It can be shown (e.g. [4]) that such a process produces a power law spectrum with a spectral index of γ with:

$$\gamma \approx \frac{P_{\mathrm{esc}}}{\Delta E} + 1. \tag{2.1}$$

For an ideal shock (in which the speed of the shock front is much faster than the speed of sound in the medium) in interstellar gas $P_{\mathrm{esc}}\ \Delta E \approx 1$ predicting a spectral index $\gamma \approx 2$, which is close to what is needed to describe the observed cosmic ray spectrum. The crucial component of this acceleration model is that the particles must be accelerated in stages, and therefore must be contained within the magnetic region for some period of time. This requirement is referred to as the *Hillas criterion* and states that particles can remain in the accelerating region as long as their Larmor radius is smaller than the size of the accelerator [5]. Thus, the maximum energy achievable, E_{max}, in an acceleration medium of radial size, R, and magnetic field strength B can be estimated according to:

$$E_{\mathrm{max}} \sim Z \cdot B \cdot R \tag{2.2}$$

With this first-order estimate some, astrophysical sources can be ruled out simply based on the charge Z of the accelerated particle, the radial size R and the magnetic field strength B. In Figure 2.1, a Hillas diagram [5] is shown in which a number of possible candidate sources are plotted in the B-R plane. The radius of the acceleration medium, stated on the x-axis, is equal to the comoving size of the source times the Lorentz factor of the flow Γ. In this plot, the solid diagonal lines show the values required to accelerate protons (red) or iron nuclei (blue) to 1×10^{20} eV where the shock velocity of the outflow is equal to the speed of light c. The dashed lines assume a slower shock velocity, e.g. $0.01\,c$. Object classes below the lines do not satisfy the Hillas criterion. As shown by the dashed diagonal lines, the required product of B and R is higher for slower shocks. Normal galaxies, supernovae (SNe) and Wolf-Rayet stars do not satisfy the Hillas criterion. For the other source classes in the plot, the criterion is met, e.g. low-luminosity gamma-ray bursts (LL GRB), high-luminosity GRBs (HL GRBs), tidal disruption events (TDE) and the lobes, hotspots and knots of active galactic nuclei (AGN). The Hillas criterion is a necessary but not sufficient condition for a given source class to produce cosmic rays at the specified energy. The sources must also be capable of accelerating cosmic rays to the necessary energy in the first place, and the timescale for this to occur must also be shorter than the associated particle cooling timescale. Dedicated modelling of a given object is used to determine whether this criterion can be met.

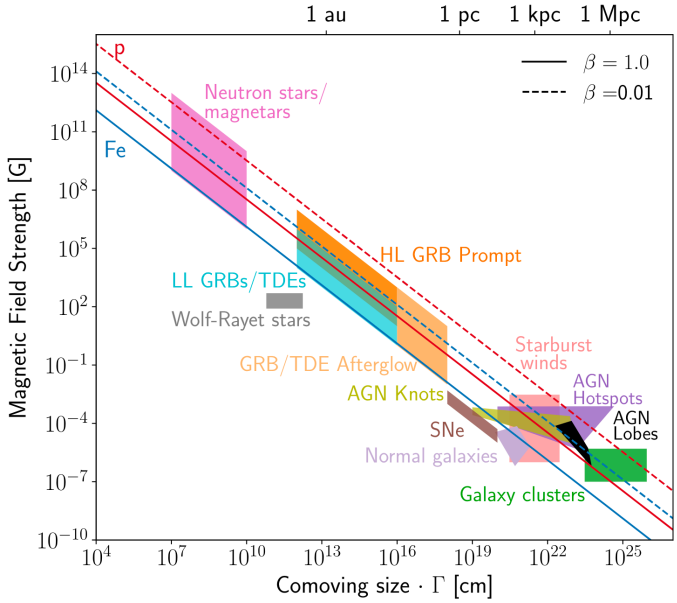

Figure 2.1: Hillas diagram. Possible candidate sources are shown as the product of their characteristic size, R, and magnetic field strength, B. The radius of the engine, stated on the x-axis, is equal to the comoving size of the source times the Lorentz factor of the flow Γ. The solid diagonal lines show the values required to accelerate protons (red) or iron nuclei (blue) to 1×10^{20} eV, where the possible outflows have a shock velocity β equal to the speed of light c. The dashed lines assume a shock velocity of 0.01 c. References for the values of B and R are given in [6]. Fig. from Ref. [6].

2.1.2 Cosmic ray spectrum and arrival direction

At the highest energies, the cosmic ray flux is low and large detection volumes are required to measure the steeply falling flux. On Earth, cosmic rays are detectable by the extensive air shower they initiate when entering the atmosphere. The energy spectrum between 10^{13} eV to 10^{20} eV as measured by various air shower experiments is shown in Figure 2.2. The cosmic ray flux decreases steadily which can be approximately described by a power law $dN\ dE \propto E^{-\gamma}$ with some breaks where the spectral index γ changes. To improve the visibility of the changes in the spectrum, the flux is scaled by some power of E, here 2.6. The two most notable changes in spectral index are referred to as the knee $\sim 3 \times 10^{15}$ eV and the ankle at $\sim 5 \times 10^{18}$ eV (which is due to the shape of this spectrum allegedly resembling a leg). It has been the convention to describe the spectrum as a set of (broken) power laws[16, 21]:

$$\frac{dN}{dE} \propto \begin{cases} E^{-2.7}, & E < 2 \times 10^{15}\ \text{eV} \\ E^{-3.3}, & 2 \times 10^{15}\ \text{eV} < 5 \times 10^{18}\ \text{eV} \\ E^{-2.5}, & 5 \times 10^{18}\ \text{eV} < 1.3 \times 10^{19}\ \text{eV} \\ E^{-3.}, & 1.3 \times 10^{19}\ \text{eV} < 4.6 \times 10^{19}\ \text{eV} \\ E^{-5.1}, & E > 5 \times 10^{19}\ \text{eV} \end{cases} \tag{2.3}$$

A suppression of the flux is observed around $\sim 7 \times 10^{19}$ eV. Measurements by the Telescope Array (TA) and the Pierre Auger Observatory (PAO), the two largest cosmic ray detectors, place this suppression at different energies, 71 EeV and 46 EeV, respectively. The spectra measured by the two experiments are basically in agreement, except for a relative shift

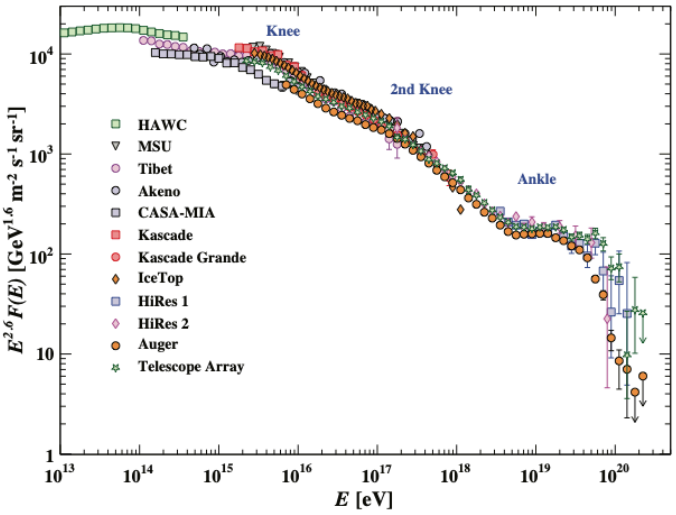

Figure 2.2: The all-particle cosmic ray spectrum as a function of E (energy-per-nucleus) from air shower measurements [7–19]. The flux is scaled by $E^{2.6}$ to further exemplify the changes in slope. The knee can clearly be seen at $\sim 3 \times 10^{15}$ eV as well as the ankle at $\sim 5 \times 10^{18}$ eV. The flux suppression has also been seen by three experiments in the range of energies near the limit predicted by the GZK mechanism. Fig. from Ref. [20]

in energy scale at a level of 9% [21]. These features of the spectrum are likely related to the origin of cosmic rays and the corresponding particle-acceleration and -propagation mechanisms and will be discussion in Section 2.1.3 and Section 2.1.4.

The arrival directions of cosmic rays at Earth are close to isotropic. At lower energies, this is to be expected due to the deflection of cosmic rays by magnetic fields, which leads to a diffuse propagation. In this process, the information about the direction of their sources is lost and cosmic rays arrive isotropic in the field of view. At ultra-high energies, a proton from a nearby extragalactic source should be deflected by only a few degrees, providing information about its origin. However, to date only large scale deviations from isotropy have been found in the directions of UHECRs. The Pierre Auger Observatory reported a large-scale, dipole-like anisotropy in the arrival directions of UHECRs with energies above $E \geq 4\,\text{EeV}$ [22] and an anisotropy in the right ascension of cosmic rays [23], while the Telescope Array discovered a clustering at energies above 57 EeV [24], called the TA hotspot. These results provide strong evidence for an extragalactic origin of cosmic rays at the highest energies, since the higher density of sources in the galactic plane should lead to a clustering of cosmic ray directions.

The TA hotspot coincides with the location of the nearby starburst galaxy M82 [25]. Data from the Pierre Auger Observatory also suggest a significant contribution from M82, as well as from the nearby radio galaxy Centaurus A [26]. Although they do not have 5σ significance, they further support an extragalactic origin of UHECRs. However, the low level of anisotropies measured from these nearby objects suggests that UHECRs do not predominantly originate from a few nearby sources, but from a larger number of more distant sources. Several correlation studies between cosmic rays and catalogues of potential source classes have been executed. But so far none of these have yielded statistically significant results at the 5σ level [27–30].

2.1.3 The Knee(s)

The knee around 3×10^{15} eV is likely caused by the transition from galactic to extra galactic cosmic rays. Applying the Hillas criterion in Eq. 2.2 on the galactic magnetic field strength, cosmic rays should only be confined in our Galaxy up to some maximal energy, $E\text{max} \simeq Z \cdot 3 \times 10^{15}$ eV [31]. Beyond this energy the cosmic rays would leak out and not be detected on Earth, directly creating a knee-like structure.

The primary source for galactic cosmic rays is assumed to be supernova remnants, which provide ideal conditions for first order Fermi acceleration. Plus, they are the most abundant galactic gamma ray sources, the Hillas criterion restricts their maximum cosmic ray energy to around $\sim 1 \times 10^{15}$ eV.

The Hillas criterion also implies that the end of the galactic component will be charge dependent and hence the composition of the spectrum would change in a systematic way through the knee region [32]. Measurements by KASCADE and its successor KASCADE-Grande showed, that the knee-energy indeed corresponds to a sharp decrease in the observed flux of light nuclei [33]. Later, KASCADE-Grande measured a second knee, sometimes called the iron knee, at 8×10^{16} eV, where a distinct softening of the spectrum for heavy elements was observed [34]. These two measurements indicate that the two distinct knees in the all-particle spectrum are due to changes in the spectra of individual elements. Furthermore, the ordering of these knees for the different mass groups provides validation for the charge-dependent interpretation of the spectrum in the knee to ankle energy range.

2.1.4 The Ankle and suppression

Studying the distribution of the cosmic ray arrival directions at the highest energies indicate an extra-galactic origin for cosmic rays with energies beyond the the ankle around $\sim 5 \times 10^{18}$ eV [35, 36].

The extra-galactic origin implies that cosmic rays travel large distances between their sources and Earth, making propagation effects particularly relevant. The primary interaction target for UHECRs during propagation is assumed to be the cosmic microwave background (CMB).

As shown in Figure 2.3, pair production is major source of energy loss for UHECRs in the energy up to 2×10^{18} eV. At higher energies hadronic interactions become dominant, and pions are produced via the delta resonance:

$$\text{proton} + \gamma_{\text{CMB}} \longrightarrow \Delta^{+} \longrightarrow \text{neutron} + \pi^{+} \tag{2.4}$$

$$\text{proton} + \gamma_{\text{CMB}} \longrightarrow \Delta^{+} \longrightarrow \text{proton} + \pi^{0} \tag{2.5}$$

The charged pion decays shortly thereafter, producing at least one neutrino, giving rise to the so-called cosmogenic neutrino flux (see Section 2.2.4). The proton threshold energy for this interaction with a CMB-photon in its rest frame is $E_p \approx 7 \times 10^{19}$ eV [4]. Thus, protons with energies above this would be strongly suppressed. This suppression is also

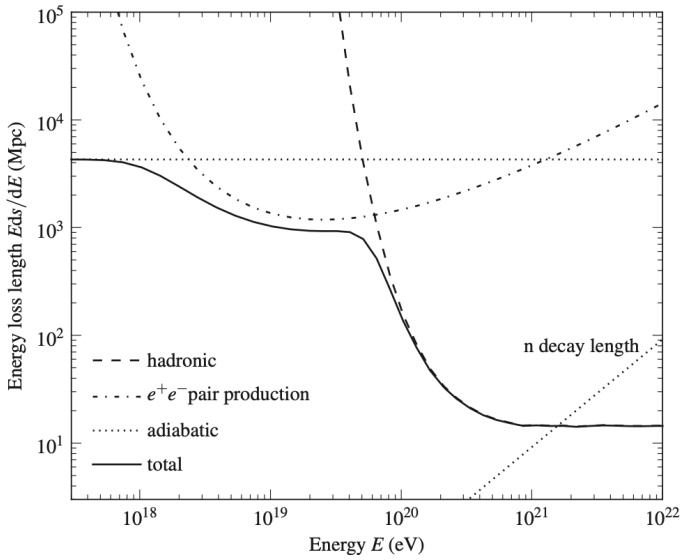

Figure 2.3: Energy loss length for protons in the CMB at redshift z=0. Given are the total energy loss length and the contributions from e^+e^- (Bethe–Heitler) pair production, hadronic production of pions, and expansion of the universe (H_0 = 70 km/s/Mpc). In addition the decay length of neutrons is shown. Fig. from Ref. [4]

referred to as the GZK-suppression, named after Greisen [37], Zatsepin, and Kuzmin [38], who independently predicted the suppression after the discovery of the CMB.

For heavier nuclei, the interaction with the CMB via photo-disintegration is the most prominent interaction at higher energies. By absorbing a photon, the nucleus transitions into an excited state and decays during deexcitation into a daughter nucleus and at least one other nucleus/nucleon. Since no neutrinos are produced in this interaction, the mass composition of UHECRs (at their source) has a great impact on the expected cosmogenic neutrino flux, which results from the propagation of cosmic rays [39]. Due to the effect of both interactions, the maximum distance, i.e., horizon, from which cosmic rays at the highest energies can reach us is limited. This is commonly referred to as the GZK-horizon and has a radius of ~75 Mpc to 150 Mpc depending on the particle mass [4].

As the suppression mechanism is commonly agreed on, the origin of the ankle has not yet been resolved. In order to explain the ankle as a transition between a galactic and extragalactic dominated spectrum, a second galactic cosmic ray "population" to bridge the gap between the 2nd knee, which is commonly interpreted as the cut-off of an iron component accelerated in the shock front of supernova remnants (SNR), and the ankle is needed. However, an anisotropy in the arrival direction of cosmic rays with energies below the Ankle (assuming a significant proton fraction) is not observed, and the absence would be difficult to explain.

Given the current cosmic ray measurements, it is extremely unlikely that one single source or process can provide a full characterization at all energies. Instead, a full description of > 1 PeV cosmic rays must involve a combination of multiple processes and/or multiple sources.

2.2 A multi-messenger approach

One of the major challenges in identifying the sources of UHECRs is their deflection by the poorly known magnetic fields. As cosmic rays occasionally interact with matter or photon fields at or near the source (see Section 2.1), they create secondary particles, most of which are pions. The charged pions decay into muons and electrons, along with the corresponding neutrinos and antineutrinos:

$$\pi^{\pm} \longrightarrow \mu^{\pm} + \overset{(-)}{\nu}_{\mu} \tag{2.6}$$

$$\mu^{\pm} \longrightarrow e^{\pm} + \overset{(-)}{\nu}_{\mu} + \overset{(-)}{\nu}_{e}. \tag{2.7}$$

Neutral pions predominantly decay into gamma photons:

$$\pi^{0} \longrightarrow \gamma + \gamma. \tag{2.8}$$

These processes imply a connection between cosmic rays, high-energy neutrinos, and gamma rays. In the following, the properties of gamma rays and neutrinos as messenger particles in connection with ultra high energy cosmic rays are briefly described.

2.2.1 Gamma rays

Gamma rays are photons of non-thermal emission, they usually result from particle acceleration and have energies between 2×10^5 eV to 2×10^8 eV. They have been observed from a large number of astrophysical objects, providing strong evidence for particle acceleration. However, they do not necessarily prove the acceleration of hadronic cosmic rays, as they can also originate from purely leptonic processes. *Inverse Compton* scattering increases the energy of a photon as high-energy electrons scatter off and transfer energy:

$$e^{-} + \gamma \longrightarrow e^{-}\gamma'. \tag{2.9}$$

In general, extensive leptonic gamma ray emission can be produced in astrophysical objects through the synchrotron self-Compton mechanism. In this case, an accelerated population of electrons generate photons through synchrotron emission, and this same electron population then scatters these photons to higher energies via the inverse Compton effect [40]. This process results in a characteristic energy spectrum, with a synchrotron peak at keV-MeV and a Compton peak at TeV energies, which has been observed at a number of gamma ray sources [41–43].

Gamma rays also have some limitations as messengers for astronomy. Above $\sim 10^{12}$ eV, gamma rays are increasingly likely to interact with photons from the Extragalactic Background Light (EBL) and the Cosmic Microwave Background. These interactions produce electron-positron pairs, dissipating the photon energy and effectively making the Universe opaque to high-energy gamma rays [44, 45]. Therefore, gamma ray astronomy is limited either to sub-TeV energies or to sources within the pair production interaction length, which is around 300 Mpc at 1 TeV [40]. Thus, high-energy gamma rays from the distant sources one expect for UHECRs are most likely invisible to us.

2.2.2 High energy neutrinos

Neutrinos have a small interaction cross section, which allows them to travel almost undisturbed over cosmic distances, but makes their detection considerably more difficult. They are also neutral and therefore not deflected by magnetic fields. High energy neutrinos can only be produced in hadronic processes (e.g. $\pi^{\pm}$ decay), making them the smoking gun for the acceleration of hadronic cosmic rays [40].

The hadronic production process through pions suggests a ratio of 1:2:0 between the three neutrino flavors ν_e:ν_μ:ν_τ at the source as long as the pion decay is not muon-damped [46]. Over the large distance to Earth mass-induced flavor oscillations changes the ratio to 1:1:1. The flavor ratio measured by the IceCube experiment is consistent with this prediction, although the uncertainties are still rather large [47, 48].

Neutrinos which are produced by photo-production during propagation of UHECRs are called *cosmogenic* neutrinos, while *astrophysical* neutrinos are produced by other mechanisms or close to sources.

2.2.3 Astrophysical Neutrinos

The existence of an astrophysical neutrino flux was first established in 2013 by the IceCube Neutrino Observatory, a cubic-kilometer detector located at the geographic South Pole [49, 50]. The experiment measured neutrinos between a few TeV and a few PeV, which originated from astrophysical sources.

Recently, the IceCube collaboration presented a combined fit of the astrophysical diffuse neutrino flux measurements using different detection channels [51]. So far, the astrophysical neutrino flux has been well-described by an unbroken single power law. The new analysis reports a spectral index of $\gamma = 2.52 \pm 0.04$ in the energy range of 2.5 TeV to 6.3 PeV for a single power law, which is close to that of cosmic rays. However, this analysis also finds, that a curvature or a spectral break in the astrophysical neutrino flux, better describes the data. The broken power low fit includes the energy range from 13.7 TeV to 4.7 PeV, with the break at 4.39 GeV. At lower energies, the spectral index is harder compared to a single power law ($\gamma_1 = 1.31^{+0.50}_{-1.21}$) and has a softening at higher energies ($\gamma_2 = 2.74^{+0.06}_{-0.07}$) [51].

With a few exceptions, e.g. the Galactic plane, most of the observed astrophysical flux exhibits no significant preference for one direction over another and is approximately isotropic. This suggests that most of the contribution comes from a combination of sources distributed across cosmological scales.

In 2023, IceCube presented the first evidence of high-energy neutrino emission from the Milky Way Galaxy [52, 53]. The result is consistent with diffuse emission of neutrinos from the Milky Way but could also arise from a population of unresolved point sources. The

ANTARES, a Cherenkov detector in the Mediterranean Sea operating until recently, nears the sensitivity to the IceCube diffuse neutrino flux. The collaboration reported a hint for a TeV neutrino emission from the Galactic Ridge [54].

The first identified extra-galactic neutrino source associated with a high-energy neutrino event was the blazar TXS 0506+056 [55]. On September 22, 2017, the IceCube Collaboration detected a high-energy muon neutrino with a 56.5% probability of astrophysical origin. This event coincided in direction and time with enhanced gamma-ray activity of the BL Lac object TXS 0506+056 observed by the Fermi Large Area Telescope (LAT) and later also by the Major Atmospheric Gamma Imaging Cherenkov (MAGIC) telescope [56]. The significance of the association was estimated to be 3σ, indicating that TXS 0506+056 is a potential cosmic ray source. In addition, archival data showed a neutrino flare from the same blazar in 2014-2015 at a significance of 3.5σ [57], but puzzlingly this was not accompanied by an increase in gamma-ray emission.

More recently, on November 4th, 2022, IceCube provided the first compelling evidence for a steady point source of high-energy neutrinos (4.2σ) [58]. The result is interpreted as direct evidence for TeV neutrino emission from the Seyfert II galaxy NGC 1068. The evidence of neutrino emission from NGC 1068 suggests that active galactic nuclei could make a substantial contribution to the diffuse neutrino flux.

However, in their respective energy ranges the sources NGC 1068 and TXS 0506+056 contribute no more than 1% to the overall diffuse flux of astrophysical neutrinos [58], leaving room for other neutrino sources.

Three new large optical Cherenkov detectors are under construction, KM3NeT [59, 60] P-ONE [61], and Baikal-GVD [62], which will improve the sensitivity to TeV–PeV neutrinos.

2.2.4 Cosmogenic neutrinos

Cosmogenic neutrinos are created when ultra-high energy cosmic rays propagate through space and interact with photon fields, such as the Cosmic Microwave Background (CMB) and the Extragalactic background light (EBL). The cosmic rays interact via by pair-production, photo-pion production and photo-disintegration, see Section 2.1.4. Since protons contain the most energy per nucleon, protons are the most likely type of cosmic rays to produce UHE neutrinos.

At a proton energy of $\sim 5 \times 10^{19}$ eV, the GZK effect is predicted to suppress the UHECR flux [37, 38]. The protons interact with CMB photons, efficiently producing charged pions via the delta resonance, which decay into neutrinos as shown in Eq. 2.6 and Eq. 2.7 [63]. One half of the energy that UHECR protons lose in this interactions ends up in neutrinos, which is typically 5% of the primary cosmic ray energy [63]. Heavier nuclei produce lower energy neutrinos due to the lower energy of their constituent nucleons. Detecting the UHE neutrinos produced by the GZK effect, or constraining their flux, would therefore allow to draw conclusions about the composition of the cosmic rays spectrum.

At lower proton energies, the extragalactic background light can also serve as a scattering target. This produces neutrinos mainly in the PeV range and is a secondary effect at EeV energies [64].

In addition to the cosmic-ray composition, the flux depends strongly on the cosmic-ray spectrum at acceleration, the cosmological evolution of the cosmic-ray sources, and the

energy of the Galactic-extragalactic transition, which in turn make cosmogenic neutrinos a valuable messenger. Up to date, no cosmogenic neutrino has been measured. The most constraining limits on UHE neutrinos come from IceCube [65], the Auger Observatory [66] and ANITA [67]. Also RICE [68, 69], ARA [70] and ARIANNA [71] published limits on the neutrino flux.

The predictions for the cosmogenic neutrinos flux are tuned to these measurements [72], which explains why no detection is expected from the current neutrino flux prediction.

The prospect and implications for the measurement of EeV neutrinos will follow in the next section.

2.3 Prospects for ultra-high energy neutrinos

The measured neutrino flux together with the diffuse fluxes for gamma rays and cosmic rays is shown Figure 2.4. The similar energy density of the three spectra suggesting a common origin, although each occurs in its own energy regime. The prediction for astrophysical neutrinos from different sources are shown in dark red. Predictions for cosmogenic neutrinos based on cosmic rays measurements are shown in dark yellow. The Figure also shows the gap in observations of UHE neutrinos beyond the energies reachable by IceCube.

The predictions for the cosmogenic neutrino flux vary by several orders of magnitude depending on the model assumptions. A lighter composition, especially one with a large proton fraction at the highest energies, generally leads to a higher cosmogenic neutrino flux (e.g. the predication based on the measured TA spectrum) because the nucleons of heavier nucleus get only a part of the energy and therefore produce lower energy neutrinos. The non-detection of cosmogenic neutrinos would allow to constrain the proton fraction at highest energy cosmic rays, because UHECR are known to exist [72].

The fraction of protons at the highest energies has implications for correlation studies between cosmic ray directions and source catalogues, since a stronger deflection by magnetic fields must be assumed. This in turn could confirm or exclude models that predict a substantial high energy proton fraction [79].

Interestingly, the evolution of UHECR source can be related to UHE neutrinos [72]. While UHECR are limited to the GZK horizon and gamma rays at are attenuated through photo-pairproduction with the EBL, neutrinos can travel almost infinitely far at any energy. Therefore, neutrinos are the only particles that can reach us from sources at high redshift. This also implies, that source classes, that are more common at higher redshifts, such as gamma ray bursts [80] or AGNs [81], should lead to a higher cosmogenic neutrino flux than sources that tend to be closer, such as TDEs [82, 83].

The previous considerations show that neutrino flux measurements can be used to constrain the properties of the cosmic ray flux, in particular the cosmic ray composition, its energy spectrum, and its source distribution. In addition, the parameters of the source environments and of hadronic interaction models at the highest energies can be constrained [84].

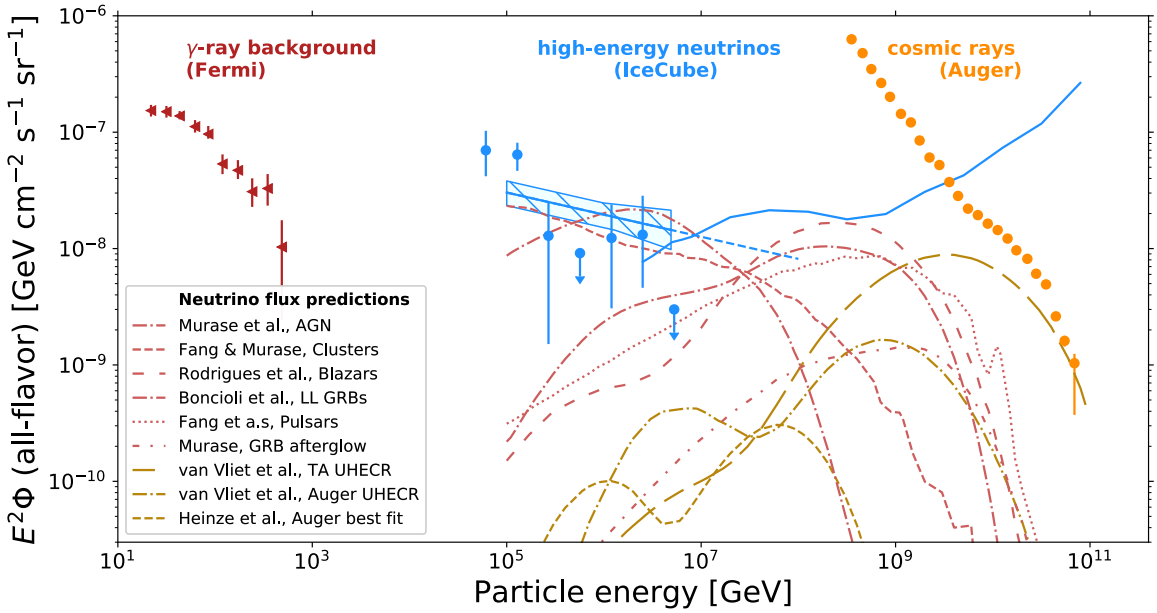

Figure 2.4: A multi-messenger view of the high-energy universe. Shown are the γ-ray measurements from Fermi [73], the IceCube neutrino measurements and the differential limit on the cosmic neutrino flux [74–76], as well as the spectrum of ultra-high energy cosmic rays as reported by the Pierre Auger Observatory [77]. Between 10^{14} eV and 10^{20} eV models are shown, predicted neutrinos from sources (in light red) and those from the interaction of the ultra-high energy cosmic rays with various photon backgrounds (in dark yellow). Fig. from Ref. [78].

Measuring the neutrino-nucleon cross section at ultra-high neutrino energies offers novel insight into the deep structure of protons and neutrons, and sensitivity to potentially transformative new physics [85]. Since the UHE neutrino flux depends on the interaction cross section these measurements should be combined [86].

The measured flavour composition of neutrinos can be used to get insight into the neutrino production mechanism, e.g. pion decay, muon-damped pion decay, and neutron decay [46, 87]. They also open the possibility of testing extreme deviations in the flavor composition due to new neutrino physics acting at ultra-high energies [88].

The optical detection in ice and water needs denser spacing of optical modules due to the scattering and absorption length of Cherenkov light [89] of $\mathcal{O}(100\,\mathrm{m})$, which makes it unfeasible to instrument the large volumes necessary for a detection of UHE neutrinos. A promising technique to fill this gap and actually observe UHE neutrinos [90] is the detection of radio signals from particle showers in glacial ice. The large attenuation length at radio frequencies allows for a sparsely instrumentation with a spacing of ~1 km. The method of radio detection will be detailed in the following chapters.

In Figure 2.5 the sensitivity for several radio experiments is shown. The Radio Observatory Greenland (RNO-G), which is part of this work, is planned to be the first deployed radio detector with sensitivities beyond the energy scale detected by IceCube. Models for cosmogenic neutrinos assuming a significant proton fraction in UHECR will either be conclusively ruled out or lead to the detection of neutrinos above PeV energies. The detection mechanism will be explained in Chapter 3.

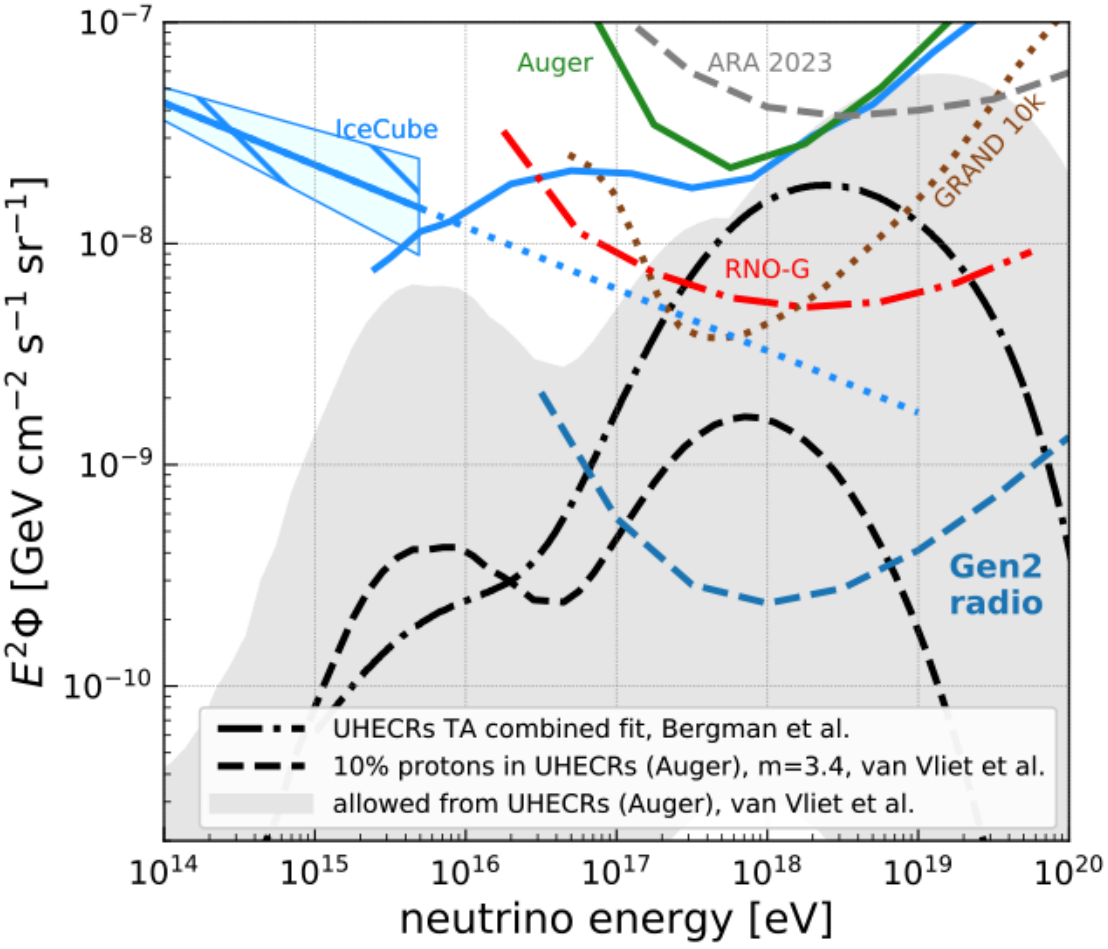

Figure 2.5: The ten year expected differential 90% CL sensitivity at trigger level for zero background of the simulated radio array to a diffuse neutrino flux is shown as dashed line. Solid lines show the astrophysical neutrino flux measured by IceCube [74] and experimental upper limits at higher energies. The expected sensitivities of ARA (for 2023), of RNO-G currently under construction and the proposed GRAND10k array (both for ten years) are also shown, as well as different predictions of the GZK neutrino flux based on UHECR data[72, 91]. Fig. from Ref. [92]

Detecting cosmic rays, muons and neutrinos with radio signals

3

The detection of cosmic rays, muons and neutrinos with radio signals is possible, if the particle induces a particle cascade. The electromagnetic component of the cascade then creates radio emission while propagating through a medium. Cosmic rays usually interact in the Earth's atmosphere and induce cascades which are referred to as extensive air showers. Neutrinos have a very low cross section, therefore dense media such as ice increase the chance for an interaction and a subsequent shower. Atmospheric muons which are created in an air shower can also induce a particle cascade both, in the air and in the ice.

Currently several radio-based air shower detectors like AERA (Auger Engineering Radio Array) [93], LOFAR (LOw Frequency ARray) [94] and Tunka-Rex (Tunka Radio Extension)[95], as well as radio-based neutrino detectors like ARIANNA (Antarctic Ross Ice Shelf Antenna Neutrino Array) [96], ARA (Askaryan Radio Array) [97] and RNO-G (Radio Neutrino Observatory Greenland) [78] are operational and are taking data.

3.1 Particle cascades

To extract information about the initial particle from the measured radio signal, the evolving particle cascade responsible for the radio emission has to be understood. The development of a radio-emitting particle shower in air induced by a cosmic ray is very similar to a neutrino- or muon-induced in-ice shower. While air showers are much more extensive with length scales of kilometers, particle cascades in dense media develop within meters [98]. Both types of showers propagate through their respective mediums at speeds close to the speed of light.

3.1.1 Cosmic ray induced air showers

The incoming cosmic ray interacts with an nucleus of an atom in the upper atmosphere. This interaction predominantly produces pions and other hadrons, such as kaons, protons, and neutrons, see Figure 3.1. Due to distinct decay channels of neutral and charged pions, air showers develop in two components: the *electromagnetic* and the *hadronic component*.

Neutral pions primarily decay via the electromagnetic interaction into two photons

$$\pi^0 \longrightarrow \gamma + \gamma, \tag{3.1}$$

with a branching fraction of 98.82% [99]. In air shower, neutral pions rather decay than interact, due to their short decay length, $\ell_{\text{decay}} = \tau_0 \cdot c \cdot \gamma_L = 25\,\text{nm}$, where τ_0 is the

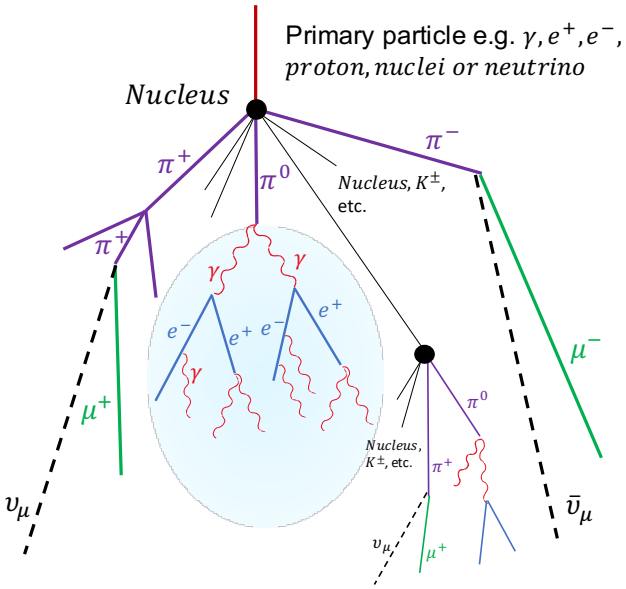

Figure 3.1: Simplified sketch of an air shower. Real air showers contain more particle types than illustrated. Shown are different processes that lead to the electromagnetic component (blue backed), the hadronic component (violet), and the muonic component (green). Radio detectors detect emission only from the electromagnetic cascade.

lifetime and γ_L is the Lorentz factor. The photons produced in the decay interact solely electromagnetically, predominantly undergoing electron pair production

$$\gamma \longrightarrow e^- + e^. \tag{3.2}$$

Electrons in turn are also most likely to interact electromagnetically, e.g. producing photons by bremsstrahlung

$$e^\pm \longrightarrow e^\pm + \gamma. \tag{3.3}$$

Together electrons, positrons and photons constitute the *electromagnetic component* of the shower. The cascade is sustained as particles continue interacting, on average after one radiation length. The shower development ceases when the individual particle energy of $e^\pm$ and γ falls below the critical energy, and the inelastic interaction cross-section drops to zero. The *critical energy* represents the energy at which losses by ionization equal losses by radiation* [101]. The critical energy can be expressed as

$$E_\mathrm{c} \approx \frac{a}{Z+b}, \tag{3.4}$$

where a is the energy loss due to ionization, b is the contribution from bremsstrahlung, and Z is the atomic number of the medium. For electrons in air, $E_\mathrm{c}^\mathrm{air} \approxeq 84\,\mathrm{MeV}$ [101]. Particles below the critical energy will continue to propagate until reaching the ground, but due to their low energy, they are likely to be captured by atmospheric molecules. Therefore, only a small fraction of the electromagnetic component reaches the ground.

The charged pions and the remaining protons, neutrons and other hadrons fuel the *hadronic component* of the shower. Charged pions decay via the weak interaction, mostly

* Rossi and Greisen [100] use a different definition of the critical energy.

into a muon and a muon neutrino:

$$\pi^{\pm} \longrightarrow \mu^{\pm} + \overset{(-)}{\nu}_{\mu} \,. \tag{3.5}$$

As it is a weak decay, their decay length in the rest frame is long, $\ell_{\text{decay}} = \tau_0 \cdot c \cdot \gamma_L = 7.8\,\text{m}$. High-energy charged pions continue to interact with nuclei in the atmosphere, creating more pions and expanding the shower. In contrast to the electromagnetic cascade, hadrons interact via the strong force. Due to the strong force's short range, interactions are less frequent, allowing hadrons to penetrate the atmosphere unhindered over several interaction lengths. The muon can later decay into an electron and its corresponding neutrino:

$$\mu^{\pm} \longrightarrow e^{\pm} + \overset{(-)}{\nu}_{\mu} + \overset{(-)}{\nu}_{e} \,. \tag{3.6}$$

The decay time of a muon is usually longer than the time it takes for the muon to reach the ground. Depending on their energy the muons will eventually be stopped somewhere underground. Neutrinos will neither interact nor decay and propagate through the Earth, unless of extremely high energy.

Air showers are formed from many subsequent interactions. With the exception of the first few, individual interactions do not matter much and fluctuations introduced by single interactions are averaged out quickly. A simple model for describing the electromagnetic cascade was first developed in 1936 by Heitler [102] and was later extended by Matthews for extensive air showers, incorporating the hadronic cascade as well [103]. The model assumes that only pions are produced. At each step in the cascade, the energy is shared equally among these pions, so that the charged pions carry 2/3 of the energy. Following this assumption the energy for a charged pion after n interaction is then:

$$E_{\pi} = \frac{E_0}{(\frac{3}{2}N_{\text{ch}})^n} \tag{3.7}$$

with E_0 being the primary energy and N_{ch} the multiplicity of charged particles.

This model proves instrumental in understanding the shower development and compute shower properties, such as the depth where the shower contains the largest electron multiplicity, called shower maximum, along with the associated energy and particle count.

The shower maximum of a proton-induced shower is expressed by Matthews [103] as:

$$X_{\text{max}}^{\text{proton}} = X_0 + \lambda_{\text{r}} \ln \frac{E_0}{3N_{\text{ch}}E_{\text{c}}^{\text{e}}} \tag{3.8}$$

Where $X_0 = \lambda_{\text{int}} \ln 2$ is the atmospheric depth at which the first interaction occurs, λ_{int} is the interaction length of the primary proton. λ_{r} indicates the radiation length and E_{c}^{e} the critical energy of an electron.

Heavier primary particles can be effectively modelled as a superposition of proton showers. In the shower development the primary energy E_0 is distributed to the sub-showers with E_0/A, where A is the mass of the nucleus (e.g. the nucleon number). The maximum

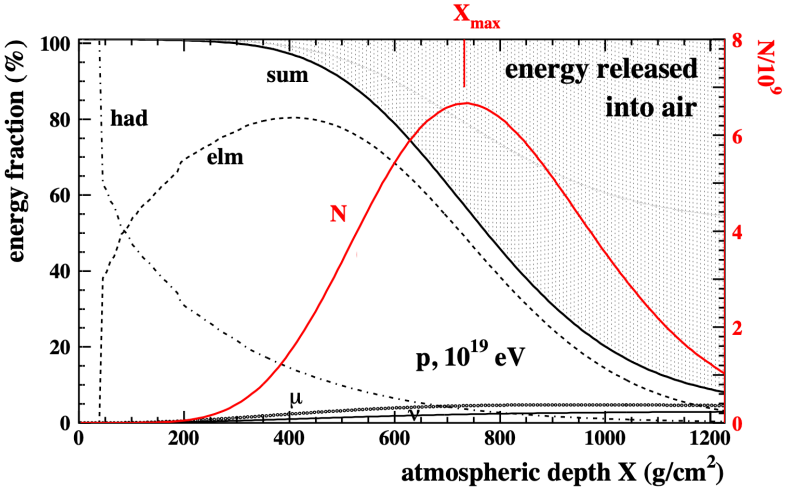

Figure 3.2: Energy flow in extensive air shower as obtained by CORSIKA shower simulations for an individual 10^{19} eV primary proton event. The energy fractions stored in hadrons, electromagnetic particles, muons, and neutrinos are shown. The difference between their sum to the initial energy indicates the total amount of energy already released into the air (shaded area). The red line is the cascade profile $N(X)$, where X_{max} indicates the maximum number of shower electrons and positrons. Figure adapted from Ref. [104].

can be written as:

$$X^A_{\mathrm{max}} = X_0 + \lambda_{\mathrm{r}} \ln \frac{E_0}{3N_{\mathrm{ch}} E^{\mathrm{e}}_{\mathrm{c}} A} \tag{3.9}$$

or simplified as:

$$X^A_{\mathrm{max}} \sim \lambda_{\mathrm{int}} + \lambda_{\mathrm{r}} \ln \frac{E_0}{A}. \tag{3.10}$$

This relation shows that the shower maximum is reached earlier for heavier nuclei, because their interaction length is shorter (e.g. $\lambda^{\mathrm{proton}}_{\mathrm{int}} \approx 70 - 90\,\mathrm{g/cm^2}$ and $\lambda^{\mathrm{iron}}_{\mathrm{int}} \approx 15 - 20\,\mathrm{g/cm^2}$ [101]). This makes it possible to distinguish between lighter and heavier primary particles.

In Figure 3.2 the longitudinal development of an air shower is illustrated. At the beginning, the hadronic cascade develops. From its products the electromagnetic cascade starts and continues to be fed in the subsequent shower process. A significant energy fraction is transferred to the electromagnetic component in each step, consequently the energy left in the hadrons decreases exponentially. The energy fraction of muons and neutrinos is almost negligible ($\sim$ 5%), as can be seen only at later stages of the shower development. Most of the initial energy is deposited into the atmosphere. The maximum of energy stored in electromagnetic particles (dashed line) is reached before the shower maximum (red line). This difference is due to the fact that at an early cascade stage, a large energy fraction is deposited in only a few high-energy particles. The high-energy particles then create new particles, to which the energy is transferred.

The Heitler-Matthew model serves to build qualitative understanding of extensive air shower development. For the ”real work” e.g. quantitative predication, Monte Carlo simulations are used. Unlike simplified models, Monte Carlo calculations are based on stochastic processes that rely on the interaction cross section of individual particles. In

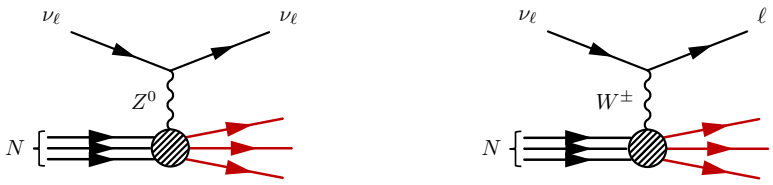

Figure 3.3: A neutrino ν_ℓ interacting with a nucleus N. Left: Neutral current (nc) interaction mediated by a Z boson, emitting a neutrino and a hadronic shower, indicated by three red lines. Right: Charged current (cc) interaction, crating a lepton ℓ and a hadronic shower (indicated by three red lines).

order to reproduce complete air showers in space and time, the algorithms include all relevant processes such as particle propagation, interaction and/or decay. A realistic model of the medium, magnetic fields and an interface for detector simulations are included in software such as CORSIKA [105]. The cross sections used are measurements from accelerators that come as close as possible to a realistic cascade development. Cross sections at the highest energies are currently missing and must be extrapolated, adding another degree of uncertainty. The Monte Carlo simulations of this work are described in detail in Section 6.1.

3.1.2 Neutrino and muon induced showers

The development of a neutrino initiated shower in ice is conceptually similar to the previously discussed air showers. A neutrino interacts with a nucleon of the ice molecules and induces a particle cascade. At these energies, the most likely interaction channel is neutrino-nucleon deep inelastic scattering, where the nucleon is broken up as the neutrino scatters off the constituents of a proton or neutron.

The neutrino interactions are distinguished in neutral current (nc) interactions, where a Z^0 boson is exchanged, and charged current (cc) interactions mediated by $W^\pm$ bosons, see Figure 3.3. In a nc interaction the lepton flavor does not change, meaning a neutrino emerges from the scattering. Therefore, all neutrino flavors (ν_e, ν_μ, ν_τ) create only a hadronic particle cascade. In a cc interaction a lepton of the corresponding neutrino flavor is created. The outgoing lepton of a cc interaction can produce additional showers. In case of an initial ν_e, two showers are produced almost immediately: one hadronic and one electromagnetic, which is induced by the resulting electron. The same is true for a $\bar{\nu}_e$ and the resulting positron. At high energies, the Landau–Pomeranchuk–Migdal (LPM) effect becomes relevant which reduces the cross section of bremsstrahlung and pair production [106, 107]. In the LPM mechanism, the characteristic length of the interaction becomes larger than atomic spacing and collective effects of the atomic fields, have to be considered, e.g. additional interactions take place [108]. Therefore, the distance an electron travels before interacting is increased, and several spatially displaced electromagnetic showers are created. The exact behavior depends on how the energy is distributed among the first few particles and results in significant fluctuations between showers [108]. An illustration with the cc interaction of a ν_e is shown in Figure 3.4. In the cc interaction of $\overset{(-)}{\nu}_\mu$ and $\overset{(-)}{\nu}_\tau$ a hadronic shower is created as well. The resulting leptons ($\mu^\pm$ and $\tau^\pm$) propagate through the medium generating lots of secondary showers over a range of kilometers until they decay [109]. Muons lose most of their energy

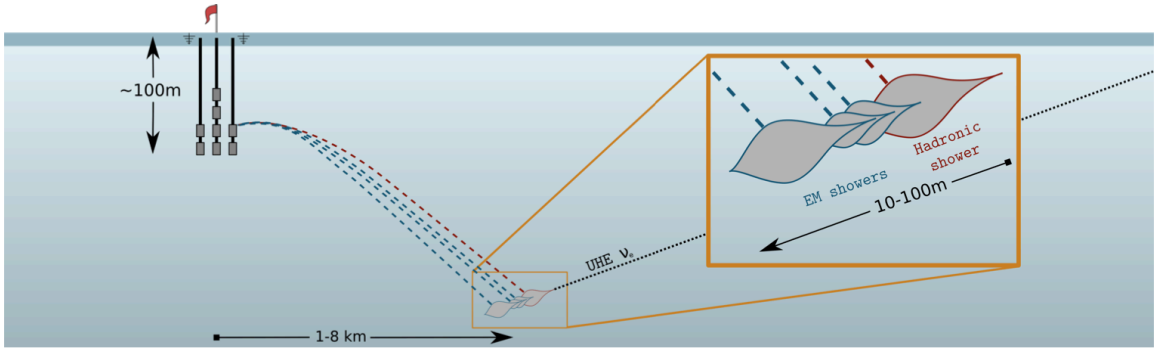

Figure 3.4: Schematic of a charged-current interaction of a UHE ν_e and its in-ice radio-detection. The primary neutrino-nucleon interaction produces a hadronic shower. The final-state electron is affected by the LPM effect, resulting in multiple, separated electromagnetic (EM) sub-showers. The change of the refractive with depth causes the trajectory of radio signals (dashed lines) to bend on their way to the stations. Fig. from. Ref. [87]

through bremsstrahlung, pair production, and nuclear interactions inducing new sub-showers. Taus radiate mainly electron-positron pairs, but larger amounts of energy via photo-nuclear interaction, which leads to hadronic cascades. Also the decay of a tau into hadronic and leptonic channels can create showers. The decay length of a tau increases roughly linearly with energy and is already approximately 5 km at 1×10^{17} eV [110].

Ultra-high energy muon originating from an air shower can also penetrate the ice and create showers along its track, as it is described for a muon resulting from a cc ν_μ interaction.

3.2 Radio emission

Two mechanism have been identified to be the main contributors to the radio emission: The geomagnetic emission [111], caused by the deflection of charged particles in the Earth's magnetic field, and the Askaryan effect [112, 113], caused by a time-varying negative net charge in the shower front (see Figure 3.5). Monte Carlo simulations suggest a tertiary effect for very inclined air showers and high magnetic fields which is connected to geosynchrotron radiation and coherence losses [114].

3.2.1 From air showers

In the Earth's magnetic field, the cloud of electrons and positrons gets separated as electrons and positrons move in different directions due to the Lorentz force:

$$\vec{F}_\mathrm{L} = q \cdot \vec{v} \times \vec{B} \tag{3.11}$$

where q is the particle charge, $\vec{v}$ is the velocity vector or direction of propagation, and $\vec{B}$ is the magnetic field vector. The net drift of electrons and positrons moving perpendicular to the shower axis, can be described as a transverse current ($\dot{q} = I$). This current varies in time ($\dot{I}$), depending on the amount of charge present in the shower and the interaction with molecules in the atmosphere [116]. This mechanism is called the *geomagnetic effect*

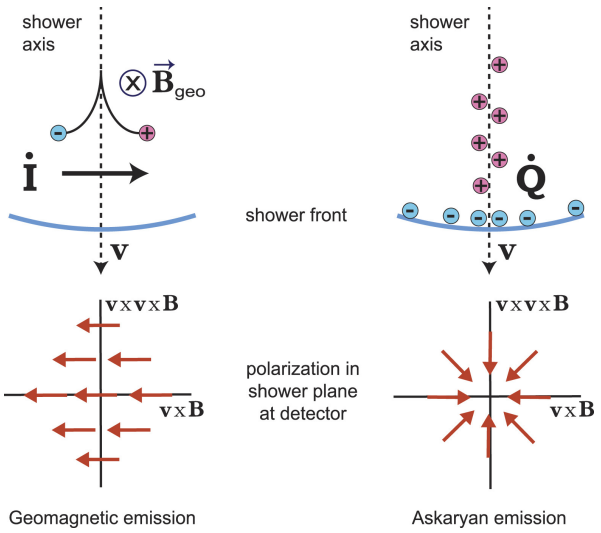

Figure 3.5: The two main emission processes of radio signals from particle cascades: Geomagnetic emission (left) and charge-excess (Askaryan) emission (right). The geomagnetic emission due to the induction of a transverse current is polarized in the direction of the geomagnetic Lorentz force. In air it is typically stronger than the radially polarized Askaryan emission (bottom right) due to the time variation of the net charge excess in the shower front, which is the main mechanism in dense media. Figure from Ref. [115].

or time varying transverse current. As this is the dominant component in radio emission of extensive air showers, the signal strength scales with the number of electrons and positrons in the shower, which scales with the energy of the primary particle. Furthermore, the electric field of the emission $\vec{E}$ scales with the angle between the shower direction ($\vec{v}$) and the local magnetic field ($\vec{B}$), according to the relation $\vec{E} \sim \vec{v} \times \vec{B}$ [111].

The so-called *Askaryan effect* [112, 113], or charge-excess, can be described as a variation of the net charge excess of the shower in time ($\dot{q}$) in combination with Cherenkov-like effects due to the refractive index of air. Effectively, the charge excess arises due to the ionization of the surrounding media by the moving shower, dragging the electrons along with the shower front, whereas the heavier positive ions stay behind (see Figure 3.5). The matter electrons are accelerated in the into the shower by Møller scattering ($e^- + e^-_{\text{medium}} \longrightarrow e^- + e^-$), Bhabha scattering ($e^+ + e^-_{\text{medium}} \longrightarrow e^+ + e^-$) and Compton scattering ($\gamma + e^-_{\text{medium}} \longrightarrow \gamma + e^-$). In addition electron-positron annihilation ($e^+ + e^- \longrightarrow \gamma + \gamma$) and Bhabha scattering decelerate shower positrons which also contributes to the charge excess in the shower [117]. In a non-absorptive, dielectric medium the time-variation of the net charge excess develops a coherent electromagnetic pulse [117]. The Askaryan effect plays a sub-dominant role in air showers, while it is the dominant contribution to the radio signal of showers in dense media.

Both time varying effects induce linearly polarized radiation, but differ in their polarization direction. A useful coordinate system to describe the polarization aligns with the shower: one axis is parallel to the shower's direction of movement, called $\vec{v}$. The second axis is perpendicular to both, $\vec{v}$ and the geomagnetic field $\vec{B}$, and named $\vec{v} \times \vec{B}$. The third axis is perpendicular to the other two axes and called $\vec{v} \times (\vec{v} \times \vec{B})$. In Figure 3.5 the polarization for geomagnetic and charge excess emission are shown in the $\vec{v} \times \vec{B}$ and $\vec{v} \times (\vec{v} \times \vec{B})$ plane.

The geomagnetic effect polarizes the electric field parallel to the Lorenz force ($\vec{v} \times \vec{B}$).

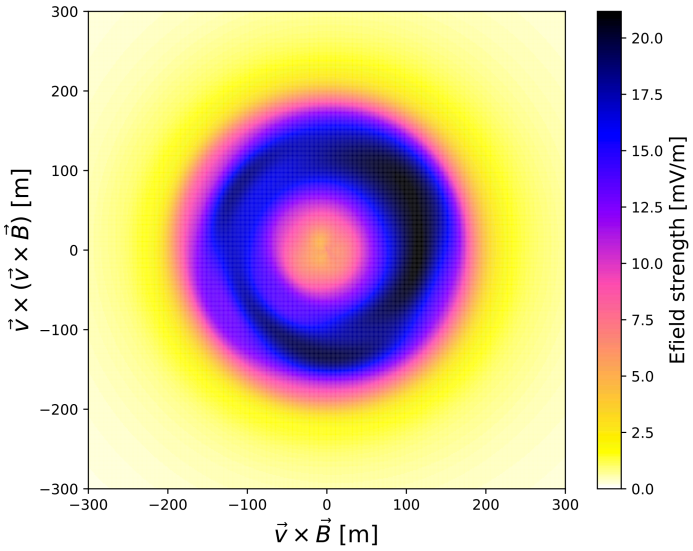

Figure 3.6: Maximum electric field strength distribution of an air shower. Simulations done with CoREAS of a 10^{18} eV air shower induced by a proton in Greenland at 3000 m. The electric field strenght is interpolated in the frequency range 50 MHz to 1000 MHz. The asymmetry due the interference of geomagnetic and Askaryan emission is visible.

Consequently, the angle of polarization remains constant regardless of the position of the observer with respect to the shower axis. The varying net-charge responsible for the Askaryan effect is radially symmetric around the shower axis. Therefore, the induced electric field vector points radially toward the shower axis, so the orientation of the electric field vector depends on the location of an observer with respect to the shower axis.

The angle of polarization, which measures both effects, therefore also depends on the position of the observer. The electric field of the resulting emission can be written as:

$$\vec{E} \propto -\sin(\alpha) \cdot \vec{e}_{\vec{v}\times\vec{B}} + a \cdot \vec{e}_r \tag{3.12}$$

where $\vec{r}_r$ is a unit vector pointing toward the shower axis and a is the so-called relative charge excess strength, which varies from event to event and also depends on the distance to the shower axis. The interference of co-aligned and counter-aligned polarization leads to an observed asymmetric radiation pattern around the shower axis (see Figure 3.6).

For wavelengths larger than the thickness of the emitting shower front and for $c \sim c_0$, the vectorial electric field adds up coherently (MHz regime). This results in a coherent broadband pulse.

The medium in which the particle shower propagates adds another effect. Since the refractive index of air is $n_{\text{air}} > 1$ with a typical value at sea level of $n_{\text{air}} \approx 1.0003$ and decreasing with atmospheric density to higher altitudes, the radio waves travel slightly slower through the air (speed of light in the medium) than the relativistically moving particle front. This causes a strong forward-beaming of the emission, and a compression of the emission in time (Cherenkov-compression). Under a certain viewing angle, so-called Cherenkov angle, the radiation emitted by the entire shower arrives simulta-

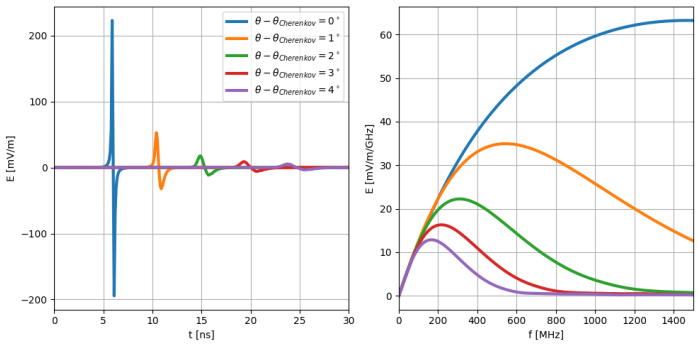

Figure 3.7: Electric field waveforms (left) and spectra (right) of the radio signal emitted at different viewing angles relative to the Cherenkov angle by a shower depositing 1 EeV in ice. For better readability, the waveforms have been shifted in time. Fig. from Ref. [78].

neously. This leads to an enhancement of the pulse with a length of a few nanoseconds [118]. The Cherenkov angle can be calculated with:

$$\cos(\theta_c) = \frac{c_0}{n \cdot v} \tag{3.13}$$

where n is the index of refraction and v/c_0 the relativistic velocity. For air, θ_c^{air} has a value of 1°, which leads, depending on Xmax and the arrival direction to a typical radius on the ground of 100 m to 200 m around the shower axis [119].

The temporal compression at the Cherenkov ring allows the detection of radio emission from air showers (or other media) at much higher frequencies than given by the coherence criterion.

3.2.2 From neutrino and muon induced showers in ice

Particle cascades in ice have a longitudinal extension of $\mathcal{O}(10\,\text{m})$, while air showers are on the scale of kilometers. This is the principle reason why geomagnetic emission is negligible in dense media, making the Askaryan charge-excess emission the only relevant mechanism [98]. As in the atmosphere, the refractive index of the ice $n_{\text{ice}} \approx 1.78$ causes a compression of the emission in time due to Cherenkov like effects (see Section 3.2.1). The shower propagates with the vacuum speed-of-light c_0 whereas the radio emission only propagates with c_0/n_{ice}. At the Cherenkov angle of $\theta_c^{\text{ice}} \approx 56°$, all the signals emitted along the path of the shower arriving at the same time, which will lead to a maximum constructive interference. A significant emission strength is only observed close to the Cherenkov angle [120]. Figure 3.7 shows a typical broad-band bipolar pulse of nanosecond length. The pulse has a slight asymmetry which is a consequence of the charge-excess distribution. The initial rise is steeper than the decay of the charge-excess [108]. At the Cherenkov angle coherence is given over frequencies ranging from a few MHz to tens of GHz. If the viewing angle is off the Cherenkov angle, the coherence disappears first at high frequencies.

In nc interactions, all flavors give similar signatures, i.e. a hadronic shower is created (see Section 3.1.2) and the outgoing neutrino remains undetected. The radio emission from the hadronic component is negligible. Due to the decay of neutral pions into two

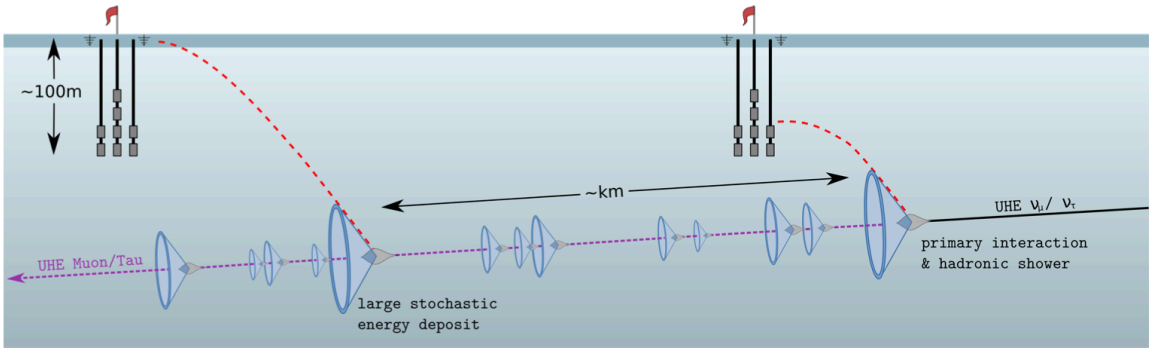

Figure 3.8: Schematic of a charged-current interaction of a UHE ν_μ or ν_τ and its in-ice radio-detection. The primary neutrino-nucleon interaction produces a hadronic shower. The final-state charged lepton, a muon or a tau, can travel several kilometers while producing sub-showers stochastically, generating Askaryan radiation which can be observed at multiple underground detector stations, resulting in a multi-shower event. The change of the refractive with depth causes the trajectory of radio signals to bend on their way to the stations. Fig. from. Ref. [87]

photons ($\pi^0 \longrightarrow \gamma + \gamma$) an electromagnetic component is created which then emits the radio signal.

In a cc interaction, in addition to the hadronic shower, additional showers may occur depending on the flavor of the neutrino. The showers produced by the outgoing lepton can be detected as a superposition with the shower from the first interaction, or isolated without the counterpart [87].

A electron-neutrino cc interaction will almost immediately produce a hadronic and an electromagnetic shower, the latter is initiated by the resulting electron. At low energies, the showers are created roughly at the same place and the radio emission interferes mostly constructively. At high energy the shower development is influenced by the LPM effect which leads to an elongation and distortion in the shower. Also, the creation of multiple sub-showers over tens of meters is possible. The electromagnetic shower maximum can be far away from the hadronic shower maximum, so the showers can interfere or their radio signal can be seen as two (or more) independent pulses.

In the cc interaction of a muon-neutrino or a tau-neutrino a hadronic shower is created as well. The resulting leptons ($\mu^\pm$ and $\tau^\pm$) propagate through the medium generating lots of secondary showers over a range of kilometers until they decay, as illustrated in Figure 3.8. Muons lose most of their energy through bremsstrahlung, pair production and nuclear interactions, and they typically have low energies when they decay. Therefore muons are susceptible to producing subsequent showers if they emit i.e. a bremsstrahlung photon or hadrons above a certain energy [109]. Taus radiate electron-positron pairs mainly, which creates electromagnetic cascades, but they tend to lose larger amounts of energy via photonuclear interaction, which creates hadronic cascades. Taus can also decay while they have large energies, into hadronic and leptonic channels which produce showers and can also result in a muon which radiates further [109]. The tau track length increases linearly with energy, so the produced showers will overlap at low energies, at the highest energies the cascades can be measured separately, or only one cascade is measured at a given observer position. The appearance of a tau neutrino induced shower closely followed by a shower generated by the created taus decay is described as double-cascade neutrino signature and should in principle be measurable in

radio neutrino detectors [109]. A prospect for flavor composition measurement of ultra-high energy cosmic neutrinos with in-ice radio neutrino detectors is given in Ref. [87].

Muons originating from air showers undergo the same energy losses in ice through bremsstrahlung, pair production and nuclear interactions as muons stemming from a neutrino interaction and can therefore create showers with a significant radio emission. Simulations indicate, that the background of atmospheric muons from cosmic rays is non-negligible for in-ice neutrino detectors [109] and will be further investigated in Chapter 7.

3.2.3 Radio waves in ice

The physics described above leads to different requirements for the medium of radio neutrino detectors. Since neutrinos rarely interact, a large volume of a dense medium is required. The Askaryan effect requires a dielectric medium, and the medium must be transparent to the radio waves produced. Liquid water is a polar molecule and the molecules are free to align themselves with the electric field shielding the radio wave. This makes deep glacial ice a suitable medium for a radio neutrino detector.

The radio signal emitted by the particle cascade propagates through the ice and is attenuated. The attenuation length is defined as the propagation distance over which the signal amplitude is reduced by a factor of $1/e$ [108]. The main quantities determining the transparency to radio waves is the chemical composition of the ice and its temperature. Since the temperature increases with depth, the attenuation length decreases. The attenuation also increases for low frequencies. At Greenland the attenuation length is about 1 km for frequencies between 145 MHz to 350 MHz[121, 122].

The path of the radio signal is determined by the index of refraction, which is related to the density of the ice. Fresh snow falls on the granular firn ($n_{\text{firn}} = 1.3$), compressing it with its weight. The firn is thus slowly compressed into clear ice. The refractive index decreases rapidly until it reaches a constant value for deep glacial ice ($n_{\text{ice}} = 1.78$ for Summit Station in Greenland at around 70 m). An upward propagating radio wave is refracted and bent downward near the surface due to the change in the refractive index, as shown in Figure 3.9. In addition, the rapid change in refractive index at the firn-air interface causes signals to be reflected, resulting in additional reflected pulses measured by the detector. Modelling the radio propagation is an important uncertainty and complicates the reconstruction of neutrino parameters [123–125]

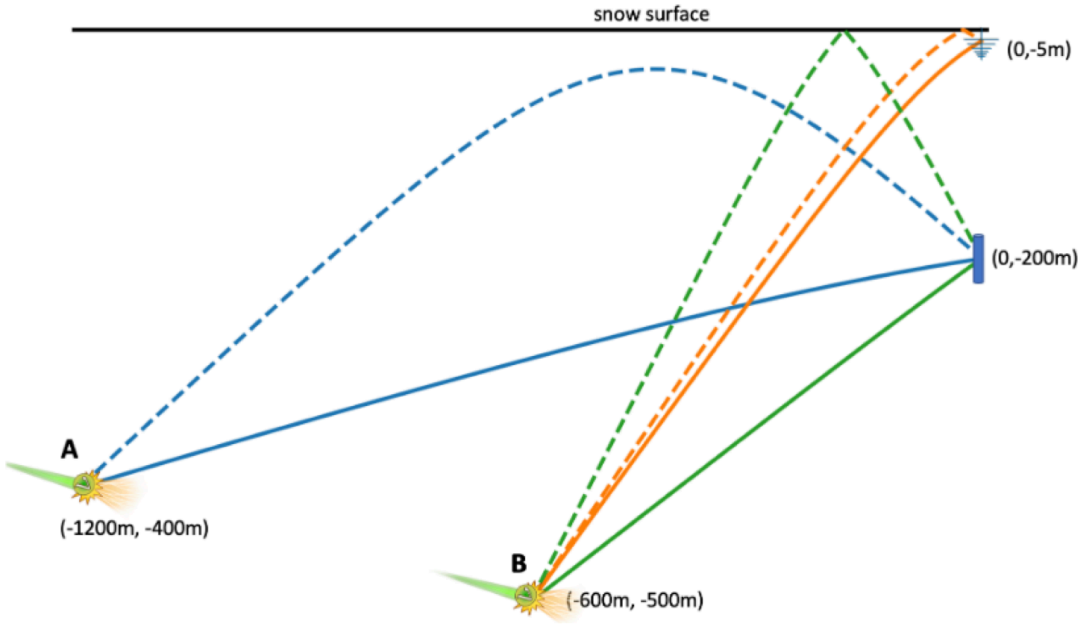

Figure 3.9: Possible radio ray paths from the point of interaction (A and B) to a Surface antenna or deep component antenna in ice with increasing density from top to bottom. Each interaction can arrive at an antenna via a direct path (solid lines) or an indirect path (dashed lines). An indirect path can be bend by the varying refraction index of the ice (blue dashed line) or by being reflected at the firn-air transition (dashed orange and green line). Fig. from Ref. [108].

4 Radio detectors

Radio detection of particle cascades has matured over the past decades, with the installation and successful operation of radio experiments and a quantitative understanding of the radio emission from atmospheric particle cascades. An overview of modern radio detectors can be found in Ref. [98].

4.1 Experimental approaches

The first prototype experiments for radio detection of neutrinos in ice were the Radio Ice Cherenkov Experiment (RICE), which operated from 1999 to 2010 [69], and the Antarctic Under-Ice Radio Array (AURA) [126], both located at the South Pole. RICE provided the first neutrino limits [68] from radio detectors and valuable experience in deploying and operating radio detectors at depths of down to 200 m. AURA build on the experience of RICE with its electronic design based on the RF specific electronic applications and studied the noise environment.

Ice has the advantage over other dense media, such as rock or lunar regolith, of larger radio wave attenuation length and the large volumes of ice available in Antarctica and Greenland. Therefore, ice appears to be the preferred medium for future large-scale detectors [127].

The balloon-borne Antarctic Impulsive Transient Antenna (ANITA) experiment made its first flight with its ANITA-lite prototype over Antarctica in 2004 [128]. In order to detect a neutrino signal, the neutrino must first interact below the surface of the ice and then travel upwards to leave the ice itself. ANITA was the first radio-neutrino experiment to report the detection of cosmic ray induced air showers [129]. Most of the cosmic ray signals were not measured directly, but detected after reflection from the ice. Balloon-borne experiments can search large ice volumes, but due to their great distance they are only sensitive above 10^{18} eV.

The next generation of in-ice pilot arrays have been installed since 2010 and have been in operation for several years. The Askaryan Radio Array (ARA) [70, 97, 130, 131] at the South Pole currently runs with five stations with 50 m to 200 m deep in-ice antenna strings. One station has an additional phased array, making ARA the first to use the interferometric beamforming technique in a borehole [132]. The Antarctic Ross Ice Shelf Antenna Neutrino Array (ARIANNA), located on the Ross Ice Shelf off the coast of Antarctica, consists of shallow antennas just below the ice surface that are also sensitive to radio signals from cosmic ray air showers [133]. Without external infrastructure, the stations operate autonomously in low-power, wireless communication mode. Although these two detectors are too small to be sensitive for neutrino detection [132, 134], much work has been done to understand the technique of in-ice detection, paving the way for a larger radio array.

As it will be discussed in Section 4.2, the Radio Neutrino Observatory Greenland (RNO-G) combines the strategies of ARA and ARIANNA by choosing a hybrid station design

with a deep and a shallow component, including a deep phased-array trigger and autonomous stations. With 35 stations, RNO-G will be sensitive to optimistic cosmogenic and astrophysical neutrino fluxes, making RNO-G the first radio detector to either make a neutrino detection in radio or rule out realistic models. A similar hybrid design approach is planned for the radio array of IceCube-Gen2, consisting of $\mathcal{O}(350)$ stations [135, 136].

Other future neutrino detectors using the radio technique are upcoming: The Payload for Ultrahigh Energy Observations (PUEO) [137], a balloon experiment and the successor to ANITA. The Earth-skimming tau neutrino detectors in mountainous regions, e.g. Beamforming Elevated Array for COsmic Neutrinos (BEACON) [138], TAROGE [139] and Giant Radio Array for Neutrino Detection (GRAND) [140]. Another approach is used by Radar Echo Telescope (RET) [141] which aims to identifying in-ice particle showers by radar reflection.

4.2 The Radio Neutrino Observatory Greenland (RNO-G)

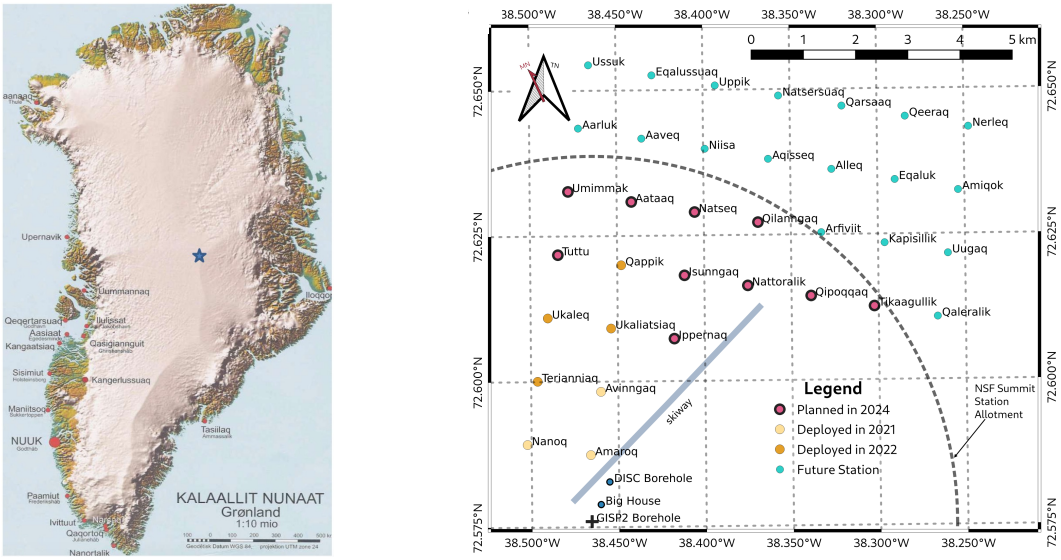

Figure 4.1: Left: Map of Greenland, the blue star marks Summit Station. Right: The planned RNO-G array with 35 stations. The RNO-G stations are located north of the Summit Camp, for which the main community building Big House is indicated. The stations are arranged in a rectangular grid with a spacing of ~ 1.25 km and are named after Greenlandic animals. The year of deployment is indicated by the station's color code. Figure produced by the RNO-G collaboration.

The Radio Neutrino Observatory Greenland (RNO-G) is designed to demonstrate the scalability of the radio detection technology. Located in Greenland at Summit Station (72°35′46″ N, 38°25′19″ W), RNO-G is atop of more than 3 km of glacial ice, see Figure 4.1. Several measurement of the ice properties at Summit Station have been performed [142, 143], indicating an attenuation length at radio frequencies of ~1 km [121, 122].

Of the 35 stations funded, seven have already been deployed and are taking data, namely stations Nanoq (polar bear), Amaroq (arctic wolf) and Avinngaq (arctic lemming, all deployed 2021), as well as Terianniaq (arctic fox), Ukaleq (arctic hare), Ukaliatsiaq (stoat) and Qappik (wolverine, all deployed 2022). The 2023 season has been used for calibration and maintenance.

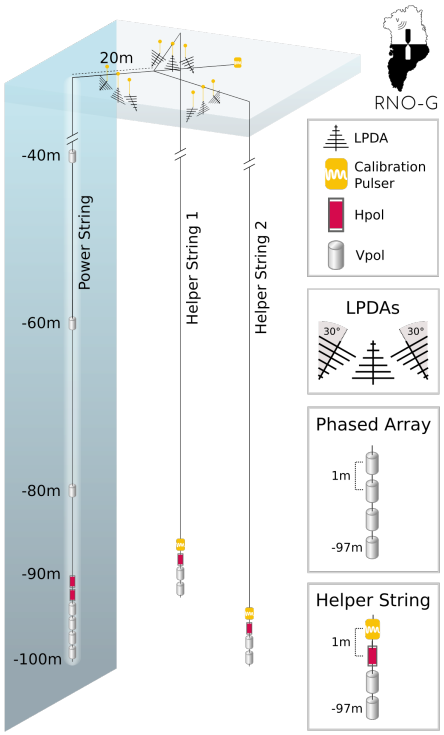

Figure 4.2: Layout of an RNO-G station consisting of a deep and a shallow part. The deep part features horizontally and vertically polarized antennas (Hpol) and Vpol) distributed over three antenna strings (power and two helper strings) down to a depth of 100 m in the ice. In addition, each of the helper strings is equipped with a calibration pulser. The shallow part consists of a calibration pulser and nine Logarithmic Periodic Dipole Antennas (LPDAs) arranged in groups of three and oriented as shown in the legend. Figure produced by the RNO-G collaboration.

4.2.1 The RNO-G station design

An RNO-G station combines a deep component, consisting of three 100 m deep in-ice strings, and a shallow component that is also sensitive to signals from above, see Figure 4.2.

The *deep component* antenna designs are driven by the 11.2″ diameter of the dry boreholes. The vertically polarized (Vpol) antennas are a fat dipole, with an azimuthally symmetric beam pattern and a usable bandwidth ranging from 150 MHz to 600 MHz [144, 145]. For horizontal polarization (Hpol), nearly azimuthally symmetric, cylindrical tri-slot antennas are used. The Hpol antennas have a narrower usable bandwidth than the fat dipoles (200 MHz to 500 MHz), due to their geometry in the narrow borehole (see Fig. 4.3).

The power string is equipped with the interferometric phased array, consisting of four closely-spaced Vpol antennas at ~100 m depth. Directly above are two Hpol antennas and three additional Vpol antennas with a 20 m spacing towards the surface. The phased array is used as a trigger for in-ice showers. Due to the proximity of the antennas, the incoming signal is almost identical except for a time delay. The trigger sums the waveforms coherently, which increases the signal-to-noise ratio (SNR) because the noise is not expected to be correlated. The two Hpols improve the ability to reconstruct the full electric field, especially its polarization. The three additional Vpols are used to reconstruct the vertex position of the first interaction and the arrival direction of the radio

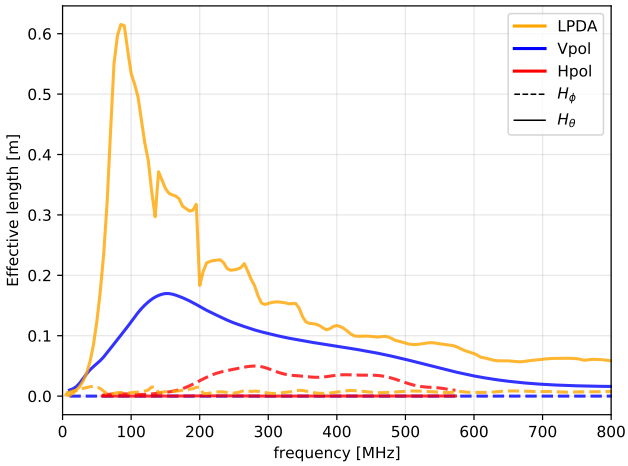

Figure 4.3: The absolute value of the effective length for the LPDA, Vpol and Hpol. For detailed explanation of effective length and the signal chain see Section 5.1. Fig. from Ref [78].

signal. To reconstruct the azimuth angle of the arrival direction, three independent measurements are needed with sufficient distance between the Vpol antennas. Therefore, a station consists of the power string and two additional helper strings. Each helper string has one Hpol, two Vpols and a calibration pulser between a depth of 94 m and 97 m. The calibration pulser ensures regular monitoring of station performance and information on the positional accuracy of all antennas.

The *surface component* consists of nine Logarithmic Periodic Dipole Antennas (LPDAs), three pointing upwards and six pointing downwards at an angle of 30°, and a calibration pulser. The LPDAs are broadband sensitive, which helps determine the radio detection angle with respect to the Cherenkov cone, improving energy reconstruction and pointing resolution. The upward-facing antennas are sensitive to air showers, and are used to reduce background. Each of the nine LPDA antennas has its own analog diode trigger, which is described in more detail in Section 5.2.

4.2.2 Data acquisition system, Power and Communications

An overview of the complete system design of one station is shown in Figure 4.4. The surface antennas are shown at the top left, with the in-ice string below. The data acquisition components are different for surface and deep channels. The surface channels go through a bandpass filter and the SURFACE board into the digitizer and surface trigger on the RADIANT board (RAdio DIgitizer and Auxiliary Neutrino Trigger). The RADIANT utilizes the LAB4D ASIC (Application Specific Integrated Circuit) [146] for readout and digitization. Each deep channel has an IGLU (In-ice Gain with Low-power Unit) as amplifier and RFoF (Radio Frequency over Fiber) transmitter co-deployed into the borehole. The now optical signals are received by the DRAB (Downhole Receiver & Amplifier Board) inside the enclosure at the surface, the DRAB converts the signal back to analog, amplifies it again before feeding it into the digitizing RADIANT or in case of the phased array on the digitizer board and low-threshold triggering FLOWER board (FLexible Octal WavEform Recorder) [147]. The recorded data is then stored on the controller board's SD card

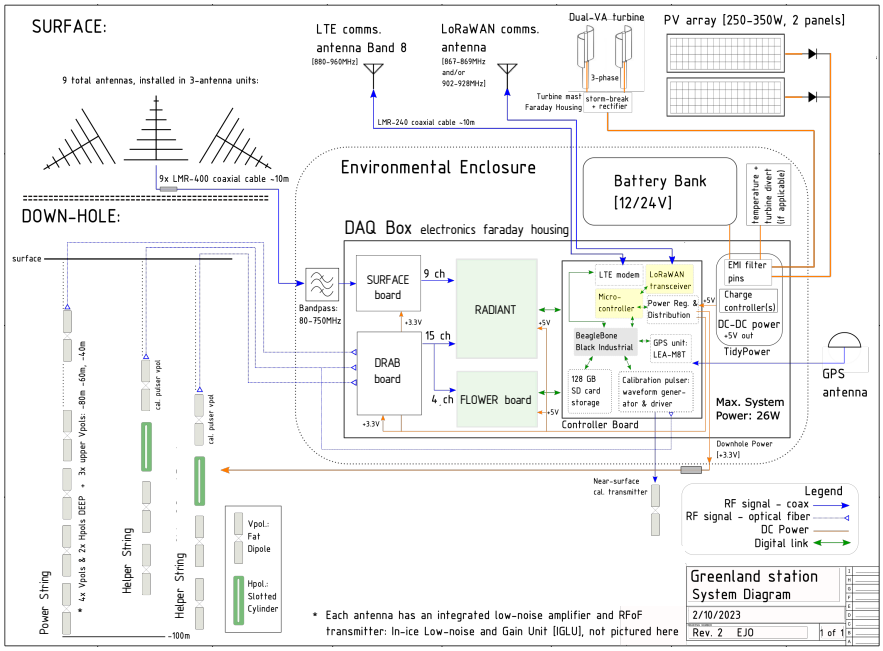

Figure 4.4: System diagram of an RNO-G station. See text for a description. Figure produced by the RNO-G collaboration.

(Secure Digital card). The controller board comprises a commercially available single board computer [147]. A picture of the DAQ box is shown in Figure 4.5.

Currently, a stored waveform consists of 2048 samples recorded at a sampling rate of 3.2 GHz, resulting in a time period of 640 ns. To allow for longer time traces the sampling rate will be adjusted to 2.4 GHz, increasing the time window to ~853 ns. The recorded data is divided into runs, with a full run being two hours of data under normal conditions, and stored on a hard drive at Summit Station. A small fraction (~5%) of the data is sent directly to a RNO-G institute via satellite, while the complete data set is hand-delivered on a hard drive at the end of the season. Communication with the stations is wireless. A commercial LTE (Long Term Evolution) base station with a band of 880 MHz to 915 MHz uplink and 925 MHz to 960 MHz downlink has been deployed at Summit Station, which is mainly used for data transfer. An additional LoRaWAN (Long Range Wide Area Network) network has been installed to provide a low-power, low-bandwidth backup link for control and monitoring.

To operate autonomously, each station is powered by two solar panels, with a maximum output of 300 W and a 5 kWh lead-acid battery bank. Wind turbines are being tested to provide power during the polar night. When operating in full-station mode, the power consumption of an RNO-G station is 24 W. By turning off the phased-array trigger and reducing data transmission to a minimum, the power consumption is reduced to 17 W, in surface-only mode 6 W are consumed.

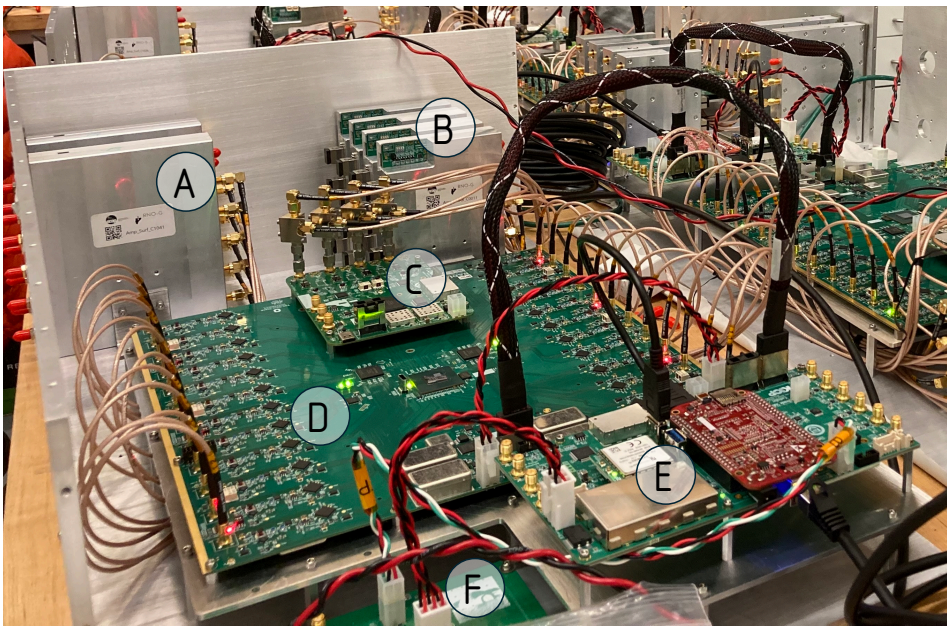

Figure 4.5: Nearly complete DAQ box, with **A** Surface amplifiers (SURFACE board), **B** Deep amplifiers and RFoF receiver (DRAB boards), **C** Low-threshold trigger (FLOWER board), **D** Digitizer (RADIANT board), **E** Controller board with single board computer, GPS unit, and calibration pulser source daughter board. **F** Power regulation board, Picture taken by E.Oberla.

4.3 Radio backgrounds

Incoherent thermal noise, (impulsive) man-made noise, and radio emission from cosmic ray air showers and their remnants are the main sources of background for neutrino detection.

Radio neutrino detectors operate very close to the intrinsic thermal noise floor, because their sensitivity scales with the amplitude of the signal. Thermal noise is caused by electrons in a conductor moving due to their thermal energy independent of the applied voltage. Each frequency is equally likely to occur, resulting on average in a flat frequency spectrum. The upward-facing antennas also measure diffuse emission, mostly from the galactic plane, with an exponential spectrum [148] over the entire MHz band, which introduces an irreducible noise floor. For RNO-G the diffuse thermal emission from the galaxy dominates the instrumental noise below $\sim$ 120 MHz. Since the Galaxy is spread across the sky, and the galactic center is below the horizon, the variation of the galactic noise temperature seen in the antennas over the day is relatively small [149]. The constant thermal emission from the Sun has only a small contribution, not exceeding 6% relative to the galactic emission below 200 MHz [150]. However, several solar flares occur per week in the frequency range and field of view relevant to RNO-G [151].

An optimal measurement site has no noise, however the most common causes of interference are narrow-band transmitters, including AM/FM radio frequencies or communications radio. All kinds of electrical equipment can also produce short pulses; typically, this occurs in combination with sparking (spark plugs, switches, etc.). First analysis suggest that anthropogenic backgrounds at Summit Station are mostly seen by the surface antennas but do not constitute a dominant persistent noise source in the deep antennas [149].

Cosmic ray air showers produce three different types of background: (I) the *in-air radio emission* of air showers can be refracted into the ice to the antennas; (II) the energy-dense *core of incompletely developed air showers* can develop further into the ice and produce Askaryan emission; and (III) in-ice particle showers following an *energy loss of an atmospheric muon*. The signatures of (I) and (II) have previously been studied and quantified [152–156]. Both signals can be triangulated close to the surface, providing signatures that can be distinguished from a neutrino event at the analysis level. Reflections in the ice can complicate the reconstruction, but this is also true for the neutrino signals themselves. For both direct air shower backgrounds, a reasonable estimate of the background rate is possible, because the distribution of shower maxima as function of energy is relatively well known. The number of muon-induced background events, however, has been studied less. It has in principle been shown that muons are a non-negligible background to radio neutrino detectors in ice [109]. However, the predicted event rate depends on the muon flux, which in turn depends strongly on the hadronic interaction model, and the cosmic ray composition, all of which are less well determined, in particular at the highest energies. With its hybrid design of surface antennas and three deep antenna strings, RNO-G is the first experiment that can measure and reconstruct air shower signals in combination with their in-ice counterparts. A detailed study of the atmospheric muon background at PeV energies is described in Chapter 7.

Characterization and modeling of the shallow component of RNO-G

5

In order to analyze the recorded data and make a detection of an air or in-ice particle cascade, it is necessary to characterize the components involved in the measurement such as the signal chain, the trigger and the variations from DAQ (data acquisition system) to DAQ. This section provides an overview of the hardware used in the shallow detector, the diode trigger and the hardware testing prior to deployment. The characterization of the deep component is still in progress and will be described elsewhere.

5.1 Signal chain of the shallow component

The shallow component consists of nine Logarithmic Periodic Dipole Antennas LPDAs, three of which face upward. The hardware used is the same for all of them, only the orientation of the antennas in the ice is different. This exposes them to radio emissions from different sources: The upward facing antennas are sensitive to signals from above, such as air showers, the Galaxy, etc., while the downward facing antennas are designed to measure particle showers in the ice. The voltage measured in the antenna over time, called waveform or trace, is amplified with the SURFACE board and digitized with the RADIANT board (RAdio DIgitizer and Auxiliary Neutrino Trigger). Within the next subsections the relevant physics and hardware will be explained in the order of signal processing.

5.1.1 The electric field and its polarization

The electric field generated by an air shower propagates along the shower axis, parallel to $\vec{v}$, its polarization is perpendicular to the shower axis, along $\vec{v} \times \vec{B}$. Therefore, the natural coordinate frame for air showers is given by the unit vectors $\hat{e}_{\vec{v}}$, $\hat{e}_{\vec{v}\times\vec{B}}$ and $\hat{e}_{\vec{v}\times\vec{v}\times\vec{B}}$ in the shower plane as shown in Figure 5.1. The observed electric field is usually measured on the ground with respect to the arrival direction, where the x-axis is pointing east and the y-axis is pointing north, the z-axis is defined as positive upwards. When describing an incoming signal, the polar coordinate system called 'on-sky' is used. A plane wave arriving at an observer on the ground in the direction of $\hat{e}_{\vec{v}}$, is described by its zenith θ and azimuth angle ϕ. The electric field is polarized along $\hat{e}_\theta$, $\hat{e}_\phi$, as defined in Figure 5.1. The polarization transformation from the natural coordinates of the air shower to 'on-sky' coordinates is a rotation along the shower axis.

In Figure 5.2 the electric field of a cosmic ray induced shower is shown in the time domain (left side) and in the frequency domain (right side). The time trace shows a sharp nanosecond pulse, and the frequency domain shows a broad spectrum with a maximum at a few MHz, falling steeply with higher frequencies. The expected electric field strength is in the millivolt per meter range.

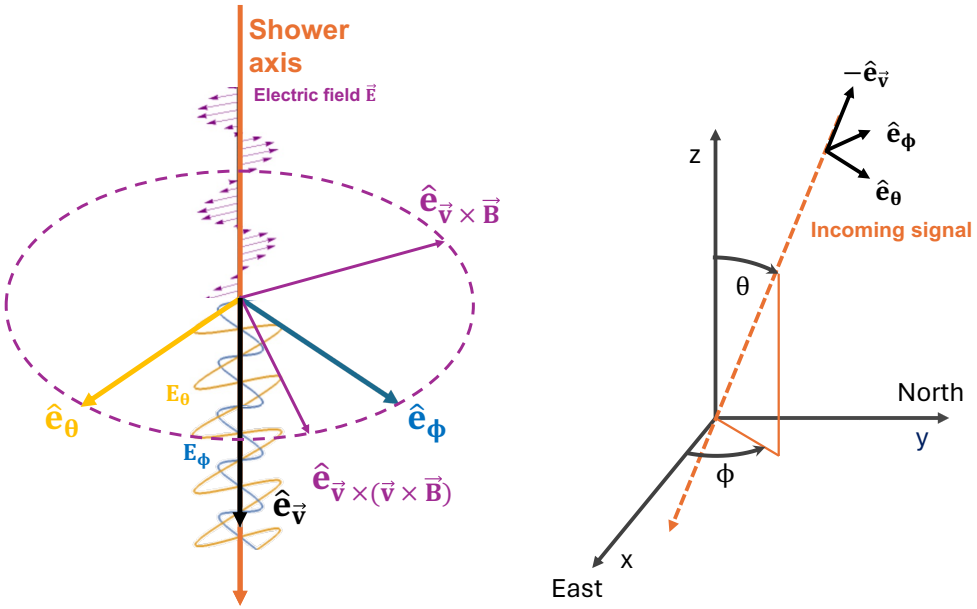

Figure 5.1: Left: Comparison of the coordinate systems important for the polarization. The orange arrow indicates the shower axis, the purple circle indicates the shower plane. The natural coordinate system for the air shower electric field is given by $\hat{e}_{\vec{v}}$, $\hat{e}_{\vec{v}\times\vec{B}}$ and $\hat{e}_{\vec{v}\times\vec{v}\times\vec{B}}$. On ground, a coordinate system with respect to arrival direction is useful, given by $\hat{e}_{\vec{v}}$, $\hat{e}_\theta$, $\hat{e}_\phi$. Therefore the electric field has the components E_θ, E_ϕ. Both coordinate systems share $\hat{e}_{\vec{v}}$. Right: 'On-sky' coordinate system as seen from ground. The x-axis is pointing east, the y-axis to the north. The incoming signal corresponds to the air shower axis. $\hat{e}_{\vec{v}}$, $\hat{e}_\theta$, $\hat{e}_\phi$ are the same as left.

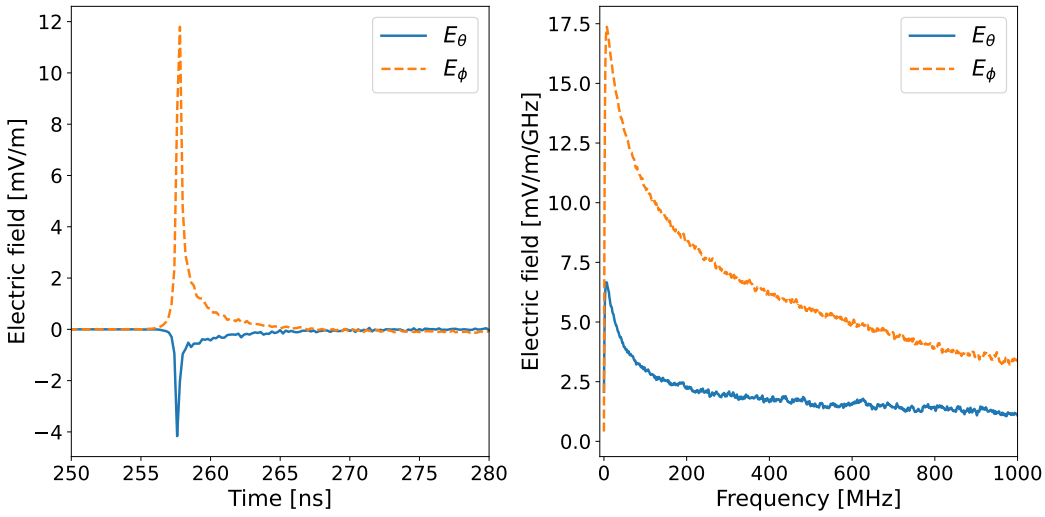

Figure 5.2: Shown are the two components E_θ and E_ϕ of the electric field generated by an air shower with energy 10^{18} eV. The left figure shows the radio pulse in the time domain. On the right the frequency spectrum is shown.

5.1.2 The logarithmic periodic dipole antenna (LPDA)

The electric field will eventually be measured by a LPDA (type: Create CLP-5130-2N), consisting of 17 half-wave dipole driven elements of gradually increasing length. The intervals between the tines following a logarithmic function of the frequency. A picture of a LPDA is shown in Figure 5.4 left.

The principle of how the LPDA receives a signal is the same as for a single half-wave dipole antenna, which consists of two metal tines connected to a receiver in the center as

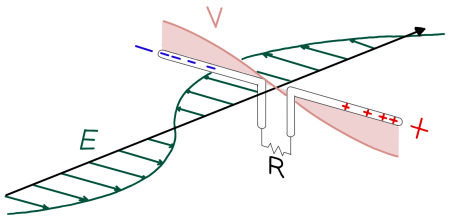

Figure 5.3: Illustration of a half-wave dipole antenna receiving a radio wave. The antenna consists of two metal tines connected to a receiver *R*. The electric field (*E*, dark green arrows) of the incoming wave pushes the electrons in the tines back and forth, charging the ends alternately positive and negative.

illustrated in Figure 5.3. The electric field of the incoming wave moves the electrons in the tine back and forth, alternately charging the ends positive and negative. Therefore, the antenna is most sensitive to electric fields which arrive perpendicular to the conductor, i.e. the tine. If the length of the dipole is half the wavelength, $\frac{\lambda}{2}$, of the incoming wave, the oscillating field induces standing waves in the conductor, because the current gets reflected at the ends of the tine. The antenna is also resonant for $\frac{\lambda}{4}k$ with k = odd numbers. Therefore, the length of the tine determines which frequencies the antenna is sensitive to. The LPDA used covers a band from 105 MHz to 1300 MHz in air. Since the antennas are buried in snow, the wave velocity is reduced and the frequency ν changes with the refractive index of the firn $n_{\text{firn}} \approx 1.3$:

$$\nu_{\text{firn}} = \frac{\nu}{n_{\text{firn}}} \tag{5.1}$$

Therefore the band changes to 80 MHz to 1000 MHz, which is favorable for air shower signals, since their spectrum is strongest at lower MHz frequency and steeply falling towards higher frequencies.

The signal measured by the antenna depends on the incoming field $\vec{E}(t)$ and its direction with zenith angle θ and azimuthal angle ϕ. Since the antennas can be deployed in various directions, a reference coordinate system has to be defined. The angles of the arriving signal with respect to the antenna are defined as shown in Figure 5.4. The zenith angle with respect to the antenna is called θ_{ant} and is measured from the longitudinal axis of the antenna, ϕ_{ant} describes the azimuth where 0° is perpendicular to the longitudinal axis of the antenna and its tines.

The response pattern of an antenna to an electric field can be described as the vector effective length (VEL). The VEL of the antenna represents the mapping between the voltage induced over the antenna and the electric field of the signal [157]. In the frequency domain, this is a simple multiplication, therefore the Fourier transform of the observed voltage $\mathcal{U}(\theta, \phi, f)$ equals the antenna response pattern, denoted $\vec{H}, (\theta, \phi, f)$ multiplied with the Fourier transform of the electric field $\vec{\mathcal{E}}(f)$:

$$\mathcal{U}(\theta, \phi, f) = \vec{H}(\theta, \phi, f) \cdot \vec{\mathcal{E}}(f). \tag{5.2}$$

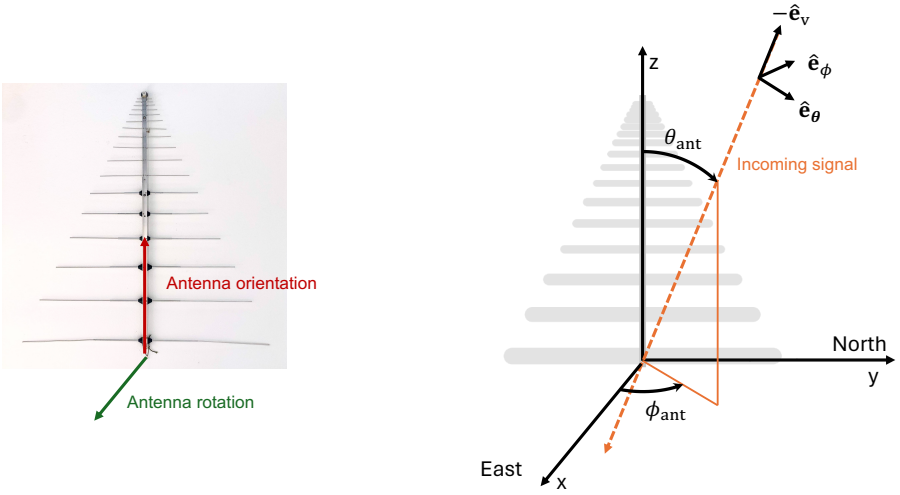

Figure 5.4: Left: Picture of the LPDA used. Right: Visualization of a LPDA structure, its tines are parallel to the east-west direction. The orientation (red) indicates the direction of the antenna tip (a rotation along the y-axis), the rotation (green) specifies the direction perpendicular to the tines (a rotation along the z-axis). The antenna orientation and rotation are always perpendicular to each other. The orange dashed line represents a signal arriving. The zenith angle θ_{ant} is counted from the top, the azimuth angle ϕ_{ant} counterclockwise from the antenna rotation.

The VEL is different for different polarizations of the electric field. It is therefore expressed as H_θ and H_ϕ. In Figure 5.5 the VEL simulated with WIPL-D [158] for the LPDA in firn is shown for different frequencies (as indicated by the color code) as a function of zenith (columns 1 and 2) and as a function of azimuth (columns 3 and 4). The sketch above the polar plots indicates the direction with respect to the antenna. The main beam is pointing forward, i.e. in the z-axis at $\theta_{ant} = 0°$. A small backlobe is visible. The first column shows the VEL for the polarization with $\hat{e}_\theta$ (H_θ), the second column for H_ϕ. Since the polarization directions are perpendicular to each other, their highest sensitivity direction differs by 90°, when the respective polarization is along the tines. The influence of the three antennas close to each other has been studied in Ref. [159], experimental tests confirmed that the effect is negligible.

In Figure 5.6, the VEL for a signal arriving at $\theta_{ant} = 55°$ and $\phi_{ant} = 0°$ (meaning perpendicular to the tines) is depicted. Within the bandwidth the VEL peaks around 80 MHz and decreases towards higher frequencies. The additional variations of the VEL in the H_ϕ component within the frequency band are due to the interaction of the dipole elements of the LPDA that resonate at different frequencies [160].

The corresponding induced voltage of the air shower pulse over the antenna is shown in Figure 5.7. The result is a fast oscillating pulse with a duration of ~40 ns. The pulse broadens in the time domain due to losses in the high frequency range, and due to the group delay of the antenna, which induces dispersion that broadens the pulse even further.

5.1.3 Amplifier - The SURFACE board

After the signal is registered by the antenna further modifications are necessary to obtain a good signal quality. A schematic visualization of the surface signal chain of a RNO-G station is shown in Figure 5.8. The electric signal generated by the antenna is filtered

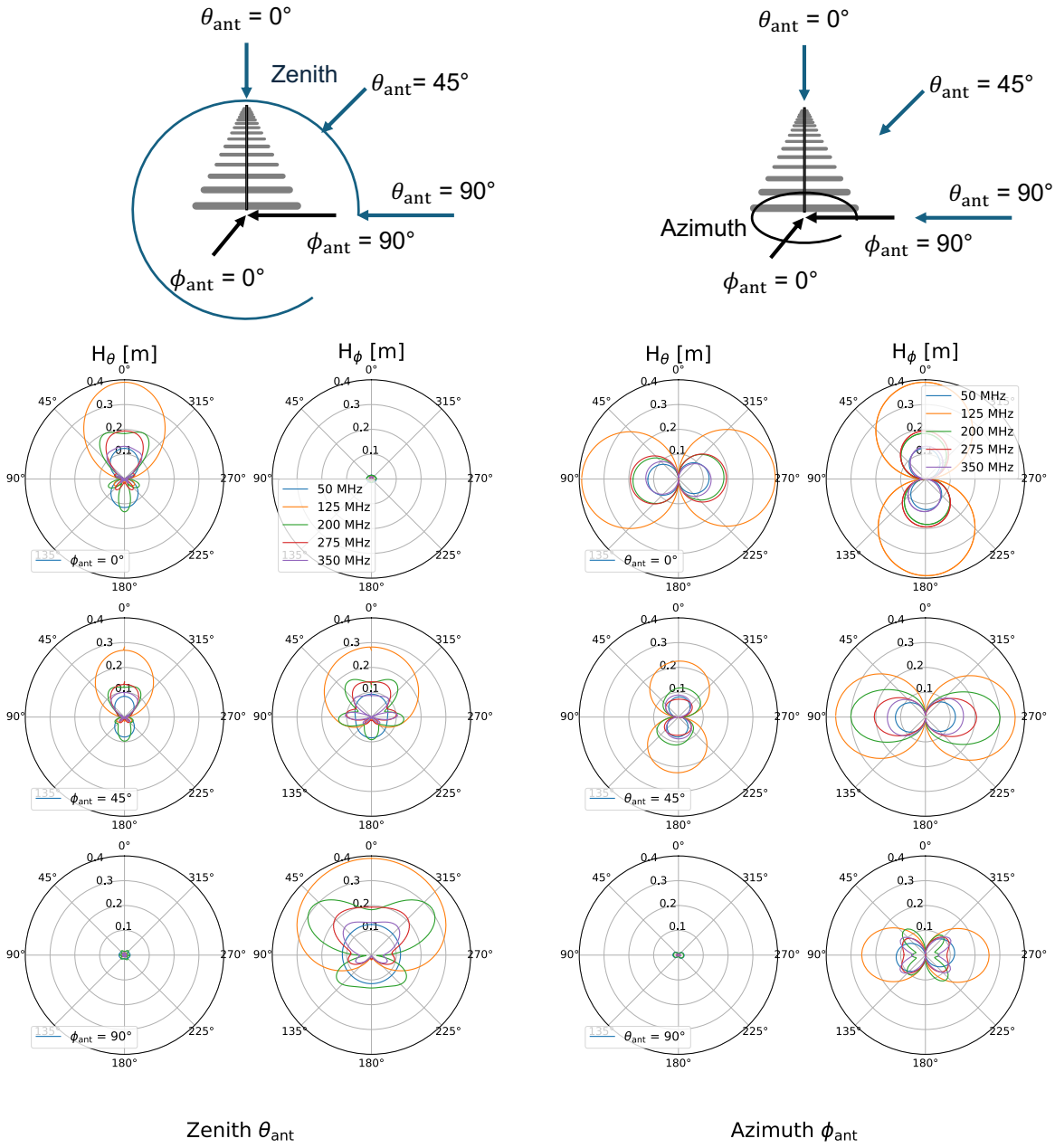

Figure 5.5: Simulated antenna response pattern of an LPDA for both polarizations in the firn. The upper left show the the zenith distribution for H_θ (first column) and H_ϕ (second column) at three different azimuth angles as stated in the legend on the left polar plot. The lower right three rows show the azimuth distribution for three different zenith angles (0°, 45° and 90°). The color code indicates the frequency (50 MHz, 1250 MHz, 200 MHz, 275 MHz, 550 MHz. On the opposite side a visualization of the antenna and its directions is shown.

and amplified by the SURFACE board. Then, the signal is fed into the RADIANT where it is split into a trigger and a signal path. The ratio of the signal strength depends on the version of the RADIANT. The version 2 RADIANT board (V2) has a power splitting ratio of 1/10, the version 3 RADIANT board (V3) uses 1/2. The trigger path modifies the waveform further, which will be described in Section 5.2. If the trigger is true, the waveform in the signal path is digitized by the analog-to-digital converter (ADC), which is the LAB4D chip. The data is stored on the SD card and transferred via LTE.

The SURFACE board is specifically designed for the requirements of the RNO-G detector.

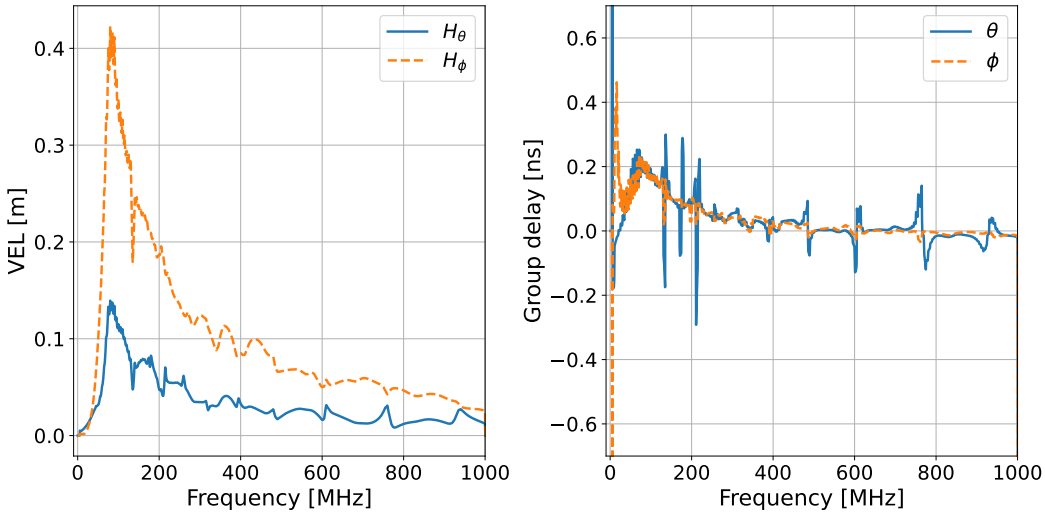

Figure 5.6: The absolute value of the vector effective length of the LPDA (left) and the group delay (right) for the signal shown in Figure 5.2, arriving at $\theta_{\text{ant}} = 55°$ and $\phi_{\text{ant}} = 0°$ with respect to the antenna.

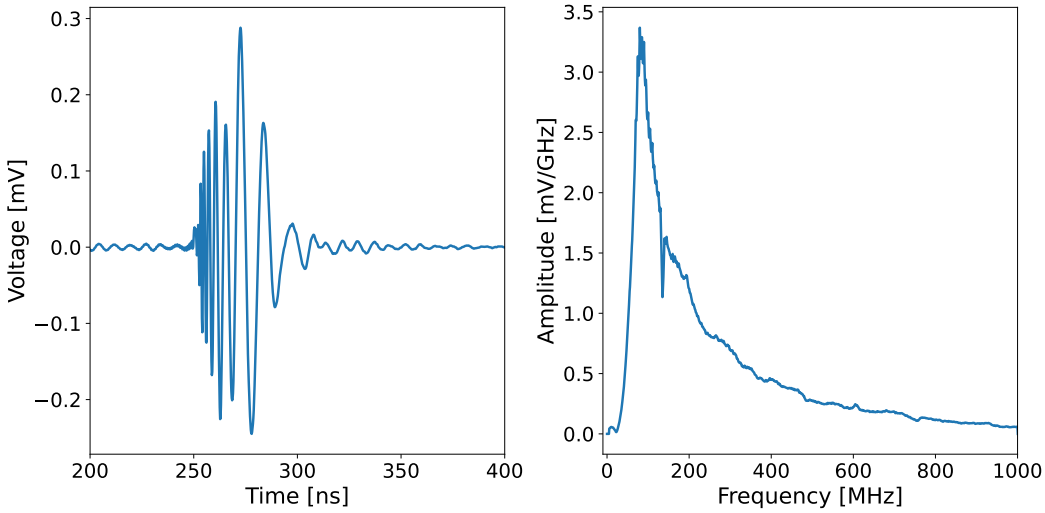

Figure 5.7: Simulated induced antenna voltage for the electric field shown in Figure 5.2. The signal arrives at $\theta_{\text{ant}} = 55°$ and $\phi_{\text{ant}} = 0°$ with respect to the antenna. The shown signal is without amplification. Left: timed domain. Right: Frequency domain.

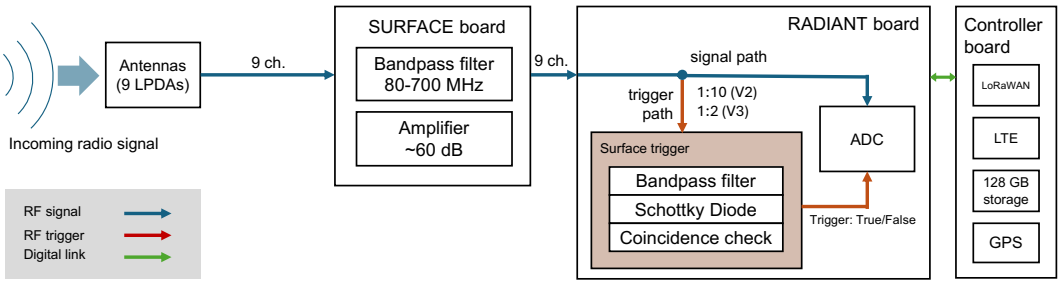

Figure 5.8: Schematic visualization of the signal chain for the surface component of one station. After the electric field is registered by the antennas, the signal is processed by the SURFACE board with bandpass filter and amplifier. The signal is then split into a trigger path and a signal going directly to the analog-to-digital converter (ADC). The version 2 RADIANT board (V2) has a power splitting ratio of 1/10, the version 3 RADIANT board (V3) uses 1/2. The ADC output is then transferred to the controller board and stored on the SD card.

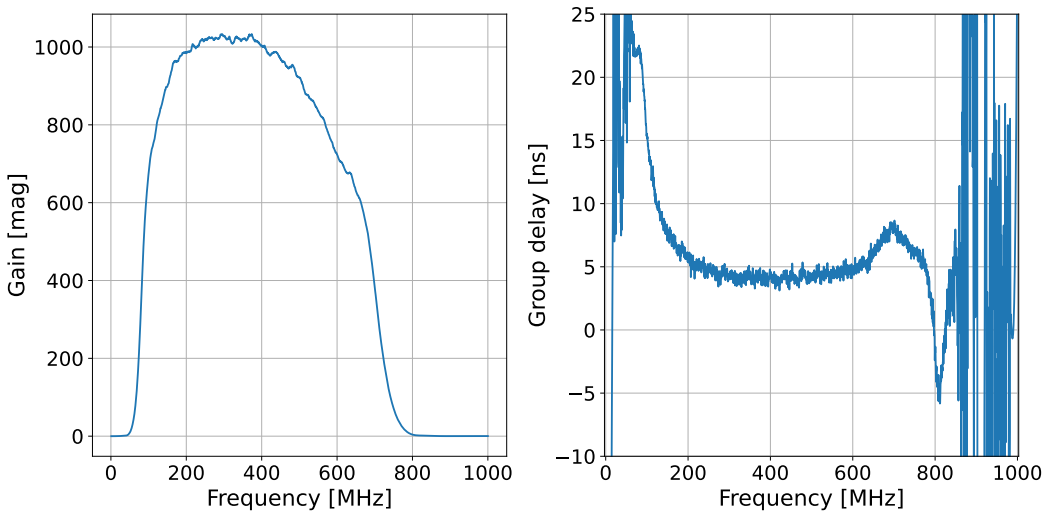

Figure 5.9: Measurements of the SURFACE board as used in NURADIORECO. Left: Gain. Right: Group delay.

To reduce background noise from galactic radio emission, frequencies below 80 MHz are suppressed (see Figure 5.9, left). To account for the LTE data transfer at 880 MHz, frequencies above 700 MHz are also suppressed. The highest gain of ~60 dB is between 100 MHz and 400 MHz. This is in order to optimize the detector not only for cosmic rays but also to reconstruct the direction and energy from in-ice showers. Figure 5.9 right shows the measured group delay for the SURFACE board. In the frequency band from 80 MHz to 200 MHz it has a group delay of approximately 15 ns. This again leads to a higher dispersion in the pulse. Between 200 MHz and 600 MHz the group delay is constant.

The combined impulse response of LPDA and SURFACE board is shown in Figure 5.10. Frequencies lower than 80 MHz and above 750 MHz are strongly suppressed. Towards higher frequencies, the effective length flattens more slowly, which matches with the amplification from the SURFACE board for frequencies between 100 MHz and 400 MHz.

The observed voltage as simulated with LPDA and SURFACE board over time and frequency is depicted in Figure 5.11. Due to the group delay of the SURFACE board, the dispersion has increased. The highest amplification is by a factor of ~ 60 dB in the range of 200 MHz. For the simulated 10^{18} eV air shower the peak-to-peak amplitude is V_{pp} ~700 mV.

5.1.4 Digitizer - The RADIANT board

The LPDA and SURFACE board are the prerequisites to describe the trigger path in Section 5.2. The system response of the RADIANT on the signal path between RF input and LAB4D is depicted in Figure 5.12. The gain is close to constant for all frequencies, −3 dB can be attributed to the power splitter dividing the input into a signal and trigger path. The group delay is higher for frequencies below 250 MHz.

The signal is read out and digitized by the LAB4D. The sampler is a CMOS (Complementary–metal-oxide-semiconductor) switched capacitor array (SCA). Each sample and hold cell consists of a complementary CMOS transmission gate (complementary switch)

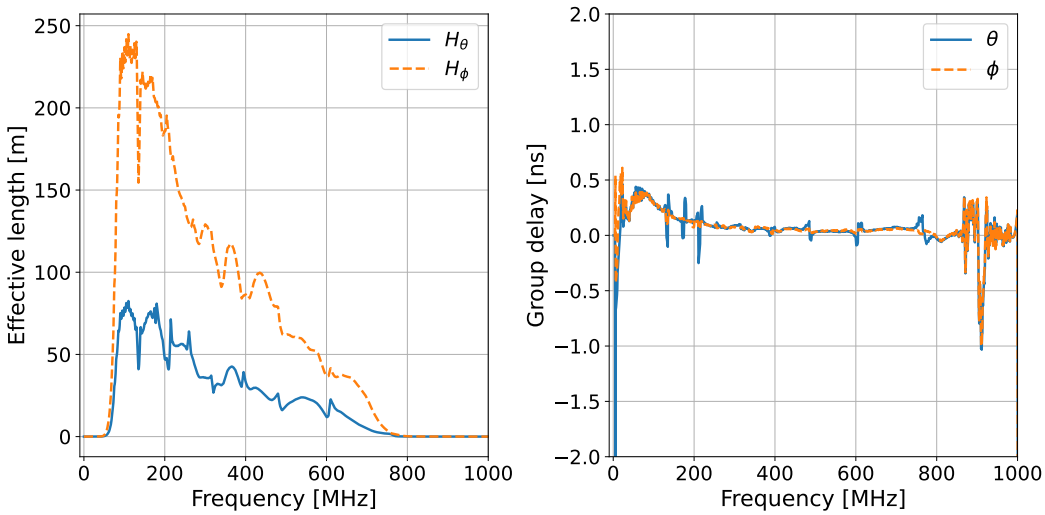

Figure 5.10: Impulse response, which is the combination of VEL of the LPDA and the amplification from the SURFACE board. The impulse response is simulated for the electric field shown in Figure 5.2. The signal arrives at $\theta_{\text{ant}} = 55°$ and $\phi_{\text{ant}} = 0°$ with respect to the antenna. Left: Effective length. Right: Group delay.

and a capacitor [161]. Each capacitor stores a voltage that corresponds to the difference between the input signal from a given channel at the time its switch is opened and the applied reference voltage [161]. Therefore time tuning (the ΔT when the switch is open and the capacity is charged) and voltage calibration are correlated. To reduce dead time, the total number of samples of the LAB4D is divided into multiple windows, that can be written to or read out separately [146]. The RF input is alternately captured by one of the two sets of 64 primary sampling cells. Data from the primary sampling cells is transferred in 64-sample chunks to the two intermediate storage cells, each of which consist of 128 samples [146]. Once the 128 samples are filled, they are transferred to the main storage array of 32 windows of 128 samples each [146]. A trigger signal is needed to read and digitize the full trace of 4096 samples [146]. The exact architecture and data flow is described in [146].

The DAQ system has several trigger options, including a software trigger, a PPS trigger relative to the GPS second, the diode trigger of the RADIANT, the trigger of the FLOWER board and an external trigger which can be used in the lab. An overview including most names used is given in Table 5.1. The column radiant refers to the firmware used for the RADIANT board [162], librno-g [163] is the input/output library for the DAQ.

With the understanding of the combination of LPDA and amplifying SURFACE board on the incoming signals, the trigger of the shallow antennas can be analyzed. In Section 5.3 the pre-deployment testing of the RADIANT, including the LAB4D will be discussed.

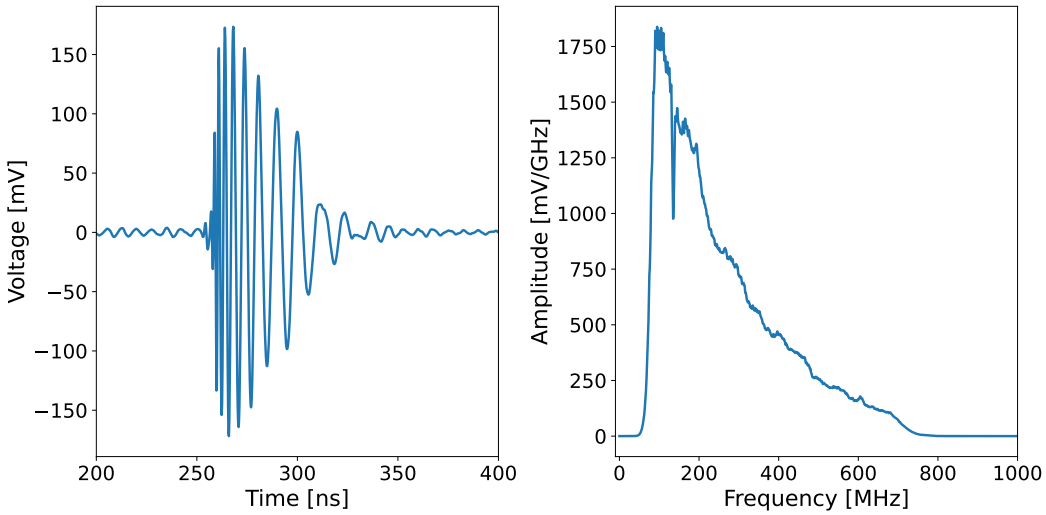

Figure 5.11: Simulated induced antenna voltage for the electric field shown in Figure 5.2. The signal arrives at $\theta_{\text{ant}} = 55°$ and $\phi_{\text{ant}} = 0°$ with respect to the antenna. The shown signal is with amplification from the SURFACE board. Left: timed domain. Right: Frequency domain.

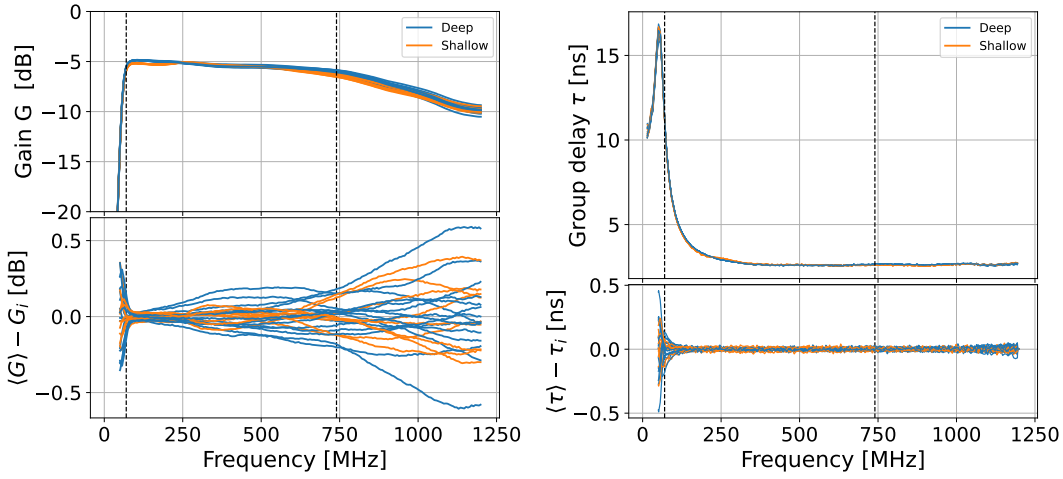

Figure 5.12: Measurement of the RADIANT V3 between RF input and test point T2 for 15 deep (blue) and 9 surface (orange) channels. The dashed lines indicate the frequency band of a RNO-G station. Top left: Gain. Bottom left: Deviation from mean per channel. Top right: Group delay. Bottom right: Deviation from mean per channel.

Table 5.1: Trigger types. The trigger names in radiant firmware have *RADIANT_TRIGGER_* as prefix, in the DAQ i/o software librno-g the prefix is *RNO_G_TRIGGER_*. The short form n.i. stands for not implemented (yet).

radiant	librno-g	analysis	slang names	description
SOFT	SOFT	FORCE	force	software trigger
n.i.	EXT	n. i.		external trigger, only present in V3 boards
EXT	RF_LT_SIMPLE	LT	deep	trigger from the FLOWER low threshold board, currently used for deep antennas
n. i.	RF_LT_PHASED	n. i.	phased array	trigger from the FLOWER low threshold board, currently not in use
INT0	RF_RADIANT0	RADIANT + which_radiant_trigger	AUX0, RF0, radiant, diode, surface, cr	trigger 1 from the RADIANT, currently used for three upward LPDAs
INT1	RF_RADIANT1	RADIANT + which_radiant_trigger	AUX1, RF1, radiant, diode, surface	trigger 2 from the RADIANT, currently used for six downward LPDAs
INTERNAL_COPY	RF_RADIANTX	RADIANT		trigger 1 or 2 from the RADIANT
PPS	PPS	PPS		pulse per second trigger relative to GPS seconds

5.2 RADIANT trigger

The RNO-G detector is designed for continuous measurement and data acquisition, but has a low data throughput. Thus, a trigger is required to determine whether the signal should be stored or discarded. If the trigger criteria are met, all channels of a station are read out and stored for later analysis. By pre-selecting events, the trigger determines the efficiency of the experiment. There are several triggers types (see Table 5.1) with the *deep* antennas using the trigger from the FLOWER board, the *shallow* antennas using the RADIANT diode trigger. In the following, the radiant diode trigger is described and characterized.

The trigger for the shallow antennas is based on a diode detector, which is implemented for all 24 channels on the RADIANT. The output of the diode detector must pass a simple threshold. A coincidence requirement for multiple channels within a time window is programmable.

5.2.1 Diode detector of the RADIANT trigger

The decision whether a signal passes a simple threshold is made by a high-speed discriminator as it will be detailed in Section 5.2.2. The nanosecond oscillating pulses from the particle cascades are broadend by a diode. This allows an FPGA (Field Programmable Gate Array) with a lower clock frequency to be used, reducing power consumption as it scales with clock frequency. Therefore, each of the 24 channels on the RADIANT has a Schottky diode detector as part of the trigger circuit, as shown in Figure 5.13.

The job of the Schottky diode is to convert input RF power into output voltage. Unlike a conventional pn-junction diode, which consists of a piece of positively doped (p-type) material (having more ”holes” than electrons) and a piece of negatively doped (n-type) material (having more electrons than ”holes”), Schottky diodes are constructed using a metal electrode bonded to a n-type semiconductor [164]. When forward biased, electrons move from the n-type material to the metal electrode, allowing current to flow [164]. The barrier to electrons on the n-side is relatively low. Since there is no p-type semiconductor material and therefore no minority carriers (holes), when reverse-biased, the diode conduction stops very quickly and changes to blocking current flow, making it a unipolar device [164]. The absence of holes in the metal also allows fast switching with relatively low noise because it does not store charge [164]. At low power levels, the transfer characteristic of a Schottky diode follows a square law, with the output voltage proportional to the input power (voltage squared) [165], see Figure 5.15 left. As the input power is increased, the slope of the curve flattens to more closely approximate a linear response (voltage output proportional to RF voltage input) [165].

The diode detector consists of the inductance *L3A*, the Schottky diode *D1A*, the capacitance *C8A* and the load resistance *R4A* [166]. A simplified sketch without bias voltage is shown in Figure 5.14. Note that the capacitor C (*C8A*) and the load resistor R_L (*R4A*) are connected in parallel. The air shower pulses change polarity quickly, the positive part of the pulse passes through the diode, while the negative part of the pulse is blocked by the diode. After the diode, the capacitor is charged and its capacity determines the

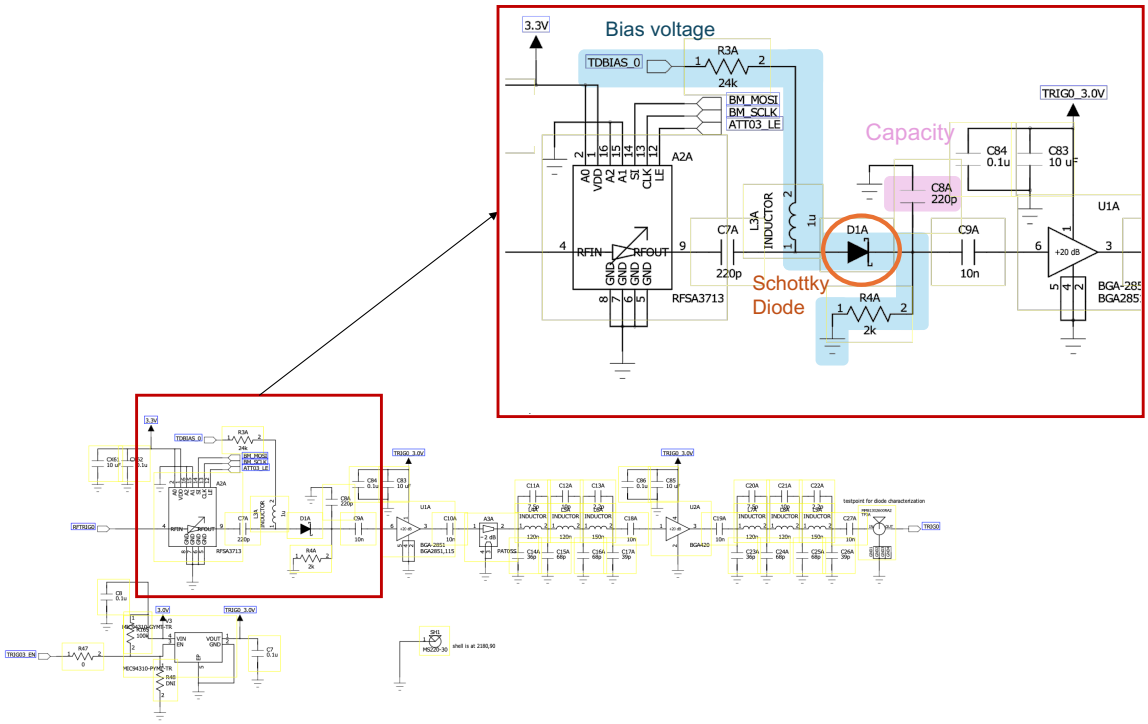

Figure 5.13: RADIANT per-channel trigger circuit. The relevant components for the diode detector are in the red rectangle and zoomed in. The orange circle marks the Schottky diode, the blue shaded path indicates the bias voltage path and the pink marked capacitance defines the integration time to ~11 ns.

integration time. The capacitor then discharges across the resistor R_L (*R4A*), providing the smoothed signal. The inductor L (*L3A*) provides a current return path for the part of the pulse blocked by the diode. The integration time τ of the capacity can be calculated with:

$$\tau = R \cdot L = 50\Omega \cdot 220\text{pF} \approx 11\text{ns} \tag{5.3}$$

with R = 50 Ω. The external bias voltage *TDBIAS_0* is a tuneable parameter, which extends the dynamic range response [166].

Figure 5.15 left shows the detector transfer curve as stated in the application note [166]. The goal is to operate in the square-law region. On the right is the slope of the transfer curve γ versus input power. Among other parameters, γ is a function of the externally applied bias voltage. The bias can be adjusted to trade sensitivity for a wider dynamic range of square-law response [166]. To obtain the matching bias voltage the following relation can be used:

$$V_{\text{bias}} = I_{\text{bias}} \cdot R_{\text{bias}} \tag{5.4}$$

with R_{bias} being the sum of all resistors:

$$R_{\text{bias}} = 24\text{k}\Omega + 2\text{k}\Omega + 2\pi f \cdot 1\mu\text{H}. \tag{5.5}$$

For a frequency f = 100 MHz the total resistance of the detector circuit is R_{bias} = 26 600 Ω. To obtain the sensitivity curve of $I_{\text{bias}} \sim 10\mu$A, the bias voltage has to be V_{bias} = 0.3 V, according to Eq. 5.4.

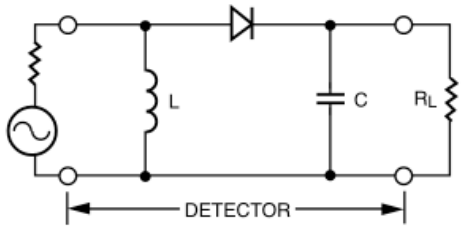

Figure 5.14: Sketch of simple diode detector without external bias voltage. Figure from [166].

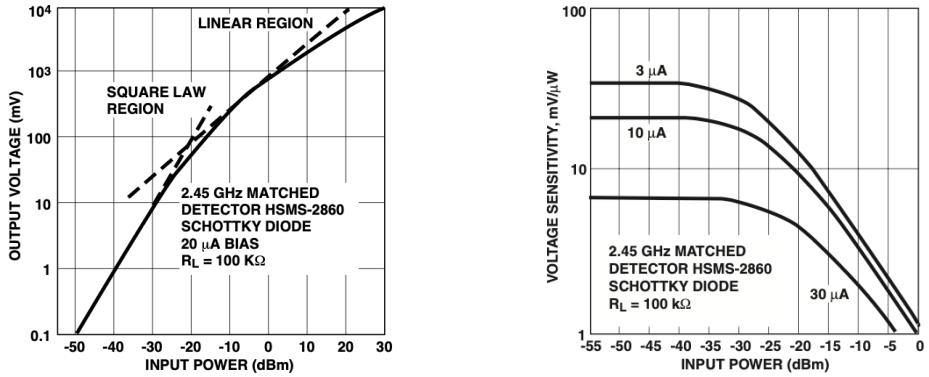

Figure 5.15: Input power is the RF input power applied to the detector circuit, the output voltage appears over *R4A*. Right: Detector transfer curve. Left: Slope of the transfer curve γ versus input power. Figures from [166].

In Figure 5.16 the response of the diode circuit to an air shower pulse is shown. The air shower pulse is no longer fastly oscillating, but has a global minimum near the peak of the input pulse and a small maximum after the pulse. The width is about the same as in the input pulse. The diode pulse has the highest amplitude at negative values. Therefore, the threshold of the trigger must be negatively exceeded, e.g. pass a minimum.

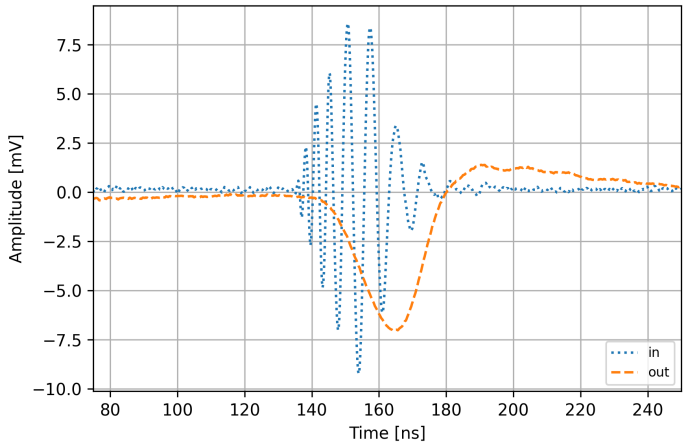

Figure 5.16: Output of the trigger circuit for a low amplitude air shower signal with a bias voltage of 1 V.

Performing an amplitude scan with a simulated cosmic ray pulse including the antenna response suggests indeed the square-law dependence. Figure 5.17 shows the absolute maximum of the diode output over the squared absolute maximum of the input pulse. The measurement ranges from 10 mV to 50 mV.

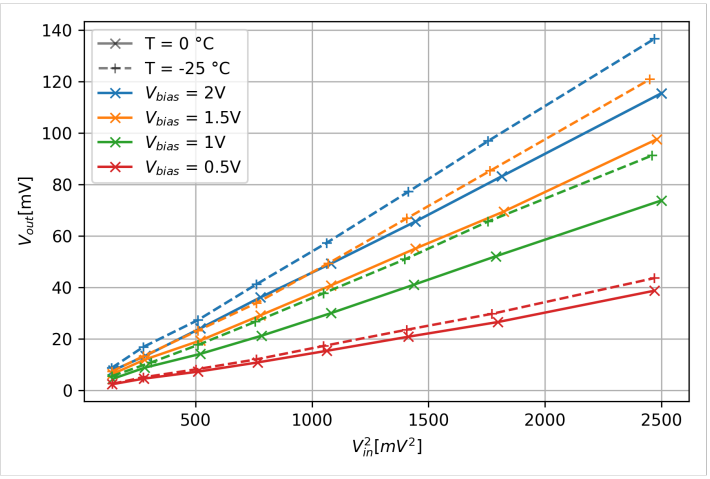

Figure 5.17: Amplitude scan with a cosmic ray pulse for different bias voltages (color code) and temperature (line style). The x-axis shows the square of the absolute maximum input pulse, the y-axis indicate the absolute maximum of the diode response.

5.2.2 Implementation in the RADIANT

Each channel of the RADIANT has a trigger with a diode detector. The measured analog signal is not digitized until it fulfilled the trigger conditions, implying that the signal is analog before the trigger. Therefore the signal has to be split into a signal that will be stored and a trigger path. If the whole analog signal would be modified by the diode circuit, it would be impossible to draw conclusions about the cascade physics behind it. The implementation of the signal and trigger path separation is different in version 2 RADIANT board (V2) and version 3 RADIANT board (V3). The V2 uses a directional coupler with −10 dB (i.e. a power ratio of 1/10), the V3 uses a power splitter with −3 dB (power ratio of 1/2). Therefore, the amplitude in the trigger path is a factor of $\sqrt{5}$ higher in the V3 board than in the V2. In Figure 5.18 a comparison between diode output at test point T3 of the version 2 RADIANT board and V3 is shown. When injecting a pulse with a maximum around 100 mV, the diode output of the V2 board has an extremum at ~ 25 mV, while the V3 has a yield around ~ 360 mV. The amplifier noise is expected to be around 10 mV. Because of the different splitting ratios, the amplitude of the input pulse is different for each version and accesses a different sensitivity range of the diode. Therefore, it is difficult to trigger with the V2 at small signals. The additional oscillations at the diode output compared to the diode board can be caused by standing waves in the cables.

Currently all stations operate with a version 2 RADIANT board (V2), this will change in the 2024 season, when all stations (old and new) will be equipped with the version 3 RADIANT board (V3).

For the nine surface channels an additional lowpass filter at 200 MHz is implemented after the splitter and before the diode detector. Simulation studies suggested, that the 80 MHz to 180 MHz band is optimal to improve to sensitivity towards air shower signals over the radio background from the Galaxy [167]. The output of the trigger path in a V3 board on an air shower signal and pure thermal noise is shown in Figure 5.19. While the output of the diode exceeds the amplitude of the input signal (~45 mV), the output on thermal noise at ~10 mV is about 5 mV. This is probably due to the dynamic range

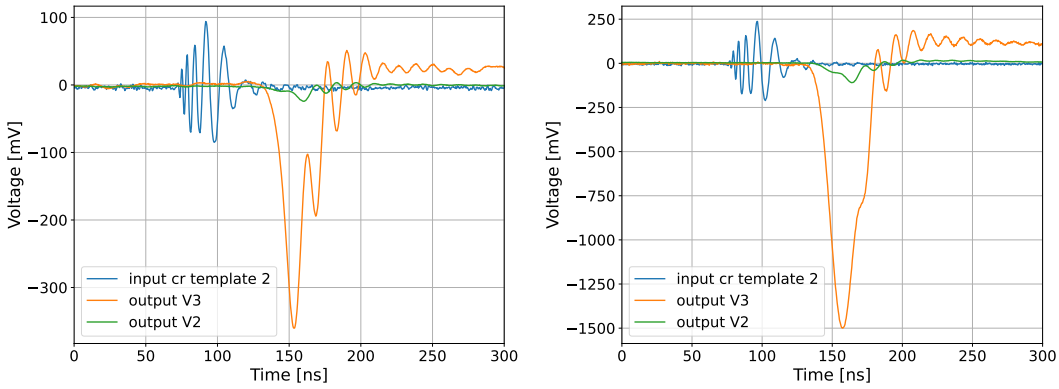

Figure 5.18: Comparison of diode characteristics as measured in the RADIANT. The blue line is the input comic ray pulse, the orange line is the output of the diode in the version 3 RADIANT board (V3) and green the output after the diode of the V2. The input pulse is split from the signal path with −10 dB V2 and −3 dB in V3.

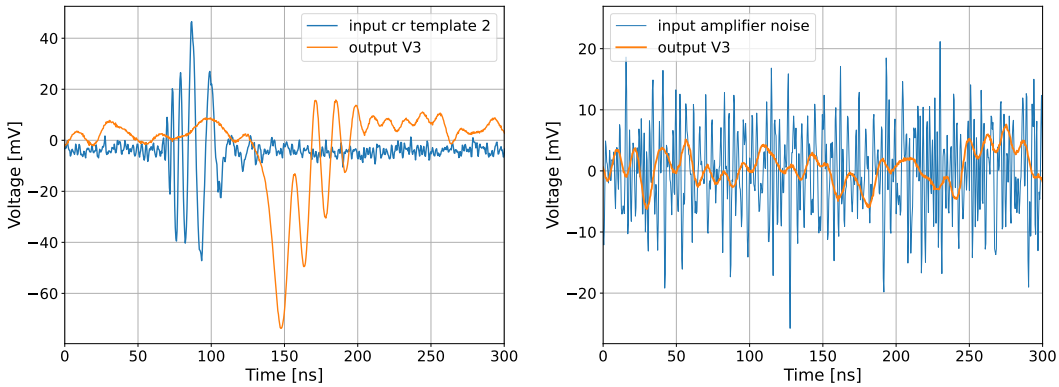

Figure 5.19: Output of the trigger path on a V3 board at testpoint T3 for a low-SNR air shower signal (left) and pure thermal noise (right).

of the diode and the bias voltage, as well as the signal shape, which is less impulsive for thermal noise.

To trigger, the falling edge of the diode output must pass the threshold (edge check). To also suppress random noise in the field, a two-out-of-three coincidence for the upward-facing antennas and a two-out-of-six coincidence for the downward-facing antennas is required within a time window of 60 ns.

The threshold criterion is evaluated by a discriminator. A discriminator is a combination of a fast comparator and a 1-shot circuit. When the signal passes the threshold, a fixed width output is provided which can then be used for coincidence checking. In the RADIANT, the LVDS (Low-Voltage Differential Signaling) comparator inputs of a FPGA are used, which has the advantage of high gain bandwidth, low electromagnetic interference, and ultra-low power consumption compared to discrete systems with comparable functionality [168]. To match the common mode of the LVDS input, the analog diode output is added to a voltage of 1.2 V [162] and connected to one pin of the differential pin pair (positive and negative pins). The other pin receives the threshold voltage from the FPGA. Since the FPGA cannot provide direct voltage, the threshold is provided via pulse-width modulation (PWM) and then fed through a capacitor, which blocks the high frequencies. The trigger decision is based on the direction of the current flow between the differential pins. Ideally, the output of a comparator becomes high i.e. triggers true,

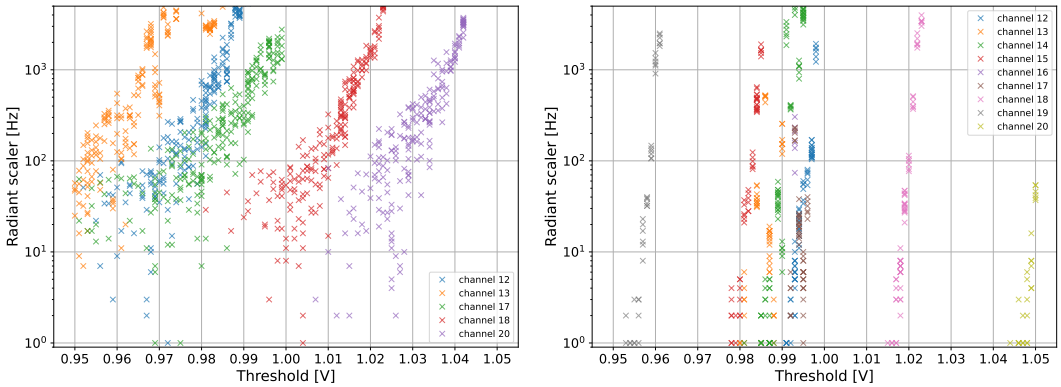

Figure 5.20: Threshold scan of several channels (see color code) of the RADIANT. The scan was performed on noise of a SURFACE board in the laboratory at room temperature. The threshold is a voltage that matches the voltage level at the FPGA input. Left: version 2 RADIANT board (V2). Right: version 3 RADIANT board (V3).

when the positive input is more positive than the negative input and vice versa. The data sheet does not describe very well how exactly the properties of the comparators are with such small voltage differences [169]. Therefore, a calibration in the laboratory is needed. A trigger decision by the FPGA can be made every 1.25 ns [162]. The logic checking for coincidences within a time window is also handled by the FPGA.

The trigger is designed to adjust to a trigger rate < 1 Hz to keep the overall data rate low. This is done by setting a scaler goal according to which the threshold is adjusted. A lower threshold results in a higher trigger rate, because it is easier for the negative extremum to pass. The scaler is a count of the number of times the diode output is below the threshold (level check) per scaler count period (typically one second). The difference to the trigger rate is, that the trigger is based on an edge-check, i.e. the signals falling edge has to pass the threshold and go from low to high, whereas the scaler compares the levels and also counts high-high. The threshold is set separately for each channel. Measurements have shown, that the same threshold results in different sensitivities per channel.

In order to test the threshold servo a SURFACE board was combined with a RADIANT in the laboratory and a threshold scan was performed, see Figure 5.20. The noise is expected to be the same for all channels, therefore the sensitivity of the channels should be the same at the same RADIANT scaler. Since the output of the diode in the V2 is much more unstable, the spread of the scaler versus threshold is much larger. For the V3, the noise seems stable and a sharp rise of the scaler can be seen at defined threshold values, which influences the trigger performance.

5.2.3 RADIANT trigger performance

To determine the trigger efficiency, test pulses must be selected. This was done based on the findings for the cosmic ray search [170]. Three templates with a Gaussian pulse of different width σ_w as the input electric field and the impulse response of the system cover almost the complete parameter space used for the cosmic ray search [170]. For the trigger efficiency the VEL of the LPDA was convolved with the electric field of an air shower, the SURFACE board is part of the measurement setup. The three different

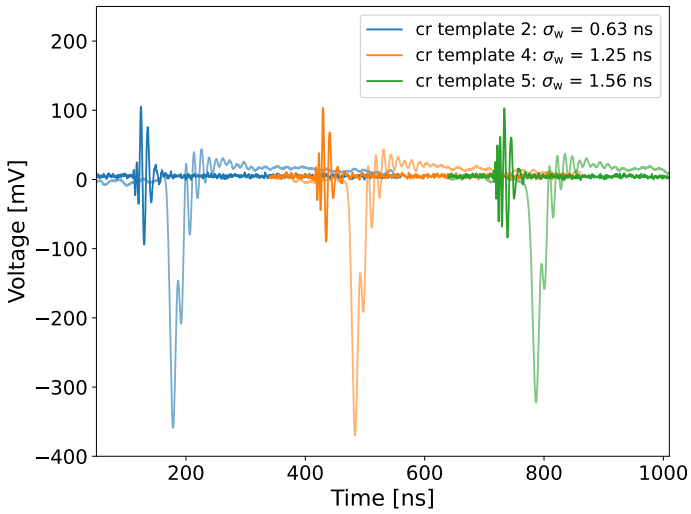

Figure 5.21: Three cosmic ray templates (bright color) and the subsequent output of the trigger path (faint color). The templates are created with a Gaussian function of different width σ_w (as stated in the legend) and the VEL of the antenna (LPDA).

templates and the corresponding output of the trigger path are shown in Figure 5.21. The outputs of the different templates vary only slightly in shape. The maximum input amplitudes differ by 3 mV, the resulting minima by 45 mV. This can mostly be attributed to the board noise of 10 mV.

The setup for the trigger efficiency measurements consists of an external signal generator, i.e. the 81160A Pulse Function Arbitrary Noise Generator, which can be programmed with an arbitrary pulse, i.e. the cosmic ray template. Two outputs of the generator are used. Both outputs are attenuated by −60 dB and then fed into the SURFACE board which has an amplification of 60 dB. The attenuation is necessary because the output of the signal generator is limited to 50 mV_{pp}, the input to the RADIANT should not exceed 1.2 V_{pp}. One of the outputs is then connected to the RF input of a RADIANT channel and used as a reference channel. The other output is connected to a RF switch that distributes the signal to the RF input of one of the nine surface channels which is then the channel under test. The RF switch is detailed in Section 5.3. The trigger efficiency is measured by injecting 100 pulses of the same amplitudes into the channel under test, and a reference pulse with a high amplitude to the reference channel. The RADIANT then triggers on the channel under test without coincidence requirements. The trigger efficiency is determined by counting true triggers that occur in close proximity to the reference pulse to avoid random noise triggers. The number of counts is then divided by the number of injected pulses. If the trigger efficiency is > 0, the waveform is recorded by the RADIANT and can be analysed to obtain e.g. the signal to noise ratio (SNR).

The triggered pulse is always stored in the second half of the waveform with a total of 2048 samples, making it possible to distinguish between signal samples and noise samples. In Figure 5.23 example pulses in the channel under test and the reference channel with a higher amplitude are shown. Since signal and trigger path are split and only the signal path is stored this is not the quantity on which the trigger is applied, but which is accessible for further analysis.

For the cosmic ray trigger efficiency measurement, the threshold is selected according

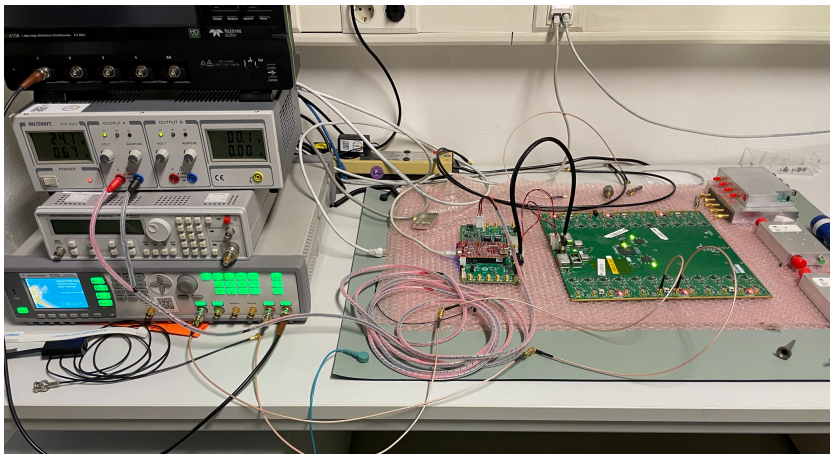

Figure 5.22: Picture of the setup in the laboratory with the RADIANT in the middle right, connected to the small controller board. On the left is the external signal generator, a power source, and an oscilloscope.

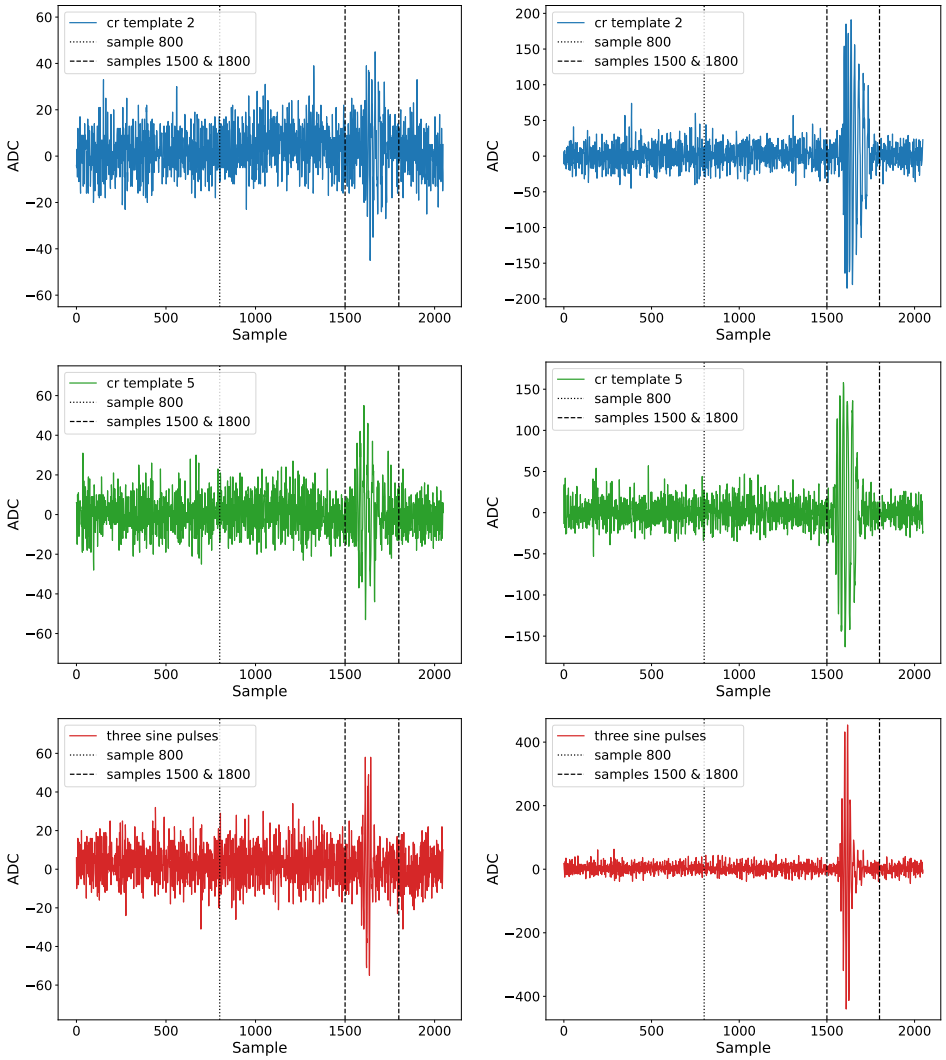

Figure 5.23: Three example pulses recorded with the RADIANT. The left column shows the channel under test with a small amplitude and the right column shows the same pulse with a high amplitude as measured in the reference channel. The vertical lines indicate the selected samples for noise (0-800) and signal (1500-1800).

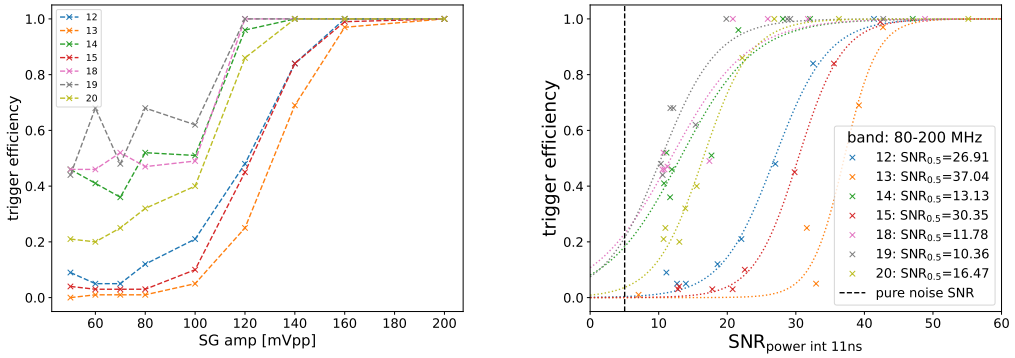

Figure 5.24: Trigger efficiency of the V3 board, measured for 100 cosmic ray pulses each, with increasing amplitudes near to thermal noise at a trigger threshold corresponding to a RADIANT scaler of 10. Left: Shown as function of amplitude from the external signal generator. Right: As function of SNR. The signal is evaluated in the trigger band of 80 MHz to 200 MHz, then power is taken and integrated over a time window of 11 ns. From the whole processed waveform the maximum has been taken.

to the scaler goal of 1 Hz in the field. Since the coincidence criterion reduces the overall trigger rate, the threshold is evaluated at a scaler of 10 Hz. For the measurements, no coincidence is required. In Figure 5.24 (left) the trigger efficiency curve over input amplitude at the external signal generator is shown. The different curves vary for the different channels, which might originate from the threshold setting. The trigger rate for channels 14, 18 and 19 is already high at low amplitudes, suggesting, that they are in the thermal noise. The trigger threshold for channels 12, 13, 15 seems to be more favorable to suppress noise triggers. Threshold servoing in the field should ideally result in trigger curves like those of channels 12 and 15, channel 13 seems slightly unstable at towards low SNR values

The recorded waveforms are further analyzed. In order to match the behaviour of the trigger path, the waveform has been filtered to the trigger band of 80 MHz to 200 MHz. The trigger is sensitive to the power of the voltage and integrates the signal over time, therefore the amplitudes has been squared and integrated over time the capacity needs to charge, i.e. $\Delta t = 11$ ns:

$$P_{\text{int}} = \sum_{i}^{i+\Delta t} V_i^2 = V_{\Delta t}^2 \tag{5.6}$$

The waveform of i samples is transformed to power integrated intervals j. The number of power integrated intervals n_j is then the number of samples n_i minus the number of samples per time interval $n_{\Delta t}$, which depends on the sampling rate f_s:

$$n_j = n_i - n_{\Delta t} = n_i - f_s \cdot \Delta t \tag{5.7}$$

The standard deviation of the noise is evaluated for the first 800 samples of the waveform (corresponding to 333 ns). The triggered quantity is always stored in the second half of the waveform, therefore the first 800 samples should contain no signal. The standard deviation σ is then the square root of the average of the squared deviations from the

mean, i.e.,

$$\sigma = \sqrt{\frac{1}{n}\sum_{i=1}^{n}(x_i - \overline{x})^2}, \text{ with } \overline{x} = \frac{1}{n}\sum_{i=1}^{n} x_i. \tag{5.8}$$

where x_i is the value of a sample, n is the number of samples, and $\overline{x}$ is the mean value.

The signal to noise ratio $\mathrm{SNR}_{\text{power int}}$ for the power integration is defined as the maximum of the power integrated trace $P_{\text{int max}}$ (given bei Eq. 5.6 divided by the standard deviation (Eq. 5.8) of the first $n_{\text{noise}} = 800$ samples (333 ns) of the power integrated trace $\sigma_{\text{power int}}$:

$$\begin{aligned}
\mathrm{SNR}_{\text{power int}} &= \frac{P_{\text{int max}}}{\sigma_{\text{power int noise}}} \\
&= \frac{\max_j(V^2_{\Delta t,j})}{\sqrt{\frac{1}{n_{\text{noise}}}\sum_{j=1}^{n_{\text{noise}}}\left(V^2_{\Delta t,j} - \overline{V^2_{\Delta t,j}}\right)^2}} \\
&= \frac{\max_j(\sum_{i=j}^{i+\Delta t} V_i^2)}{\sqrt{\frac{1}{n_{\text{noise}}}\sum_{j=0}^{n_{\text{noise}}}\left(\sum_{i=j}^{i+\Delta t} V_i^2 - \left(\frac{1}{n_{\text{noise}}}\sum_{i=j}^{n_{\text{noise}}}\sum_{i=j}^{i+\Delta t} V_i^2\right)\right)^2}}
\end{aligned} \tag{5.9}$$

In Figure 5.24 (right) the trigger efficiency as a function of $\mathrm{SNR}_{\text{power int}}$ from the triggered waveforms is shown. The differences between the channels still persist and probably result from the threshold settings, which were obtained in the threshold scan. The spread could be taken as an indication of the uncertainties of the threshold servoing.

To understand the influence of changes in noise on the $\mathrm{SNR}_{\text{power int}}$ the distributions for the signal, noise and $\mathrm{SNR}_{\text{power int}}$ are shown in Figure 5.25 top row. The spread of the signal increases towards higher amplitudes, where more events have been recorded, while the noise remains relatively constant. The signal to noise distribution is therefore quite similar to the signal distribution, with an uncertainty of ~8 $\mathrm{SNR}_{\text{power int}}$ for small amplitudes.

In order to also obtain the $\mathrm{SNR}_{\text{power int}}$ for pulses that do not trigger, a second measurement has been done. Here, the trigger was set on the reference channel and at a fairly insensitive threshold to avoid noise trigger. Once the data was stored the channel under test was analyzed and the $\mathrm{SNR}_{\text{power int}}$ was calculated according to Eq. 5.9. The distribution is shown in Figure 5.25 bottom row. In the direct comparison the quantities from the triggered events and the ones obtained by triggering on the reference channel do not vary a lot. The waveforms obtained by triggering on the reference channel contain more events, especially at the lower amplitudes, the distributions are therefore clearer separated. The $\mathrm{SNR}_{\text{power int}}$ values stated in the legend agree within their uncertainties. The triggered waveforms do not seem to have a special property, therefore it seems legitimate to obtain the input amplitude to $\mathrm{SNR}_{\text{power int}}$ in a separate measurement.

To get an idea, which parameters influence the trigger efficiency, temperature, thresholds and bias voltages will be tested. For each setting and a linear conversion from signal generator amplitude to SNR will be obtained and used. To make weaker assumption about the pulse form a different definition for signal and noise will be used. The signal is defined as maximum peak-to-peak amplitude, calculated in a sliding window

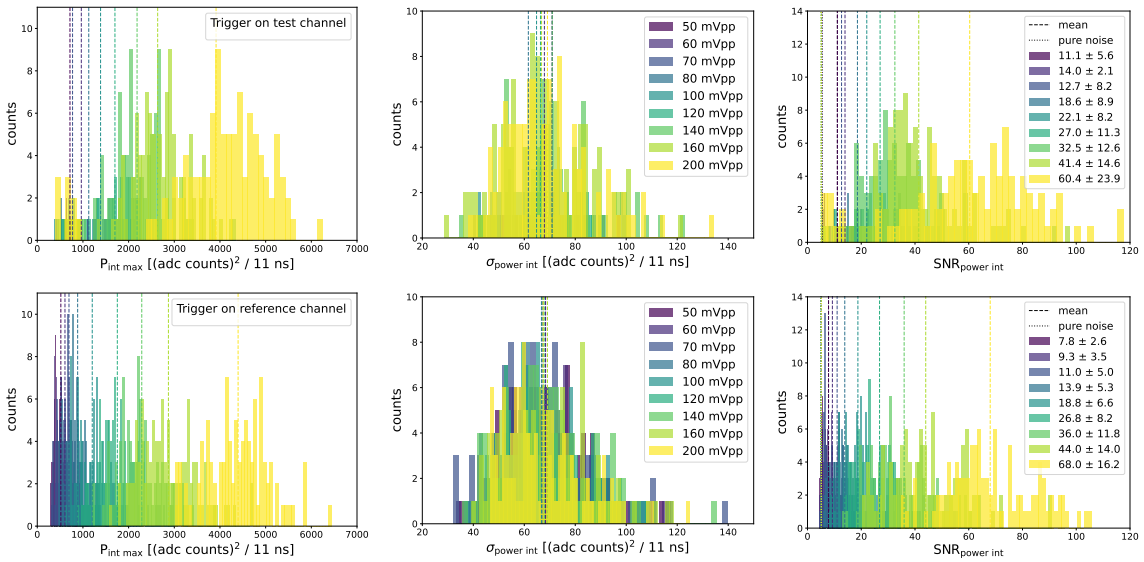

Figure 5.25: Distributions of signal (maximum of samples 1500-1800, left), noise (standard deviation of samples 0-800, center), and $\mathrm{SNR}_{\mathrm{power\ int}}$ (right) as determined by analyzing the power-integrated waveforms in the trigger band of 80 MHz to 200 MHz of channel 12 as recorded by the RADIANT. The top row consists of waveforms that were triggered, the bottom row consists of waveforms where the trigger was set on the reference channel. The definitions of signal and noise are explained in the text. The color code indicates the injected amplitude at the external signal generator and is the same for all plots, the dashed line indicates the mean for each distribution. The dotted line indicates the SNR value for pure noise.

of 30 samples (12.5 ns) within sample 1400 and 1900 to account for the sliding window. The noise $\sigma_{\mathrm{V\ noise}}$ is evaluated for the first 800 samples of the waveform (corresponding to 333 ns) according to Eq. 5.8, where x_i is the ADC count of the sample. The SNR is calculated according to

$$\begin{aligned} \mathrm{SNR} &= \frac{V_{\mathrm{pp}}}{2 \cdot \sigma_{V\mathrm{noise}}} \\ &= \frac{V_{\mathrm{pp}}}{2 \cdot \sqrt{\frac{1}{n_{\mathrm{noise}}} \sum_{i=1}^{n_{\mathrm{noise}}} (V_i - \bar{V})^2}}. \end{aligned} \tag{5.10}$$

The SNR of pure noise is higher than one and depends on the maximum peak-to-peak amplitude of the noise. A comparison for the same data set discussed in Figure 5.25 of the 'simple' SNR of triggered waveforms and the 'simple' SNR obtained in a second measurement are shown in Figure 5.26. The distributions are again pretty similar. The mean SNR value differs most at small amplitudes, where the sample size is small (n = [9, 5, 5, 12, 21] for amplitudes 50 mVpp to 100 mVpp) due to the low trigger efficiency. For input amplitude of 60 mVpp the pure noise SNR is higher for triggered events than for the waveforms obtained by triggering on the reference channel. This value is close to the noise and could be an upward fluctuation. The same holds true for input amplitude of 50 mVpp and 70 mVpp, where the SNR is higher than for 100 externally triggered events. Therefore the SNR values obtained in a second measurements are only comparable for SNR well above the pure noise, where both distributions agree within their uncertainties. In comparison to the power integration definition $\mathrm{SNR}_{\mathrm{power\ int}}$, the SNR values are lower,

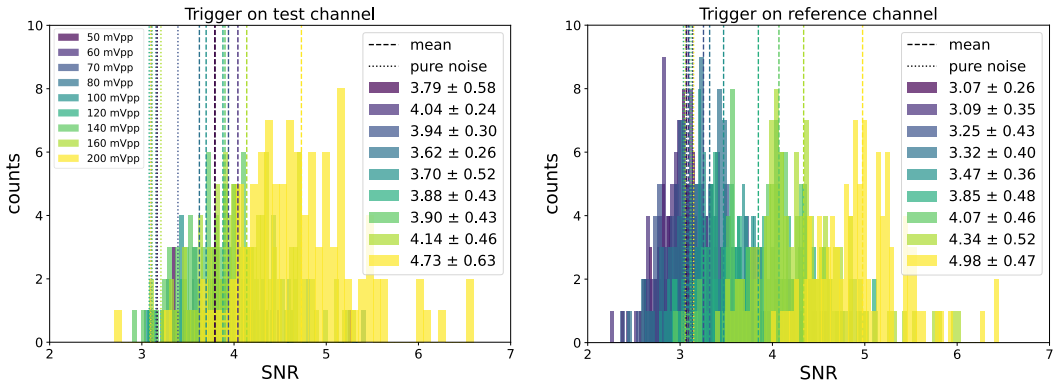

Figure 5.26: Comparison of the 'simple' SNR described in Eq. 5.10 in the full band of 80 MHz to 800 MHz. The data set and color code is the same as in Figure 5.25. Left: Events that triggered. Right: Events that were recorded by triggering the reference channel.

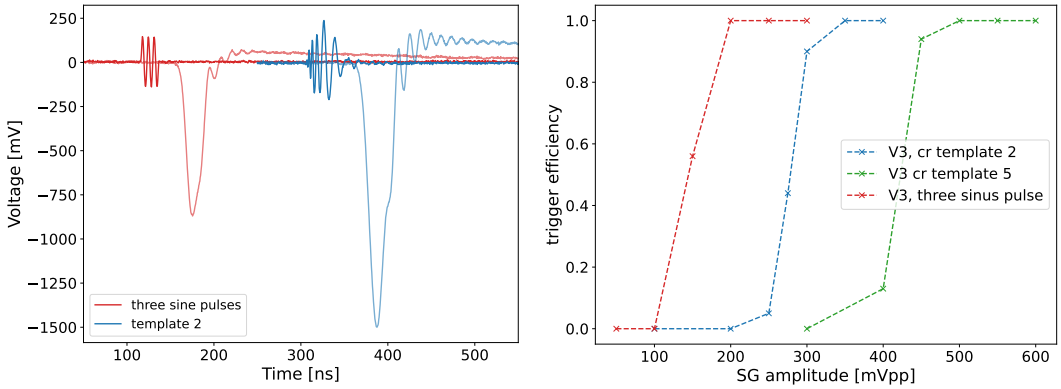

Figure 5.27: Left: RADIANT input pulse (first) and diode output at test point T3 (second) measured with an oscilloscope for different pulse shapes. Right: Trigger efficiency at a threshold of 0.92 V for a RADIANT V3 for different pulses as indicates in the legend as function of peak-to-peak amplitude at the external signal generator (SG).

indicating a worse separation between signal and noise. This is expected, since the power integration analysis in the trigger band of 80 MHz to 200 MHz was optimized on the signal of cosmic ray pulses. The $\mathrm{SNR}_{\text{power int}}$ is therefore preferred for trigger simulation, while the 'simple' SNR is easier to apply to recorded data. In the following SNR always refers to the 'simple' SNR = $\frac{V_{\mathrm{pp}}}{2 \cdot \sigma_{\text{V noise}}}$ according to Eq. 5.10.

In Figure 5.27 the trigger efficiency at a threshold of 0.92 V for two different cosmic ray templates and three sine waves are shown. The three sine waves reaches 100% efficiency first, but there is also a difference between the two cosmic ray templates. The differences could originate from the settings in the external signal generator, i.e. the peak-to-peak amplitude is easier to set for a symmetric pulse as it is for the cosmic ray templates. Therefore it is necessary to analyze the recorded data.

The SNR was obtained in a second measurement, with the trigger set on the reference channel as described before. The relation for amplitude at the external signal generator to SNR according to Eq. 5.10 is shown in Figure 5.28. It clearly shows, that the recorded SNR is different for the three templates and the spread of SNR per amplitude is relatively large. The conversion function from signal generator amplitude and SNR has been obtained with a linear fit:

$$f_{\text{lin}}(x) = a \cdot x + b \tag{5.11}$$

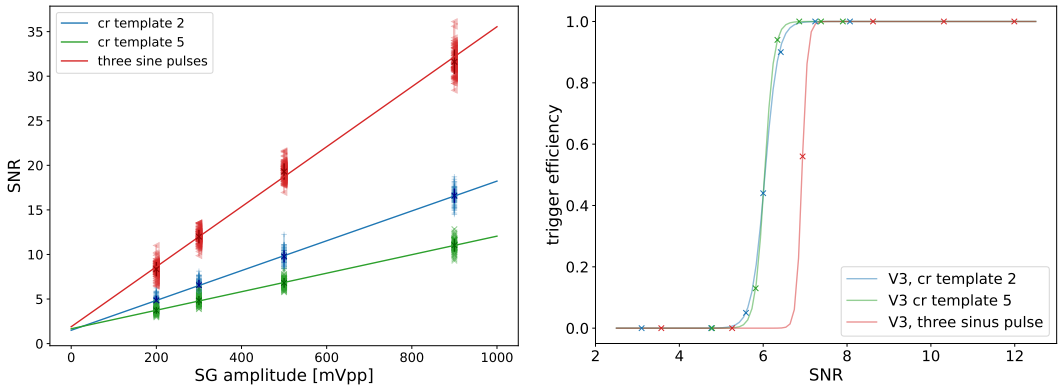

Figure 5.28: Left: Measurement of the signal to noise ratio (SNR) at different amplitudes as set at the external signal generator (SG). The color code indicates the pulses injected. Right: Trigger efficiency as function of SNR obtained left. The solid lines is the fit function described in the text.

In the resulting trigger curve, the two cosmic ray templates are now almost identical and reach 100% efficiency at lower SNR values as the three sine pulses. This might be due to the different frequency content of the pulses and the trigger band, which is optimized for cosmic ray pulses. In order to make the trigger efficiency measurements comparable when testing multiple boards, they have been fitted with a hyperbolic tangent function:

$$f_{\tanh}(x) = \frac{1}{2}\left(\tanh\left(\frac{x-b}{c}\right) + 1\right) \tag{5.12}$$

The same two measurements (obtaining a conversion for SNR and trigger efficiency) were taken for the cosmic ray template 2 with a threshold of 0.92. The result is shown in Figure 5.29. The slope of the linear fit of SNR over the signal amplitude is nearly identical for all surface channels, small variations could occur due to the switch used and will be further investigated in Section 5.3. The largest difference is in the trigger efficiency between the channels, with channel 20 being the least sensitive. When comparing the channels per date, the variation in trigger efficiency is negligible. The sensitivity to the trigger threshold seems to be a characteristic of each channel and needs to be calibrated. Therefore, when comparing different pulses, temperatures, etc., it is important to compare per channel.

In Figure 5.30 the trigger curves for cosmic ray template 2 at different thresholds are shown. The trigger becomes more sensitive at higher thresholds, because it is easier for the minimum to exceed. A different threshold seems to change the SNR sensitivity but not the shape of the curve. This happens when changing the diode bias voltage, a bias voltage of 0.8 V leads to the highest trigger efficiency around 4.3 SNR but yields a slightly lower value at a SNR of 4.6. The rise is less steep for this value. The theoretical determined value according to Eq. 5.5 of 0.3 V sits in the middle. All tested bias voltages achieve 100% trigger efficiency at an SNR of 5. Therefore the diode bias voltage of 0.8 V is favorable, since it provides the highest sensitivity at low SNR.

Changing the temperature to 0 °C improves the trigger efficiency slightly (0.1 SNR) compared to room temperature. A typical operation temperature of the RADIANT is between −10 °C to 10 °C.

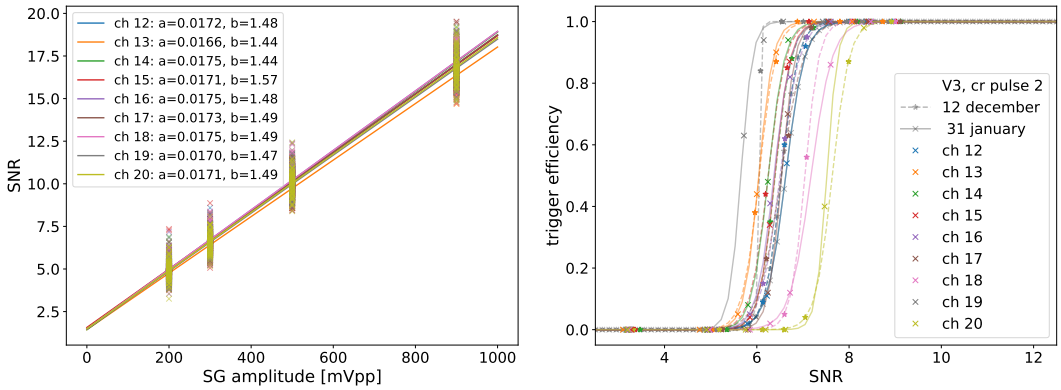

Figure 5.29: Left: Comparison of the amplitude conversion slope for the surface channels of one board. Right: Trigger efficiency scan for all surface channels (color code) taken at two different dates as stated in the legend. The solid lines is the hyperbolic tangent fit function described in the text.

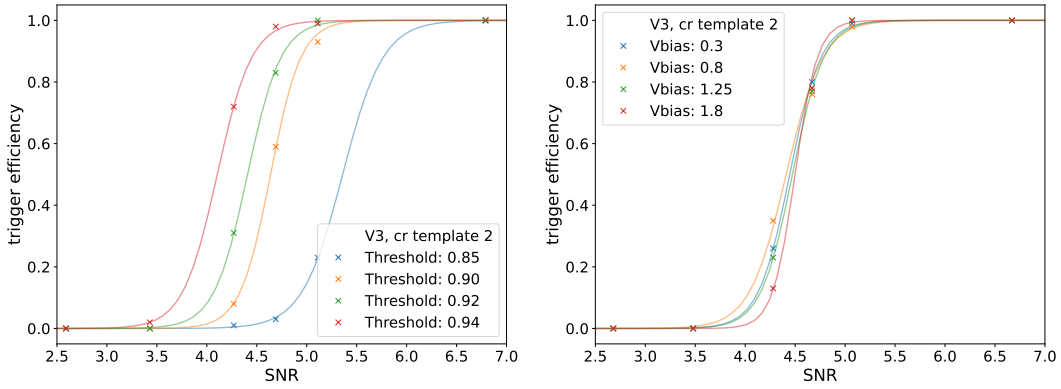

Figure 5.30: Trigger efficiency as function of SNR for different threshold values (left) and different diode bias voltages (right) as indicated in the label. The measurements were performed with a V3 RADIANT, template 2 as input pulse at a default diode bias voltage of 1.25 V and default threshold 0.92 V at room temperature. The conversion from signal generator amplitude to SNR was obtained in a second measurement.

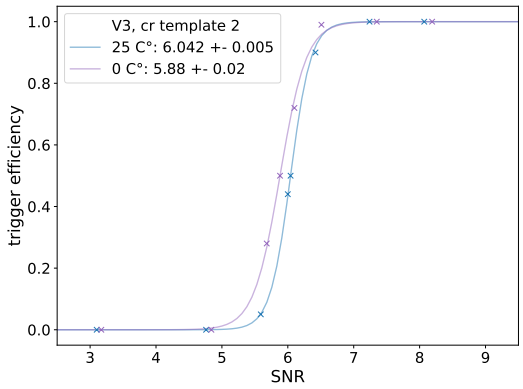

Figure 5.31: Trigger efficiency as function of SNR for different temperatures as indicated in the label. The measurements were performed with a V3 RADIANT, template 2 as input pulse at a threshold of 0.9 V with a diode bias voltage of 1.25 V. The conversion from signal generator amplitude to SNR was obtained in a second measurement.

In summary, the RADIANT trigger is able to trigger on cosmic ray signals close to thermal noise, given a well adjusted threshold. Unfortunately, the threshold cannot taken as absolute but has to be adjusted for each channel. It seems difficult to model the exact shape of diode output as it has been done for the tunnel diode of the ANITA experiment [171], given that the behaviour is not linear, the sensitivity of the LVDS input at small voltage differences is unclear and the measurement already show huge differences between the channels, although the same components are used according to the circuit diagram [162]. Therefore the influence of threshold, diode bias voltage, pulse shape and temperature have been measured. A trigger efficiency curve for cosmic ray pulses was obtained on which the trigger simulations will be based. This exact implementation will be part of Section 6.3.2. The trigger efficiency measurement is part of the pre-deployment testing. All version 3 RADIANT board (V3) and channels will be tested with cosmic ray template 2 at a threshold of 0.92 V with a bias voltage of 1.25 V, which was the default value for the version 2 RADIANT board (V2). The results will show the deviations from board to board and give a handle on the uncertainties to expect. The procedure and results are detailed in Section 5.3.

5.3 Pre-deployment testing of the RADIANT

To ensure the functionality and performance of the RADIANT board and their trigger in the field, 13 V3 boards were tested at the laboratories of Erlangen Centre for Astroparticle Physics (ECAP) and Deutsches Elektronen-Synchrotron (DESY). In the following the performed tests are listed and briefly explained. The performance tests give an indication of the modeling of the RADIANT trigger and are therefore discussed in detail.

Testing was conducted in three test suits focused on environmental, functional and performance testing. The software written for the testing is available at github [172]. The test results are stored and displayed in the RNO-G hardware database [173]. An overview over the test procedure is given in Table 5.2. The test procedure started with a thermal shock test in a climate chamber. Each RADIANT board (turned off) underwent five temperature cycles from −40 °C to 100 °C to simulate aging and test for broken connections and bad solder joints. The RADIANT board was then powered up from the controller board at room temperature and the LAB4D chips were time-tuned. Functional and performance tests were performed at room temperature and 0 °C. After each temperature change, the time tuning was repeated. Due to time constraints, only functional tests were performed at −20 °C. Typical operating temperature is between −10 °C and 10 °C, depending on the season. Once the board is turned off, it no longer provides heat and the temperature can drop to −35 °C. Therefore, a cold boot test has been performed at −30 °C to ensure that the station can be powered up from the cold.

The functional tests include ten different procedures listed in Table 5.3. They test the power drawn by the system (SystemPower) and the RADIANT (RADIANTPower), the communication between the controller board, the RADIANT (uCComms) and the FPGA (FPGAComms), and the functionality of the LAB4D ASIC (LAB4DTune, LAB4DGlitch, BiasScan and WindowStability). The on-board sine wave generator is used at 90 MHz, 240 MHz and 510 MHz (SigGenSine and HarmonicDistortion) testing the analog channels

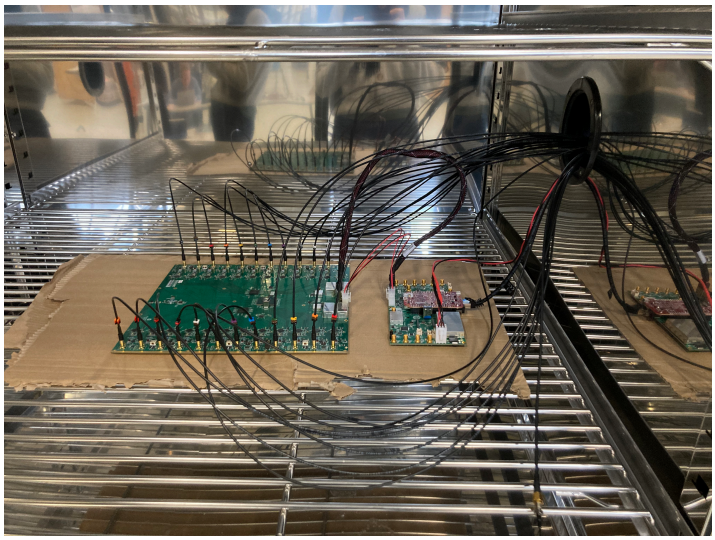

Figure 5.32: The RADIANT and the controller board in the climate chamber, with all 24 RF inputs connected to cables.

and the front-end noise spectrum is recorded and analyzed (FrontEndNoise). Due to different controller board versions the SystemPower test was not always performed.

The performance tests stated in Table 5.4 were done using the same setup described previously for the RADIANT trigger efficiency measurements (Section 5.2.3). The external signal generator (81160A Pulse Function Arbitrary Noise Generator) was programmed with the cosmic ray template 2, shown in Figure 5.21. Two outputs of the signal generator were then attenuated by −60 dB and fed into the SURFACE board. One output is connected to the RF input of a RADIANT channel and used as a reference channel. The other output is connected to a RF switch that distributes the signal to the RF input of one of the 24 channels which is then the channel under test.

The RF switch consists of four small circuit boards, each with one input and eight outputs that can be selected by the on-board binary decoder circuit [174]. The boards are combined so that three boards are connected to the 24 channels of the RADIANT, and one board is used to distribute the input signal to the other three boards. All four boards are powered and controlled by a microcontroller accessible via Python. A picture before assembly is shown in Figure 5.33. The gain and group delay of all 24 path have been measured, see Figure 5.34. The first circuit has the biggest influence on the gain, as three set of curves are visible. The group delay is between 11 ns to 13 ns. The switch is necessary to test all 24 channels in the chamber without having to manually connect each cable to the external signal generator.

First, the SignalGen2LAB4D was run, injecting 100 cosmic ray pulses into the RF input of the channel under test and into a reference channel. While the amplitude was increased in the test channel (200 mVpp, 300 mVpp, 500 mvps, 900 mVpp), the amplitude on the reference channel was constant at 900 mVpp. The waveforms were recorded with the RADIANT, the trigger was on a threshold of 0.9 V without coincidence triggering on the reference channel. The recorded data was analyzed, calculating the SNR according to Eq. 5.10. The $V_{\text{noise rms}}$ was evaluated for the first 800 samples of the waveform (corresponding to 333 ns) using Eq. 5.8. This can be done, because the trigger time is always saved in the second half of the waveform consisting of 2048 samples (see also Figure

Table 5.2: Overview of test procedure for the RADIANT V3. Detailed description in the text.

test procedure	temperature
thermal shock test	−40 °C to 100 °C
bring up & time tuning functional tests performance tests	room temperature
time tuning functional tests performance tests at	0 °C
time tuning functional tests	−20 °C
cold boot	−30 °C

5.23). The peak-to-peak amplitude of the signal was calculated in a sliding window of 30 samples (12.5 ns) within sample 1400 and 1900 to account for the window time. The result for one board is shown in Figure 5.35. The linear fit according to Eq. 5.11 was performed, where the fit parameter were used as pass/fail criterion. Channel 0 clearly fails the test. The spread of the measured SNR increases with higher input amplitudes.

The results for all boards and channels are shown in Figure 5.36. The distributions become wider as the input amplitude increases. The differences between the measurements taken at 0 °C (dashed line) give slightly lower SNR values at all amplitudes. The minimum standard deviation is 0.5 SNR, which can be interpreted as the uncertainty of the SNR measurement. At the highest amplitude it is about 0.9 SNR. By highlighting the different boards and channels tested, as in Figure 5.37 left and right, it can be seen that most boards give similar SNR values. Board ULB-007 has the lowest SNR value, due to the broken channel 0. Some channels (e.g. 22, 23) seem to perform better than others (e.g. channel 1, 2).

The recorded waveforms were further analyzed for the FrontEndResponse test. A reference template of the injected pulse was created using the average of 100 waveforms measured with a reference RADIANT. The measured waveforms at different amplitudes were cross-correlated with the template in a correlation window of 200 ns according to

$$\text{xcorr} = \max(\rho(\Delta n)) = \max\left(\frac{\sum_i^m (V_1)_i \cdot (V_2)_{i+\Delta n}}{\sqrt{\sum_i^m (V_1)_i^2} \cdot \sqrt{\sum_{j=\Delta n}^{m+\Delta n} (V_2)_j^2}}\right) \tag{5.13}$$

where V_1, V_2 are the data and template voltage traces and Δ_n is the number of samples by which the two traces are shifted relative to each other [170].

Figure 5.38 shows one waveform per injected amplitude. The black pulse at the beginning of the trace is the reference template and not recorded in the measurement. Channels 5 and 15 have block offsets. The exact cause of the block offsets is unclear, they seem to be related to the readout window, and might be a result of an unstable bias voltage in the intermediate storage array. In channel 7 the amplitudes are too small, Channel 13 is

Table 5.3: Overview of functional tests performed with the RADIANT V3.

id	name	procedure	purpose
FT1	System-Power	Read voltages and currents from controller board	Verify that RADIANT is running and that current draw is within reasonable boundaries
FT2	uCComms	Read board manager (BM) BM_-ID and BM_DATEVERSION via the serial Consistent Overhead Byte Stuffing (COBS) connection.	Verify serial communication between RADIANT and microcontroller on controller board works properly
FT3	Radiant-Power	Read board manager status and board manager analog inputs	Verify voltages on the RADIANT board
FT4	FPGA-Comms	Read FPGA_ID and FPGA_DAT-EVERSION registers	Verify slow communication to the FPGA through the microcontroller works properly
FT5	LAB4D-Tune	Read out seam / slow sample	Verify that tuning of ΔTs on all (24) LAB4Ds is correct
FT6	LAB4D-Glitch	Compare voltage differences at the boundaries of a readout window to check if the signal is continuous	Confirm there is no switching in the readout order of the windows (glitching)
FT7	BiasScan	Checks if the DC voltage response of each capacity in the main storage array is linear	Verify linear response of each digitizing cell/sample
FT8	FrontEnd-Noise	Measure noise spectrum with no input connected	Check of analog front-end quality
FT9	SigGenSine	Use on-board sine wave generator, record and fit sine waves	Check signal generator functionality and validate front-end quality
FT10	Window-Stability	Use on-board sine wave generator and measure the power distribution of the sine wave in the same readout window over several events	Check that all windows have equal properties
FT11	Harmonic-Distortion	Use on-board sine wave generator and checks the power of the harmonics in the frequency domain	Verify that the internal signal generator works properly and validate front-end quality

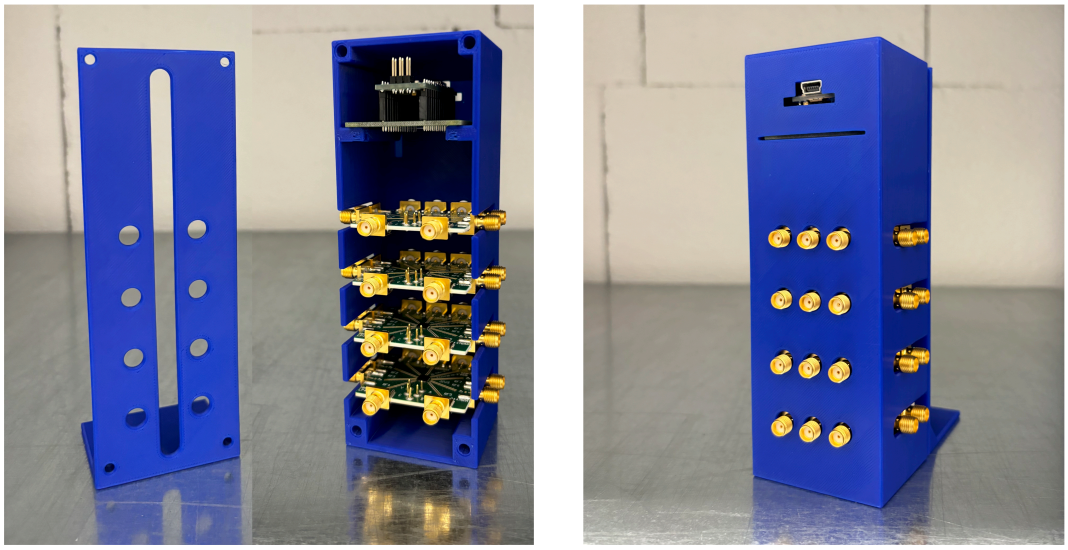

Figure 5.33: Picture of the RF switch before assembling, therefore the cables are missing. The four RF boards with nine SMA (Sub Miniature version A) connectors are controlled by a micro controller, here an Arduino nano, which sits on the highest level in the case. The case is 3D printed. The input signal is fed into the first board and is then distributed to the three lower boards, which have to be connected to the RF input on each RADIANT. The route to a certain channel is then selected from a computer which controls the Arduino.

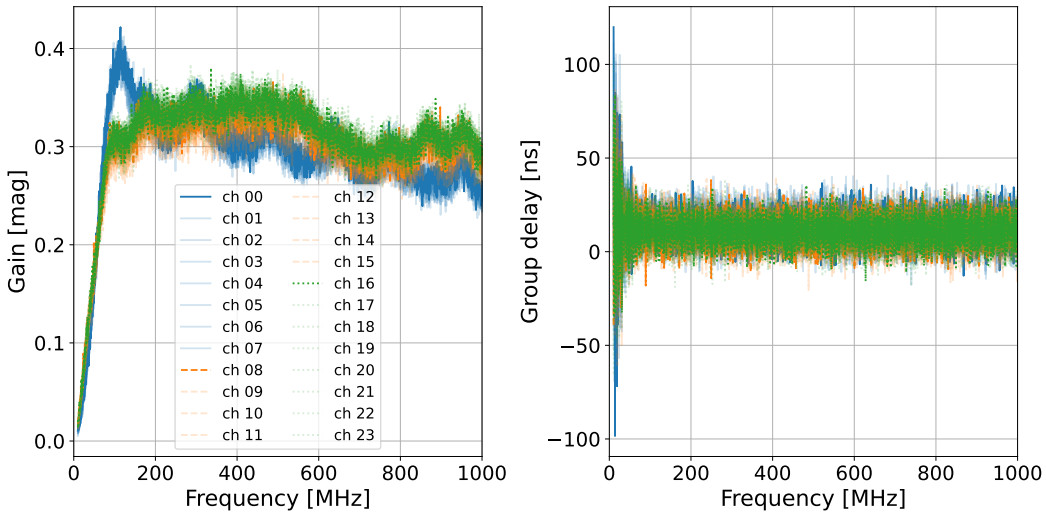

Figure 5.34: Measurement of the RF switch between input and output each of the 24 channel paths. One circuit board can switch between eight channels, therefore three group of eight channels can be distinguished and are color coded. Left: Gain. Right: Group delay.

Table 5.4: Overview of performance tests performed with the RADIANT V3.

id	name	procedure	purpose
PT1	SignalGen-2LAB4D	Inject cr pulse with different amplitude and analyze amplitude from LAB4D	Verify that waveforms are recorded correctly and increase linearly with amplitude
PT2	FrontEnd-Response	Compare recorded waveform of cr pulse between channels	Verify waveforms are comparable between all channels
PT3	AUX-Trigger-Response	Inject cr pulse with different amplitudes and determine the trigger efficiency at a fixed threshold	Verify that the RADIANT trigger is working properly

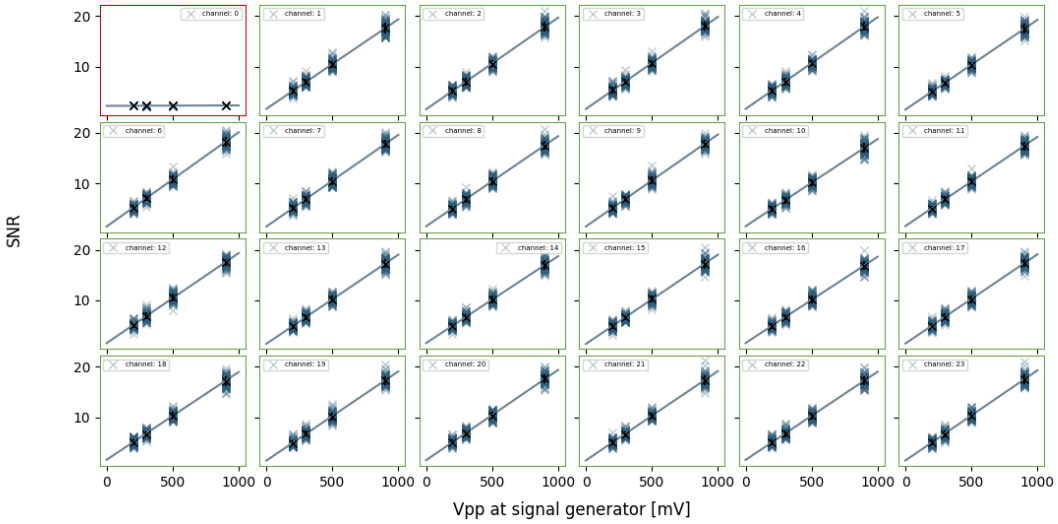

Figure 5.35: Display of the results of the SignalGen2LAB4D test for the ULB-007 board. The x-axis shows the peak-to-peak amplitude of the cosmic ray pulse at the external signal generator. The y-axis shows the SNR of the recorded waveforms, calculated according to Eq. 5.10 and Eq. 5.8. The green frame indicates that the channel passed the test, i.e. the linear fit parameters are within the expected values. Channel 0 clearly fails the test.

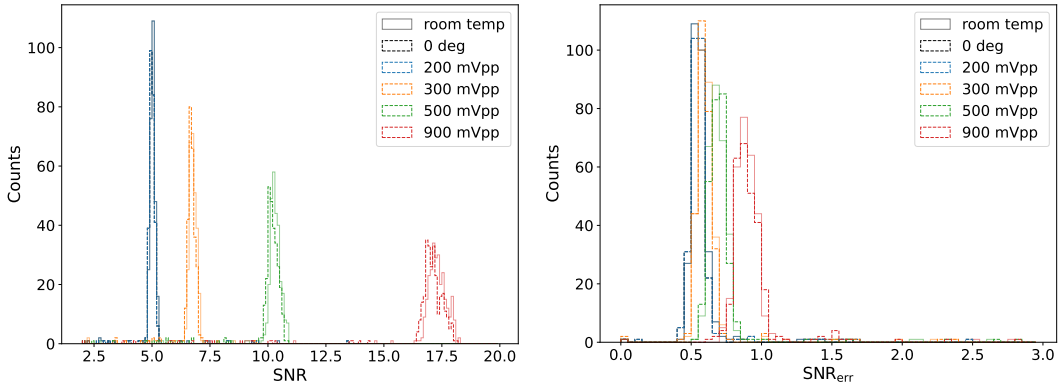

Figure 5.36: Distribution of SignalGen2LAB4D test results for all channels and board. The color code indicates the input temperature at the external signal generator, the line style indicates the temperature (solid = room temperature, dashed = 0 °C. Left: Distribution of signal to noise ratio (SNR). Right: Distribution of the standard deviation of the SNR values shown on the left.

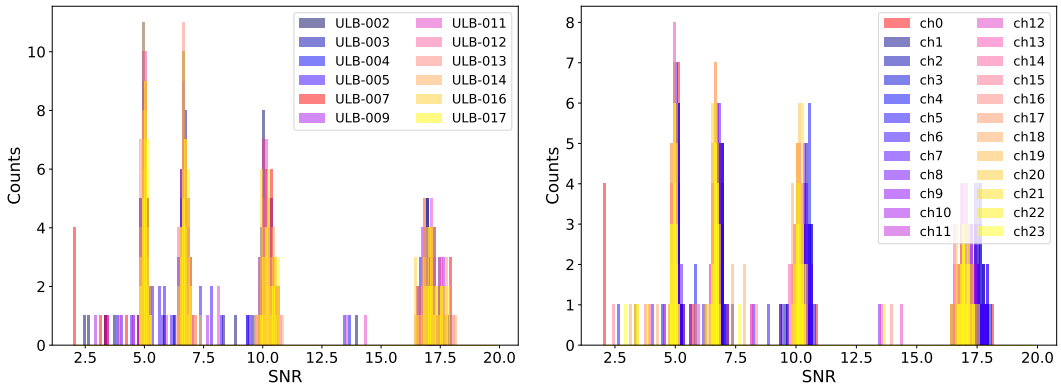

Figure 5.37: Results of the SignalGen2LAB4D at 0 °C, where the color code indicates the tested board (left) and the channel (right).

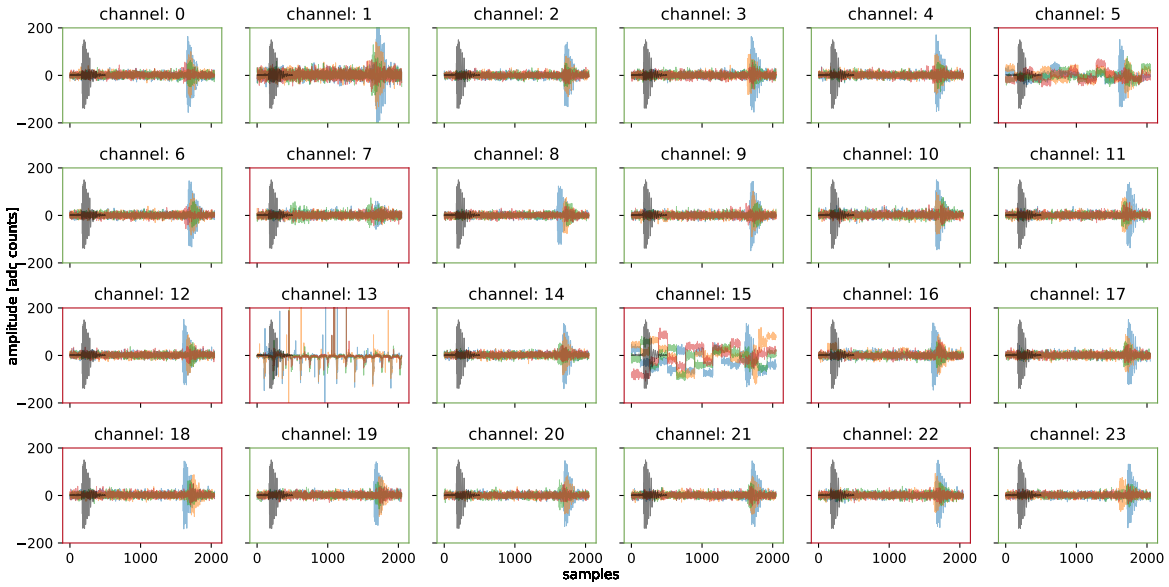

Figure 5.38: Display of 1 of 100 recorded waveforms per amplitude analyzed for the SignalGen2LAB4D and the FrontEndResponse test for the ULB-002 board. The black pulse at the beginning of each waveform is the reference template pulse. Blue corresponds to a waveform with an input pulse of 200 mVpp at the external signal generator, orange to 300 mVpp, green to 500 mVpp, and red to 900 mVpp. The color of the frame indicates whether the FrontEndResponse cross-correlation value for at least one waveform is outside the expected range (red) or all are within the expected range (green).

clearly broken. In Figure 5.39 all traces are normalized to one to make it easier to compare the pulse shape. The black pulse at the beginning is again the reference template. In general, the correlation is better for pulses with a higher amplitude. Channel 1 has a higher overall amplitude, which is due to the direct connection of SURFACE board to RF channel input, all other channels are fed through the RF switch. The cross-correlation value was used as a pass/fail criterion. The red frame indicates that at least one cross-correlation value (out of the four different amplitudes injected) was outside the expected range.

In Figure 5.40 the results for all channels and board are shown. The temperature at which the measurements where take does not seem to influence the cross-correlation value significantly (left). Therefore all temperatures are shown in the middle and left. Board ULB-002 has a very bad cross-correlation value, as many channels failed the tests (see Figure 5.39). Channel 1 has a better cross-correlation value which is due to the direct connection to the SURFACE board without the switch, which also result in a higher overall amplitude.

For each of the surface channels (channel 12-20) the diode trigger was tested at a threshold of 0.92 mV without coincidence. The procedure is the same as described in Section 5.2.3. 100 cosmic ray pulses are injected at the same amplitudes. The true triggers were counted if they occur in proximity (±62.5 ns) to the reference pulse. The trigger efficiency is the counted triggers divided by the number injected pulses. The trigger efficiency curve was then fitted with a hyperbolic tangent according to Eq. 5.12. The fit parameters were used as pass/fail criterion. In Figure 5.41 the result for one board are shown. As previously noted, channel 20 has a later turn on while channel 19 has the earliest turn on in this measurement. In Figure 5.42 the measurements for boards without broken channels are shown. The difference of channel 20 to others is still visible.

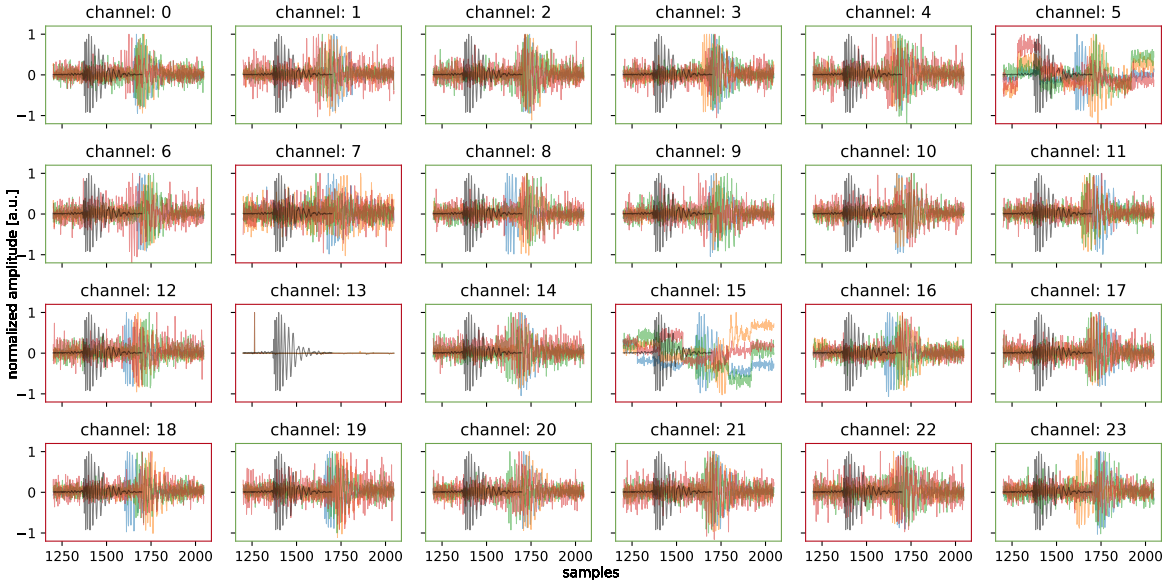

Figure 5.39: Same data as in Figure 5.38. Here the waveforms are normalized to one to obtain a cross-correlation value.

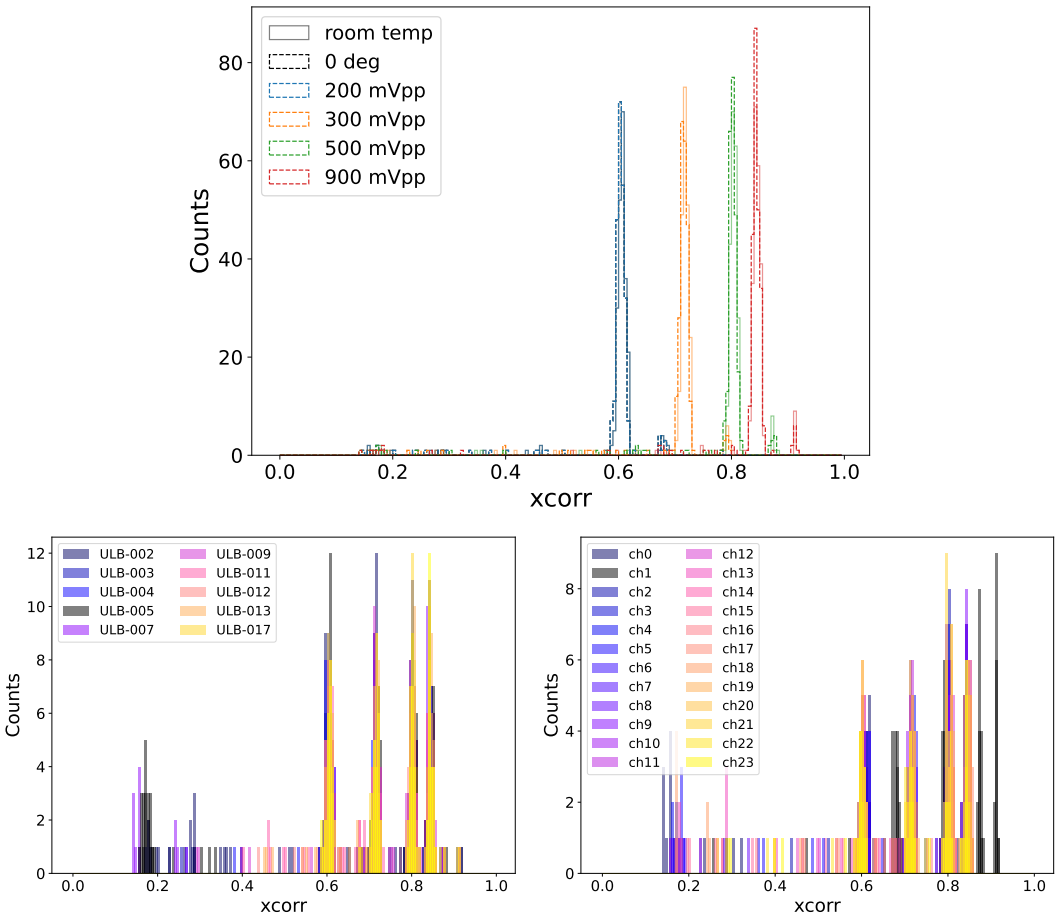

Figure 5.40: Display of the FrontEndResponse test results for all boards and channels. The cross-correlation value xcross is calculated according to Eq. 5.13. Left: The color code differentiates the board, the data includes all temperatures and channels. Right: The color code differentiates the channels, the data includes all temperatures and boards.

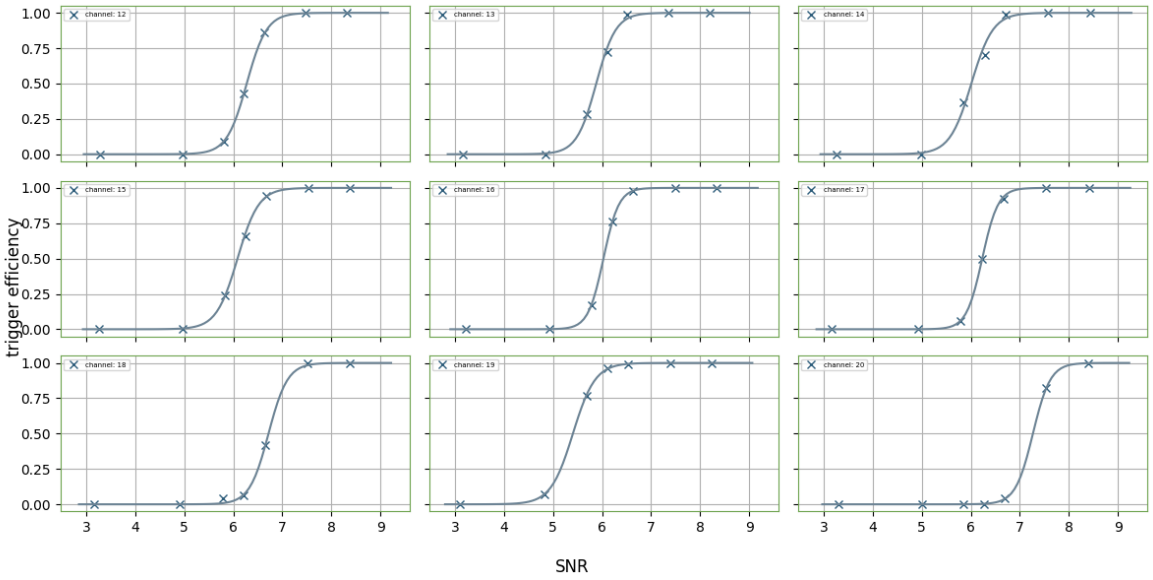

Figure 5.41: Display of the results of the AUXTriggerResponse test for board ULB-14. The solid line is the fitted hyperbolic tangent as in Eq. 5.12.

When comparing the SNR value where the trigger efficiency reaches 50%, the average of channel 20 over all boards considered is ~ 1.5 SNR points higher than channel 19. In the field, these differences in sensitivity can be adjusted with the threshold setting. At cold temperature the trigger efficiency is around 0.3 SNR points better. The standard deviation is roughly at around 0.3 SNR. This is an irreducible uncertainty on the trigger setting.

The main purpose of the testing was to select at least seven boards which can be deployed in the field. After some iterations with the manufactures to replace parts, nine boards were shipped for integration to Chicago. For the trigger efficiency it became clear, that a channel to channel setting of the threshold will be necessary in the field. At the same threshold, the boards deviate by roughly 0.3 SNR when triggering 50% of the injected events. This describes the uncertainties on the trigger process, e.g. diode behaviour, discriminator.

The recorded amplitudes are quite comparable across the boards but have a standard deviation of at least 0.5 SNR when injecting the same pulse with the external signal generator. This includes variation of the transmitted signals and digitization, without trigger. The variation of the amplitudes injected from the external signal generator is assumed to be small, so 0.5 SNR is the uncertainty of the maximum amplitude along the signal path and the digitization. The standard deviation did not change when only triggered waveforms were considered.

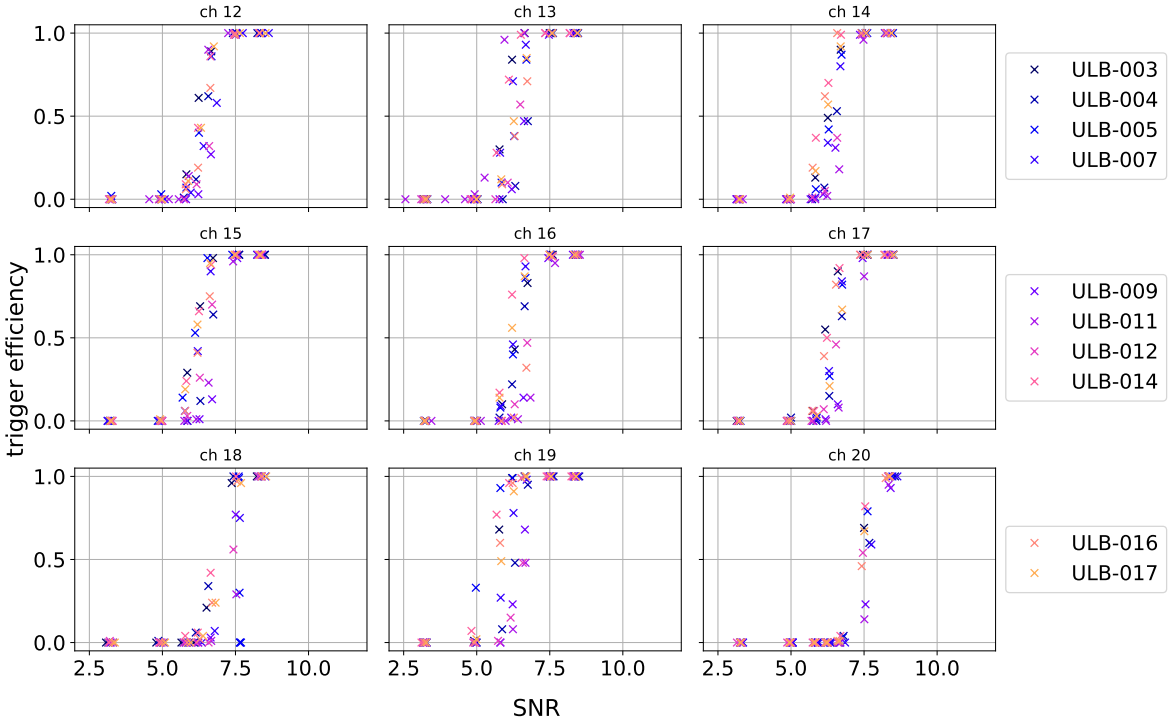

Figure 5.42: Display of the results of the AUXTriggerResponse test at 0 °C. Boards that failed all previous tests are not shown.

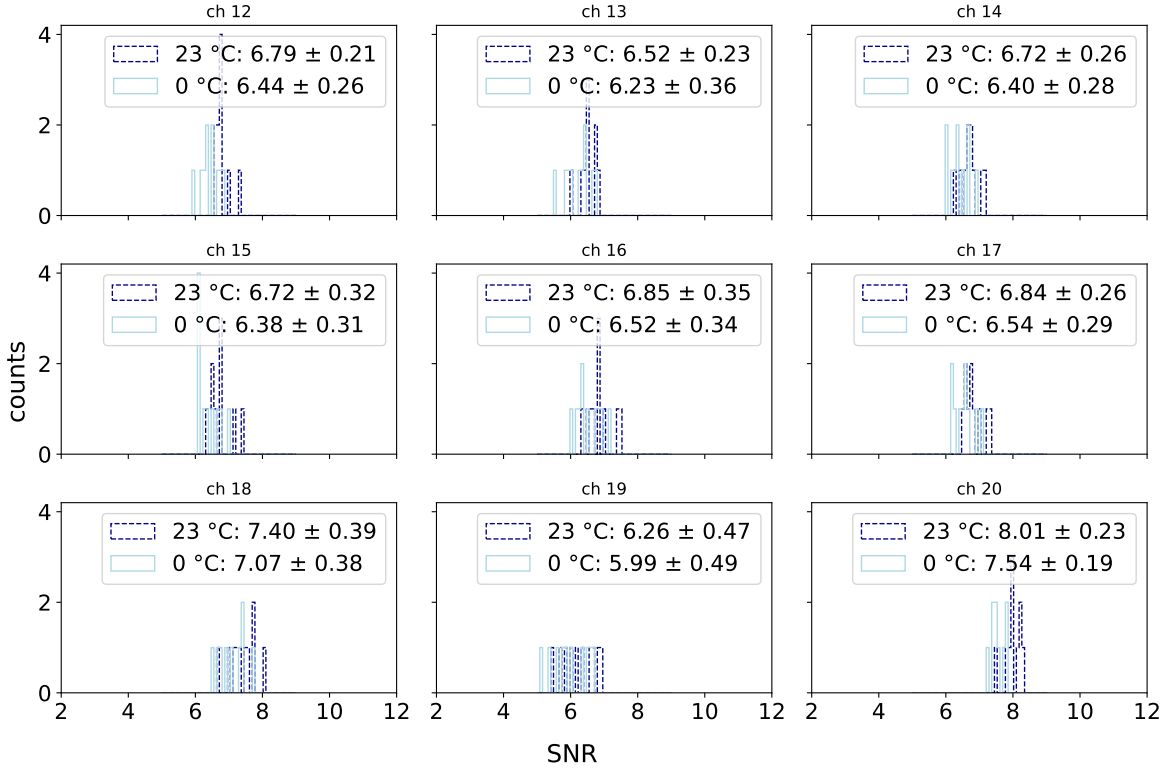

Figure 5.43: Comparison of the SNR value at a trigger efficiency of 0.5. The mean value of each distribution and the standard deviation are stated in the legend. The color code indicates the temperature at which the measurement was taken.

5.4 Intermediate Conclusion

The RADIANT trigger is able to trigger on cosmic ray signals close to thermal noise, given a well adjusted threshold. The trigger outcome is mainly influenced by threshold, diode bias voltage, pulse shape, and temperature. The discriminator introduces additional uncertainties, because the behavior at low voltages is not described in the data sheet. A channel to channel setting of the threshold will be necessary in the field. Since the servo adjustes the threshold continuously to a set scaler rate this poses no problem for the operation of the detector. However, it will lead to extra work in the analysis to predict the number of expected cosmic ray events. Using the internal signal generator in pulse mode would provide an in-situ calibration of the trigger. At the same threshold, the boards deviate by roughly 0.3 SNR when triggering 50% of the injected events. This can be taken as the uncertainty of the trigger path, including diode output and discriminator. The recorded amplitudes are quite comparable along the boards with a standard deviation of at least 0.5 SNR. The analysis of one board indicates an uncertainty of 0.4 SNR. This includes variation of the transmitted signals and digitization, without trigger.

6 Air shower detection

To predict the number of expected cosmic ray events for seven RNO-G stations, Monte Carlo simulations are used. The particle cascade in the atmosphere initiated by a cosmic ray is simulated together with its radio emission. The electric field is then combined with the antenna pattern and the surface signal chain described in Section 5.1. The trigger efficiency determines the final cosmic ray event rate. In the following, the simulation chain including the particle cascade, the radio emission and the detector response is described. The RADIANT trigger as characterized in the laboratory is evaluated, leading to an expected cosmic ray event rate. Based on the results, further implications for RNO-G are discussed.

6.1 Monte Carlo simulations of extensive air shower and their radio emission

A numerical Monte Carlo algorithm is used to predict the complete cascade of secondary particles in the atmosphere and to calculate the emission and propagation of electromagnetic radiation. The method is based on stochastic processes that depend on the interaction cross section of individual particles. Taking into account this probabilistic aspect has an advantage over analytical or semi-analytical calculation methods, since the behavior of a particle is indeed probabilistic. In the following, the simulated air shower set and the procedure are described.

To simulate the particle cascade the CORSIKA (COsmic Ray SImulations for KAscade) code [105] was used. CORSIKA was developed for detailed simulation of extensive air showers initiated by high-energy cosmic ray particles. The particles are tracked through the atmosphere until they react with air nuclei or decay. For particle decays, all decay branches down to the 1% level are considered.

The emission and propagation of the electromagnetic radiation from the secondary electromagnetic shower particles is computed by the CoREAS (Corsika-based Radio Emission from Air Showers) code [175]. It implements the endpoint formalism to calculate the electromagnetic radiation of each electron and proton directly in CORSIKA. The endpoint formalism is based on the fact that all radiation from particle acceleration can be described as a superposition of instantaneous accelerations (endpoints) [176]. From the point of emission, the electromagnetic radiation is propagated to predefined observer positions on the ground. The electric field contribution can be derived either in the frequency domain:

$$\vec{E}_{\pm}(\vec{x}, \nu) = \pm \frac{q}{c} \frac{e^{ikR(t_0')}}{R(t_0')} \frac{e^{2\pi i \nu t_0'}}{1 - n\vec{\beta}^* \cdot \hat{r}} \hat{r} \times [\hat{r} \times \vec{\beta}^*] \tag{6.1}$$

or in the time domain:

$$\vec{E}_{\pm}(\vec{x}, t) = \pm \frac{1}{\Delta t} \frac{q}{c} \left(\frac{\hat{r} \times [\hat{r} \times \vec{\beta}^*]}{(1 - n\vec{\beta}^* \cdot \hat{r})R} \right) \tag{6.2}$$

These equations describe the electric field $\vec{E}$ for an acceleration at time $t = t_0$ to a velocity $\vec{\beta} = \frac{\vec{v}}{c} = \vec{\beta}^*$. The indices ± indicate an acceleration from rest (positive) or an acceleration to rest (negative). The charge of the particle (in CGS units) is q, R is the distance from the point of emission to the observer, $\hat{r}$ is a unit vector in the direction of the observer, and n is the index of refraction of the medium. The relation between the wavenumber k and the frequency ν is $k = 2\pi\nu n/c$ (see [176]).

To simulate the radio emission, the particle trajectories are dissected into a large enough number of these endpoints. The radio emission from each particle subtrajectory can then be calculated individually, taking into account coherence effects at the observer's position. To keep the computation time reasonable for high-energy air showers, the electron and positron distributions can be thinned. Multiple low-energy particles are approximated by single particles of higher weight. However, this introduces artificial coherence and thus artifacts in the resulting predicted radio signals, which is not a problem as long as these artifacts are below the typical noise level [177]. Since the relative arrival time at an observer position must be recomputed for each position, the number of observers has a significant impact on the overall computation time. After simulating the radio emission, a so-called "star-shape" grid is used for the observer positions. The observer positions form a radial grid in the shower plane, which has the incoming direction $\vec{v}$ as normal vector, with the geomagnetic field $\vec{B}$ as the other defining axis, see Figure 6.2. Several interpolation methods are based on this star-shape pattern, e. g. [178, 179]

An alternative to CORSIKA and CoREAS are the simulation codes AIRES [180] for the simulation of particle cascades and ZHAireS [181] for the prediction of the radio emission. In ZHAireS the radio emission is simulated using the "ZHS" algorithm [182, 183]. It has been shown that the prediction of the total radio emission from both codes is in agreement at the level of ~ 5% [184].

6.2 CoREAS Set

For this analysis, a total of 407 air showers with protons as the primary particle were available, generated with CORSIKA 7.6400 [105] using QGSJetII-04 [185] and UrQMD [186] as hadronic interaction models. The radio emission is generated by the

Table 6.1: Number of showers in each shower energy interval and zenith interval. In total, 407 showers were simulated. There are 109 air shower with energies larger 10^{18} eV, 31 of them arrive under a zenith angle smaller than 30°.

Shower energy	0° – 10°	10° – 20°	20° – 30°	30° – 40°	40° – 50°	50° – 60°	60° – 70°	70° – 80°	80° – 90°	Sum
1×10^{16} eV – 3.2×10^{16} eV	10	18	20	17	12	16	20	20	10	143
1×10^{17} eV – 3.2×10^{17} eV	9	16	19	19	20	20	20	20	12	155
1×10^{18} eV – 3.2×10^{18} eV	8	12	11	9	9	19	20	20	1	109
Sum	27	46	50	45	41	55	60	60	23	407

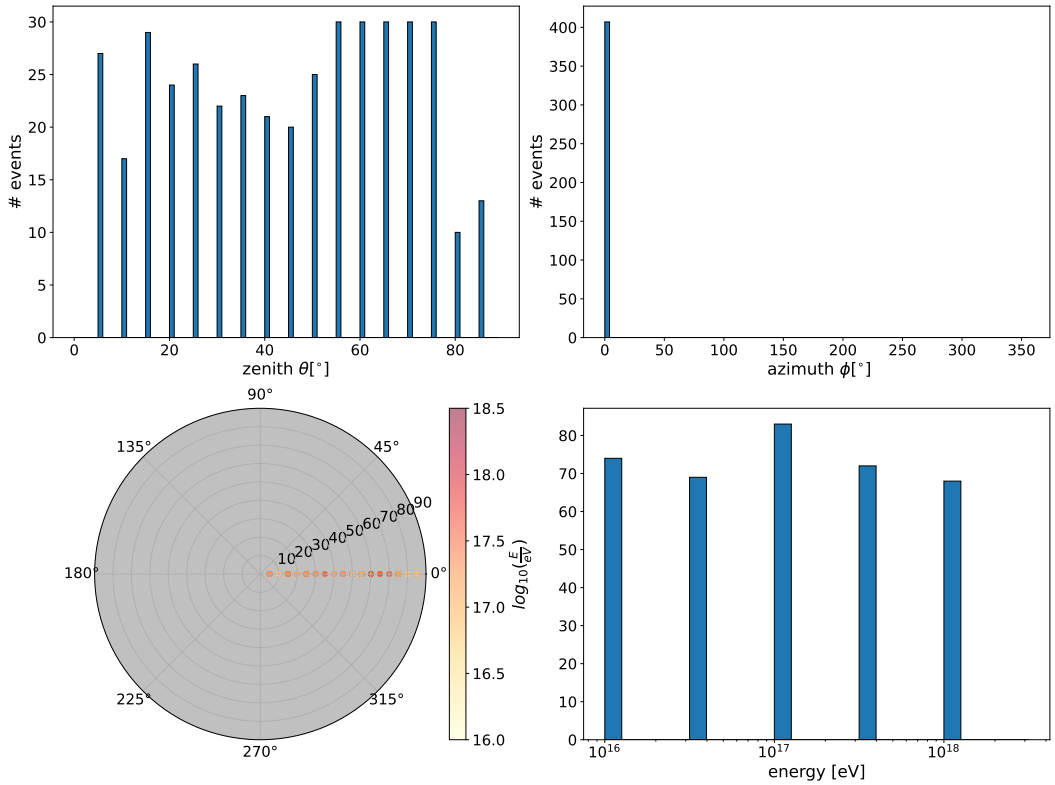

Figure 6.1: Combination of panels with the parameters of the 407 CoREAS air showers used. Top left: Zenith arrival angle distribution. Top right: Azimuth arrival angle distribution. Bottom left: The position indicated the arrival direction, the color code the energy of the shower. Bottom right: Shower energy distribution.

CoREAS plugin [175]. The simulations are performed on a star-shaped grid of 240 observer positions. The CoREAS simulations provide the resulting electric field per observer position as a function of time. Protons have the largest variation in X_{max}, which has a large influence on the radio footprint on the ground. Therefore, simulating only protons is rather conservative and covers different realizations of the shower profile. The simulated energies and arrival directions are shown in Figure 6.1. The exact numbers can be found in Table 6.1. Five energies have been simulated from 10^{16} eV to 3.2×10^{18} eV in half decade bins, the zenith angle θ is covered from from 5° to 85°, where 0° are vertical showers. Only one azimuth direction was simulated (arriving from the east), since the magnetic field $\vec{B}$ with declination 26.06°W, inclination 81.12° downwards, is almost perpendicular to the surface and the plane of the azimuth angle ϕ. To account for the missing azimuth angles, the detector is rotated, as it will be explained in Section 6.3.2.

6.3 Event simulation chain

To make a prediction of the expected signal in the field, the CoREAS simulation must be combined with the array layout and detector response of RNO-G. This is done using the software framework NuRadioReco which is now part of NuRadioMC [110, 187]. The shower core of the CoREAS simulation is placed inside a rectangle encompassing the detector array plus 1000 m in each direction. Seven stations, the number currently

deployed, were simulated in order to estimate the cosmic ray rate. Each CoREAS shower was used to generate 50 events at 50 random core positions.

6.3.1 Simulating the electric field

The electric field is derived from the CoREAS simulations. Since the antenna positions of the RNO-G array do not correspond to the observer position in the star-shaped grid, an interpolation of the electric field at the antenna position is performed. This is done using the interpolation algorithm described in [179], which reconstructs the full waveform in time series. For this analysis, the interpolation method has been implemented in NuRadioReco*. The procedure of the interpolation method is summarized below.

Interpolation method

The interpolation in [179] is performed in the frequency domain, since the pulse arrival times, polarization, and pulse shape change gradually but not linearly along the footprint. The full spectrum at each position (x_i, y_i) can be written as a combination of the absolute amplitude spectrum $|F(\nu)|$ and the phase spectrum $\phi(\nu)$, where ν is the frequency:

$$F(\nu) = \mathscr{F}(E(t)) = |F(\nu)| \exp(i\phi(\nu)) \tag{6.3}$$

The amplitude is interpolated using the absolute spectrum per frequency and polarization. To exploit the rotational symmetry of the radio emission mechanism, the interpolation is performed in the shower plane, expressing the positions in the (2D) shower plane in polar coordinates (r, β). The geomagnetic emission is circularly symmetric around the shower axis, and the Askaryan emission variation is proportional to $\cos(\beta)$.

To perform the interpolation, the variation of the pulse energy given by the eight observer positions at a fixed radius is expressed as a Fourier series. The Fourier components are given by a Fast Fourier Transform (FFT).

The Fourier components are then expressed in (real) cosine and sine amplitudes $c_k(r_i)$ and $s_k(r_i)$ at each simulated radius r_i. To obtain the radial dependence, each of the Fourier components is radially interpolated using cubic splines.

The interpolated estimate of the footprint energy $f(r, \beta)$ at a given position is then expressed as

$$f(r, \beta) = \sum_{k=0}^{n/2} c_k(r) \cos(k\beta) + s_k(r) \sin(k\beta). \tag{6.4}$$

The interpolation of the phase spectrum is more difficult due to its intrinsic periodicity. For a short, coherent pulse, the phase spectrum is mainly determined by a linear function of frequency, i.e.:

$$\phi(\nu) = \phi_0 + 2\pi\nu\Delta t \tag{6.5}$$

where ϕ_0 and Δt define the arrival time.

* https://github.com/nu-radio/NuRadioMC/blob/coreas_interp

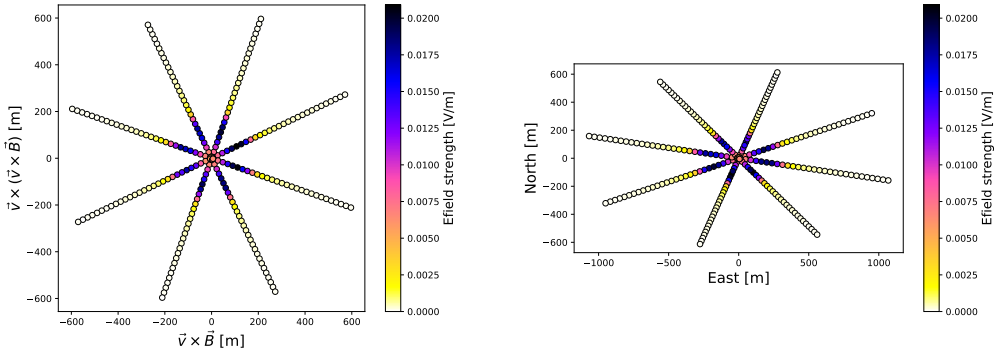

Figure 6.2: Grid of 240 observer positions on which the air shower was simulated. Left: Observer positions in shower plane. The direction of the shower axis is $\vec{v}$, the direction of the magnetic field $\vec{B}$. Right: Positions of the observers projected onto ground. The color code shows the maximal amplitude of the electric field. The simulated air shower arrived under a zenith angle $\theta = 55°$ with a shower energy of 10^{18} eV. The convention is to align the axis of the star pattern with the magnetic field, however, the convention was not followed here.

Δt is defined by the maximum of the Hilbert envelope and calculated in the upsampled signal filter to a 30 MHz to 80 MHz band where the signal is the strongest. The phase constant ϕ_0 is obtained by summing over the complex spectrum after taking out the time shift Δt, and taking the argument, e.g. the angle between the positive real axis of the complex number and the line connecting the origin and the value of the complex number:

$$\phi_0 = \arg \sum_{\nu} F(\nu). \tag{6.6}$$

For each observer position, ϕ_0 and Δt are obtained. Δt can now be interpolated with the same method as the amplitude. ϕ_0 is obtained by taking for neighboring values the multiple of 2π that minimizes the difference, also called unwrapping. This is done first along the radial axis and then along circles.

To obtain higher-order terms of the phase spectrum, pulse timing and phase constant are calculated as above in a sliding frequency window of $\nu \pm$ 25 MHz. This is done up to a cutoff frequency where the coherency drops below a threshold level and the timing cannot be accurately timed or measured due to the weak and less coherent signal. Beyond the frequency cutoff, the arrival time values are kept constant. For the remainder of the phase spectrum, which is almost zero, the nearest-neighbor values are taken to ensure that the algorithm returns the exact values at the simulated antenna locations that were given as input

Following this procedure, for each shower and core position, the 21 antenna positions on the ground are transformed in the shower plane with respect to the shower core. The amplitude and phase spectrum of the signal in each polarization is reconstructed at the antenna position in the shower plane. Afterwards, a Fourier transform is applied to convert the interpolated electric field from the frequency domain to the time domain.

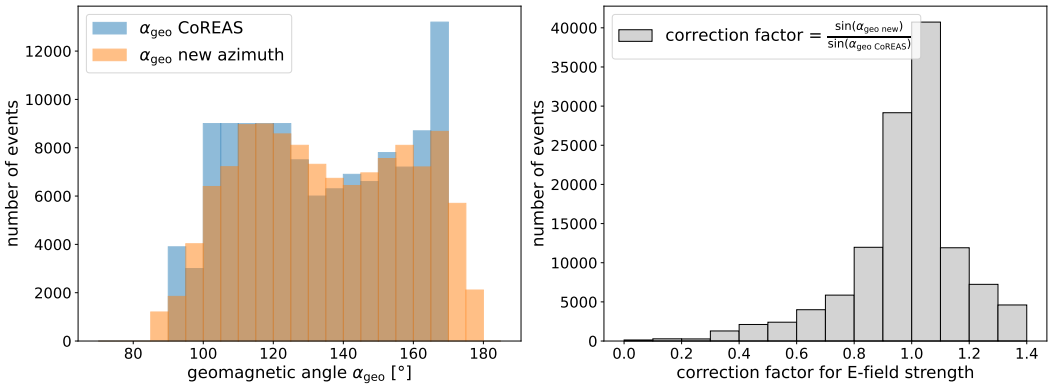

Figure 6.3: Left: Distribution of the geomagnetic angle after the randomly changing of the azimuth. The geomagnetic angle is the angle between the geomagnetic field and the arrival direction of the air shower. Since the magnetic field points downwards with a deviation of ~ 8°, the geomagnetic angle for horizontal showers is just above 80°. Right: Obtained correction factor for the electric field amplitude based on the difference in geomagnetic angle as explained in the text.

Azimuth correction

To account for the missing azimuth angles, in each event the antennas of the entire array were rotated by the same random azimuth angle between 0° to 360°. Altering the azimuth angle also changes the geomagnetic angle α_{geo}, which is the angle between the geomagnetic field and the arrival direction of the air shower. This affects the observed radiation energy S_{obs}, which is the sum of the radiation energy of the geomagnetic emission and the radiation energy of the charge-excess emission. While the radiation energy of the charge-excess component $S_{Askaryan}$ does not depend on the geomagnetic field, the radiation of the geomagnetic emission S_{geo} scales with the geomagnetic angle α_{geo}. Therefore, the radiation energy and thus the amplitude of the simulated electric field must be corrected according to [188] as:

$$S_{obs}(\theta, \phi, \vec{B}) = \frac{S_{geo\perp}(\vec{B}) + S_{Askaryan}}{S_{Askaryan} + (1 - S_{Askaryan}) \sin^2(\alpha_{geo}(\theta, \phi, \vec{B}))} \tag{6.7}$$

where $S_{geo\perp}(\vec{B})$ is the maximal possible geomagnetic emission at which the propagation direction $\vec{v}$ is perpendicular to the magnetic field $\vec{B}$.

The radiation energy scales linear with the quadratic electric field strength, the fraction of the charge excess radiation is assumed to be zero. Therefore 6.7 simplifies to:

$$\sqrt{S_{obs}(\theta, \phi, \vec{B})} = E_{obs}(\theta, \phi, \vec{B}) = \frac{E_{max\ geo}}{\sin(\alpha_{geo}(\theta, \phi, \vec{B}))} \tag{6.8}$$

where E is the electric field amplitude. To modify the electric field amplitude of an existing air shower with E_1, ϕ_1 according to the new azimuth ϕ_2, the following relation is used:

$$E_2(\phi_2) = \frac{\sin(\alpha_{geo2}(\phi_2))}{\sin(\alpha_{geo1}(\phi_1))} \cdot E_{obs}(\phi_1). \tag{6.9}$$

Since the magnetic field is nearly perpendicular (the deviation is ~ 8°), the correction for

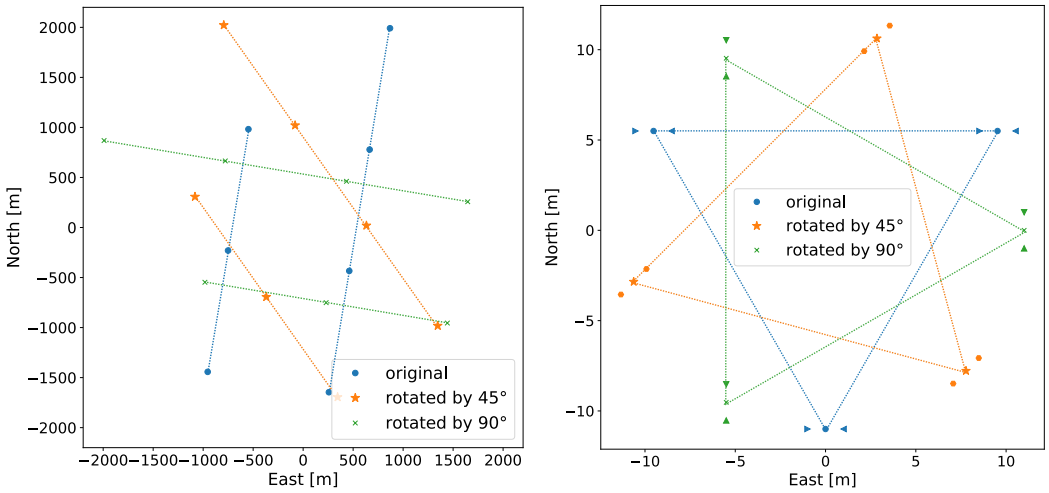

Figure 6.4: Three azimuthal rotations of the array (left) and a station (right) for 0°, 45°, 90°. The dotted lines between the station (left) and antennas (right) are for better visibility. The three markers per antenna indicate the direction of the tines. For the simulations, only these three array geometries were used, while the antennas were randomly rotated between 0° to 360° to account for the different geomagnetic angles.

the electric field strength is close to 1, as shown in Figure 6.3. This correction covers a slightly larger range of the geomagnetic angle.

To also cover the array topography at different azimuth angles, three detector layouts with azimuthal rotations of 0°, 45° and 90° were used, see Figure 6.4. With the rotation of the detector, the antennas and the correction of the electric field amplitude, the missing parameter space of the azimuth angles of the CoREAS simulation is now taken into account, which affects the station coincidence, the antenna sensitivity and the electric field strength.

Energy scaling

Air showers at ultra-high energies require long computation times and are rare in the field due to the steeply falling spectrum. To obtain a rate prediction for energies $>10^{19}$ eV, showers at lower energies can be scaled up. This is based on the relation, that the primary particle energy is roughly proportional to the number of electrons in the shower. As a consequence of coherence, the amplitude of the radio emission scales linearly with the number of electrons in the shower [98]. In this simulation set, all showers have been used a second time with an upscaling factor of 10 applied to the primary energy and electric field. Considering the 407 air shower, using 50 random core positions, three detector configurations and the upscaling, a total of 122 100 events. The parameter distribution is shown in Figure 6.5.

6.3.2 Detector simulation and RADIANT trigger

Seven stations are simulated to obtain the cosmic ray rate. The upward-facing LPDA antennas are the only antennas with relevant sensitivity to air showers. The signal received by the antennas is amplified by the SURFACE board and then split into a trigger and a signal path. The complete signal chain for the surface component is described in

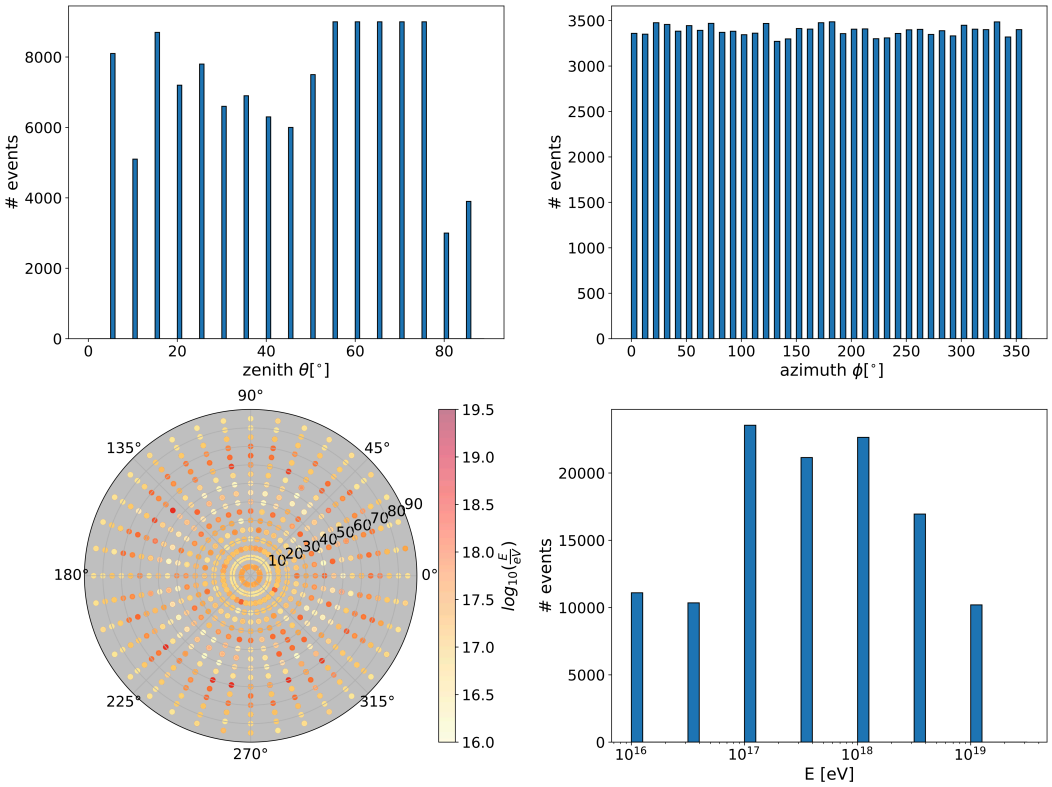

Figure 6.5: Parameter distribution of the 122100 simulated events, which are based on 407 CoREAS air showers used.

Section 5.1. The relevant quantity that determines the event rate is the trigger efficiency. Prior to triggering, the electric field is convolved with the vector effective length (VEL) of the antenna and the SURFACE board response. The changes in the signal path after the trigger decision, such as the RADIANT response, are not modeled because the exact waveform as stored in the data is not relevant to this analysis.

RADIANT trigger

The trigger simulations are based on the measurements and trigger characterizations described in Section 5.2.3. The trigger path is modeled by filtering the signal in a band of 80 MHz to 200 MHz and taking a power integration, i.e. squared and integrated over $\Delta t = 11$ ns:

$$P_{\text{int}} = \sum_{i}^{i+\Delta t} V_i^2 \tag{6.10}$$

In Section 5.2.3 the trigger efficiency is measured in relation to the standard deviation of the noise $\sigma_{\text{power int}}$. A detailed analysis of the noise in the laboratory, in the field and the simulations will follow in Section 6.4. In the figure on left, the standard deviation of the power integrated noise $\sigma_{\text{power int}}$ is calculated for each channel according to Eq. 5.8. In simulations, 200 samples are stored before the trigger sample, therefore the first 130 samples (416 ns at a sampling rate of 3.2 GHz) are considered noise. In Section 5.2.3 (right) the SNR of the simple amplitude trace in the full frequency band in shown for comparison. The SNR is defined according to Eq. 5.10, with the maximum of the trace divided

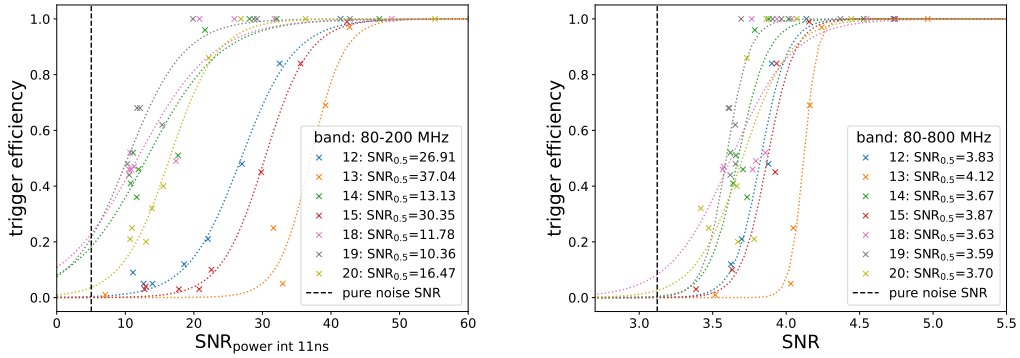

Figure 6.6: Trigger efficiency measured for 100 cosmic ray like pulses each, with increasing amplitudes near to thermal noise at a trigger threshold corresponding to a RADIANT scaler of 10. Left: For the power integrated signal to noise ration in the trigger band. Right: Same events shown for 'simple' signal to noise ratio described in Eq. 5.10

by the standard deviation of the noise without power integration.

The trigger threshold is set as a multiple of $\sigma_{\text{power int}}$ and therefore changes with each simulated waveform. This is desired because the servo adjusts the threshold in the field to a given trigger rate. The signal to noise ration $\text{SNR}_{\text{power int}}$ is then the maximum of the power integrated trace divided by $\sigma_{\text{power int}}$ (see Eq. 5.9). For the RADIANT V3, the measurements show that a trigger efficiency of 50% is achieved at a $\text{SNR}_{\text{power int}}$ between 10 and 37 for different channels. This range is due to the different hardware trigger settings, which is based on a scaler of 10 in the lab, given the amplifier noise. In the field, a performance similar to channels 12 and 15 is desired, which have a trigger efficiency of zero, or very close to zero at pure noise to avoid high data rates and are then monotonic increasing with $\text{SNR}_{powerint}$. These channels yield a threshold of 27-30 $\sigma_{\text{power int}}$ for the V3 board, or expressed in terms of the 'simple' SNR a threshold of 4 σ.

For the simulations the threshold was set to the 50% trigger efficiency, e.g. 30 $\sigma_{\text{power int}}$, directly at the threshold and below the trigger is counted as *False* above the threshold the trigger is counted as *True*. Given the sharp rise and symmetric curvature near zero and one of the trigger efficiency, this definition of the threshold allows for reproducibility while preserving the average trigger efficiency.

The threshold triggers for the three antenna channels are then evaluated for a coincidence within 60 ns. If two out of three antennas fulfil this criterion, the event is triggered *True*.

6.4 Noise simulations

Three sources of noise are considered in simulations: thermal noise from the ice, thermal noise from the system, and Galactic background emission.

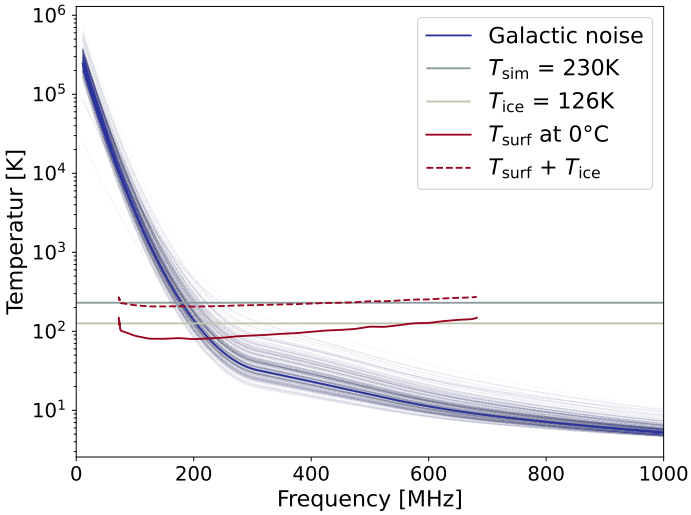

Figure 6.7: Noise temperature as a function of frequency. The different blue lines show the Galactic noise temperature obtained from the GSM 2016 model for different zenith and azimuth angles. The solid red line shows the measurements of the noise temperature of the surface chain. The light blue line shows the noise temperature of the ice at 130 K, the gray line shows the thermal noise temperature of 230 K used for the simulations, which approximated the dashed, red line

6.4.1 Components of the noise

The *thermal noise* from the ice is calculated using the ice temperature. The average ice temperature is then the integral over the temperature profile weighted by the field of view of the antenna, here expressed as the vector effective length (VEL). For the downward facing antennas this results in a noise temperature of 230 K. The upward facing antennas are exposed to less ice, but also see reflections from the surface, resulting in a temperature of ~ 126 K.

The SURFACE board amplifier, which is part of the surface chain, adds additional noise, which is quantified in [189]. The noise temperature is about 80 K and increases at higher frequencies, see Figure 6.7. The cable losses add another 20 K, resulting in a system noise temperature of ~100 K.

Combining the thermal noise from ice, surface chain, and cable gives a noise temperature of 230 K. Since the noise from the amplifier varies little with frequency and the other contributions are constant, the thermal noise is assumed to be constant within frequency.

The noise temperature is used to calculate the root mean square of the thermal noise $V_{\text{rms}}^{\text{thermal}}$ for a bandwidth of $\Delta\nu$ according to:

$$V_{\text{rms}}^{\text{thermal}} = \sqrt{k_B \cdot \Delta\nu \cdot T_{\text{eff}} \cdot R} \tag{6.11}$$

where R is the resistance and T_{eff} is the effective temperature. Since the thermal noise is expected to be uniform around the antenna, no antenna response is taken into account when calculating the pure thermal noise. As a rough estimate, the noise is applied in a band of 50 MHz to 800 MHz, which corresponds to the bandpass filter in the SURFACE board. With the impedance of R = 50 Ω and T_{eff} = 230 K, the $V_{\text{rms}}^{\text{thermal}}$ = 10.91 µV. The frequency spectrum follows the Rayleigh distribution.

The *Galactic noise* or diffuse Galactic radio emission is computed using the Galactic Sky Model 2016 (GSM2016) [190, 191], which is based on the 2008 GSM model [192]. It predicts the all-sky temperature at frequencies between 10 MHz and 5 THz based on 29 sky maps. The accuracy is expected to be between 5% and 15% for most frequencies.

The output of the GSM2016 map can be converted to a spectral radiance B per solid angle as a function of frequency ν, declination δ, and right ascension α. For low frequencies, the Rayleigh-Jeans law approximates the spectral radiance at a given temperature T [193]. The spectral radiance is

$$B(\alpha, \delta, \nu) = \frac{2k_B}{c^2}\nu^2 T(\alpha, \delta, \nu) \tag{6.12}$$

where k_B is the Boltzmann constant and c is the speed of light, giving the unit $[B] = \mathrm{W\ m^{-2}Hz^{-1}sr^{-1}}$. The received spectral power density S_ν at the antenna is then:

$$S(\alpha, \delta, \nu) = \frac{2k_B}{c^2}\nu^2 \int_\Omega T(\alpha, \delta, \nu) d\Omega. \tag{6.13}$$

with the integral over the visible solid angle.

Before integrating over the visible sky, the (α, δ) equatorial coordinates are converted to local (θ, ϕ) celestial coordinates, which introduces a time dependence, because the antenna field of view changes with the Earth rotation. For a monochromatic plane wave, the electric field is related to the spectral power density by:

$$E(\theta, \phi, \nu) = \sqrt{\frac{S(\theta, \phi, \nu)}{c \cdot \epsilon_0}} \tag{6.14}$$

where c is the speed of light and ϵ_0 is the permittivity of vacuum. The total electric field arriving at the antenna is the sum over all frequencies.

$$E_{\text{total}} = \int E(\theta, \phi, \nu) d\nu \tag{6.15}$$

The variations of the Galactic noise over a day are small at Summit Station, Greenland because the Galactic center, where most of the emission originates, is not visible at any time. However, the analysis of the first RNO-G data showed a power variation in the frequency spectrum for the upward facing antenna, which is assumed to be aligned with the Galactic emission [149].

The simulated noise components are shown in Figure 6.8. The Galactic noise dominated up to 150 MHz, with higher frequencies the contribution from the Galactic noise decreases and the thermal component is dominant.

6.4.2 Comparison to field and laboratory measured noise

To get an idea of whether the noise simulations are reasonable, they can be compared to data already collected in the field. Until summer 2024, all data has been collected with a RADIANT board V2. In Figure 6.9 an overview of the standard deviation σ_{adc} after baseline correction is shown for all stations and the three upward facing LPDAs considering all

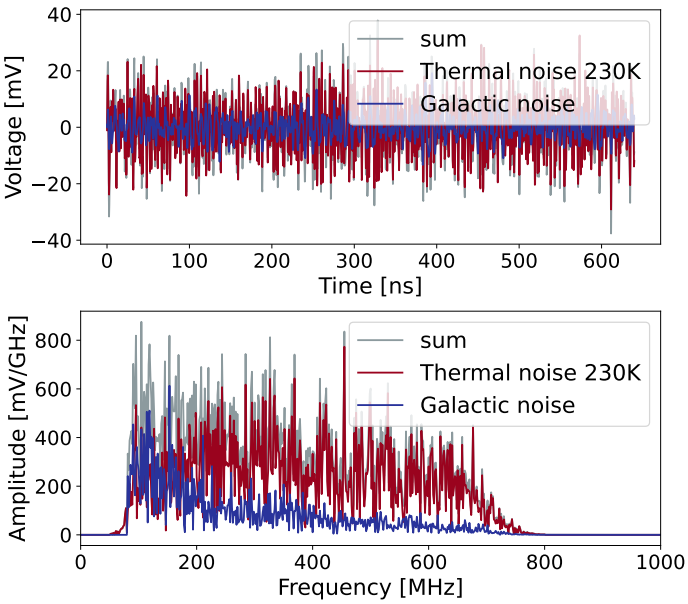

Figure 6.8: Simulation of the Galactic and thermal noise at a temperature of 230 K for an upward pointing LPDA in Summit Station, Greenland. Top: Time domain. Bottom: Frequency domain.

trigger types. At the beginning of the season the rms is lower than usual. It has been shown that the amplifiers used are temperature sensitive and produce less noise at colder temperatures [194]. Since they are deployed only 1 m below the surface, they experience seasonal variations. Another contributor may be (less) human activity at the camp, as only 5 people stay over the winter and no planes arrive. Most of the time, the standard deviation is between 9 σ_{adc} and 13 σ_{adc} in adc counts. The characterization of the SURFACE board also showed variations between different boards [194], which likely contributes to the differences between stations. Also visible are noisy periods. The peaks in trigger rate and standard deviation have been studied elsewhere, e.g. [195, 196]

For the noise comparison, a quiet day (October 3, 2023) was chosen, and only events that were transmitted by satellite (i.e. the burn sample) and triggered by the software trigger, i.e. recorded every second without any physical reason, were selected. For each station, the upward facing LPDAs were used. Stations 21 and 22 did not record any data that day. The standard deviation was calculated according to eq. 5.8. The result is shown in Figure 6.10 (left). In the same figure the standard deviation of the simulations is shown, taking into account the Galactic noise and the thermal noise of 230 K. The station noise varies between 9.28 and 10.46 $\sigma_{\text{noise mV}}$, station 11 seems to be particularly quiet. The other 5 stations agree within their uncertainties. The simulated noise is between the quiet station and the other stations.

The noise level has an effect on the trigger efficiency, which was obtained in the laboratory with a V3 RADIANT board and a SURFACE board, as described in Section 5.2.3. In Figure 6.10 (right) the comparison of the $\sigma_{\text{noise adc}}$ for the V3 board and the V2 board in the field in adc counts is shown. The standard deviation is between 15.2 $\sigma_{\text{noise adc}}$ for station 11 and 17.1 $\sigma_{\text{noise adc}}$ for station 12. The V3 board has a standard deviation of 13.9 $\sigma_{\text{noise adc}}$, which is even lower than station 11. The boards are exposed to different noise, e.g. the V2 boards are also exposed to Galactic noise and the noise from the ice. The V2 boards also have a slightly higher gain in the signal path due to the different splitting ratio

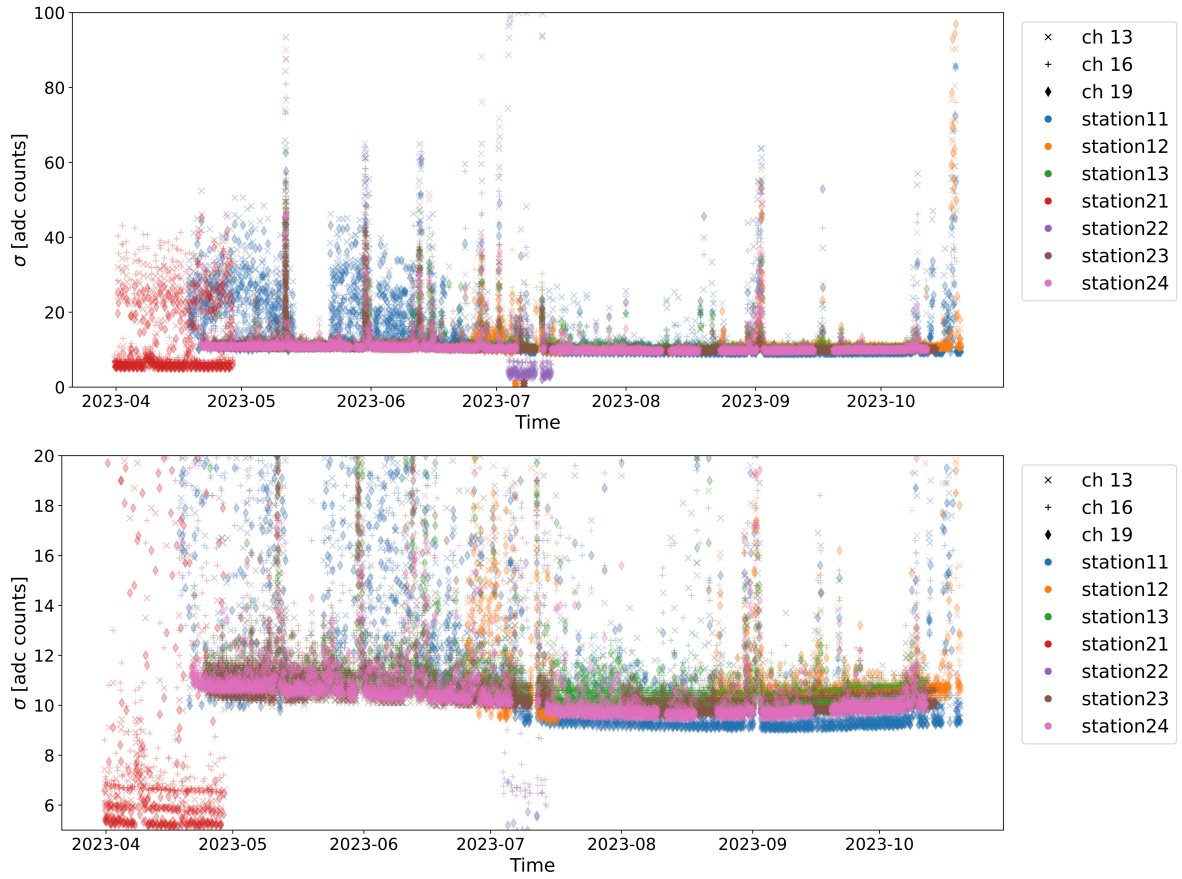

Figure 6.9: Overview of the σ_{adc} per run (~2 hours) in adc counts with baseline correction. About 10 000 events are shown for the 2023 season for all stations and the three upward facing LPDAs. The data is the burn sample transmitted via satellite for monitoring. All trigger types are considered. Top: σ in the range of 0 adc counts to 100 adc counts. Bottom: Same data but zoomed in.

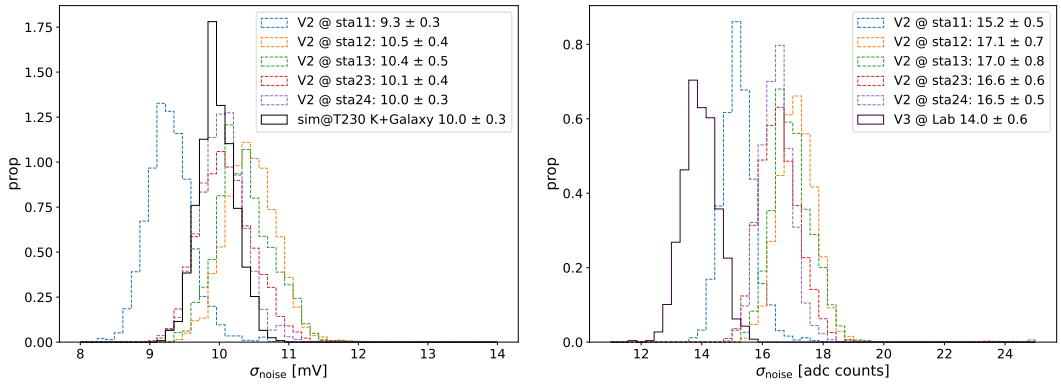

Figure 6.10: Left: Comparison of the standard deviation of the noise calculated from the software trigger on a quiet day in the field (October 3, 2023) for stations 11, 12, 13, 23, and 24 for the three upward-facing LPDAs with the distribution obtained by simulation (left) and measured with a V3 board and the SURFACE board in the laboratory (right). The distributions are normalized so that each integral is equal to one.

for signal and trigger path (see Section 5.2.2). Since the exact behavior of the diode is non-linear, it is unclear how the lower noise level affects the trigger efficiency. Using a fixed noise standard deviation for the trigger simulations to set a threshold would not correctly model thresholding and servoing in the field. Therefore, the same noise is assumed for the signal and trigger paths. The differences between the stations do not give a clear indication of what to simulate, so the trigger simulations are performed with thermal noise of 230 K and galactic noise from the GSM2016 sky map, which is between the measured $\sigma_{\text{noise adc}}$ in the field.

6.5 Rate predictions

In order to determine the cosmic ray rate the effective area is computed, which describes the area around the detector array in which an air shower with a certain energy and arrival direction will be detected. The effective area is calculated by multiplying the simulated area in which the shower cores are placed by the trigger efficiency, e.g. the number of triggered events divided by the number of detected events. Since the detector is flat, the cosmic ray flux is only orthogonal to the projected simulated area and the area has to be corrected by a factor of $\cos(\theta)$:

$$A_{\text{eff}} = A_{\text{proj}} \cdot \frac{N_{\text{trig}}}{N_{\text{sim}}} = A_{\text{sim}} \cdot \cos(\theta) \cdot \frac{N_{\text{trig}}}{N_{\text{sim}}}. \tag{6.16}$$

The simulated area is a rectangle containing the area covered by the seven stations, plus an additional 1000 m in each direction. The station spacing is 1.25 km, which would allow for a maximum distance to a station of 880 m within the array.

The result for the effective area of the seven deployed stations is shown in Figure 6.11. All simulations were performed with the radiant auxiliary trigger, the threshold being a multiple of the standard deviation of the power integrated noise $\sigma_{\text{power int}}$ (see Eq. 5.9) in the trigger band of 80 MHz to 200 MHz. A coincidence of two out of three antennas per station within 60 ns is required. The uncertainties stem from the number of counted e.g. triggered events, therefore the uncertainty is calculated with $\sqrt{N_{\text{trig}}}$. The effective are increases with higher energies, in the lowest energy bin starting from 3.16×10^{16} eV, the effective area is almost to zero for a $15\,\sigma_{\text{power int}}$ and $20\,\sigma_{\text{power int}}$ threshold, and zero for higher thresholds. A more sensitive threshold increases the effective area at all energies, the differences between the selected thresholds become smaller when comparing higher thresholds. For a $30\,\sigma_{\text{power int}}$ threshold the zenith distribution is shown in Figure 6.11 (right). For energies above 10^{18} eV, the effective area is largest around a zenith angle of 70°. For lower energies the maximum is at slightly more vertical showers (~60°), the effective area at these energies is however pretty small. This can be explained by the fact, that inclined air showers illuminate larger areas but since the air-shower energy is distributed over a larger area, the electric field registered by one antenna is fainter, which makes inclined air-showers only visible at higher energies or with a low trigger-threshold. Vertical showers have a small footprint, plus they align with the magnetic field in Greenland and therefore the geomagnetic emission is low, which decreases the

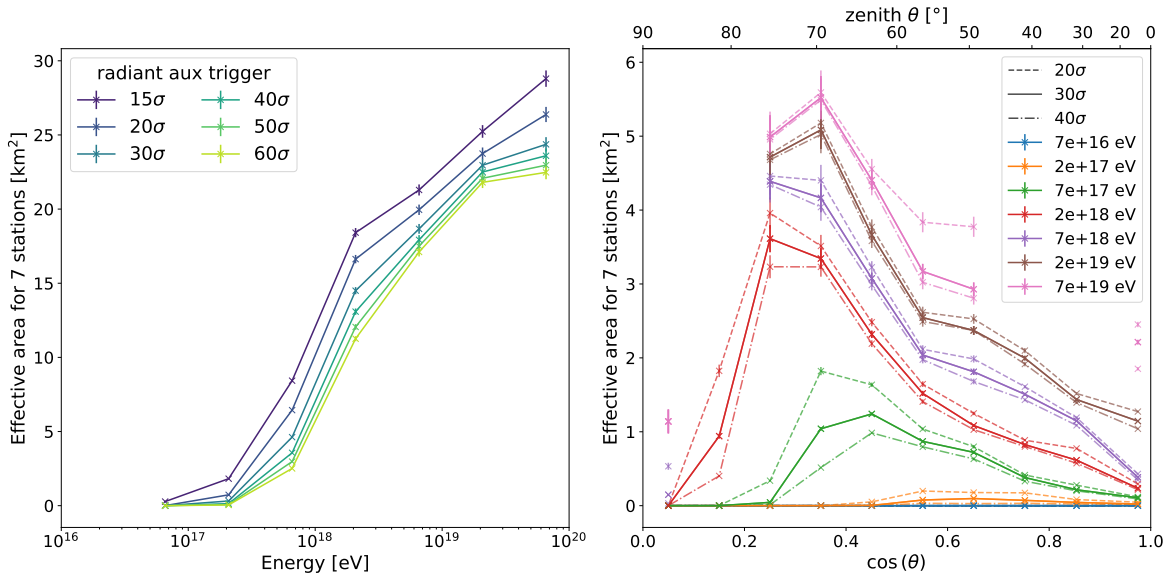

Figure 6.11: Distribution of the projected effective area of the seven RNO-G stations for different energy and zenith bins. The uncertainty is the square root of the number of events triggered. The markers are in the center of each bin. Left: Effective area for different trigger thresholds as given in the legend. Right: The effective area for a 20 $\sigma_{\text{power int}}$ (dashed line), 30 $\sigma_{\text{power int}}$ (solid line) and 40 $\sigma_{\text{power int}}$ (dash-dotted line) trigger.

radiated energy. Therefore, the shower core needs to be very close to an antenna in order to trigger.

The expected event rate is obtained combining the effective area with the cosmic ray flux J integrated over energy E and the solid angle Ω of the visible sky:

$$\Gamma_{\text{CR}}(E,\theta) = \int_{t_1}^{t_2}\int_{E_1}^{E_2} A_{\text{eff}}^{\text{proj}}(E,\theta)\cdot J(E,\theta,\phi)\cdot \Omega dE dt \tag{6.17}$$

The solid angle depends on the zenith angle range with the limits θ_1, θ_2 and on the azimuth ϕ. Since all azimuth angles are visible, the integral over $d\phi$ yields 2π.

$$\Omega = \int_{\phi_1}^{\phi_2}\int_{\theta_1}^{\theta_2} \sin(\theta) d\theta d\phi = 2\pi\cdot(\cos(\theta_1)-\cos(\theta_2)) \tag{6.18}$$

The cosmic ray flux of 3.16×10^{16} eV to 1×10^{20} eV is measured and published by the Pierre Auger Collaboration [197], see Figure 6.12. The measured flux multiplied by the cubed energy highlights the features of the steeply falling spectrum around 10^{17} eV and 3×10^{18} eV. Around 10^{20} eV the cosmic ray flux is suppressed.

The expected number of cosmic ray events per day and seven stations is given in Figure 6.13. With a trigger threshold of 30 $\sigma_{\text{power int}}$, which is the threshold value obtained in the laboratory, 5 cosmic rays are expected per day and seven stations. Most of the events are in the energy bins of 10^{17} eV to 10^{18} eV. If the trigger changes to 20 $\sigma_{\text{power int}}$ or 40 $\sigma_{\text{power int}}$, 10 or 4 events are expected. The 15 $\sigma_{\text{power int}}$ trigger threshold has the largest effective area at energies below 10^{17} eV, combined with the steeply falling flux, the event rate increases to 38 events. However, given the current predictions it seems unlikely that a relevant

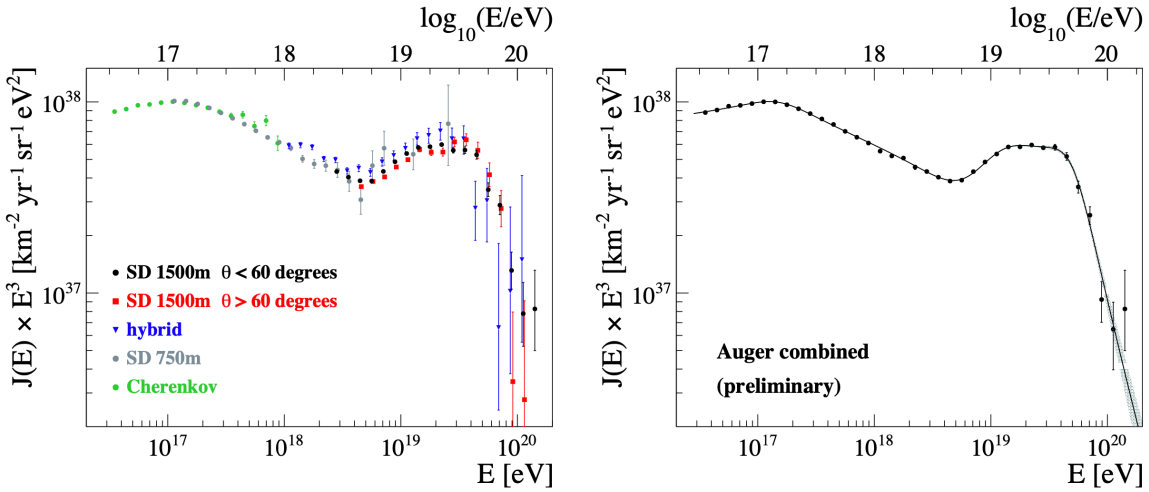

Figure 6.12: Energy spectra measured by the Pierre Auger Observatory. Left: Several independent and complementary data sets, namely events detected with the the surface detector (SD), hybrid events, detected with the fluorescence detector and at least one water-Cherenkov detector, and events detected with the High Elevation Auger Telescopes (HEAT), here labeled as Cherenkov. Right: Spectrum obtained by combining the different measurements. Fig. from Ref. [197]

number of events can be measured at energies below 10^{17} eV. The uncertainties given are derived from the effective area calculations. As the effective area calculations already suggested, the preferred zenith angle depends on the energy, with lower energy showers mostly detected at a zenith angle of 50°. For higher energies, the zenith angle peaks at higher inclinations because the area over which the shower is detectable becomes larger.

The distribution of the distance from the shower core to the nearest triggered station for a threshold of 30 $\sigma_{\text{power int}}$ as a fraction of the total number of events is shown in Figure 6.14. Showers arriving below a zenith angle of $\leq 37°$ are only measurable if the shower core is within 200 m of the station. More inclined showers can be measured further away because the area where the radio emission is detectable increases. However, showers arriving at an angle of about 60° rarely trigger within 100 m of a station. This may be due to the fact that the radio emission near the core is weak and has a radius in the direction of arrival of the order of 100 m. Most events (97%) trigger only one station, as shown in Figure 6.14 (right). The number of station coincidences increases for more inclined showers because the footprint covers a larger area. With a trigger threshold of 30 $\sigma_{\text{power int}}$, about 30 events per season of 200 days are expected to trigger more than one station.

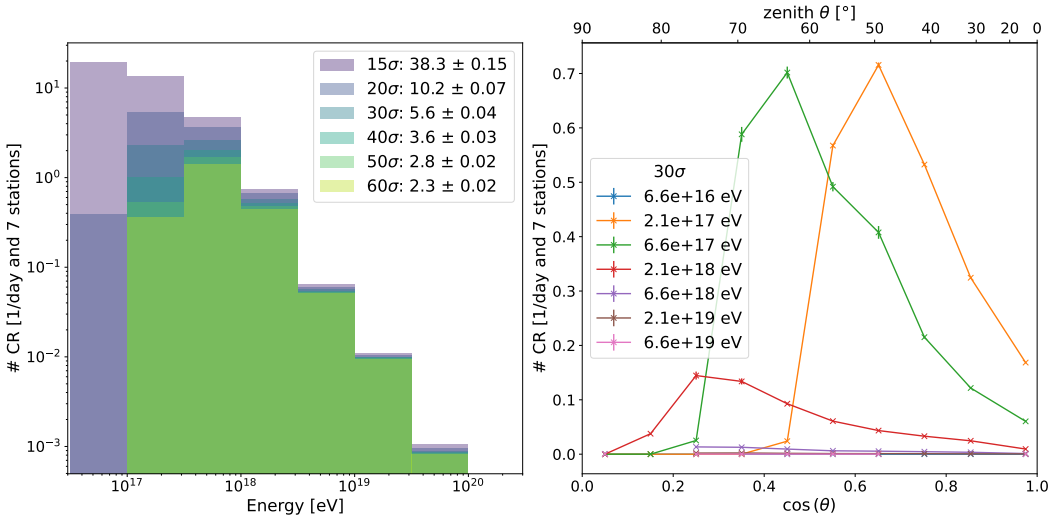

Figure 6.13: Number of expected cosmic ray events per energy and zenith bin. Left: The color code indicates the trigger threshold. The number in the legend is the sum over all energy bins with the uncertainties from the effective area calculations. Right: Zenith distribution for a 30 $\sigma_{\text{power int}}$ threshold. The legend indicates the center of the energy bin for each color.

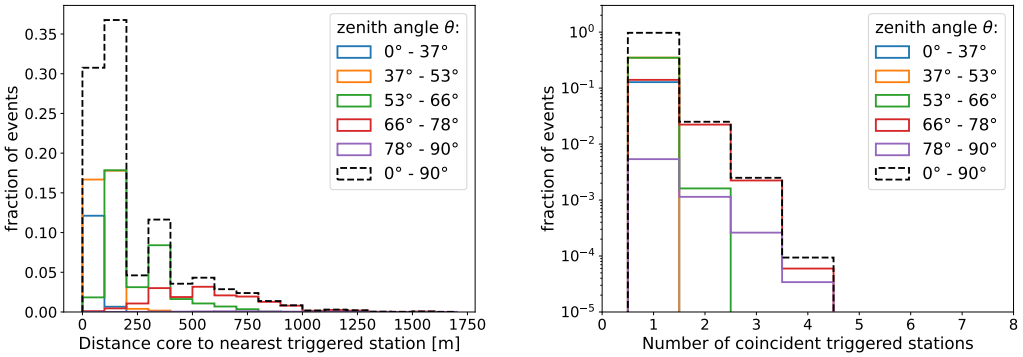

Figure 6.14: Distributions for different zenith angles as given in the legend for a 30 $\sigma_{\text{power int}}$ trigger threshold. The fraction is with respect to the total number of expected cosmic ray events. The last bin contains all events with a distance > 1600 m. Left: Distribution of the distance between the closest triggered station and the shower core. Right: Distribution of the number of stations that triggered on the same event.

6.6 RADIANT trigger and implications for RNO-G

The trigger threshold has a direct effect on the number of cosmic rays measured, since the threshold determines the accessible energy. The distribution of the trigger efficiency is shown in Figure 6.15. The best trigger efficiency for all energies is when the shower core is within 100 m of the station. A more sensitive threshold will increase the trigger efficiency. However, to get close to 100% trigger efficiency for energies ≥3.16 eV, a trigger threshold of $15\,\sigma_{\text{power int}}$ and a spacing of 400 m is required.

The current estimate from laboratory measurements is about $30\,\sigma_{\text{power int}}$ ($4\,\sigma$), with a detection threshold at 10^{17} eV. With the steeply falling cosmic ray flux, achieving sensitivity in the energy range below 10^{17} eV significantly increases the number of measured events. A higher threshold leads to a reduced number of measured events, but the predictions are still about 3 events per day and seven stations.

The hardware threshold is set in the field by servoing, which adjusts the threshold according to a target scaler that is proportional to the trigger rate. The reason for the limited trigger rate is the limited bandwidth to transfer the data from the DAQ at the station to the hard disk via LTE.

The trigger rate is highly dependent on the current noise. When testing the servoing in the lab, the corresponding trigger thresholds varied between $15\,\sigma_{\text{power int}}$ and $37\,\sigma_{\text{power int}}$. Subsequent analysis indicated that a threshold of $30\,\sigma_{\text{power int}}$ is most likely to result in the desired trigger rate. This corresponds to a threshold of $4\,\sigma$ when analyzing the same events in the full band and as simple amplitude divided by the stand deviation of the noise. However, the servoing is still subject to large uncertainties. In the lab, only the noise from the SURFACE board at room temperature was assumed, but it is possible that other sources of noise from the external signal generator or the climate chamber were present.

The upward-facing LPDAs in the field indicate different noise sources. Several narrowband and broadband backgrounds are known to be associated with air traffic, handheld radios, or (daytime) human activity [149]. Continuous waves should not affect the LPDA's upward trigger rate, since the diode trigger is sensitive to impulsive events. However, trigger rates increase during periods of high wind speed, which may be due to the so-called triboelectric effect, which occurs when metal surfaces on snow get charged and then discharge [196, 198]. In a later analysis the increased threshold has to be taken into account.

Considering the uncertainties of the existing noise and the subsequent threshold setting and servoing, a trigger threshold of $(30\pm10)\,\sigma_{\text{power int}}$ seems reasonable. The optimistic limit of the trigger threshold is about $15\,\sigma_{\text{power int}}$, based on measurements in the lab. However, this is only achieved for short periods of time. To improve the trigger sensitivity, more complex triggers than the simple diode circuit must be considered, which would require digitization before triggering. Several approaches are possible, e.g. using interferometry as in the phased array trigger, a trigger in the frequency domain, or a trigger based on a neural network as presented in [199, 200].

Another way to increase the detected event rate with the present trigger is a denser array. In this simulation set, 87% of the shower cores trigger within 400 m of the shower

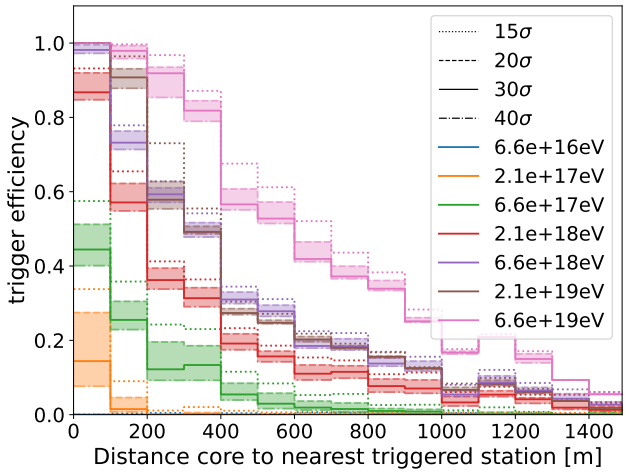

Figure 6.15: Trigger efficiency over distance between core and nearest triggered station. The color code indicate the energy range, with the center of the energy bin stated in the legend. The line style indicate the trigger threshold. The current estimate for RNO-G is 30 $\sigma_{\text{power int}}$, with an uncertainty on the trigger threshold of 10 $\sigma_{\text{power int}}$.

core, and almost all of the showers trigger only one station. The current station spacing of 1.25 km with a diagonal of 1.77 km is therefore not optimal for measuring the cosmic ray flux, which is not surprising since the array layout is optimized to archive the largest possible detection volume for in-ice neutrino events. However, adding additional surface antennas between the stations would reduce the diagonal distance to 880 m, nearly doubling the event rate. A proposal for a denser infill of the RNO-G array is in progress. Simulation studies also suggest that four LPDAs arranged in a square configuration, instead of three antennas in a triangle, increases the detection efficiency at lower energies [201]. The square antenna configuration will be used starting in season 2025.

Finally, given the difficulties in characterizing the trigger due to diode nonlinearity and pulse shape dependence, the uncertain discriminator, and the additional time in data analysis to account for changing threshold settings, the RADIANT trigger is low in power consumption at the cost of additional time in characterization and data analysis. A more advanced trigger is desirable to achieve better cosmic ray sensitivity and background rejection.

6.7 Intermediate conclusion

RNO-G is capable of measuring cosmic rays. The projected event rate is 5^{+5}_{-2} events per day and seven stations, with an energy threshold of 10^{17} eV. The dominant uncertainty is the setting of the trigger threshold, which is determined to be at (30±10) $\sigma_{\text{power int}}$. The $\sigma_{\text{power int}}$ is the standard deviation of the power integrated trace over 11 ns within the trigger frequency band of 80 MHz to 200 MHz which approximated the trigger path. Analyzing the full band and the simple amplitude divided by the standard deviation of the noise, this corresponds to a threshold of 4 σ. The trigger efficiency and therefore the detection efficiency of cosmic rays strongly depends on the energy, the zenith angle of the air shower and the distance between the shower core and the detector station. More

inclined showers cover larger areas, but at the same time their radio emission becomes weaker at a given antenna position. Therefore, inclined showers are only visible above a certain energy while more vertical showers are less likely to be close enough to a station. A trigger efficiency close to 100% is achieved when the shower core is within a distance of 200 m and at energies $\geq$3.16 eV. Therefore a denser array increases the event rate significantly. More air shower simulations in smaller energy intervals and more directions (zenith and azimuth) are necessary to obtain a robust prediction of the trigger threshold.

Modeling the RADIANT trigger and its threshold setting poses some difficulties. In the field the threshold is set according to a scaler target that corresponds to a trigger rate. This has the advantage of avoiding a high data rate, but at the same time it is difficult to model the existing noise and to account for the changing thresholds in an analysis. A comparison of the noise present in the field shows variations between the stations. The analog RADIANT trigger is optimized for low power consumption, with the diode being a passive element. Characterization of the trigger is challenging due to diode nonlinearity, pulse shape dependence, and an uncertain discriminator. More advanced triggers such as interferometry, frequency domain triggers, or neural network triggers are typically based on a digital waveform. The current digitizer requires an external trigger to convert the measured samples, therefore implementing a more complex trigger for the upward facing LPDAs requires further modifications to the RADIANT board.

Increased sensitivity to air shower signals and other signals from above would improve neutrino event identification by rejecting backgrounds. In particular, air shower remnants are a less studied background to which RNO-G is sensitive as one of the first experiments. These include geomagnetic emission propagating into the ice, dense air shower cores developing further into the ice and producing Askaryan emission, and in-ice particle cascades induced by an ultra-high energy muon originating from an air shower. The latter will be discussed in Chapter 7.

7 Atmospheric muons

Parts of this chapter have been published in:

L. Pyras, C. Glaser, S. Hallmann and A. Nelles: "Atmospheric muons at PeV energies in radio neutrino detectors", JCAP, vol. 10, p. 043, 2023, DOI:10.1088/1475-7516/2023/10/043

As neutrino detectors in ice will be the first ones to achieve sufficient sensitivity to the low fluxes of ultra-high energy neutrinos they will be also exposed to rare backgrounds. One of these are ultra-high energy muons from cosmic ray air showers that penetrate the ice. Like neutrinos, they can induce particle cascades in the ice that create emission which can be detected by a radio array [109]. The event rate depends on the atmospheric muon flux, which in turn depends strongly on the hadronic interaction models and the cosmic ray composition, all of which are not well-constrained at the highest energies. A study of the atmospheric muon flux and the expected event rate in RNO-G type detectors is presented below.

7.1 Predictions of muons at PeV energies and beyond

Atmospheric muons are produced in extensive air showers, which occur when high-energy cosmic rays penetrate the Earth's atmosphere. The cosmic ray nucleon interacts with an air nucleus and produces short-lived intermediate particles, mostly pions (the lightest known meson) and a few heavier particles with shorter lifetimes, such as kaons, D-mesons, etc. (see Section 3.1.1 for a detailed description of the particle cascade development). Their decay gives rise to an atmospheric lepton flux, including muons. The energy range in which atmospheric muons can be detected with radio neutrino experiments is limited by the minimum muon energy that is required to produce an in-ice particle cascade with a measurable radio signal (around 10 PeV). At these energies, the flux of parent cosmic rays is low, resulting in a very small muon flux. Nevertheless, this muon rate is likely to be comparable to the expected neutrino rate at these energies, making radio neutrino detectors the first experiments where atmospheric muons of EeV energies become relevant. While the much-discussed *Muon Puzzle* [202] describes a discrepancy between predicted and observed muon production in air showers for muons with energies around 1 GeV (more muons are measured than predicted by Monte Carlo simulations), the situation is different for muons above PeV energy: these muons are typically produced within the first three interactions of an air shower, rather than continuously throughout the shower development [103]. The energy of a parent particle is distributed among its children, resulting in lower energy particles with each subsequent interaction in the cascade. Consequently, one has to concentrate on the highest energy interactions to study the relevant muon background. Unfortunately, these interactions are far outside of the energy regime currently observable at accelerators, which makes far-reaching extrapolations necessary.

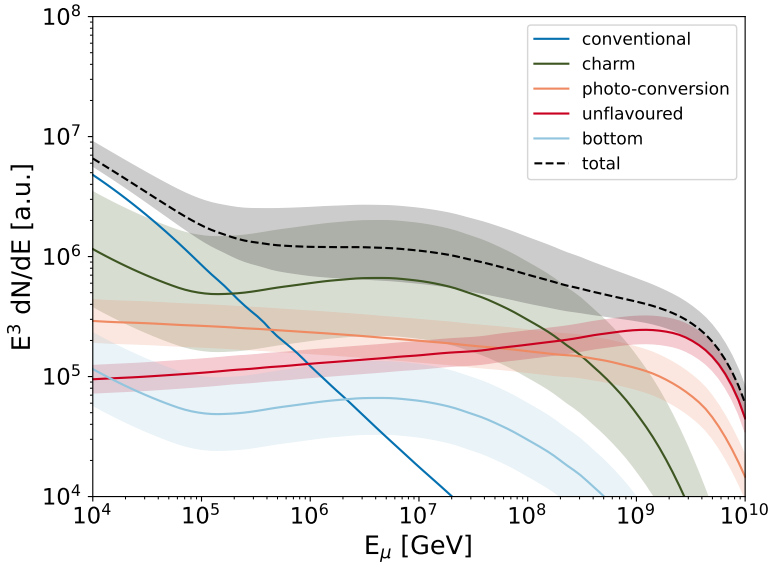

Figure 7.1: Contributions to the muon count stemming from a $10^{10.5}$ GeV proton induced vertical air shower according to [203]. The bottom contribution is assumed to be 10% of the charm contribution [204]. The photo-conversion includes muons from $\gamma \to \mu\mu$ and from $\gamma \to \rho, J/\Psi \to \mu\mu$. The uncertainties are a conservative estimate (constant factor in energy), taking into account experimental limitations and comparison between different event generators, they are meant rather as illustration of the current state of the field than as firm estimate, compare [205–208].

7.1.1 Muon production in air showers

Atmospheric muons are produced in the hadronic cascade of an air shower mainly through the decay of short-lived mesons, namely charged pions and kaons (*conventional component*) [209]. At very high energies the Lorentz time dilatation increases the decay length of pions and kaons to a multiple of their interaction length (ℓ_{int}) in air, making it more likely that they will interact and lose energy before they can decay. The contribution of particles with a shorter lifetime τ then becomes dominant as shown in Figure 7.1. Due to their almost immediate decay the contribution of short-lived hadrons with $c\tau \ll \ell_{\text{int}}$ is called *prompt flux* and dominates above 10^6 GeV. Charmed hadrons (with $D^0, D^+, D_s^+, \Lambda_c^+, \Omega_c^0$ and their antiparticles) have large (~10%) branching ratios into semi-leptonic modes and a lifetime $\tau \sim 10^{-12}$ s, implying a prompt decay with a probability of order 1 up to energies around 10^7 GeV [208]. In principle, also bottom hadrons ($B^0, B^+, B_s^+, B_c^+, \Lambda_b^0, \Xi_b^0, \Xi_b^+$), which have similar lifetimes and semi-leptonic decays, contribute to the prompt muon flux. B-mesons are less frequently produced by cosmic rays in the atmosphere, but their decay length is smaller, yielding a contribution to the 10^7 GeV muon flux which is 10% of the one from charm hadron decays [204]. Additional significant contributions are: unflavored mesons ($\eta, \eta', \rho^0, \omega, \phi$) [204], photo-conversion into a muon pair ($\gamma Z \to \mu^+\mu^- Z$) e.g. Bethe-Heitler process, Drell-Yan processes [204] and photon conversion into a vector meson decaying into muons. These dominate the muon flux above $\sim 3 \times 10^8$ GeV [203, 210]. A sketch of the contributions according to [203] is shown in Figure 7.1. The uncertainties are a rough estimate considering experimental limitations and differences between event generators [206–208, 211].

Taking into account these different sources, the atmospheric muon flux can then be expressed as the sum of five components:

$$\phi_\mu(E,\theta) = \phi_\mu^{\text{conv}}(E,\theta) + \phi_\mu^{\text{charm}}(E,\theta) + \phi_\mu^{\text{unflav}}(E,\theta) + \phi_\mu^{\gamma}(E,\theta) + \phi_\mu^{\text{bottom}}(E,\theta). \tag{7.1}$$

The high energy muon flux is mainly driven by the outcome of the first interaction of an air shower. The relativistic hadron-ion collisions under low momentum transfer are in the non-perturbative regime of quantum chromodynamics (QCD) [202, 212], where hadron production cannot be calculated directly from first principles. Instead, effective theories and phenomenology are used. An explicit prediction of the muon flux from perturbative QCD (pQCD) is not present, but judging by the variation in different first-principle pQCD calculations predictions for the muon neutrino flux [205, 206, 213–217] there is a sizable uncertainty. To simulate the hadron production, different (phenomenological) hadronic interaction models are used. In air shower simulations, hadronic interactions are the largest source of uncertainties, because the center-of-mass energy in the first interactions significantly exceeds the maximum energy studied at the LHC and interactions in the forward direction, i.e. high pseudorapidities are not well covered [209, 218]. When extrapolating to higher energies, the model predictions thus diverge even further, also with respect to the pQCD calculations. A detailed discussion of post-LHC hadronic interaction models follows in Section 7.1.3.

Next to the particle physics processes in the air shower, the atmospheric muon flux is determined by the cosmic ray composition. The type of the primary particle entering the atmosphere and its number of nucleons has an influence on the number of muons produced. The muon number grows less-than-linear with the primary energy of an air shower [103]. This is a consequence of the energy fraction f given to charged pions in each interaction $f \sim (2/3)^n$, after n generations (see also Section 3.1.1). For nuclear primaries, a nucleus with atomic number A can be treated as the sum of A separate proton air showers all starting at the same point, each with $1/A$ of the primary energy [103]. The lower energy nucleons which initiate the shower generate fewer interaction generations, and so lose less energy to electromagnetic components [103]. Therefore the number of muons is larger for heavy primaries than for showers initiated by light nuclei of the same energy. For very high-energy muons, which are created within the first interactions, this picture changes: since a proton contains the kinetic energy in one nucleon, it can produce higher energy particles than an iron primary with the same energy. Therefore, a $3{\times}10^{10}$ GeV proton shower can produce muons up to 10^{10} GeV, while an iron-induced shower with the same energy and arrival direction only produces muons up to 2×10^8 GeV [203], as shown in Figure 7.2.

7.1.2 Muon flux simulations

The atmospheric muon flux is calculated using Matrix Cascade Equations (MCEq) [207], which describe the evolution of particle densities as they propagate through the atmosphere, using the CORSIKA parametrizations [105] as atmospheric model. The 1-dimensional cascade equations neglect the lateral versus the longitudinal development of the shower, which is important at lower energies, where the transverse momentum of the particles may be relatively important and imply a larger lateral displacement. Since this study focuses on energies > 1 PeV this seems an acceptable limitation. Compared to computational extensive Monte Carlo codes like AIRES [219] and CORSIKA [105], MCEq

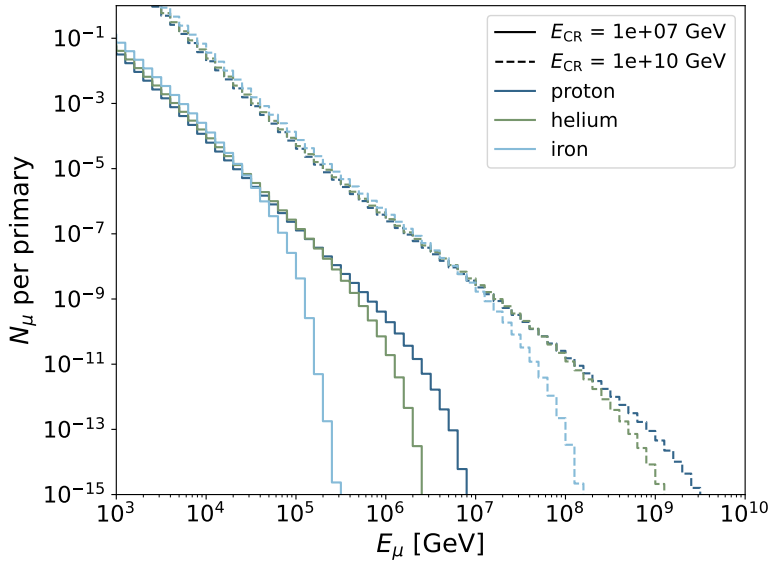

Figure 7.2: Number of muons for air showers with different primaries (proton, helium, and iron) and energies (10^7 GeV and 10^{10} GeV) with 60° zenith arrival direction at 3200 m (Summit Station, Greenland). Calculations were performed with SIBYLL-2.3C.

provides a way to estimate the relative importance of a given parameter, for which accurate studies with full shower simulations would require very large statistics.

7.1.3 Dependence on hadronic interaction models

Several theoretical approximations describing particle production are available for different energy ranges and kinematic regimes. Different approaches have to be combined to model all hadronic interactions in air showers. For this study, the post-LHC hadronic interaction models EPOS-LHC [220], QGSJET-II.04 [221], and SIBYLL-2.3C [222] are considered. While EPOS-LHC has a more general focus on minimum-bias proton-proton and heavy ion collisions, the latter two are focused on air shower simulation.

A theoretical prediction of the muon flux above PeV energies should include at least four components (see 7.1), which are, however, not all taken into account in the same way in the hadronic interaction models. While the *conventional* flux is implemented in all models considered, only SIBYLL-2.3C includes *charm* production (D^+, D^0, D_s, Λ_c) through a parametrization; forward charm production is intrinsically included in the nucleon parton distribution function (PDF) [202]. SIBYLL-2.3C also includes muons from *unflavored mesons* and J/Ψ. EPOS-LHC does not include charm, its prompt component arises from the decay of unflavored mesons. QGSJET-II.04 only considers η decay as a production channel for prompt muons [223]. The calculated muon fluxes, therefore, start to vary widely at 1 PeV where the prompt flux dominates, see Figure 7.3 left. EPOS-LHC and QGSJET-II.04 yield the lowest muon flux because they neglect the charm component and in the latter case most unflavored mesons. The *photo-production of muon pairs* that becomes relevant at PeV energies is not implemented in any model [224]. Given that only SIBYLL-2.3C includes charm and unflavored mesons, it is currently the most complete model to predict the muon flux above PeV energies. However, even SIBYLL-2.3C

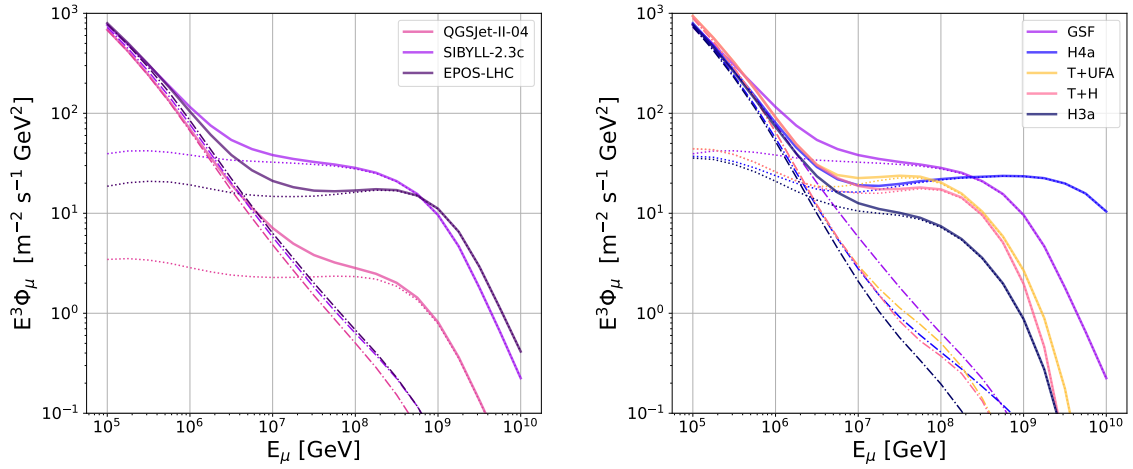

Figure 7.3: Simulated muon flux as function of muon energy for different hadronic interaction models (left) and cosmic ray composition models (right). Shown are the predictions for QGSJET-II.04 [221], SIBYLL-2.3C [222], and EPOS-LHC [220] for the Global Spline Fit (GSF) [225] cosmic ray composition. Dashed lines represent the prompt muon flux and dash-dotted is conventional muon flux. The right shows different cosmic ray composition models using SIBYLL-2.3C: GSF [225], HillasGaisser (H4a) [226], T+UFA, [227, 228], T+H [227, 229] and HillasGaisser (H3a) [226].

still under-predicts the flux of muons at the highest energies due to missing production channels from photo-conversion and B-mesons, which should be addressed in future theoretical work. Given our current understanding, these components only become dominant above 3×10^8 GeV, so they should be a minor contribution to the background in radio detectors. The main theoretical uncertainties arise from charm cross-section calculations. The theoretical calculations are limited by the uncertainties in the scale, charm mass, and the nuclear PDF [202]. A non-perturbative intrinsic charm component may also contribute [206].

This short overview illustrates the difficulty of predictions beyond LHC energies. On the one hand, theoretical uncertainties are present due to the non-availability of measurements, and on the other hand, known processes have not been implemented in all codes, since the priorities have been weighted differently for existing hadronic interaction models. Therefore, the spread between the three hadronic interaction models is used as indication of the current uncertainties, while keeping in mind that they do not provide the full range of possible systematic uncertainties at this point.

7.1.4 Dependence on cosmic ray composition

The cosmic ray spectrum covers several decades of energy up to 10^{11} GeV, including particles from galactic and extra-galactic origin. Just below the so-called ankle at 8×10^9 GeV, the transition region from galactic to extra-galactic cosmic rays is expected [230, 231], with detailed explanations still varying.

Measurements of the cosmic ray composition above a few 10^5 GeV suffer from the uncertainties in the hadronic interaction models, since the composition has to be inferred from shower parameters such as the position of the shower maximum X_{max}, which provides composition models with much room for interpretation. Since the ultra-high energy muon flux directly depends on the cosmic ray composition, different models have been

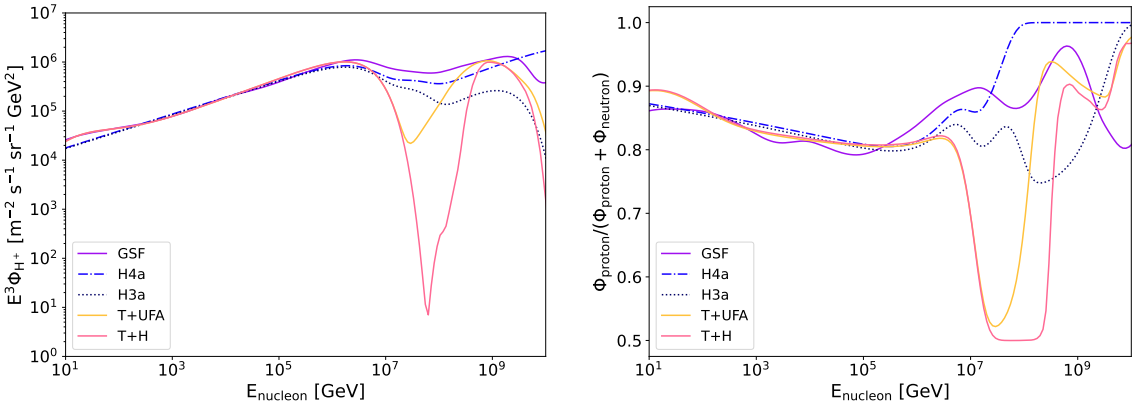

Figure 7.4: Contribution of protons in terms of nucleon energy for the same composition models as in Figure 7.3 and indicated in the label. Left: Absolute hydrogen (proton) flux, where the nucleon energy equals the particle energy. Right: Evaluating all types of nuclei, shown is the fraction of protons relative to neutrons; The nucleon energy is 1/A of the particle energy, with A being the atomic number of the particle.

investigated to study the uncertainty stemming from this aspect. The combination of different models allows to study the influence of galactic and extra-galactic components. This is done to show the spread in models, rather than choosing one over the other for correctness.

The well-known Hillas Gaisser models are theoretical simplifications for extreme scenarios: a heavy composition after the ankle (H3a) [226] and a proton-rich composition (H4a) [226]. This is contrasted by the Global Spline Fit (GSF) [225], a data-driven parameterization that considers measurements of more than ten experiments and provides uncertainties at each energy. GSF is agnostic to theoretical models explaining the derived composition in terms of sources and propagation.

Thoudam et al. [227] published different theory-driven cosmic ray spectra up to EeV energies. In the following, their prediction for cosmic rays stemming from Supernova remnants (SNR-CR) and Wolf-Rayet stars (WR-CR) is used as a galactic component, labeled *T*, and are combined with different extra-galactic components.

The model by Unger, Farrar and Anchordoqui (UFA) [228] predicts a strong pure-proton component concentrated at only about one order of magnitude in energy below the ankle. For our combination into the T+UFA model the results are optimized for a pure nitrogen galactic composition, which matches the predicted composition for WR-CR [227].

The extra-galactic component of Heinze et al. [229] is based on a framework in which an ensemble of generalized ultra-high energy cosmic ray accelerators is characterized by an universal spectral index (equal for all injection species), a maximal rigidity, and the normalizations for five nuclear element groups. The source evolution is included as an additional free parameter. This allows for a parameter scan with a best fit result. The composition used in this study is obtained by a fit to the Auger data from 2019. The resulting muon flux is shown in Figure 7.3 for Sibyll-2.3c as hadronic interaction model.

As discussed in Section 7.1.1, the relevant quantity to produce high-energy muons from different primaries is the energy per nucleon. For hydrogen as a primary (with $A = 1$) the nucleon energy is equal to the primary energy, for heavier elements the energy scales

with $1/A$ where A is the atomic number. On the left-hand side of Figure 7.4 the proton flux for the chosen models is shown, while on the right-hand side the proton fraction taking into account all nuclei, relative to their neutron number is shown. For a pure proton flux, the fraction would be 1, given that hydrogen consists only of one proton and one electron. For pure iron (with 26 protons and 30 neutrons), the fraction would be ~0.46. The models start to deviate at 10^7 GeV, close to the transition region from galactic cosmic rays to extra-galactic cosmic rays. Here, the theory-based models (T+UFA, T+H) have a dip in the proton flux. The proton fraction of the GSF flux only decreases in the transition region to a fraction of 0.9 and is significantly higher than the theoretical models (around 0.5). The GSF model therefore also predicts the highest muon flux, with the exception of the proton-only scenario at energies $>3 \times 10^{17}$ eV. Therefore, GSF will mainly be used to estimate the muon numbers going forward to remain conservative, keeping in mind that it is just one realization of the uncertainty stemming from the cosmic ray composition.

7.2 Signatures of muons in radio instruments

When a muon travels through the ice it initiates showers along its track. At PeV energies and above, the relevant shower production mechanisms are hard bremsstrahlung and pair creation events, referred to as catastrophic energy losses. As a rule of thumb, the energy of the parent particle inducing the cosmic ray air shower is roughly one decade higher than the subsequent muon. The in-ice particle cascade on the other hand typically has a shower energy one decade lower than the initiating muon. The in-ice shower energy is the important quantity for the radio emission and hence the one which determines if a muon triggers the in-ice radio detector. The Monte Carlo framework NuRadioMC [110] with its extension to simulate secondary interactions [109, 232] is used to simulate the muon interaction in-ice, the subsequent Askaryan radio emission, the propagation of the radio signal to the detector, and finally the detector response to the electric field. In order to also track secondary losses of all types of leptons, the lepton propagation code PROPOSAL [233] has been included in NuRadioMC and is used for our simulations.

The dependence on the instrument details (Section 7.2.1), on the muon flux itself (Section 7.2.2), as well as strategies to mitigate this muon background for neutrino detection (Section 7.3.1) are studied.

A detector array of 35 stations is simulated, which is similar to the Radio Neutrino Observatory Greenland (RNO-G). Each station is comprised of a dipole antenna (Vpol) located at a depth of 100 m in the ice (*deep component*), and three log-periodic dipole antennas (LPDA) pointing straight down located at the surface (*shallow component*). The stations are arranged in a square grid with a spacing of 1.25 km.

Simulations are performed for several triggers to study the dependence on instrument details. The assumed noise temperature is 300 K, in both deep and shallow component. At a depth of 100 m signal-only trigger with a simple threshold of $1.5\sigma_{\text{noise}}$ and $2.5\sigma_{\text{noise}}$ in the band of 96 MHz to 220 MHz is evaluated. For the shallow component a high-low threshold trigger of $2.5\sigma_{\text{noise}}$ and a two-out-of-three coincidence in the band of 80 MHz

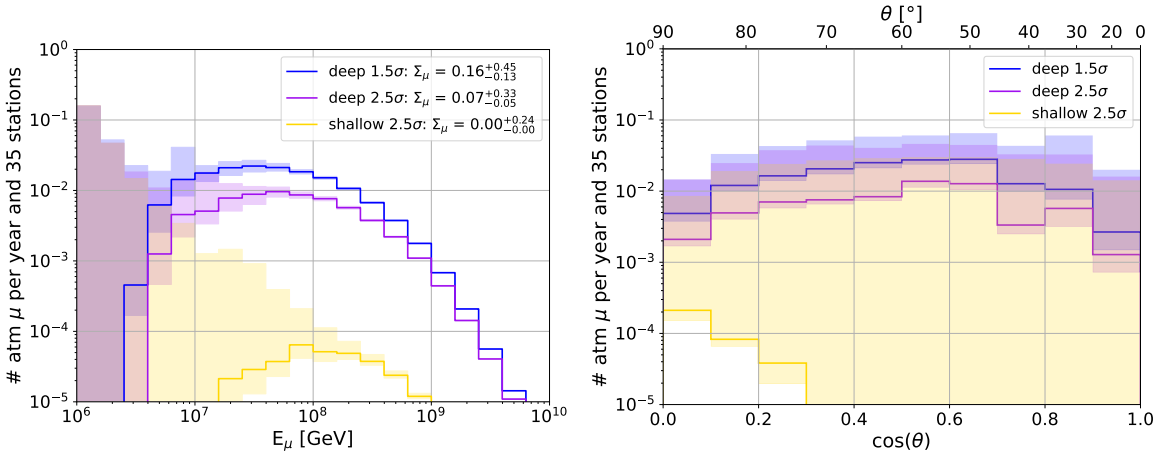

Figure 7.5: Number of triggered muons in one year and an array of 35 stations. The Σ_μ denotes the sum over all bins shown. The color code indicates the trigger and its setting. Blue is a deep simple threshold trigger at 100 m with a 1.5σ threshold, violet is a 2.5σ simple threshold trigger. Yellow is a high-low threshold 2.5σ trigger with a two-out-of-three coincidence just below the surface (2 m). The assumed flux is calculated with Sibyll-2.3c and GSF as cosmic ray composition model. The shaded region indicates the 68% CL derived from the effective area calculations of the detector. Left depicts the distribution for different energies, right for different zenith arrival directions.

to 180 MHz is applied. The triggers for the deep component are a simplification of the phased array trigger that is the current state of the art in radio neutrino detection [132]. Simulating a true phased array using a fixed trigger rate would be the best approximation of a real instrument, as done in e.g. [92]. To save computing time, a simplified trigger of a single dipole is used. While the 2.5σ case is likely close to the current implementation for RNO-G [234], a 1.5σ trigger is used as a proxy for potential future optimizations. A true phased array implementation will likely affect the absolute event numbers (e.g. [109]), but should not affect the relative scaling of different effects. The shallow trigger represents an optimistic performance of the current RNO-G trigger.

In order to express the detector performance, the effective area is calculated. This is done by simulating muon interactions within an ice volume containing the detector array, the initial muon position is on the air-ice planar interface. Since only the projection of the detector is perpendicular to the direction of the flux, the simulated area has to be corrected with $\cos(\theta)$. The effective area (A_{eff}) is the projected surface area multiplied with the trigger efficiency:

$$A_{\text{eff}} = A_{\text{proj}} \cdot \frac{N_{\text{trig}}}{N_{\text{sim}}} = A_{\text{sim}} \cdot \cos(\theta) \cdot \frac{N_{\text{trig}}}{N_{\text{sim}}}. \tag{7.2}$$

The expected event rate is obtained combining the effective area with an incident muon flux integrated over energy and the solid angle element of the flux, which in spherical coordinates yields an additional factor of $\sin(\theta)$:

$$\Gamma_\mu(E,\theta) = \int_{t_1}^{t_2}\int_{E_1}^{E_2}\int_{0}^{2\pi}\int_{\theta_1}^{\theta_2} \Phi_\mu(E,\theta,\phi) \cdot A_{\text{eff}}(E,\theta) \cdot \cos(\theta) \cdot \sin(\theta) d\theta d\phi dE dt. \tag{7.3}$$

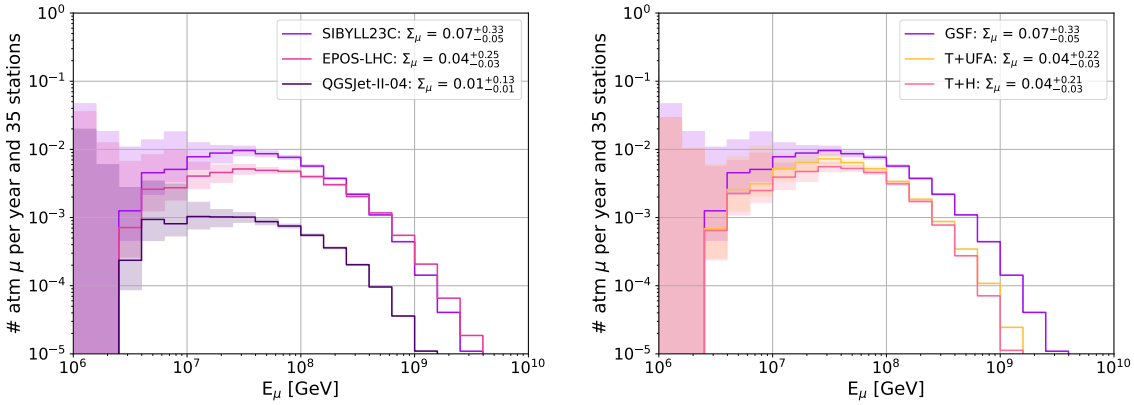

Figure 7.6: Number of triggered muons per year and an array of 35 stations with a $2.5\sigma_{\text{noise}}$ trigger in deep component. Left: for three different hadronic interaction models [220–222] and GSF as cosmic ray composition model. Right: For selected cosmic ray compositions of Figure 7.3 as indicated in the label [225, 227–229] and Sibyll-2.3c as hadronic interaction model.

7.2.1 Dependence on instrumental details

As shown in Figure 7.5, the shallow antennas detect the fewest muons. This is expected, as the LPDAs also have a comparatively smaller neutrino effective volume, due to their location close to the surface. As a consequence of the ice profile, in which the index of refraction increases with depth, signals propagate less often to the surface, but are bent instead towards the denser ice. The shallow LPDAs detect mostly horizontal muons above 65° zenith angle, because of the geometry constraint by the Cherenkov cone, while the deep antennas have a broad detection range with a peak around 55° zenith angle. A lower detection threshold increases the number of muons from 0.07 per year and 35 stations to 0.16 per year and 35 stations. The higher muon yield can mostly be attributed to muons in the range of 10^7 GeV to 10^8 GeV. The uncertainties shown in Figure 7.5 are statistical uncertainties only based on the Feldman Cousins confidence belts [235], which provide upper limits for null results and two-sided confidence intervals for non-null results, which converge to a Poisson error. At lower energies, only a few geometries allow the antenna to register a signal, hence the statistics are small, and uncertainties increase due to the comparatively high muon flux at low energy. Most events (97%) are only seen in one station, regardless of the trigger configuration.

7.2.2 Dependence on hadronic interaction models and cosmic ray composition

The differences in the flux predictions due to the hadronic interaction models propagate almost directly into the muon rate of an in-ice radio detector. Figure 7.6 left shows the number of muons predicted for three different hadronic interaction models per year and 35 stations and the same cosmic ray composition. As discussed in Section 7.1.3, Sibyll-2.3c includes the most production mechanisms, which explains the larger flux. In Figure 7.6 right, the expected muon rate for the same hadronic interaction model, but for three different cosmic ray compositions are shown. The GSF model yields the highest muon rate with a maximum between 10^7 GeV to 10^8 GeV muon energy, which is expected due to the higher proton content.

7.3 Relation to parent air shower

While the projected number of muons is relatively small, muons can still pose a problem if the neutrino rate is comparatively low. One possibility to distinguish between an atmospheric muon and a neutrino is to detect the air shower from which the muon originates. This would identify the muon and provide a veto mechanism on muon events, as also discussed in [108].

7.3.1 Detectability of the parent air shower

To calculate the veto efficiency, it is essential to have information about the energy and arrival direction of the air shower, as well as the distance to the nearest detector station. As high-energy muons are boosted along the air shower's axis, the cosmic ray arrival direction can assumed to be the same as the muon arrival direction. The location of the air shower core can be determined by projecting the muon vertex position along the arrival direction until it intersects the boundary between the ice and air.

To establish a relationship between a muon and the corresponding cosmic ray energy, Bayes' theorem can be applied. By solving the Matrix Cascade Equation with Sibyll-2.3c as hadronic interaction model for different types of primary cosmic rays (pr) - namely proton, helium, carbon, and iron - and over a range of cosmic ray energies (10 bins between 10^6 GeV to 10^{11} GeV) the muon flux at ground-level can be calculated. Once the muon flux for a specific cosmic ray induced shower is known, it has to be folded with the actual flux of the primary to obtain the muon flux for all cosmic rays. Here, the number of the different primaries is drawn from the GSF cosmic ray spectrum. The probability to produce a muon with a certain energy given a cosmic ray energy $p(E_{\mathrm{CR}}|E_\mu)$ is calculated by

$$p(E_{\mathrm{CR}}|E_\mu) = \frac{\sum_{\mathrm{pr}} N_\mu(E_{\mathrm{CR}}, E_\mu, \theta, \mathrm{pr}) \cdot N_{\mathrm{CR}}(E_{\mathrm{CR}}, \theta, \mathrm{pr})}{\sum_{E_{\mathrm{CR}}} \sum_{\mathrm{pr}} N_\mu(E_{\mathrm{CR}}, E_\mu, \theta, \mathrm{pr}) \cdot N_{\mathrm{CR}}(E_{\mathrm{CR}}, \theta, \mathrm{pr})}. \tag{7.4}$$

The number of muons N_μ is calculated for each shower, therefore it has to be summed over all possible primaries, pr. The number of cosmic rays N_{CR} is calculated from the cosmic ray flux and also needs to be summed over all primaries. This sum is normalized by summing over all possible cosmic ray energies the muon can stem from. The distribution for different muon energies stemming from a cosmic ray with a certain energy is shown in Figure 7.7 for Sibyll-2.3c and GSF. The plot shows, that a muon with a given energy can stem from a variety of cosmic ray energies, most likely from a cosmic ray with an energy $\sim 10\times$ higher than the muon energy. Since few cosmic rays have been measured above 10^{11} GeV the predictions for the rate are very uncertain. Correspondingly the shape of the highest energy muon distributions vary significantly between flux models. Muons with $E_\mu = 3 \times 10^8$ GeV (dark blue) most likely originate from proton and helium induced showers. Their probability distribution features a second peak around 2×10^{10} GeV, which is likely associated to the cosmic ray spectrum. The GSF model provides a steep falling proton flux around 1×10^{10} GeV and a rising helium flux with a peak around 2×10^{10} GeV. The relation between muon and cosmic ray energy depends on the choice of hadronic interaction model and cosmic ray composition.

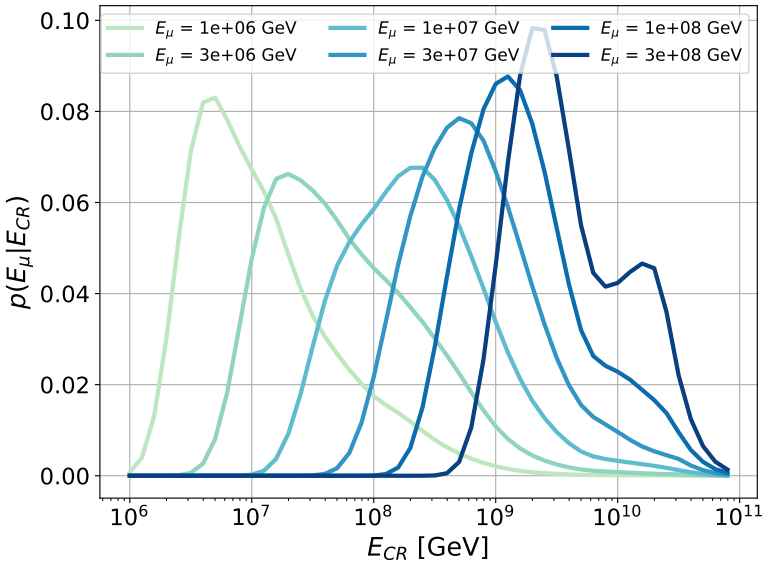

Figure 7.7: Distribution of the probability for a muon with a given energy (color code) to stem from a cosmic ray as a function of the cosmic ray energy. The x-axis indicates the energy of the inducing cosmic ray, the y-axis shows the probability that a muon with the energy indicated in the label originates from a certain cosmic ray. The relation was obtained using Sibyll-2.3c as hadronic interaction model and GSF as cosmic ray composition. While differing in detailed shape, other combinations of hadronic interaction models and cosmic ray composition provide qualitatively similar distributions.

To calculate the veto efficiency in a RNO-G like array, for each muon event, an air shower is selected according to muon arrival direction and placed inside the array as previously described. The resulting radio signal is simulated with CORSIKA [105] and the radio extension CoREAS [175] and then folded with the detector response using NuRadioReco [187]. Since the amplitude of the air shower signal scales linearly with the cosmic ray energy [236] it can now be calculated, which air shower energy is necessary to exceed a simple $2.5\sigma_{\text{noise}}$ trigger threshold in an upward-pointing shallow LPDA antenna and hence veto the muon event. In the last step, the probability that a muon event stems from an air shower with an energy higher than the trigger threshold energy is calculated and assigned to that muon. Combined with the predicted muon flux, the number of muons that can be vetoed by detecting the parent cosmic ray can be calculated. Figure 7.8 shows a veto efficiency close to 100% for muon energies > 10^9 GeV. Muons originating from inclined air showers are more likely to be vetoed since the radio signal covers a larger area but becomes fainter at the same time. Therefore the veto efficiency increases with higher zenith angles only for higher energies.

In Figure 7.9, the event rate is shown for different trigger threshold for the cosmic ray veto. A lower threshold improve the veto, especially at the highest energies. Those event with a cosmic ray energy around 10^{11} GeV are, however, very rare. To improve the veto efficiency, a denser array of antennas would be needed. However, such an in-fill array would have to have a spacing of $\mathcal{O}(100)$m, making it too dense to be feasibly installed.

To get a better understanding of the event geometries the station multiplicity and the relation of cosmic ray trigger to muon trigger have been investigated. Figure 7.10 left shows, that almost all deep muons trigger only one station. This is expected, as the station spacing of 1.25 km has been optimized to cover the largest possible volume, rather

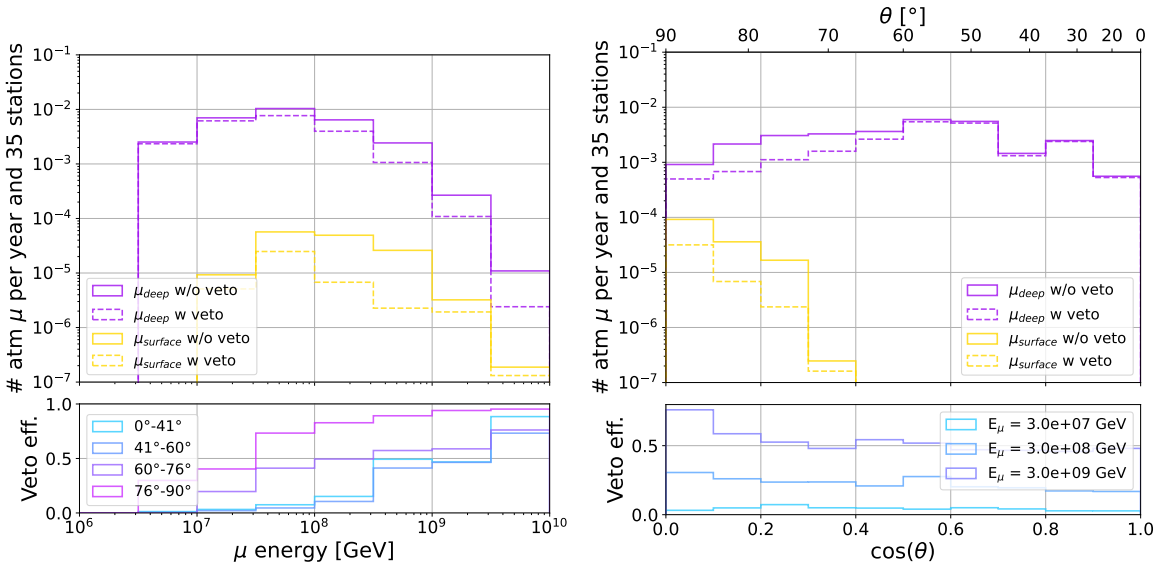

Figure 7.8: Number of triggered muons per year and an array of 35 stations for the GSF cosmic and Sibyll-2.3c as hadronic interaction model. The trigger threshold is at $2.5\sigma_{\text{noise}}$ in the deep (purple) and the shallow (yellow) trigger. The solid line shows the trigger muon without veto, the dashed line shows the muon number when a muon event is vetoed by the parent air shower. The air shower radio signal has to exceed a simple $2.5\sigma_{\text{noise}}$ trigger threshold without coincidence in the shallow antennas to count as a veto. Left: with respect to the muon energy, right, with respect to the zenith arrival direction. The two lower plots show the veto efficiency for events that triggered the deep component for different zenith bands (left) and energies (right).

then focus on multiple triggers. Most air showers do not trigger in the vicinity of the muon trigger (85%), but have to self-trigger another station, see Figure 7.10 right. This is especially true for inclined air showers, where the muon can travel up to 4 km in the ice before inducing a visible radio signal. For ~10% of the deep muon events, the cosmic ray triggers the same station, which would allow for a sub-threshold search. This behavior is similar for all triggers, since the detection location is determined mostly three factors: the travel distance of the muon, before it induces an visible shower (I), the Cherenkov cone (II), where the radio signal is strongest and therefore measurable (opening angle of 56°). Plus, the radio signal gets bend down while propagation through the ice. This is a consequence of the changing refractive index (III). Therefore, most events who have muon and cosmic ray trigger in the same station arrive at a zenith angle of $\theta \approx 50°$.

7.3.2 Timing of air shower and muon

While the muon and the air shower stem from the same cosmic ray, the signal arrival time at the detector and subsequently at the data acquisition unit (DAQ) differs. The air shower propagates through the atmosphere with a zenith angle θ. The position where the air shower axis intersects with the ice surface is called core position, with $t = 0$. Here, the radio emission from the air shower is assumed to be a plane wave at the shower front, traveling the distance from the axis to the shallow antenna according to its arrival direction θ and the velocity of light in air, see 7.5. The muon travels along the arrival direction of the air shower and continues into the ice until it creates a shower. From there the radio emission propagates through the ice on a bent path to the antennas. Once received by a deep antenna, the signal travels along the cable to the DAQ at the surface, see 7.6. The time difference as registered in the DAQ of the radio signal stemming directly from

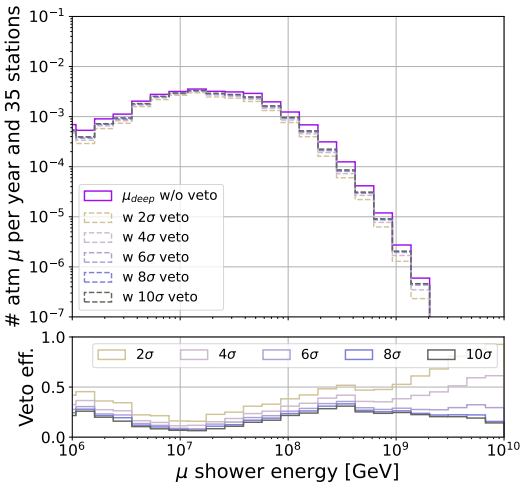

Figure 7.9: Cosmic ray veto for muon events using Sibyll-2.3c as hadronic interaction model and GSF as cosmic ray composition. Expected event rate for all muon events (solid line) and muons without measured air shower (dashed). The color code indicates the different trigger threshold for the cosmic ray veto. The lower panel shows the veto efficiency.

the air shower and the subsequent muon is the difference of $t_{\mu\to\text{DAQ}}$ and $t_{\text{CR}\to\text{DAQ}}$ with the following definitions:

$$t_{\text{CR}\to\text{DAQ}} = d_{\text{core}\to\text{shallow ant}} \cdot \cos(\theta) \cdot \frac{1}{c_{\text{air}}} + t_{\text{cable delay shallow}} \tag{7.5}$$

$$t_{\mu\to\text{DAQ}} = d_{\text{core}\to\text{vertex}} \cdot \frac{1}{c_{\text{vac}}} + t_{\text{ice propagation deep ant}} + t_{\text{cable delay deep}}. \tag{7.6}$$

The cable delay for 100 m coaxial cable is ~500 ns, with $c_{\text{coax}} = 2/3c$. The cable from the shallow antennas is typically 10 m, which provides a lower bound of the time difference at ~450 ns. The full distribution is shown in Figure 7.11. The muon can travel up to 4 km in the ice which increases the possible travel time up to several microseconds, moreover the propagation velocity in ice is slower than in air according to the refractive index. Any air shower veto would need to take this travel time into account, by either allowing for read-out with no trigger dead-time (i.e. double-buffering) or sufficiently long record lengths. Self-triggering on the air shower is challenging due to the potentially small signals and the resulting high trigger rate. A longer record length would allow a post-processing search, which simplifies background identification, however, its implementation into a low-power DAQ system is not easily possible.

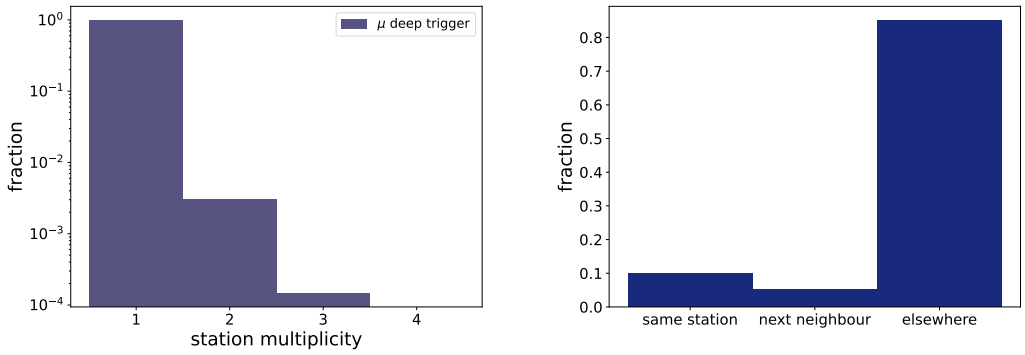

Figure 7.10: Event geometry inside the array. Right: Fraction of the muon events where the deep trigger triggers one, two or three different stations of the array. Left: Relation of cosmic ray triggered station to deep muon triggered station. For ~10% of the muon event the cosmic ray trigger occurs in the same station as the deep muon trigger, in ~5% of the cases the cosmic ray trigger occurs in the nearest neighboring station, the rest of the cosmic rays is expected to trigger elsewhere in the array.

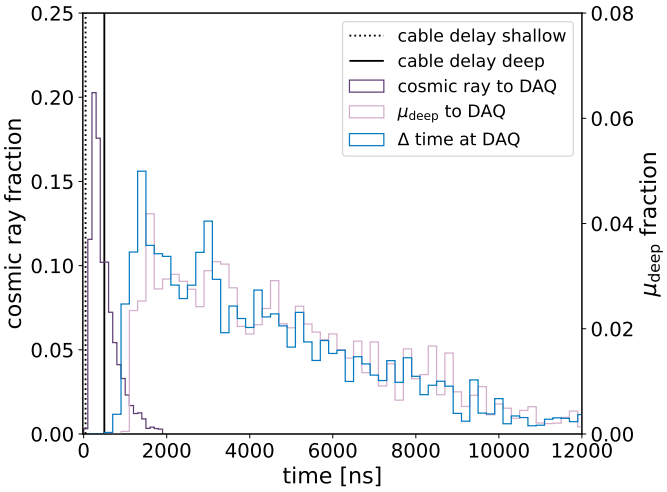

Figure 7.11: Travel time distributions for cosmic ray signals (dark purple) and muon events (light purple) traveling from the air shower core position at the ice/air interface to the data acquisition unit (DAQ) of the detector. The blue line shows the absolute time difference as registered in the DAQ of an air shower signal and the subsequent muon signal. The dotted line is the shallow cable delay relevant for cosmic rays, the solid line indicated the cable delay for muon signals, assuming 100 m coaxial cable.

7.4 Consequences for experiments

After having studied dependencies of the muon flux predictions on hadronic interaction models, composition, and instrumental details to set the stage of the uncertainties in the flux predictions, experimental consequences and mitigation strategies can be discussed.

It will investigated whether neutrino and muon flux predictions can be treated as independent (Section 7.4.1), whether neutrinos and muons can be distinguished based on their experimental signature in terms of expected rates, energy or zenith distribution (Section 7.4.2), and whether radio detectors can be used to measure the prompt muon flux at 100 PeV energies and above (Section 7.4.3).

7.4.1 Possible connection between muon flux and neutrino flux

In Section 7.1.4, it was established that the muon flux strongly depends on the cosmic ray composition at Earth, specifically the proton fraction, which is in turn related to the cosmic ray composition at the sources. The production of cosmogenic neutrinos is also influenced by the cosmic ray composition, as ultra-high energy cosmic rays interact with the cosmic microwave background and the extra-galactic background light [72]. Moreover, the proton component plays a significant role in the generation of neutrinos, since protons produce more neutrinos than heavier nuclei when propagating through the Universe [237, 238]. This raises the question whether background and signal can be treated as independent from each other.

In the following analysis, different cosmic ray compositions consistent with the Auger published data from 2019 are assumed and evaluate the resulting neutrino and muon events for an in-ice radio neutrino detector. The galactic component by Thoudam (denoted T) is combined with three extra-galactic components by Heinze et al. [229]: the best fit ($H_{\text{best fit}}$) with a maximal rigidity R = 1.58×10^9 GeV, a source evolution parameter m = 4.0, and spectral index γ = -0.7; a fit with a flat source evolution ($H_{\text{flat evol}}$: R = 2.81×10^9 GeV; m = 0.0; γ = 0.75) and a fit with a high maximal rigidity ($H_{\text{high Rmax}}$: R = 4.46×10^9 GeV; m = -5.6; γ = 1.6). As the fits are supposed to resemble the measured cosmic ray composition on Earth, the resulting muon flux is expected to be similar, but the large measurement uncertainties still leave room to accommodate different interpretations. The neutrino flux is calculated using the method described in [229], while the muon flux is calculated using the Matrix Cascade Equations, as detailed in Section 7.1.2. The result is shown in Figure 7.12. While the different models alter the numbers of detected muons by only a factor of two, the variation in the number of detected neutrinos changes by about a factor of ten. Since the galactic component stays unchanged, this means that only a small influence of the extra-galactic component is visible in the muon flux. The flux differs strongest at muon energies above 10^7 GeV, which is in agreement with the expected transition region from galactic to extra-galactic cosmic rays.

In other words, most muons at the relevant energies are generated by cosmic rays of 10^8 GeV to $10^{9.5}$ GeV while cosmogenic neutrinos relevant for radio neutrino detectors stem from cosmic rays of above 10^{10} GeV. This can also be seen in the fact that the change in muon number is significantly smaller than in the neutrino number from the same

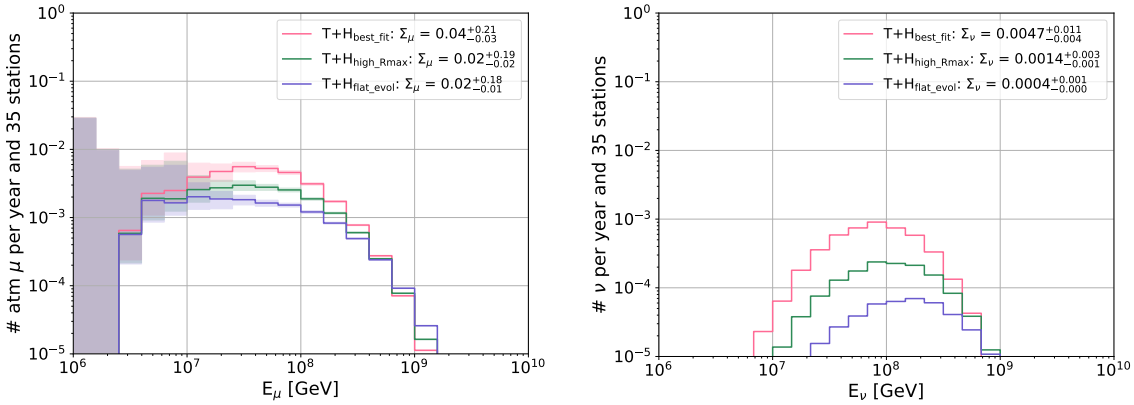

Figure 7.12: Expected event rate for muons (left) and neutrinos (right) for the same cosmic ray compositions in an RNO-G like detector with 35 station and a deep 2.5σ trigger. Shown are three different extra-galactic components by Heinze [229] (best fit, high maximal rigidity and flat evolution) combined with the same galactic component by Thoudam [227].

models. This means that the muon background expectation can in general be treated independently from the neutrino production models. Of course, keeping in mind that some model-dependent cases are imaginable, where background and signal need to be considered together, in particular when including new physics.

7.4.2 Observational signatures

The practical implications for neutrino observations and analyses with a radio neutrino telescope will be considered. The observational signature for in-ice radio neutrino detectors is an electric field whose amplitude is proportional to the shower energy. The signal strength depends on the fractional energy which is deposited in the shower, so the shower energy rather than the muon or neutrino energy is the relevant observational quantity. The shower energy (which requires a reconstructed vertex distance and viewing angle, see e.g. [108, 234] for details), together with the arrival direction are likely the only two reconstructed quantities that can be used to distinguish signal from background, unless a veto from air shower tagging or multiple station/pulses coincidences is possible.

The detected arrival directions of muon and neutrinos differ only slightly, as shown in Figure 7.13, because they are dominated by the detector geometry, which is also illustrated by the different shape of the distributions for shallow and deep component. This, however, prohibits a distinction between muons and neutrinos on an event-by-event basis and complicates it even using the whole distributions at low statistics. The only unique signature of neutrinos is an arrival direction > 90° zenith, since muons get absorbed in the Earth. However, this is only a very small fraction of the expected events.

To summarize, Figure 7.14 combines the most conservative and optimistic models for muon and neutrino predictions for an RNO-G like detector in terms of shower energy. In the most conservative case, an RNO-G like detector will detect 0.07 muons a year (0.16 muons with a 1.5σ trigger), and in the most optimistic case, only 0.002 muons (0.01 muons with a 1.5σ trigger). While there are thus differences in the extreme case of $\mathcal{O}(30)$

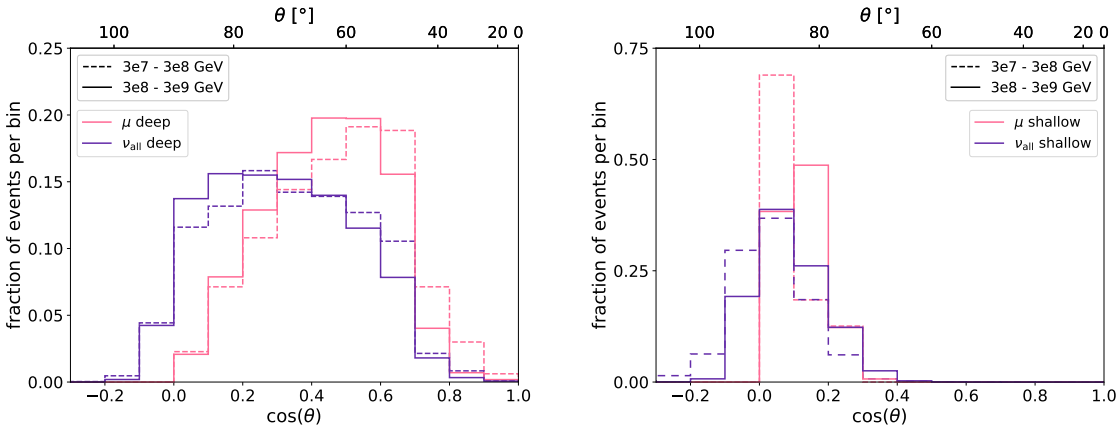

Figure 7.13: Comparison of the zenith arrival direction of triggered muon (pink) and triggered neutrinos (purple) with a 2.5σ deep trigger (left) and a 2.5σ shallow trigger (right). The line styles indicate different energy ranges: from 3×10^7 GeV to 3×10^8 GeV (dashed) and from 3×10^8 GeV to 3×10^9 GeV (solid).

between the muon predictions, current neutrino flux predictions in contract vary by more than a factor of $\mathcal{O}(150)$.

The combination of Sibyll-2.3c as hadronic interaction model and the Global Spline Fit (GSF) yields the highest muon rate, the theoretically driven model T+H is approximately a factor two lower. QGSJet-II.04 combined with T+H and the proton-poor cosmic ray composition of H3a together yields almost no muons. Recall that QGSJet-II.04 does not include charm which results in an underestimation of the muon flux above PeV energies, where the prompt muon component dominates. The differences using Sibyll-2.3c and GSF, and T+H respectively are therefore likely a better estimate for the uncertainties of the muon event rate, reducing the uncertainty budget to a factor of 2, keeping in mind that Sibyll-2.3c still does not model all components of the muon production. The neutrino flux predictions are influenced by source and propagation modeling, as well as the cosmic ray composition, as indicated by the two predictions for the composition as reported by the Pierre Auger Collaboration and the Telescope Array (TA). Without additional experimental evidence the entire neutrino parameter space has to be considered equally likely for discovery experiments.

The maxima of the muon distributions predicted in all considered scenarios are at around 10^7 GeV and fall steeply towards higher energies. Above 10^8 GeV all shown neutrino predictions are higher than the muon expectation, which provides an avenue towards a possible analysis cut at high energies. A recent study of the discovery potential for the diffuse flux of ultra-high energy cosmic neutrinos also showed the usefulness of using the reconstructed shower energy as a discriminator for the atmospheric muon background [239].

In addition, it should be noted that all showers with an energy $< 10^6$ GeV have their vertex position within 20 m radius of the deep antenna. While the community is pushing towards lowering the energy threshold of detectors to gain an overlap to existing (optical) experiments, the current simulations make a number of approximations which are no longer completely valid in these cases, e.g. observing the far field of the radio emission, the separation of emission and propagation, and a constant index of refraction in the emission zone. The predictions of event rates at low energies therefore carry

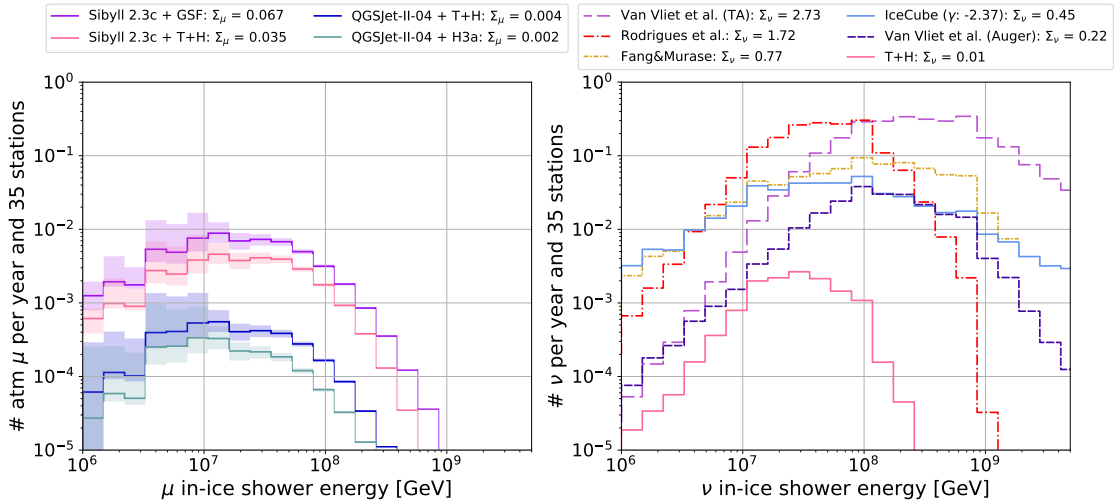

Figure 7.14: Left: Expected muon event rate for a 2.5σ trigger in the deep component evaluating four extreme scenarios in combining hadronic interaction model and cosmic ray composition as stated in the label. Right: Various predictions for an expected neutrino event rate with a 2.5σ trigger in the deep component, including cosmogenic neutrinos (TA [72, 91, 240], Auger [72], T+H [227, 229]) and neutrinos from sources (Fang and Murase [241], Rodrigues et al. [242]).

additional uncertainties. However, Figure 7.14 also shows that the background problem likely becomes larger at low energies, in particular since the muon flux rises much more steeply towards lower energies than the neutrino flux predictions. This is shown in a different way in Figure 7.15, which illustrated potential minimum energy cuts that could be imposed to gain a cleaner neutrino sample. For instance, cutting at a shower energy of $10^{7.5}$ GeV would retain 80% or more of all expected neutrinos, but improve the signal-to-background ratio with a factor of 5 – 10 depending on the model. This in turn, however, raises the question how successful an extension of the detector sensitivities to lower neutrino energies can be, given the increasing muon background.

7.4.3 Measuring the muon flux

Finally, one can invert the approach taken above and ask whether radio detectors can be used to measure the prompt muon flux above PeV energies. As shown in Figure 7.8, across all energies and arrival directions, roughly 50% of the detected muons can be related to an air shower that is also detected by the same instrument, meaning that a clear identification of muon events will be possible. In the case of RNO-G, ~0.3 tagged muon events are expected in 10 years at a trigger threshold of 2.5σ based on Sibyll-2.3c and GSF. Hence, the array will be too small to make a probable detection of a muon over the planned operation time. Even with an optimized trigger to 1.5σ noiseless signal equivalent, the largest flux predictions (Sibyll-2.3c and GSF) still predict < 1 tagged events in 10 years of operations. In addition, all muon signals will be very close to the threshold and thus the yet unknown analysis efficiency, as well as unstudied properties of the near-surface ice will have to be considered to solidify this number.

However, future radio detectors are already being planned, in particular, IceCube-Gen2 [135]. While the precise expected event numbers will depend on the details of the detector such as the exact hardware implementation of the trigger, bandwidth of the system, and analysis efficiencies, at this point an estimate is already possible. Using

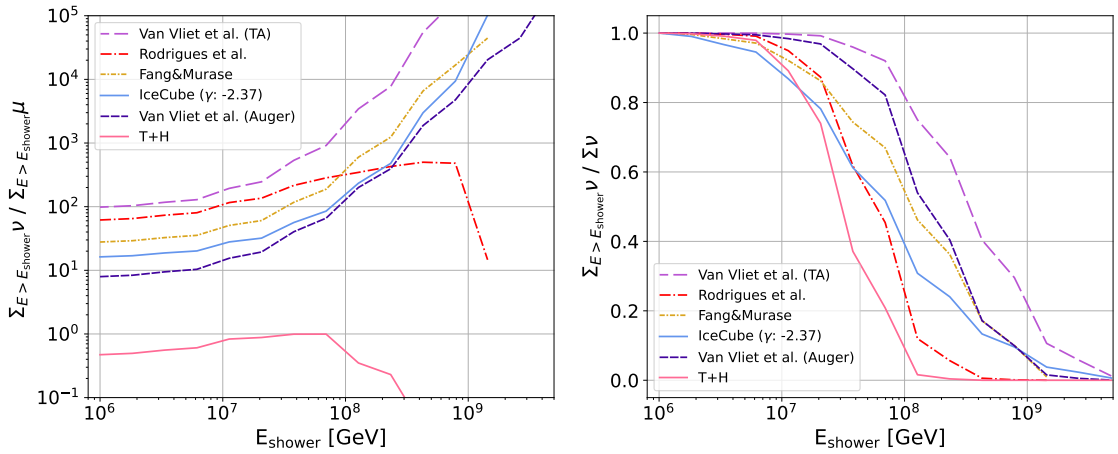

Figure 7.15: Left: Shown is the ratio of signal to background: the cumulative sum of neutrino events above the indicated shower energy in the x-axis is divided by the cumulative sum of expected muon events above the same shower energy. The color code represents the same neutrino flux models as in Figure 7.14. The assumed muon rate is calculated with Sibyll-2.3c and GSF as cosmic ray composition. Right: Fraction of neutrino events with shower energies higher than indicated in the x-axis.

the detector configuration and trigger settings as foreseen for IceCube-Gen2 [92] which includes a full simulation of the phased array trigger system, the atmospheric muon rates were simulated and find that IceCube-Gen2 will observe ~1.9 tagged muon events in 10 years for the currently highest flux expectations of Sibyll-2.3c and GSF and ~0.1 for QGSJet-II.04 and H3a. With an optimized trigger, one can envision improving on these numbers to reach an expectation significantly > 0. This would allow the in-ice radio array of IceCube-Gen2 to provide the first measurements of the prompt muon flux at 10 PeV. The expected muon background as a function of shower energy and incident direction for all cosmic ray composition and interaction models discussed in this study are published as supplemental material of [243], so that this forecast can be incorporated in future analyses such as [239].

7.5 Intermediate conclusion and outlook

The ultra-high energy muon flux is highly dependent on hadronic interaction models and the proton fraction of cosmic ray composition. Sibyll-2.3c currently provides the most complete hadronic interaction model for these high energies, since it considers the conventional component, the contribution from charmed hadrons and muons from unflavored mesons, neglecting only the subdominant contribution from B-mesons and photo-conversion into muon pairs. An explicit muon flux prediction from pQCD above 10 PeV is lacking, leaving experiments with large uncertainties on their prediction of the high-energy muon rate. The main uncertainties arise from the unknown charm cross-section, which is not accessible in current particle colliders. Judging by the variations in pQCD prediction for the muon neutrino flux [214, 244] there is a sizable uncertainty and more work from the theoretical side would help to establish better predictions for the muon background.

The cosmic ray composition influences the muon rate mostly through the parameter of the proton fraction. Changing from a proton-rich to a proton-poor model, yields a

difference of a factor of two in flux prediction.

The total observed flux is very sensitive to instrument geometry and in particular trigger settings. An RNO-G like detector will, at full completion, observe about 0.07 muons per year, using the Sibyll-2.3c prediction and a 2.5σ-threshold. At a trigger of 1.5σ this number would rise to 0.16 muons per year. These numbers should be compared to the very uncertain flux predictions for neutrinos, which are ranging from 2.7 neutrinos to 0.01 neutrinos per year in RNO-G.

Since both the neutrino and muon fluxes depend on the proton fraction of the cosmic ray composition, it was studied whether they are correlated. It could be shown, that muon and neutrino flux predictions mostly decouple. Most ultra-high energy muons stem from cosmic rays at energies lower than those that cause the cosmogenic neutrino flux. On the downside, one can therefore not reduce uncertainties through a combined treatment of signal and background.

A possible mitigation strategy is to detect cosmic rays and thereby identify muon events: if the parent air shower of the muon can be detected, it provides a signature unique to muon events. In a detector with shallow antennas, such an air shower tagging is possible directly, using the same system. The efficiency of this mechanism is energy and arrival direction dependent with good efficiency for showers with zenith angles lower than 55° and muon energies above 10^9 GeV. One could consider adding a more closely spaced array in shallow-only stations for RNO-G, which will likely improve the veto efficiency for less inclined showers. However, for high efficiency, such an in-fill array would have to have a spacing of $\mathcal{O}(100)$m, making it too dense to be feasibly installed.

A discrimination between muon and neutrino signals only based on the arrival direction is unlikely, as the distributions follow mostly the detector acceptance. It is, however, likely that neutrinos and muons show a different energy spectrum. The muon flux will likely not be measurable above 10^9 GeV shower energy, already being smaller than most neutrino fluxes at 10^8 GeV shower energy. The obtainable resolution of the shower energy of radio neutrino detectors is expected to be better than a factor of two [234], which seems sufficient to assign a significant signalness probability for high energy events. Combined with an air shower veto, which is most efficient at high energies, this should allow for a relatively background-free neutrino shower detection above 10^8 GeV.

An RNO-G-like detector is likely too small to make a first measurement of the prompt muon flux at energies above 10 PeV. This could be done by using those muons that are identified as stemming from an air shower, but the expected number of these kinds of events is < 1 in 10 years. However, a much larger detector like the planned radio array of IceCube-Gen2 has the potential for the first muon measurements at these energies. Given the incompleteness of current hadronic models and lacking pQCD predictions for muons at these energies, a direct measurement will provide important additional handles, in particular on forward charm production in QCD. Measuring the muon background will also contribute to our understanding of cosmic ray composition.

8 Conclusion

The focus of this work is the precise estimate of the event rate of air showers and atmospheric muons in RNO-G.

For this purpose, the signal chain of the shallow detector component, i.e. the signal path from electric field in the air, to antenna and digitization and its diode trigger has been characterized. The trigger used for air shower detection consists of a diode circuit for signal smoothing and a discriminator for threshold evaluation. Both components are optimized for low power consumption and introduce uncertainties: the diode signal is non-linear in amplitude and depends on the bias voltage of the diode, the incoming pulse shape, and the temperature. The behavior of the discriminator at the low voltages used in RNO-G is not specified by the manufacturer, so one has to rely on calibration measurements. The laboratory studies indicate that the diode trigger is able to trigger on cosmic ray signals close to thermal noise given a well-tuned threshold. In the field, a channel-by-channel adjustment of the threshold is necessary. The servo mechanism continuously regulates the threshold according to a set scaler rate. Therefore the threshold adjustment on noise is not a problem for the operation of the detector. However, it will result in an additional step in the analyses to predict the number of expected cosmic rays. Using the internal signal generator in pulse mode would allow in-situ calibration of the trigger, but is currently not implemented in the firmware. The trigger threshold obtained in the laboratory is $(30\pm10)\,\sigma_{\text{power int}}$. The $\sigma_{\text{power int}}$ is the standard deviation of the power integrated trace over 11 ns within the trigger frequency band of 80 MHz to 200 MHz that approximates the trigger path. Analyzing the full band and the simple amplitude divided by the standard deviation of the noise, this corresponds to a threshold of $(4\pm0.5)\,\sigma$. Pre-deployment testing of the RADIANT digitizer board showed that the boards differ by about 0.3σ in their trigger efficiency. The recorded amplitudes vary by 0.5σ, even when recorded with the same board, this includes variation of the transmitted signals and digitization, without trigger.

Modeling the RADIANT trigger and its threshold setting for air shower simulations poses some difficulties. As mentioned before, the threshold depends on the present noise level to avoid high data rates. Therefore, the noise must be accurately simulated to obtain an appropriate trigger threshold. A comparison of the noise present during detector operation shows that variations between the stations are larger than the differences to the simulation assuming thermal noise of 230 K and Galactic noise, which dominates up to 200 MHz

The Monte Carlo simulations of air showers, together with the detector response of RNO-G and the RADIANT trigger as characterized in the laboratory, show that RNO-G can measure cosmic rays. The predicted event rate is 5^{+5}_{-2} air shower per day and seven stations, with an energy threshold of 10^{17} eV. The dominant uncertainty is the setting of the trigger threshold. The trigger efficiency and therefore the detection efficiency of cosmic rays depends strongly on the energy. The measured amplitude of the electric field also depends on the zenith angle of the air shower and the distance between the shower core and the detector station. More inclined showers cover larger areas, but at the same time their radio emission becomes weaker at a given antenna position.

Therefore, inclined showers are only visible above a certain energy, while more vertical showers are less likely to be close enough to a station. A trigger efficiency close to 100% is achieved when the shower core is within a distance of 200 m and at energies exceeding 3.16×10^{17} eV. Therefore, a denser array increases the event rate significantly.

Air shower remnants are a less studied background to which RNO-G is sensitive. An ultra-high energy muon originating from an air shower can penetrate the ice and induce a particle cascade which is similar to a neutrino induced particle cascade in ice. A prediction of the exact event rate is difficult, since the muon flux above PeV energies is highly dependent on hadronic interaction models and the cosmic ray composition.

At energies above 1 PeV, prompt muons dominate the flux with contributions from charmed hadrons, unflavored mesons, B-mesons and photo-conversion into muon pairs. An explicit muon flux prediction from pQCD above 10 PeV is lacking. The main uncertainties arise from the unknown charm cross-section, which is not accessible in current particle colliders.

The cosmic ray composition influences the muon rate mostly through the parameter of the proton fraction. Changing from a proton-rich to a proton-poor model, yields a difference of a factor of two in flux prediction.

The muon event rate is very sensitive to instrument geometry and in particular trigger settings. An RNO-G like detector with 35 stations observes 0.07 muons per year (2.5σ-trigger threshold) or 0.16 muons per year (1.5σ-trigger threshold). These numbers should be compared to the very uncertain flux predictions for neutrinos, which range from 2.7 neutrinos to 0.01 neutrinos per year.

Since both neutrino and muon fluxes depend on the proton fraction of the cosmic ray composition, it was investigated whether they are correlated. It was shown that muon and neutrino flux predictions mostly decouple. Ultra-high energy muons tend to stem from cosmic rays at energies lower than those that cause the cosmogenic neutrino flux. Therefore the uncertainties cannot be reduced by a combined treatment of signal and background.

A possible mitigation strategy to neutrino-muon confusion is the detection of the air shower from which the muon originates and thereby identify in-ice particle cascade as originating from a muon. The efficiency of this mechanism is energy and arrival direction dependent with good efficiency for showers with zenith angles lower than 55° and muon energies above 10^9 GeV. A smaller spacing is likely to improve the veto efficiency.

Muons and neutrinos show different energy spectra which should in combination with an air shower veto allow for a relatively background-free detection of neutrino induced shower above 10^8 GeV

A larger detector like the planned radio array of IceCube-Gen2 has the potential for the first muon measurements which would provide a handle on forward charm production in QCD and contribute to our understanding of the cosmic ray composition.

Appendix

List of Figures

List of Tables

Special Terms

A

ADC analog-to-digital converter.
AERA Auger Engineering Radio Array.
AGN active galactic nuclei.
Amaroq Greenlandic for arctic wolf, name of station 21.
ANITA Antarctic Impulsive Transient Antenna.
ARA Askaryan Radio Array.
ARIANNA Antarctic Ross Ice Shelf Antenna Neutrino Array.
ASIC Application Specific Integrated Circuit.
AURA Antarctic Under-Ice Radio Array.
Avinngaq Greenlandic for arctic lemming, name of station 22.

B

BEACON Beamforming Elevated Array for COsmic Neutrinos.
BM board manager.

C

cc charged current.
Cherenkov angle Angle at which the radiation emitted along a path arrives simultaneously and adds up coherently, making the observed signal particularly high in amplitude..
CMB cosmic microwave background.
CMOS Complementary–metal-oxide-semiconductor.
COBS Consistent Overhead Byte Stuffing.
CoREAS Corsika-based Radio Emission from Air Showers.
CORSIKA COsmic Ray SImulations for KAscade.

D

DAQ data acquisition system.
DESY Deutsches Elektronen-Synchrotron.
Drab Downhole Receiver & Amplifier Board.

E

EBL extragalactic background light.
ECAP Erlangen Centre for Astroparticle Physics.

F

FFT Fast Fourier Transform.
Flower board FLexible Octal WavEform Recorder, this is the 4-channel low-threshold trigger and digitizer board used for the phased array.
FPGA Field Programmable Gate Array.

G

GRAND Giant Radio Array for Neutrino Detection.
GRB gamma-ray burst.

GSF Global Spline Fit.
GZK Greisen, Zatsepin and Kuzmin.

H

helper string Part of the deep component of an RNO-G station. The helper string features one horizontally polarized antennas, two vertically polarized antennas and a calibration pulser.

I

IGLU In-ice Gain with Low-power Unit.
impulse response Describes how a system (i.e. a detector) responds to a given impulse (i.e., what the detector adds to the impulse when looking at the output). In the case for the surface component of RNO-G, the combination of VEL determined by the LPDA and amplification determined by the SURFACE board.

L

LAB4D The Application Specific Integrated Circuit (ASIC) of the Large Analog Bandwidth Recorder and Digitizer with Ordered Readout (LABRADOR) family, for use in direct wide-band radio frequency digitization and successor to the LAB3 digitizer.
LOFAR LOw Frequency ARray.
LoRaWAN Long Range Wide Area Network.
LPDA Logarithmic Periodic Dipole Antenna.
LPM Landau–Pomeranchuk–Migdal.
LTE Long Term Evolution.
LVDS Low-Voltage Differential Signaling.

N

Nanoq Greenlandic for polar bear, name of station 11.
nc neutral current.
n-type negatively-doped.

P

PAO Pierre Auger Observatory.
PDF parton distribution function.
pn-junction A p-n junction is a boundary or interface between two types of semiconductor materials, p-type and n-type, within a single semiconductor crystal.
power string Part of the deep component of an RNO-G station. The power string features the phased array, two horizontally polarized antennas and three vertically polarized antennas.
pQCD perturbative QCD.
p-type positively-doped.
PUEO Payload for Ultrahigh Energy Observations.
PWM pulse-width modulation.

Q

Qappik Greenlandic for wolverine, name of station 24.
QCD quantum chromodynamics.

R

RADIANT RAdio DIgitizer and Auxiliary Neutrino Trigger.
RET Radar Echo Telescope.
RFoF Radio Frequency over Fiber.
RICE Radio Ice Cherenkov Experiment.
RNO-G Radio Neutrino Observatory Greenland.

S
SCA switched capacitor array.
Schottky diode A type of metal-semiconductor diode having a low forward voltage drop and a very fast switching speed.
SD card Secure Digital card.
SG signal generator.
SMA Sub Miniature version A.
SN supernovae.
SNR signal to noise ratio.
SNR-CR cosmic rays stemming from supernova remnants.
Summit Station Research station near the apex of the Greenland ice sheet.
SURFACE board This is the 5-channel full-chain amplification and filtering board for the surface antennas.

T
TA Telescope Array.
TDE tidal disruption event.
Terianniaq Greenlandic for arctic fox, name of station 12.
Tunka-Rex Tunka Radio Extension.

U
UFA Unger, Farrar and Anchordoqui.
UHE ultra high energy.
UHECR ultra-high energy cosmic ray.
Ukaleq Greenlandic for arctic hare, name of station 13.
Ukaliatsiaq Greenlandic for stoat, name of station 23.

V
V2 version 2 RADIANT board.
V3 version 3 RADIANT board.
VEL vector effective length.

W
WR-CR cosmic rays stemming from Wolf-Rayet stars.

References

[1] G. Brianti and P. Jenni, "The Large Hadron Collider (LHC): The Energy Frontier," *Adv. Ser. Direct. High Energy Phys.*, vol. 27, C. Fabjan, T. Taylor, D. Treille, and H. Wenninger, Eds., pp. 263–326, 2017. DOI: 10.1142/9789814749145_0008.

[2] V. F. Hess, "Über Beobachtungen der durchdringenden Strahlung bei sieben Freiballonfahrten," *Phys. Z.*, vol. 13, pp. 1084–1091, 1912.

[3] K.-H. Kampert, A. A. Watson, and A. A. Watson, "Extensive Air Showers and Ultra High-Energy Cosmic Rays: A Historical Review," *Eur. Phys. J. H*, vol. 37, pp. 359–412, 2012. DOI: 10.1140/epjh/e2012-30013-x.

[4] T. K. Gaisser, R. Engel, and E. Resconi, *Cosmic Rays and Particle Physics: 2nd Edition*. Cambridge University Press, Jun. 2016.

[5] A. M. Hillas, "The Origin of Ultrahigh-Energy Cosmic Rays," *Ann. Rev. Astron. Astrophys.*, vol. 22, pp. 425–444, 1984. DOI: 10.1146/annurev.aa.22.090184.002233.

[6] R. Alves Batista *et al.*, "Open Questions in Cosmic-Ray Research at Ultrahigh Energies," *Front. Astron. Space Sci.*, vol. 6, p. 23, 2019. DOI: 10.3389/fspas.2019.00023.

[7] R. Alfaro *et al.*, "All-particle cosmic ray energy spectrum measured by the HAWC experiment from 10 to 500 TeV," *Phys. Rev. D*, vol. 96, no. 12, p. 122 001, 2017. DOI: 10.1103/PhysRevD.96.122001.

[8] Y. A. Fomin, G. B. Khristiansen, G. B. Kulikov, V. G. Pogorely, V. I. Solovjeva, and V. P. Sulakov, "Energy spectrum of cosmic rays at energies of 5e15 - 5e17 eV," *Proceedings of the 22nd International Cosmic Ray Conference. 11-23 August, 1991. Dublin, Ireland.*, pp. 85–88, 1991, Under the auspices of the International Union of Pure and Applied Physics (IUPAP), Volume 2, Contributed Papers, OG Sessions 6-11. Dublin: The Institute for Advanced Studies.

[9] M. Amenomori *et al.*, "The All-particle spectrum of primary cosmic rays in the wide energy range from 10**14 eV to 10**17 eV observed with the Tibet-III air-shower array," *Astrophys. J.*, vol. 678, pp. 1165–1179, 2008. DOI: 10.1086/529514.

[10] M. Nagano *et al.*, "Energy Spectrum of Primary Cosmic Rays Between 10**14.5-ev and 10**18-ev," *J. Phys. G*, vol. 10, p. 1295, 1984. DOI: 10.1088/0305-4616/10/9/016.

[11] M. A. K. Glasmacher *et al.*, "The cosmic ray energy spectrum between 10**14-eV and 10**16-eV," *Astropart. Phys.*, vol. 10, pp. 291–302, 1999. DOI: 10.1016/S0927-6505(98)00070-X.

[12] W. D. Apel *et al.*, "KASCADE-Grande measurements of energy spectra for elemental groups of cosmic rays," *Astropart. Phys.*, vol. 47, pp. 54–66, 2013. DOI: 10.1016/j.astropartphys.2013.06.004.

[13] K. Andeen and M. Plum, "Cosmic Ray Spectrum and Composition from PeV to EeV from the IceCube Neutrino Observatory," *PoS*, vol. ICRC2019, p. 172, 2021. DOI: 10.22323/1.358.0172.

[14] R. U. Abbasi *et al.*, "First observation of the Greisen-Zatsepin-Kuzmin suppression," *Phys. Rev. Lett.*, vol. 100, p. 101 101, 2008. DOI: 10.1103/PhysRevLett.100.101101.

[15] A. Aab *et al.*, "Features of the Energy Spectrum of Cosmic Rays above 2.5×10^{18} eV Using the Pierre Auger Observatory," *Phys. Rev. Lett.*, vol. 125, no. 12, p. 121 106, 2020. DOI: 10.1103/PhysRevLett.125.121106.

[16] A. Aab *et al.*, "Measurement of the cosmic-ray energy spectrum above 2.5×10^{18} eV using the Pierre Auger Observatory," *Phys. Rev. D*, vol. 102, no. 6, p. 062 005, 2020. DOI: 10.1103/PhysRevD.102.062005.

[17] P. Abreu *et al.*, "The energy spectrum of cosmic rays beyond the turn-down around 10^{17} eV as measured with the surface detector of the Pierre Auger Observatory," *Eur. Phys. J. C*, vol. 81, no. 11, p. 966, 2021. DOI: 10.1140/epjc/s10052-021-09700-w.

[18] D. Ivanov, "Energy Spectrum Measured by the Telescope Array," *PoS*, vol. ICRC2019, p. 298, 2020. DOI: 10.22323/1.358.0298.

[19] R. U. Abbasi *et al.*, "The Cosmic-Ray Energy Spectrum between 2 PeV and 2 EeV Observed with the TALE detector in monocular mode," *Astrophys. J.*, vol. 865, no. 1, p. 74, 2018. DOI: 10.3847/1538-4357/aada05.

[20] R. L. Workman *et al.*, "Review of Particle Physics," *PTEP*, vol. 2022, p. 083C01, 2022. DOI: 10.1093/ptep/ptac097.

[21] R. Abbasi *et al.*, "Joint analysis of the energy spectrum of ultra-high-energy cosmic rays as measured at the Pierre Auger Observatory and the Telescope Array," *PoS*, vol. ICRC2021, p. 337, 2021. DOI: 10.22323/1.395.0337.

[22] A. Aab *et al.*, "Large-scale cosmic-ray anisotropies above 4 EeV measured by the Pierre Auger Observatory," *Astrophys. J.*, vol. 868, no. 1, p. 4, 2018. DOI: 10.3847/1538-4357/aae689.

[23] A. Aab *et al.*, "Cosmic-ray anisotropies in right ascension measured by the Pierre Auger Observatory," *Astrophys. J.*, vol. 891, p. 142, 2020. DOI: 10.3847/1538-4357/ab7236.

[24] R. U. Abbasi *et al.*, "Indications of Intermediate-Scale Anisotropy of Cosmic Rays with Energy Greater Than 57 EeV in the Northern Sky Measured with the Surface Detector of the Telescope Array Experiment," *Astrophys. J. Lett.*, vol. 790, p. L21, 2014. DOI: 10.1088/2041-8205/790/2/L21.

[25] R. U. Abbasi *et al.*, "Evidence for a Supergalactic Structure of Magnetic Deflection Multiplets of Ultra-High Energy Cosmic Rays," *Astrophys. J.*, vol. 899, no. 1, p. 86, 2020. DOI: 10.3847/1538-4357/aba26c.

[26] A. Aab *et al.*, "An Indication of anisotropy in arrival directions of ultra-high-energy cosmic rays through comparison to the flux pattern of extragalactic gamma-ray sources," *Astrophys. J. Lett.*, vol. 853, no. 2, p. L29, 2018. DOI: 10.3847/2041-8213/aaa66d.

[27] A. Aab *et al.*, "Searches for Anisotropies in the Arrival Directions of the Highest Energy Cosmic Rays Detected by the Pierre Auger Observatory," *Astrophys. J.*, vol. 804, no. 1, p. 15, 2015. DOI: 10.1088/0004-637X/804/1/15.

[28] A. Aab *et al.*, "Search for magnetically-induced signatures in the arrival directions of ultra-high-energy cosmic rays measured at the Pierre Auger Observatory," *JCAP*, vol. 06, p. 017, 2020. DOI: 10.1088/1475-7516/2020/06/017.

[29] M. G. Aartsen *et al.*, "Search for correlations between the arrival directions of IceCube neutrino events and ultrahigh-energy cosmic rays detected by the Pierre Auger Observatory and the Telescope Array," *JCAP*, vol. 01, p. 037, 2016. DOI: 10.1088/1475-7516/2016/01/037.

[30] A. di Matteo *et al.*, "UHECR arrival directions in the latest data from the original Auger and TA surface detectors and nearby galaxies," *PoS*, vol. ICRC2021, p. 308, 2021. DOI: 10.22323/1.395.0308.

[31] V. S. Ptuskin, S. I. Rogovaya, V. N. Zirakashvili, L. G. Chuvilgin, G. B. Khristiansen, and E. G. Klepach, "Diffusion and drift of very high energy cosmic rays in galactic magnetic fields," *Astron. Astrophys.*, vol. 268, pp. 726–735. 1993.

[32] B. Peters, "Primary cosmic radiation and extensive air showers," *Nuovo Cim.*, vol. 22, no. 4, pp. 800–819, 1961. DOI: 10.1007/bf02783106.

[33] T. Antoni *et al.*, "KASCADE measurements of energy spectra for elemental groups of cosmic rays: Results and open problems," *Astropart. Phys.*, vol. 24, pp. 1–25, 2005. DOI: 10.1016/j.astropartphys.2005.04.001.

[34] W. D. Apel *et al.*, "Kneelike structure in the spectrum of the heavy component of cosmic rays observed with KASCADE-Grande," *Phys. Rev. Lett.*, vol. 107, p. 171 104, 2011. DOI: 10.1103/PhysRevLett.107.171104.

[35] A. Aab *et al.*, "Observation of a Large-scale Anisotropy in the Arrival Directions of Cosmic Rays above 8×10^{18} eV," *Science*, vol. 357, no. 6537, pp. 1266–1270, 2017. DOI: 10.1126/science.aan4338.

[36] C. Ding, N. Globus, and G. R. Farrar, "The Imprint of Large Scale Structure on the Ultra-High-Energy Cosmic Ray Sky," *Astrophys. J. Lett.*, vol. 913, no. 1, p. L13, 2021. DOI: 10.3847/2041-8213/abf11e.

[37] K. Greisen, "End to the cosmic ray spectrum?" *Phys. Rev. Lett.*, vol. 16, pp. 748–750, 1966. DOI: 10.1103/PhysRevLett.16.748.

[38] G. T. Zatsepin and V. A. Kuzmin, "Upper limit of the spectrum of cosmic rays," *JETP Lett.*, vol. 4, pp. 78–80, 1966.

[39] R. Aloisio, D. Boncioli, A. di Matteo, A. F. Grillo, S. Petrera, and F. Salamida, "Cosmogenic neutrinos and ultra-high energy cosmic ray models," *JCAP*, vol. 10, p. 006, 2015. DOI: 10.1088/1475-7516/2015/10/006.

[40] M. Spurio, *Probes of Multimessenger Astrophysics: Charged cosmic rays, neutrinos, γ-rays and gravitational waves* (Astronomy and Astrophysics Library). Springer, 2018.

[41] R. de Menezes, R. Nemmen, J. D. Finke, I. Almeida, and B. Rani, "Gamma-ray observations of low-luminosity active galactic nuclei," *Mon. Not. Roy. Astron. Soc.*, vol. 492, no. 3, pp. 4120–4130, 2020. DOI: 10.1093/mnras/staa083.

[42] J. Aleksić *et al.*, "Measurement of the Crab Nebula spectrum over three decades in energy with the MAGIC telescopes," *JHEA*, vol. 5-6, pp. 30–38, 2015. DOI: 10.1016/j.jheap.2015.01.002.

[43] E. Prandini *et al.*, "MAGIC eyes to the extreme: testing the blazar emission models on EHBLs," *PoS*, vol. ICRC2019, p. 768, 2021. DOI: 10.22323/1.358.0768.

[44] A. Domínguez *et al.*, "Detection of the cosmic \gamma-ray horizon from multiwavelength observations of blazars," *Astrophys. J.*, vol. 770, p. 77, 2013. DOI: 10.1088/0004-637X/770/1/77.

[45] H. Abdalla *et al.*, "Measurement of the EBL spectral energy distribution using the VHE γ-ray spectra of H.E.S.S. blazars," *Astron. Astrophys.*, vol. 606, A59, 2017. DOI: 10.1051/0004-6361/201731200.

[46] N. Song, S. W. Li, C. A. Argüelles, M. Bustamante, and A. C. Vincent, "The Future of High-Energy Astrophysical Neutrino Flavor Measurements," *JCAP*, vol. 04, p. 054, 2021. DOI: 10.1088/1475-7516/2021/04/054.

[47] R. Abbasi *et al.*, "Detection of astrophysical tau neutrino candidates in IceCube," *Eur. Phys. J. C*, vol. 82, no. 11, p. 1031, 2022. DOI: 10.1140/epjc/s10052-022-10795-y.

[48] M. G. Aartsen *et al.*, "Flavor Ratio of Astrophysical Neutrinos above 35 TeV in IceCube," *Phys. Rev. Lett.*, vol. 114, no. 17, p. 171 102, 2015. DOI: 10.1103/PhysRevLett.114.171102.

[49] M. G. Aartsen *et al.*, "Evidence for High-Energy Extraterrestrial Neutrinos at the IceCube Detector," *Science*, vol. 342, p. 1 242 856, 2013. DOI: 10.1126/science.1242856.

[50] M. G. Aartsen *et al.*, "Observation of High-Energy Astrophysical Neutrinos in Three Years of IceCube Data," *Phys. Rev. Lett.*, vol. 113, p. 101 101, 2014. DOI: 10.1103/PhysRevLett.113.101101.

[51] R. Naab, E. Ganster, and Z. Zhang, "Measurement of the astrophysical diffuse neutrino flux in a combined fit of IceCube's high energy neutrino data," in *38th International Cosmic Ray Conference*, Jul. 2023.

[52] S. Sclafani *et al.*, "Observation of High-Energy Neutrinos from the Galactic Plane," *PoS*, vol. ICRC2023, p. 1108, 2023. DOI: 10.22323/1.444.1108.

[53] R. Abbasi *et al.*, "Observation of high-energy neutrinos from the Galactic plane," *Science*, vol. 380, no. 6652, adc9818, 2023. DOI: 10.1126/science.adc9818.

[54] A. Albert *et al.*, "Hint for a TeV neutrino emission from the Galactic Ridge with ANTARES," *Phys. Lett. B*, vol. 841, p. 137 951, 2023. DOI: 10.1016/j.physletb.2023.137951.

[55] M. G. Aartsen *et al.*, "Multimessenger observations of a flaring blazar coincident with high-energy neutrino IceCube-170922A," *Science*, vol. 361, no. 6398, eaat1378, 2018. DOI: 10.1126/science.aat1378.

[56] S. Ansoldi *et al.*, "The blazar TXS 0506+056 associated with a high-energy neutrino: insights into extragalactic jets and cosmic ray acceleration," *Astrophys. J. Lett.*, vol. 863, p. L10, 2018. DOI: 10.3847/2041-8213/aad083.

[57] M. G. Aartsen *et al.*, "Neutrino emission from the direction of the blazar TXS 0506+056 prior to the IceCube-170922A alert," *Science*, vol. 361, no. 6398, pp. 147–151, 2018. DOI: 10.1126/science.aat2890.

[58] R. Abbasi *et al.*, "Evidence for neutrino emission from the nearby active galaxy NGC 1068," *Science*, vol. 378, no. 6619, pp. 538–543, 2022. DOI: 10.1126/science.abg3395.

[59] S. Adrian-Martinez *et al.*, "Letter of intent for KM3NeT 2.0," *J. Phys. G*, vol. 43, no. 8, p. 084 001, 2016. DOI: 10.1088/0954-3899/43/8/084001.

[60] S. R. Gozzini, "Latest Results with the KM3NeT Neutrino Telescope," *PoS*, vol. TAUP2023, p. 176, 2024. DOI: 10.22323/1.441.0176.

[61] M. Agostini *et al.*, "The Pacific Ocean Neutrino Experiment," *Nature Astron.*, vol. 4, no. 10, pp. 913–915, 2020. DOI: 10.1038/s41550-020-1182-4.

[62] V. A. Allakhverdyan *et al.*, "Diffuse neutrino flux measurements with the Baikal-GVD neutrino telescope," *Phys. Rev. D*, vol. 107, no. 4, p. 042 005, 2023. DOI: 10.1103/PhysRevD.107.042005.

[63] V. S. Berezinsky and G. T. Zatsepin, "Cosmic rays at ultrahigh-energies (neutrino?)" *Phys. Lett. B*, vol. 28, pp. 423–424, 1969. DOI: 10.1016/0370-2693(69)90341-4.

[64] K. Kotera, D. Allard, and A. V. Olinto, "Cosmogenic Neutrinos: parameter space and detectabilty from PeV to ZeV," *JCAP*, vol. 10, p. 013, 2010. DOI: 10.1088/1475-7516/2010/10/013.

[65] M. G. Aartsen *et al.*, "A combined maximum-likelihood analysis of the high-energy astrophysical neutrino flux measured with IceCube," *Astrophys. J.*, vol. 809, no. 1, p. 98, 2015. DOI: 10.1088/0004-637X/809/1/98.

[66] A. Aab *et al.*, "Improved limit to the diffuse flux of ultrahigh energy neutrinos from the Pierre Auger Observatory," *Phys. Rev. D*, vol. 91, no. 9, p. 092 008, 2015. DOI: 10.1103/PhysRevD.91.092008.

[67] C. Deaconu *et al.*, "Searches for Ultra-High Energy Neutrinos with ANITA," *PoS*, vol. ICRC-2019, p. 867, 2020. DOI: 10.22323/1.358.0867.

[68] I. Kravchenko *et al.*, "RICE limits on the diffuse ultrahigh energy neutrino flux," *Phys. Rev. D*, vol. 73, p. 082 002, 8 Apr. 2006. DOI: 10.1103/PhysRevD.73.082002.

[69] I. Kravchenko *et al.*, "Updated Results from the RICE Experiment and Future Prospects for Ultra-High Energy Neutrino Detection at the South Pole," *Phys. Rev. D*, vol. 85, p. 062 004, 2012. DOI: 10.1103/PhysRevD.85.062004.

[70] P. Allison *et al.*, "Constraints on the diffuse flux of ultrahigh energy neutrinos from four years of Askaryan Radio Array data in two stations," *Phys. Rev. D*, vol. 102, no. 4, p. 043 021, 2020. DOI: 10.1103/PhysRevD.102.043021.

[71] A. Anker *et al.*, "A search for cosmogenic neutrinos with the ARIANNA test bed using 4.5 years of data," *JCAP*, p. 053, 2020. DOI: 10.1088/1475-7516/2020/03/053.

[72] A. van Vliet, R. Alves Batista, and J. R. Hörandel, "Determining the fraction of cosmic-ray protons at ultrahigh energies with cosmogenic neutrinos," *Phys. Rev. D*, vol. 100, no. 2, p. 021 302, 2019. DOI: 10.1103/PhysRevD.100.021302.

[73] M. Ackermann *et al.*, "The spectrum of isotropic diffuse gamma-ray emission between 100 MeV and 820 GeV," *Astrophys. J.*, vol. 799, p. 86, 2015. DOI: 10.1088/0004-637X/799/1/86.

[74] C. Haack, C. Wiebusch, *et al.*, "A measurement of the diffuse astrophysical muon neutrino flux using eight years of IceCube data.," *PoS*, vol. ICRC2017, p. 1005, 2018. DOI: 10.22323/1.301.1005.

[75] C. Kopper *et al.*, "Observation of Astrophysical Neutrinos in Six Years of IceCube Data," *PoS*, vol. ICRC2017, p. 981, 2018. DOI: 10.22323/1.301.0981.

[76] M. G. Aartsen *et al.*, "Differential limit on the extremely-high-energy cosmic neutrino flux in the presence of astrophysical background from nine years of IceCube data," *Phys. Rev.*, vol. D98, no. 6, p. 062 003, 2018. DOI: 10.1103/PhysRevD.98.062003.

[77] A. Aab *et al.*, "The Pierre Auger Observatory: Contributions to the 34th International Cosmic Ray Conference (ICRC 2015)," in *Proceedings, 34th International Cosmic Ray Conference (ICRC 2015): The Hague, The Netherlands, July 30-August 6, 2015*, 2015.

[78] J. A. Aguilar *et al.*, "Design and Sensitivity of the Radio Neutrino Observatory in Greenland (RNO-G)," *JINST*, vol. 16, no. 03, P03025, 2021, [Erratum: JINST 18, E03001 (2023)]. DOI: 10.1088/1748-0221/16/03/P03025.

[79] B. Eichmann, J. P. Rachen, L. Merten, A. van Vliet, and J. Becker Tjus, "Ultra-High-Energy Cosmic Rays from Radio Galaxies," *JCAP*, vol. 02, p. 036, 2018. DOI: 10.1088/1475-7516/2018/02/036.

[80] D. Wanderman and T. Piran, "The luminosity function and the rate of Swift's Gamma Ray Bursts," *Mon. Not. Roy. Astron. Soc.*, vol. 406, pp. 1944–1958, 2010. DOI: 10.1111/j.1365-2966.2010.16787.x.

[81] G. Hasinger, T. Miyaji, and M. Schmidt, "Luminosity-dependent evolution of soft x-ray selected AGN: New Chandra and XMM-Newton surveys," *Astron. Astrophys.*, vol. 441, pp. 417–434, 2005. DOI: 10.1051/0004-6361:20042134.

[82] J. Law-Smith, E. Ramirez-Ruiz, S. L. Ellison, and R. J. Foley, "Tidal Disruption Event Host Galaxies in the Context of the Local Galaxy Population," *Astrophys. J.*, vol. 850, no. 1, p. 22, 2017. DOI: 10.3847/1538-4357/aa94c7.

[83] C. Guépin, K. Kotera, E. Barausse, K. Fang, and K. Murase, "Ultra-High Energy Cosmic Rays and Neutrinos from Tidal Disruptions by Massive Black Holes," *Astron. Astrophys.*, vol. 616, A179, 2018, [Erratum: Astron.Astrophys. 636, C3 (2020)]. DOI: 10.1051/0004-6361/201732392.

[84] M. S. Muzio, G. R. Farrar, and M. Unger, "Probing the environments surrounding ultrahigh energy cosmic ray accelerators and their implications for astrophysical neutrinos," *Phys. Rev. D*, vol. 105, no. 2, p. 023 022, 2022. DOI: 10.1103/PhysRevD.105.023022.

[85] V. B. Valera, M. Bustamante, and C. Glaser, "The ultra-high-energy neutrino-nucleon cross section: measurement forecasts for an era of cosmic EeV-neutrino discovery," *JHEP*, vol. 06, p. 105, 2022. DOI: 10.1007/JHEP06(2022)105.

[86] V. B. Valera, M. Bustamante, and O. Mena, "Joint measurement of the ultra-high-energy neutrino spectrum and cross section," Aug. 2023, [arXiv:2308.07709].

[87] A. Coleman, O. Ericsson, M. Bustamante, and C. Glaser, "The flavor composition of ultra-high-energy cosmic neutrinos: measurement forecasts for in-ice radio-based EeV neutrino telescopes," Feb. 2024, [arXiv:2402.02432].

[88] R. W. Rasmussen, L. Lechner, M. Ackermann, M. Kowalski, and W. Winter, "Astrophysical neutrinos flavored with Beyond the Standard Model physics," *Phys. Rev. D*, vol. 96, no. 8, p. 083 018, 2017. DOI: 10.1103/PhysRevD.96.083018.

[89] M. G. Aartsen *et al.*, "Measurement of South Pole ice transparency with the IceCube LED calibration system," *Nucl. Instrum. Meth. A*, vol. 711, pp. 73–89, 2013. DOI: 10.1016/j.nima.2013.01.054.

[90] L. Pyras, I. Plaisier, C. Welling, and Z. S. Meyers, *Radio Detection of EeV Neutrinos in Dielectric Media using the Askaryan Effect *for Babies*. Hamburg: DESY, 2022, pp. 1–14, doi: 10.3204/PUBDB-2021-03021.

[91] D. Bergman *et al.*, "Telescope Array Combined Fit to Cosmic Ray Spectrum and Composition," *PoS*, vol. ICRC2021, p. 338, 2021. DOI: 10.22323/1.395.0338.

[92] R. Abbasi *et al.*, "Sensitivity studies for the IceCube-Gen2 radio array," *PoS*, vol. ICRC2021, p. 1183, 2021. DOI: 10.22323/1.395.1183.

[93] C. Glaser *et al.*, "Results and Perspectives of the Auger Engineering Radio Array," *EPJ Web of Conferences*, vol. 135, S. Buitink, J. Hörandel, S. de Jong, R. Lahmann, R. Nahnhauer, and O. Scholten, Eds., p. 01 006, 2017. DOI: 10.1051/epjconf/201713501006.

[94] A. Horneffer *et al.*, "Air Shower Measurements with LOFAR," *Nucl. Instrum. Meth. A*, vol. 604, F. Ameli, A. Capone, G. De Bonis, F. Lucarelli, and F. Simeone, Eds., S20–S23, 2009. DOI: 10.1016/j.nima.2009.03.027.

[95] F. Schröder *et al.*, "Tunka-Rex: Status, Plans, and Recent Results (ARENA 2016)," *EPJ Web of Conferences*, vol. 135, Nov. 2016. DOI: 10.1051/epjconf/201713501003.

[96] A. Nelles *et al.*, "Recent results from the ARIANNA neutrino experiment," *EPJ Web of Conferences*, vol. 135, S. Buitink, J. Hörandel, S. de Jong, R. Lahmann, R. Nahnhauer, and O. Scholten, Eds., p. 05 002, 2017. DOI: 10.1051/epjconf/201713505002.

[97] P. Allison *et al.*, "Design and initial performance of the Askaryan Radio Array prototype EeV neutrino detector at the South Pole," *Astroparticle Physics*, vol. 35, no. 7, pp. 457–477, 2012. DOI: https://doi.org/10.1016/j.astropartphys.2011.11.010.

[98] F. G. Schröder, "Radio Detection of Cosmic-Ray Air Showers and High-Energy Neutrinos," *Progress in Particle and Nuclear Physics*, vol. 93, pp. 1–68, 2017. DOI: 10.1016/j.ppnp.2016.12.002.

[99] R. L. Workman *et al.*, "Review of Particle Physics," *PTEP*, vol. 2022, p. 083C01, 2022. DOI: 10.1093/ptep/ptac097.

[100] B. Rossi and K. Greisen, "Cosmic-Ray Theory," *Rev. Mod. Phys.*, vol. 13, pp. 240–309, 4 Oct. 1941. DOI: 10.1103/RevModPhys.13.240.

[101] P. K. F. Grieder, *Extensive Air Showers: High Energy Phenomena and Astrophysical Aspects - A Tutorial, Reference Manual and Data Book*. 2010.

[102] W. Heitler, *The quantum theory of radiation* (International Series of Monographs on Physics). Oxford: Oxford University Press, 1936, vol. 5.

[103] J. Matthews, "A Heitler model of extensive air showers," *Astropart. Phys.*, vol. 22, pp. 387–397, 2005. DOI: 10.1016/j.astropartphys.2004.09.003.

[104] M. Risse, "Properties of extensive air showers," *Acta Phys. Polon. B*, vol. 35, M. Jezabek and H. Wilczynski, Eds., pp. 1787–1798, 2004.

[105] D. Heck, J. Knapp, J. N. Capdevielle, G. Schatz, and T. Thouw, *CORSIKA: A Monte Carlo code to simulate extensive air showers*, http://bibliothek.fzk.de/zb/berichte/FZKA6019.pdf, Feb. 1998.

[106] L. D. Landau and I. Pomeranchuk, "Limits of applicability of the theory of bremsstrahlung electrons and pair production at high-energies," *Dokl. Akad. Nauk Ser. Fiz.*, vol. 92, pp. 535–536, 1953.

[107] A. B. Migdal, "Bremsstrahlung and Pair Production in Condensed Media at High Energies," *Phys. Rev.*, vol. 103, pp. 1811–1820, 6 Sep. 1956. DOI: 10.1103/PhysRev.103.1811.

[108] S. W. Barwick and C. Glaser, "Chapter 6: Radio Detection of High Energy Neutrinos in Ice," G. G. Fazi, Ed., pp. 237–302, 2023. DOI: 10.1142/9789811282645_0006.

[109] D. García-Fernández, C. Glaser, and A. Nelles, "Signatures of secondary leptons in radio-neutrino detectors in ice," *Phys. Rev. D*, vol. 102, no. 8, p. 083 011, 2020. DOI: 10.1103/PhysRevD.102.083011.

[110] C. Glaser, D. García-Fernández, A. Nelles, *et al.*, "NuRadioMC: Simulating the radio emission of neutrinos from interaction to detector," *Eur. Phys. J. C*, vol. 80, no. 2, p. 77, 2020. DOI: 10.1140/epjc/s10052-020-7612-8.

[111] O. Scholten, K. Werner, and F. Rusydi, "A macroscopic description of coherent geomagnetic radiation from cosmic-ray air showers," *Astroparticle Physics*, vol. 29, no. 2, pp. 94–103, Mar. 2008. DOI: 10.1016/j.astropartphys.2007.11.012.

[112] G. A. Askar'yan, "Excess negative charge of an electron-photon shower and its coherent radio emission," *Zh. Eksp. Teor. Fiz.*, vol. 41, pp. 616–618, 1961.

[113] G. A. Askar'yan, "Coherent Radio Emission from Cosmic Showers in Air and in Dense Media," *Soviet Journal of Experimental and Theoretical Physics*, vol. 21, p. 658, May 1965.

[114] S. Chiche *et al.*, "New features in the radio-emission of very inclined air-showers," *PoS*, vol. ARENA2022, p. 035, 2023. DOI: 10.22323/1.424.0035.

[115] F. Schröder, "Status of the radio technique for cosmic-ray induced air showers," *Nuclear and Particle Physics Proceedings*, vol. 279-281, pp. 190–197, Oct. 2016. DOI: 10.1016/j.nuclphysbps.2016.10.027.

[116] O. Scholten, K. D. de Vries, and K. Werner, "Coherent radiation from extensive air showers," *Nuclear Instruments and Methods in Physics Research Section A: Accelerators, Spectrometers, Detectors and Associated Equipment*, vol. 662, S80–S84, Jan. 2012. DOI: 10.1016/j.nima.2010.11.125.

[117] A. Zilles, "Emission of Radio Waves in Particle Showers: Validation of microscopic simulations with the SLAC T-510 experiment and their potential in the future Square Kilometre Array," PhD Thesis, KIT, Karlsruhe, 2016. DOI: 10.5445/IR/1000065046.

[118] K. Werner, K. D. de Vries, and O. Scholten, "A realistic treatment of geomagnetic Cherenkov radiation from cosmic ray air showers," *Astroparticle Physics*, vol. 37, pp. 5–16, 2012. DOI: https://doi.org/10.1016/j.astropartphys.2012.07.007.

[119] A. Nelles *et al.*, "Measuring a Cherenkov ring in the radio emission from air showers at 110–190 MHz with LOFAR," *Astropart. Phys.*, vol. 65, pp. 11–21, 2015. DOI: 10.1016/j.astropartphys.2014.11.006.

[120] J. Alvarez-Muñiz, W. R. Carvalho, M. Tueros, and E. Zas, "Coherent Cherenkov radio pulses from hadronic showers up to EeV energies," *Astroparticle Physics*, vol. 35, no. 6, pp. 287–299, Jan. 2012. DOI: 10.1016/j.astropartphys.2011.10.002.

[121] J. A. Aguilar *et al.*, "In situ, broadband measurement of the radio frequency attenuation length at Summit Station, Greenland," Jan. 2022. DOI: 10.1017/jog.2022.40.

[122] J. Avva *et al.*, "An in situ measurement of the radio-frequency attenuation in ice at Summit Station, Greenland," *J. Glaciol.*, vol. 61, pp. 1005–1011, 2015. DOI: 10.3189/2015JoG15J057.

[123] C. Deaconu *et al.*, "Measurements and Modeling of Near-Surface Radio Propagation in Glacial Ice and Implications for Neutrino Experiments," *Phys. Rev.*, vol. D98, no. 4, p. 043 010, 2018. DOI: 10.1103/PhysRevD.98.043010.

[124] I. Kravchenko, D. Besson, and J. Meyers, "In situ index-of-refraction measurements of the South Polar firn with the RICE detector," *Journal of Glaciology*, vol. 50, no. 171, pp. 522–532, 2004. DOI: 10.3189/172756504781829800.

[125] S. V. Schytt, *Snow studies at Maudheim. Snowstudies inland. The inner structure of the ice shelf at Maudheim asshown by core drilling. (Glaciology II.)* (Sci. Results.). Norsk Polarinstitutt, 1958, pp. 1–64, Norwegian-British Swedish Antarctic Expedition. 1949-52.

[126] H. Landsman, L. Ruckman, and G. Varner, "AURA—A radio frequency extension to IceCube," *Nuclear Instruments and Methods in Physics Research Section A: Accelerators, Spectrometers, Detectors and Associated Equipment*, vol. 604, no. 1, Supplement, S70–S75, 2009, ARENA 2008. DOI: https://doi.org/10.1016/j.nima.2009.03.030.

[127] A. Hallgreen, "In ice neutrino radio detection projects," *PoS*, vol. NEUTEL2015, p. 035, 2016. DOI: 10.22323/1.244.0035.

[128] S. W. Barwick *et al.*, "Constraints on Cosmic Neutrino Fluxes from the Antarctic Impulsive Transient Antenna Experiment," *Phys. Rev. Lett.*, vol. 96, p. 171 101, 17 May 2006. DOI: 10.1103/PhysRevLett.96.171101.

[129] H. Schoorlemmer *et al.*, "Energy and flux measurements of ultra-high energy cosmic rays observed during the first ANITA flight," *Astroparticle Physics*, vol. 77, pp. 32–43, Apr. 2016. DOI: 10.1016/j.astropartphys.2016.01.001.

[130] P. Allison *et al.*, "Performance of two Askaryan Radio Array stations and first results in the search for ultrahigh energy neutrinos," *Phys. Rev.*, vol. D93, no. 8, p. 082 003, 2016. DOI: 10.1103/PhysRevD.93.082003.

[131] A. Connolly *et al.*, "Recent Results from The Askaryan Radio Array," *PoS*, vol. ICRC2019, p. 858, 2021. DOI: 10.22323/1.358.0858.

[132] P. Allison *et al.*, "Design and performance of an interferometric trigger array for radio detection of high-energy neutrinos," *Nucl. Instrum. Meth. A*, vol. 930, pp. 112–125, 2019. DOI: 10.1016/j.nima.2019.01.067.

[133] S. W. Barwick *et al.*, "Design and Performance of the ARIANNA HRA-3 Neutrino Detector Systems," *IEEE Trans. Nucl. Sci.*, vol. 62, no. 5, pp. 2202–2215, 2015. DOI: 10.1109/TNS.2015.2468182.

[134] A. Anker *et al.*, "Targeting ultra-high energy neutrinos with the ARIANNA experiment," *Advances in Space Research*, vol. 64, no. 12, pp. 2595–2609, Dec. 2019. DOI: 10.1016/j.asr.2019.06.016.

[135] M. G. Aartsen *et al.*, "IceCube-Gen2: the window to the extreme Universe," *J. Phys. G*, vol. 48, no. 6, p. 060 501, 2021. DOI: 10.1088/1361-6471/abbd48.

[136] R. Abbasi *et al.*, *The IceCube-Gen2 Neutrino Observatory*, https://icecube-gen2.wisc.edu/science/publications/TDR.

[137] Q. Abarr *et al.*, "The Payload for Ultrahigh Energy Observations (PUEO): a white paper," *JINST*, vol. 16, no. 08, P08035, 2021. DOI: 10.1088/1748-0221/16/08/P08035.

[138] D. Southall *et al.*, "Design and initial performance of the prototype for the BEACON instrument for detection of ultrahigh energy particles," *Nucl. Instrum. Meth. A*, vol. 1048, p. 167 889, 2023. DOI: 10.1016/j.nima.2022.167889.

[139] S.-H. Wang *et al.*, "TAROGE-M: radio antenna array on antarctic high mountain for detecting near-horizontal ultra-high energy air showers," *JCAP*, vol. 11, p. 022, 2022. DOI: 10.1088/1475-7516/2022/11/022.

[140] J. Álvarez-Muñiz *et al.*, "The Giant Radio Array for Neutrino Detection (GRAND): Science and Design," *Sci. China Phys. Mech. Astron.*, vol. 63, no. 1, p. 219 501, 2020. DOI: 10.1007/s11433-018-9385-7.

[141] S. Prohira *et al.*, "The Radar Echo Telescope for Cosmic Rays: Pathfinder experiment for a next-generation neutrino observatory," *Phys. Rev. D*, vol. 104, no. 10, p. 102 006, 2021. DOI: 10.1103/PhysRevD.104.102006.

[142] C. Welling and the RNO-G Collaboration, "Precision measurement of the index of refraction of deep glacial ice at radio frequencies at Summit Station, Greenland," *EGUsphere*, vol. 2023, pp. 1–14, 2023. DOI: 10.5194/egusphere-2023-745.

[143] J. A. Aguilar *et al.*, "Radiofrequency Ice Dielectric Measurements at Summit Station, Greenland," *Journal of Glaciology*, pp. 1–12, 2023. DOI: 10.1017/jog.2023.72.

[144] I. Kravchenko *et al.*, "Performance and simulation of the RICE detector," *Astropart. Phys.*, vol. 19, pp. 15–36, 2003. DOI: 10.1016/S0927-6505(02)00194-9.

[145] J. Avva *et al.*, "Development Toward a Ground-Based Interferometric Phased Array for Radio Detection of High Energy Neutrinos," *Nucl. Instrum. Meth.*, vol. A869, pp. 46–55, 2017. DOI: 10.1016/j.nima.2017.07.009.

[146] J. M. Roberts *et al.*, "LAB4D: A Low Power, Multi-GSa/s, Transient Digitizer with Sampling Timebase Trimming Capabilities," *Nucl. Instrum. Meth. A*, vol. 925, pp. 92–100, 2019. DOI: 10.1016/j.nima.2019.01.091.

[147] J. A. Aguilar *et al.*, "Hardware Development for the Radio Neutrino Observatory in Greenland (RNO-G)," *PoS*, vol. ICRC2021, p. 1058, 2021. DOI: 10.22323/1.395.1058.

[148] R. S. Roger, C. H. Costain, T. L. Landecker, and C. M. Swerdlyk, "The radio emission from the Galaxy at 22 MHz," *Astronomy and Astrophysics Supplement Series*, vol. 137, no. 1, pp. 7–19, May 1999. DOI: 10.1051/aas:1999239.

[149] S. Hallmann *et al.*, "Status and recent results from the Radio Neutrino Observatory in Greenland (RNO-G)," *PoS*, vol. ICRC2023, p. 1043, 2023. DOI: 10.22323/1.444.1043.

[150] M. Büsken, T. Fodran, and T. Huege, "Uncertainties of the 30–408 MHz Galactic emission as a calibration source for radio detectors in astroparticle physics," *Astron. Astrophys.*, vol. 679, A50, 2023. DOI: 10.1051/0004-6361/202245382.

[151] S. Agarwal *et al.*, "Solar flare observations with the Radio Neutrino Observatory Greenland (RNO-G)," Apr. 2024, [arXiv:2404.14995].

[152] D. Seckel, S. Seunarine, J. Clem, and A. Javaid, "In-Ice radio detection of air shower cores," in *30th International Cosmic Ray Conference*, vol. 5, Jul. 2007, pp. 1029–1032.

[153] K. D. de Vries, S. Buitink, N. van Eijndhoven, T. Meures, A. Ó Murchadha, and O. Scholten, "The cosmic-ray air-shower signal in Askaryan radio detectors," *Astropart. Phys.*, vol. 74, pp. 96–104, 2016. DOI: 10.1016/j.astropartphys.2015.10.003.

[154] R. Rice-Smith *et al.*, "Assessing the Background Rate due to Cosmic Ray Core Scattering from Internal Reflection Layers in the South Pole Ice Cap," *Zenodo*, Jul. 2022. DOI: 10.5281/zenodo.6785120.

[155] S. De Kockere, K. D. de Vries, N. van Eijndhoven, and U. A. Latif, "Simulation of in-ice cosmic ray air shower induced particle cascades," *Phys. Rev. D*, vol. 106, no. 4, p. 043 023, 2022. DOI: 10.1103/PhysRevD.106.043023.

[156] S. De Kockere *et al.*, "Simulation of radio signals from cosmic-ray cascades in air and ice as observed by in-ice Askaryan radio detectors," Mar. 2024, [arXiv:2403.15358].

[157] J. Reed, *An Introduction to Ultra Wideband Communication Systems* (Prentice Hall communications engineering and emerging technologies series). Prentice Hall PTR, 2005.

[158] B. Kolundzija, "WIPL-D: from university software to company product," *Proceedings of the 5th European Conference on Antennas and Propagation*, vol. EUCAP 2011, pp. 2844–2846, 2011.

[159] A. Eimer, "Study of the log-periodic dipole antenna for the Radio Neutrino Observatory Greenland," Master Thesis, Friedrich-Alexander Universität Erlangen-Nürnberg, 2023.

[160] P. Abreu *et al.*, "Antennas for the detection of radio emission pulses from cosmic-ray induced air showers at the Pierre Auger Observatory," *Journal of Instrumentation*, vol. 7, no. 10, P10011–P10011, Oct. 2012. DOI: 10.1088/1748-0221/7/10/p10011.

[161] S. Kleinfelder, "A 4096 cell switched capacitor analog waveform storage integrated circuit," *IEEE Transactions on Nuclear Science*, vol. 37, no. 3, pp. 1230–1236, 1990. DOI: 10.1109/23.57371.

[162] P. Allison, *RADIANT*, https://github.com/barawn/radiant/tree/master, 2023.

[163] C. Deaconu, F. Schlüter, and R. Krebs, *librno-g*, https://github.com/RNO-G/librno-g/tree/master, 2020.

[164] U. Mishra and J. Singh, *Semiconductor device physics and design*, en, 2008th ed. New York, NY: Springer, Nov. 2007.

[165] Hewlett-Packard, "Designing Detectors for RF/ID Tags," Hewlett-Packard, Application Note AN 1089, 1997.

[166] Hewlett-Packard, "The Zero Bias Schottky Diode Detector at Temperature Extremes – Problems and Solutions," Hewlett-Packard, Application Note AN 1090, 1997.

[167] L. Pyras, "Optimizing the triggering strategy for the detection of cosmic rays with the Radio Neutrino Observatory Greenland (RNO-G)," Master Thesis, Humboldt-Universität zu Berlin, 2020.

[168] G. S. Varner, "The modern FPGA as discriminator, TDC and ADC," *JINST*, vol. 1, P07001, 2006. DOI: 10.1088/1748-0221/1/07/P07001.

[169] Xilinx products, *Artix-7 FPGAs Data Sheet: DC and AC Switching Characteristics*, https://docs.amd.com/v/u/en-US/ds181_Artix_7_Data_Sheet.

[170] J. Henrichs *et al.*, "Searching for cosmic-ray air showers with RNO-G," *PoS*, vol. ICRC2023, p. 259, 2023. DOI: 10.22323/1.444.0259.

[171] B. Mercurio, "A simulation of the ANITA experiment with a focus on secondary interactions," Doctoral dissertation, Ohio State University, 2009.

[172] T. Karg, F. Schlüter, L. Pyras, and J. Henrichs, *radiant-test*, https://github.com/RNO-G/radiant-test, 2023.

[173] RNO-G Collaboration, *RNO-G Hardware Database*, https://radio.zeuthen.desy.de/Display_RADIANT_tests.

[174] Analog Devices, *HMC321ALP4E*, https://www.analog.com/media/en/technical-documentation/data-sheets/hmc321a.pdf.

[175] T. Huege, M. Ludwig, and C. W. James, "Simulating radio emission from air showers with CoREAS," *AIP Conf. Proc.*, vol. 1535, no. 1, R. Lahmann *et al.*, Eds., p. 128, 2013. DOI: 10.1063/1.4807534.

[176] C. W. James, H. Falcke, T. Huege, and M. Ludwig, "General description of electromagnetic radiation processes based on instantaneous charge acceleration in "endpoints"," *Physical Review E*, vol. 84, no. 5, Nov. 2011. DOI: 10.1103/physreve.84.056602.

[177] T. Huege, "Radio detection of cosmic ray air showers in the digital era," *Phys. Rept.*, vol. 620, pp. 1–52, 2016. DOI: 10.1016/j.physrep.2016.02.001.

[178] S. Buitink *et al.*, "Method for high precision reconstruction of air shower X_{max} using two-dimensional radio intensity profiles," *Phys. Rev. D*, vol. 90, no. 8, p. 082 003, 2014. DOI: 10.1103/PhysRevD.90.082003.

[179] A. Corstanje *et al.*, "A high-precision interpolation method for pulsed radio signals from cosmic-ray air showers," *JINST*, vol. 18, no. 09, P09005, 2023. DOI: 10.1088/1748-0221/18/09/P09005.

[180] J. Alvarez-Muniz, W. R. Carvalho Jr., and E. Zas, "Monte Carlo simulations of radio pulses in atmospheric showers using ZHAireS," *Astropart. Phys.*, vol. 35, pp. 325–341, 2012. DOI: 10.1016/j.astropartphys.2011.10.005.

[181] J. Alvarez-Muñiz, W. R. Carvalho Jr., H. Schoorlemmer, and E. Zas, "Radio pulses from ultra-high energy atmospheric showers as the superposition of Askaryan and geomagnetic mechanisms," *Astropart. Phys.*, vol. 59, pp. 29–38, 2014. DOI: 10.1016/j.astropartphys.2014.04.004.

[182] E. Zas, F. Halzen, and T. Stanev, "Electromagnetic pulses from high-energy showers: Implications for neutrino detection," *Phys. Rev. D*, vol. 45, pp. 362–376, 1992. DOI: 10.1103/PhysRevD.45.362.

[183] J. Alvarez-Muniz, A. Romero-Wolf, and E. Zas, "Cherenkov radio pulses from electromagnetic showers in the time-domain," *Phys. Rev. D*, vol. 81, p. 123 009, 2010. DOI: 10.1103/PhysRevD.81.123009.

[184] M. Gottowik, C. Glaser, T. Huege, and J. Rautenberg, "Determination of the absolute energy scale of extensive air showers via radio emission: systematic uncertainty of underlying first-principle calculations," *Astropart. Phys.*, vol. 103, pp. 87–93, 2018. DOI: 10.1016/j.astropartphys.2018.07.004.

[185] S. Ostapchenko, "Monte Carlo treatment of hadronic interactions in enhanced Pomeron scheme: QGSJET-II model," *Phys. Rev. D*, vol. 83, p. 014 018, 1 2011. DOI: 10.1103/PhysRevD.83.014018.

[186] M. Bleicher *et al.*, "Relativistic hadron-hadron collisions in the ultra-relativistic quantum molecular dynamics model," *Journal of Physics G: Nuclear and Particle Physics*, vol. 25, no. 9, pp. 1859–1896, Sep. 1999. DOI: 10.1088/0954-3899/25/9/308.

[187] C. Glaser *et al.*, "NuRadioReco: A reconstruction framework for radio neutrino detectors," *Eur. Phys. J. C*, vol. 79, no. 6, p. 464, 2019. DOI: 10.1140/epjc/s10052-019-6971-5.

[188] C. Glaser, M. Erdmann, J. R. Hörandel, T. Huege, and J. Schulz, "Simulation of Radiation Energy Release in Air Showers," *JCAP*, vol. 09, p. 024, 2016. DOI: 10.1088/1475-7516/2016/09/024.

[189] E. Oberla *et al.*, "Low-Power Radiofrequency Systems for the RNO-G Project," *PoS*, vol. ICRC2023, p. 1171, 2023. DOI: 10.22323/1.444.1171.

[190] H. Zheng *et al.*, "An improved model of diffuse galactic radio emission from 10 MHz to 5 THz," *Mon. Not. Roy. Astron. Soc.*, vol. 464, no. 3, pp. 3486–3497, 2017. DOI: 10.1093/mnras/stw2525.

[191] D. C. Price, *Data Files for PyGSM: Python interface to the Global Sky Model*, Zenodo, Oct. 2019. DOI: 10.5281/zenodo.3479985.

[192] A. de Oliveira-Costa, M. Tegmark, B. M. Gaensler, J. Jonas, T. L. Landecker, and P. Reich, "A model of diffuse Galactic radio emission from 10 MHz to 100 GHz," *Monthly Notices of the Royal Astronomical Society*, vol. 388, no. 1, pp. 247–260, Jul. 2008. DOI: 10.1111/j.1365-2966.2008.13376.x.

[193] G. Rybicki and A. Lightman, *Radiative Processes in Astrophysics* (Physics textbook). Wiley, 2008.

[194] N. Feigl, "Development of a standard test and calibration procedure for the hardware of the Radio Neutrino Detector RNO-G," Master Thesis, Friedrich-Alexander Universität Erlangen-Nürnberg, 2020.

[195] T. Glüsenkamp *et al.*, "VAE-based latent-space classification of RNO-G data," *PoS*, vol. ICRC-2023, p. 1056, 2023. DOI: 10.22323/1.444.1056.

[196] P. Laub, "Machine-Learning-based Background Identification for the Radio Neutrino Observatory Greenland," Master Thesis, Friedrich-Alexander Universität Erlangen-Nürnberg, 2023.

[197] V. Verzi *et al.*, "Measurement of the energy spectrum of ultra-high energy cosmic rays using the Pierre Auger Observatory," *PoS*, vol. ICRC2019, p. 450, 2020. DOI: 10.22323/1.358.0450.

[198] J. A. Aguilar *et al.*, "Triboelectric backgrounds to radio-based polar ultra-high energy neutrino (UHEN) experiments," *Astropart. Phys.*, vol. 145, p. 102 790, 2023. DOI: 10.1016/j.astropartphys.2022.102790.

[199] A. Coleman *et al.*, "Enhancing the Sensitivity of RNO-G Using a Machine-learning Based Trigger," *PoS*, vol. ICRC2023, p. 1100, 2023. DOI: 10.22323/1.444.1100.

[200] C. Glaser, A. Coleman, and T. Glusenkamp, "NuRadioOpt: Optimization of Radio Detectors of Ultra-High Energy Neutrinos through Deep Learning and Differential Programming," *PoS*, vol. ICRC2023, p. 1114, 2023. DOI: 10.22323/1.444.1114.

[201] R. Valk, "Cosmic ray efficiency studies for the Radio Neutrino Observatory Greenland (RNO-G)," Bachelor Thesis, Friedrich-Alexander Universität Erlangen-Nürnberg, 2024.

[202] J. Albrecht *et al.*, "The Muon Puzzle in cosmic-ray induced air showers and its connection to the Large Hadron Collider," *Astrophys. Space Sci.*, vol. 367, no. 3, p. 27, 2022. DOI: 10.1007/s10509-022-04054-5.

[203] C. Gámez, M. Gutiérrez, J. S. Martínez, and M. Masip, "High energy muons in extensive air showers," *JCAP*, vol. 01, p. 057, 2020. DOI: 10.1088/1475-7516/2020/01/057.

[204] J. I. Illana, M. Masip, and D. Meloni, "Atmospheric lepton fluxes at ultrahigh energies," *JCAP*, vol. 09, p. 008, 2009. DOI: 10.1088/1475-7516/2009/09/008.

[205] A. Bhattacharya, R. Enberg, M. H. Reno, I. Sarcevic, and A. Stasto, "Perturbative charm production and the prompt atmospheric neutrino flux in light of RHIC and LHC," *JHEP*, vol. 06, p. 110, 2015. DOI: 10.1007/JHEP06(2015)110.

[206] A. Bhattacharya and J. R. Cudell, "Forward charm-production models and prompt neutrinos at IceCube," *Journal of High Energy Physics*, vol. 2018, no. 11, Nov. 2018. DOI: 10.1007/jhep11(2018)150.

[207] Fedynitch, Anatoli and Engel, Ralph and Gaisser, Thomas and Riehn, Felix and Stanev, Todor, "Calculation of conventional and prompt lepton fluxes at very high energy," *EPJ Web of Conferences*, vol. 99, Mar. 2015. DOI: 10.1051/epjconf/20159908001.

[208] J. I. Illana, P. Lipari, M. Masip, and D. Meloni, "Atmospheric lepton fluxes at very high energy," *Astropart. Phys.*, vol. 34, pp. 663–673, 2011. DOI: 10.1016/j.astropartphys.2011.01.001.

[209] R. Engel, D. Heck, and T. Pierog, "Extensive air showers and hadronic interactions at high energy," *Ann. Rev. Nucl. Part. Sci.*, vol. 61, pp. 467–489, 2011. DOI: 10.1146/annurev.nucl.012809.104544.

[210] L. V. Volkova, "Cosmic-ray muons at ultrahigh energies," *Phys. Atom. Nucl.*, vol. 74, pp. 318–323, 2011. DOI: 10.1134/S1063778811020207.

[211] S. Ostapchenko, M. V. Garzelli, and G. Sigl, "On the prompt contribution to the atmospheric neutrino flux," *Phys. Rev. D*, vol. 107, no. 2, p. 023 014, 2023. DOI: 10.1103/PhysRevD.107.023014.

[212] S. I. Sinegovsky, A. A. Kochanov, T. S. Sinegovskaya, A. Misaki, and N. Takahashi, "Atmospheric muon flux at PeV energies," *Int. J. Mod. Phys. A*, vol. 25, pp. 3733–3740, 2010. DOI: 10.1142/S0217751X10049748.

[213] R. Enberg, M. H. Reno, and I. Sarcevic, "Prompt neutrino fluxes from atmospheric charm," *Phys. Rev. D*, vol. 78, p. 043 005, 2008. DOI: 10.1103/PhysRevD.78.043005.

[214] M. V. Garzelli, S. Moch, and G. Sigl, "Lepton fluxes from atmospheric charm revisited," *JHEP*, vol. 10, p. 115, 2015. DOI: 10.1007/JHEP10(2015)115.

[215] R. Gauld, J. Rojo, L. Rottoli, and J. Talbert, "Charm production in the forward region: constraints on the small-x gluon and backgrounds for neutrino astronomy," *JHEP*, vol. 11, p. 009, 2015. DOI: 10.1007/JHEP11(2015)009.

[216] A. Bhattacharya *et al.*, "Prompt atmospheric neutrino fluxes: perturbative QCD models and nuclear effects," *JHEP*, vol. 11, p. 167, 2016. DOI: 10.1007/JHEP11(2016)167.

[217] Y. S. Jeong, W. Bai, M. Diwan, M. V. Garzelli, F. K. Kumar, and M. H. Reno, "Neutrinos from charm: forward production at the LHC and in the atmosphere," *PoS*, vol. ICRC2021, p. 1218, 2021. DOI: 10.22323/1.395.1218.

[218] T. Pierog, "Air Shower Simulation with a New Generation of post-LHC Hadronic Interaction Models in CORSIKA," in *Proceedings of 35th International Cosmic Ray Conference — PoS(ICRC2017)*, vol. 301, 2017, p. 1100. DOI: 10.22323/1.301.1100.

[219] S. J. Sciutto, "AIRES: A system for air shower simulations," Nov. 1999. DOI: 10.13140/RG.2.2.12566.40002.

[220] T. Pierog, I. Karpenko, J. M. Katzy, E. Yatsenko, and K. Werner, "EPOS LHC: Test of collective hadronization with data measured at the CERN Large Hadron Collider," *Phys. Rev. C*, vol. 92, no. 3, p. 034 906, 2015. DOI: 10.1103/PhysRevC.92.034906.

[221] S. Ostapchenko, "Monte Carlo treatment of hadronic interactions in enhanced Pomeron scheme: I. QGSJET-II model," *Phys. Rev. D*, vol. 83, p. 014 018, 2011. DOI: 10.1103/PhysRevD.83.014018.

[222] F. Riehn, H. P. Dembinski, R. Engel, A. Fedynitch, T. K. Gaisser, and T. Stanev, "The hadronic interaction model SIBYLL 2.3c and Feynman scaling," *PoS*, vol. ICRC2017, p. 301, 2018. DOI: 10.22323/1.301.0301.

[223] D. Soldin, "Laterally Separated Muons from Cosmic Ray Air Showers Measured with the ICECUBE Neutrino Observatory," Ph.D. dissertation, Wuppertal U., 2017.

[224] A. Fedynitch, F. Riehn, R. Engel, T. K. Gaisser, and T. Stanev, "Hadronic interaction model sibyll 2.3c and inclusive lepton fluxes," *Phys. Rev. D*, vol. 100, no. 10, p. 103 018, 2019. DOI: 10.1103/PhysRevD.100.103018.

[225] H. P. Dembinski, R. Engel, A. Fedynitch, T. Gaisser, F. Riehn, and T. Stanev, "Data-driven model of the cosmic-ray flux and mass composition from 10 GeV to 10^{11} GeV," *PoS*, vol. ICRC2017, p. 533, 2018. DOI: 10.22323/1.301.0533.

[226] T. K. Gaisser, "Spectrum of cosmic-ray nucleons, kaon production, and the atmospheric muon charge ratio," *Astroparticle Physics*, vol. 35, no. 12, pp. 801–806, Jul. 2012. DOI: 10.1016/j.astropartphys.2012.02.010.

[227] S. Thoudam *et al.*, "Cosmic-ray energy spectrum and composition up to the ankle: the case for a second Galactic component," *Astron. Astrophys.*, vol. 595, A33, 2016. DOI: 10.1051/0004-6361/201628894.

[228] M. Unger, G. R. Farrar, and L. A. Anchordoqui, "Origin of the ankle in the ultrahigh energy cosmic ray spectrum, and of the extragalactic protons below it," *Phys. Rev. D*, vol. 92, no. 12, p. 123 001, 2015. DOI: 10.1103/PhysRevD.92.123001.

[229] J. Heinze, A. Fedynitch, D. Boncioli, and W. Winter, "A new view on Auger data and cosmogenic neutrinos in light of different nuclear disintegration and air-shower models," *Astrophys. J.*, vol. 873, no. 1, p. 88, 2019. DOI: 10.3847/1538-4357/ab05ce.

[230] J. P. Rachen, T. Stanev, and P. L. Biermann, "Extragalactic ultrahigh-energy cosmic rays. 2. Comparison with experimental data," *Astron. Astrophys.*, vol. 273, p. 377, 1993.

[231] V. S. Berezinsky, S. I. Grigoreva, and B. I. Hnatyk, "Extragalactic UHE proton spectrum and prediction of flux of iron-nuclei at 10^8 GeV – 10^9 GeV," *Nucl. Phys. B Proc. Suppl.*, vol. 151, P. K. F. Grieder, B. Pattison, and L. K. Resvanis, Eds., pp. 497–500, 2006. DOI: 10.1016/j.nuclphysbps.2005.07.088.

[232] C. Glaser, D. García-Fernández, and A. Nelles, "Prospects for neutrino-flavor physics with in-ice radio detectors," *PoS(ICRC2021)1231*, 2021. DOI: 10.22323/1.395.1231.

[233] J. H. Koehne *et al.*, "PROPOSAL: A tool for propagation of charged leptons," *Comput. Phys. Commun.*, vol. 184, pp. 2070–2090, 2013. DOI: 10.1016/j.cpc.2013.04.001.

[234] J. A. Aguilar *et al.*, "Reconstructing the neutrino energy for in-ice radio detectors: A study for the Radio Neutrino Observatory Greenland (RNO-G)," *Eur. Phys. J. C*, vol. 82, no. 2, p. 147, 2022. DOI: 10.1140/epjc/s10052-022-10034-4.

[235] G. J. Feldman and R. D. Cousins, "A Unified approach to the classical statistical analysis of small signals," *Phys. Rev. D*, vol. 57, pp. 3873–3889, 1998. DOI: 10.1103/PhysRevD.57.3873.

[236] A. Aab *et al.*, "Measurement of the Radiation Energy in the Radio Signal of Extensive Air Showers as a Universal Estimator of Cosmic-Ray Energy," *Phys. Rev. Lett.*, vol. 116, no. 24, p. 241 101, 2016. DOI: 10.1103/PhysRevLett.116.241101.

[237] E. Roulet, G. Sigl, A. van Vliet, and S. Mollerach, "PeV neutrinos from the propagation of ultra-high energy cosmic rays," *JCAP*, vol. 01, p. 028, 2013. DOI: 10.1088/1475-7516/2013/01/028.

[238] R. Alves Batista *et al.*, "CRPropa 3 - A Public Astrophysical Simulation Framework for Propagating Extraterrestrial Ultra-High Energy Particles," *JCAP*, vol. 05, p. 038, 2016. DOI: 10.1088/1475-7516/2016/05/038.

[239] V. B. Valera, M. Bustamante, and C. Glaser, "Near-future discovery of the diffuse flux of ultrahigh-energy cosmic neutrinos," *Phys. Rev. D*, vol. 107, no. 4, p. 043 019, 2023. DOI: 10.1103/PhysRevD.107.043019.

[240] A. Anker *et al.*, "White Paper: ARIANNA-200 high energy neutrino telescope," Apr. 2020, [arXiv:2004.09841].

[241] K. Fang and K. Murase, "Linking High-Energy Cosmic Particles by Black Hole Jets Embedded in Large-Scale Structures," *Nature Phys.*, vol. 14, no. 4, pp. 396–398, 2018. DOI: 10.1038/s41567-017-0025-4.

[242] X. Rodrigues, J. Heinze, A. Palladino, A. van Vliet, and W. Winter, "Active Galactic Nuclei Jets as the Origin of Ultrahigh-Energy Cosmic Rays and Perspectives for the Detection of Astrophysical Source Neutrinos at EeV Energies," *Phys. Rev. Lett.*, vol. 126, no. 19, p. 191 101, 2021. DOI: 10.1103/PhysRevLett.126.191101.

[243] L. Pyras, C. Glaser, S. Hallmann, and A. Nelles, "Atmospheric muons at PeV energies in radio neutrino detectors," *JCAP*, vol. 10, p. 043, 2023. DOI: 10.1088/1475-7516/2023/10/043.

[244] A. Bhattacharya, F. Kling, I. Sarcevic, and A. M. Stasto, "Forward neutrinos from charm at the large hadron collider," *Phys. Rev. D*, vol. 109, p. 014 040, 1 Jan. 2024. DOI: 10.1103/PhysRevD.109.014040.

Acknowledgements

First, I would like to thank Anna Nelles for being my supervisor, for giving me the opportunity to work on RNO-G and for supporting me in every way possible.

Since the time I started as a master student, RNO-G has evolved from a project without funding to an operating detector, producing scientific results. The work on RNO-G does not fail to fill my working days with wonder and excitement and I am truly grateful to be able to take part in this adventure. Thank you, to all members of the collaboration, for sharing your expertise and knowledge and introducing me to the different aspects and stages of building and running an experiment. It was an unforgettable experience to be part of the deployment team and to drill holes for the station in Greenland (and an outfall hole for the Big House).

Furthermore, I want to thank Timo for supervising me while I tinkered with hardware and allowing me to make all the mistakes on my own without losing any patience. It was a great pleasure to work with you.

I would like to thank the radio neutrino group at ECAP and DESY. Thank you, Jakob, for working with me on cosmic rays, discussing physics, and complaining about boards. Thank you, Steffen, for reliably answering all my physics and coding questions and forcing me to train overhang. Thank you, Ilse, Christoph and Zack for getting me started and through the covid years with a book or two. Thanks to Felix, Jakob and Timo (again) for completing the Radiant testing together.

I also want to thank all the people at DESY who guided me, cheered me up and supported me. Thank you, JvS, for discussing muons and being the instance for computing and cluster issues. Thank you, Marko, for patiently explaining all the electronic stuff and trick circuits which I came across.

Thank you, felix, for proofreading everything at the last minute and for not getting tired to discuss both current and future matters of physics with me.

Finally, I would like to thank my friends and family who put up with me while I was working on my PhD. I could not have done it without you, especially Josh, Raphael, Maro, Sophia, Tim, Maik, Pauline, Christine, Olaf, Vivian, Michael, Helene und Hannah. I can't wait to celebrate with you.